

***In Vitro* Evaluation of Cytotoxicity and Cellular Uptake of
Alternating Copolymers for use as Drug Delivery Vehicles**

by

Michelle Teresa Miller

B.S., Chemical Engineering
Massachusetts Institute of Technology, 2000

Submitted to the Department of Chemical Engineering
in partial fulfillment of the requirements for the degree of

DOCTOR OF PHILOSOPHY IN CHEMICAL ENGINEERING

at the

MASSACHUSETTS INSTITUTE OF TECHNOLOGY

June 2009

© Massachusetts Institute of Technology 2009
All Rights Reserved

Signature of Author: _____
Department of Chemical Engineering
May 28, 2009

Certified by: _____
Clark K. Colton
Professor of Chemical Engineering
Thesis Supervisor

Accepted by: _____
William M. Deen
Professor of Chemical Engineering
Chairman, Committee for Graduate Students

-Intentionally Left Blank-

***In Vitro* Evaluation of Cytotoxicity and Cellular Uptake of Alternating Copolymers for Use as Drug Delivery Vehicles**

by

Michelle Teresa Miller

Submitted to the Department of Chemical Engineering on May 28, 2009 in partial fulfillment of the requirements for the degree of Doctor of Philosophy in Chemical Engineering

Abstract

Cancer is the collective group of diseases distinguished by uninhibited growth and spread of abnormal cells. It often results in death if the spread is not controlled. Most cancers are treated by surgery, radiation, chemotherapy, hormones, or immunotherapy. However, currently there are many issues with these forms of treatment, namely the lack of ability to consistently remove the entire tumor and the side effect of killing normal cells during the treatment process. Therefore there has been an increased interest in targeted drug delivery to tumors to specifically kill cancer cells.

We have developed a highly adaptable amphiphilic alternating copolymer system that self-assembles into micelles for therapeutic delivery applications in cancer. The synthetic scheme includes the enzymatic polymerization of multifunctional linker molecules (dimethyl 5-hydroxyisophthalate) with poly(ethylene glycol). This chemo-enzymatic synthesis is much faster and more convenient than an entirely chemical synthesis. Subsequent synthetic steps have been developed to attach ligands (for targeting), perfluorocarbons (^{19}F MR imaging), fluorescent dyes (NIRF imaging), and radioiodine (nuclear imaging and radioimmunotherapy) to the backbone. Attachment of hydrocarbon or perfluorocarbon sidechains provides amphiphilicity to produce the multimodal self-assembling micelles. Additionally, encapsulation procedures for chemotherapeutic agents, doxorubicin and paclitaxel, have been established. These unique alternating copolymer micelle nanoparticles were designed as delivery vehicles targeted to human cancer cells expressing the underglycosylated mucin-1 antigen, which is found on almost all epithelial cell adenocarcinomas, by use of the peptide EPPT or the folate receptor (FR) by use of folate.

Development of the synthetic schemes has been coupled with *in vitro* toxicity experiments using various cell viability assays to minimize the toxic effect of these copolymer structures. Overall the polymers used in this study were largely non-toxic when studied *in vitro*. The non-toxic polymers were brought forward into drug delivery and uptake experiments. Cell death due to doxorubicin increased with encapsulation in these alternating copolymers and increased slightly more with the addition of targeting ligand to the encapsulating polymer. Encapsulating paclitaxel in polymer also increased cell death as compared to free drug. These results demonstrate that these alternating copolymers have had some success as drug delivery vehicles.

Other *in vitro* studies included the investigation of cellular uptake by ^{125}I or ^3H radioactive analysis and fluorescence confocal microscopy. Microscopy images of the

fluorescently labeled polymer alone demonstrated that the polymer was likely confined to vesicles within the cytoplasm and it was not found in the nucleus, but encapsulated doxorubicin was shown to be largely confined to the nucleus. Theoretical models of polyvalent binding were employed to guide the design of the targeting polymers, however, the polymers used in this study appeared largely non-specific for the targeted cells when studied *in vitro*. The cellular uptake of polymer targeted with EPPT was twice that of untargeted polymer, although the difference was not statistically significant. For polymers containing folate, regardless of the amount of folate attached, the length of the spacer used, or the type of radioactive label used, the uptake did not decrease in the presence of an excess of folate, indicating a high amount of non-specific uptake for all folate-containing polymers.

When all of the folate-containing polymers were used to competitively inhibit ^3H -folate, almost all inhibited the uptake by 1 or 2 orders of magnitude, suggesting that the targeted polymers bind to the FR. An in-depth study of the cell-association of these polymers clarified that polymer was taken up non-specifically in high amounts. An excess of unlabeled folate, up- or down-regulation of the FR, and cleaving the FR did not measurably affect polymer uptake, but did alter folate uptake. It was also determined that a low level of polymer does bind to the FR. The amount of surface bound polymer was much lower than the total uptake of polymer in folate-free media for each polymer concentration investigated. In addition, the amount of surface bound folate and polymer decreased when the FR was cleaved, confirming the attachment of polymer to the FR.

Light scattering measurements showed that polymers that contain folate form aggregates of multiple polymers chains. It is possible that this aggregation was allowing a portion of the folate ligands to be hidden in the aggregate and unavailable for binding to the FR, the most likely mechanistic cause of the failure of the folate-containing polymers to demonstrate targeting. The versatility of these polymer constructs allows for continued optimization of a targeting delivery system for drugs and imaging agents as lessons discovered from passed studies are incorporated into the design.

Initial *in vivo* biodistribution studies were begun to explore the behavior of these polymers in mouse models of human cancers. The alternating copolymers used in this study do accumulate in tumors *in vivo*, comparable to the levels of accumulation observed in the literature. It is desirable to minimize the accumulation in other organs, while maximizing the accumulation in the tumor tissue. Therefore, this preliminary study warrants continued investigation of our polymer platform as a delivery vehicle *in vitro* and *in vivo*.

Thesis Supervisor: Clark K. Colton
Title: Professor of Chemical Engineering

Acknowledgements

The completion of my thesis would not have been possible without the advice, support, love, and friendship of many people. First, I would like to thank my advisor, Prof. Clark K. Colton, for all of his guidance and his continual demand for excellence. I would also like to thank my thesis committee members: Prof. Paula T. Hammond for her expertise in the field of polymer drug delivery, Prof. Robert J. Fisher for his continual feedback during the writing of my thesis, Prof. Anna V. Moore for her insight into *in vitro* and *in vivo* experiments and her willingness to demonstrate techniques in the lab, and Prof. Arthur C. Watterson for his knowledge of polymer chemistry and enthusiasm for supplying the materials for the work described here. In addition, I thank all those who have encouraged and inspired me throughout my career, from my professors at MIT to all those I worked with at Merck.

I have had the pleasure of collaborating with many other students and postdocs in the past 6 years. First and foremost, I must thank Kevin Brower in the Colton Lab. I could not have asked for a better colleague to work with so closely. Thank you for always taking the time to listen when I needed to think out loud and for trusting my guidance when you were seeking other opinions. I am a better researcher and team member for having worked with you. And most importantly, thank you for complimenting my retro-orbital injections with your organ harvesting. I would also like to specifically thank Dr. Jin Zhou Dawson from the Colton Lab for her collaboration on this project and Dr. Rahul Tyagi, Dr. Mukesh Pandey, and Bhavna Gupta from the Watterson Lab at the University of Massachusetts at Lowell for their continual patience with supplying material for my experiments. Additionally, I would like to thank Julie Shi, an undergraduate researcher from MIT, who supplemented my research with her experiments on this project.

I would like to thank all of the members of the Colton Lab throughout my years in graduate school. In particular, I thank Dr. Amy Johnson and Dr. Anna Pisanía for friendship and fun. I thank Amy, Anna, Dr. Daryl Powers, and Dr. Mike Rappel for teaching me the necessary techniques to get started on my research and providing insight throughout the years. I also thank Jeff Millman and Jit Hin Tan for making the lab fun my last year at MIT and always listening when I needed to vent. I could not have asked for better labmates.

My family has always supported me, in ways that I will likely never realize. I thank my parents, Rose (Mum) and Peter Ruel for teaching me the value of hard work and always believing I could do anything. I thank my sister, Rebecca Ruel, for continually showing me how to be optimistic in the face of any experience and amazing me with wisdom beyond her years. I thank my brother, Gerard Hardiman, my oldest friend, for repeatedly giving me the gift of laughter throughout our three decades together. I also thank my in-laws: Kay, Dennis, Eric, Sarah, Doug, and Andrea Miller for their faith in me and prayers for me. I thank all of my extended family and friends who are family to me: Gerard (Dad), Charlene, and Kelsey Hardiman; Scott and Christine (Tina) Dinesen for their continued interest in my pursuit of science; Andrea Dixon for always caring; and Allison Maher, Kerin Gregory, and Naomi Ouellette for being inspirational, successful, fun and loving friends for the past twenty years. I have also been fortunate to form many friendships at MIT that made my graduate school experience enjoyable and helped me keep my work and life in balance. A special thanks

to Kristin Mattern, Jane Rempel, Katharina Wilkins, Kris Wood, Ben Wang, and my entire ChemE softball team for all of the fun times. Thanks also to all of my friends from church – Margaret Sloat, Dave Sloat, Christina Gajewski, and Jahera Otieno – for all of their prayers and support.

And most importantly, I would like to thank my husband, Andy. On a daily basis, I am amazed that God has blessed me with such a supportive, caring, and loving husband. Not only has Andy helped me to relax when I needed to forget about my thesis, but he has also helped me to focus when necessary. He has listened to my rants during times of frustration and patiently given advice when I was discouraged by my project. I am also thankful for how much care he has provided over the past few months by cooking and cleaning when I needed to focus on my work. I could not have achieved this without him and I look forward to moving into the next phase of our life together.

Table of Contents

Chapter 1.	Introduction	25
1.1.	Cancer	25
1.2.	Circulating delivery systems.....	25
1.2.1.	<i>Liposomes</i>	26
1.2.2.	<i>Dendrimers</i>	27
1.2.3.	<i>Polymeric micelles</i>	28
1.3.	Alternating copolymer micelle nanoparticles	31
1.4.	Targeting of tumor cells.....	32
1.4.1.	<i>Passive targeting by the enhanced permeability and retention (EPR) effect</i>	32
1.4.2.	<i>Active targeting with ligand/antigen pairs</i>	33
1.5.	Chemotherapy	40
1.5.1.	<i>Doxorubicin</i>	43
1.5.2.	<i>Paclitaxel</i>	44
1.6.	Objectives	47
1.7.	Overview.....	47
1.8.	References.....	50
Chapter 2.	Synthesis of Alternating Copolymer Structures	65
2.1.	Enzymatic polymerization	65
2.2.	Attachment of hydrocarbon side chains.....	68
2.3.	Attachment of perfluorocarbon side chains	70
2.4.	Attachment of fluorescent labels	71
2.5.	Attachment of targeting ligands.....	72
2.5.1.	<i>EPPT</i>	72
2.5.2.	<i>Folate</i>	74
2.6.	Radiolabeling of polymers.....	75
2.7.	Encapsulation of chemotherapeutic drugs in polymer micelles	76
2.8.	Physical Characterization.....	77
2.9.	References.....	79
Chapter 3.	<i>In Vitro</i> Cytotoxicity of Polymers as Drug Delivery Vehicles	81
3.1.	Introduction.....	81
3.2.	Methods.....	82

TABLE OF CONTENTS

3.2.1.	<i>Materials and reagents</i>	82
3.2.2.	<i>Cell lines and culture</i>	83
3.2.3.	<i>Cytotoxicity assay</i>	83
3.2.4.	<i>Imaging of aggregation</i>	84
3.2.5.	<i>Encapsulation of drug</i>	85
3.2.6.	<i>Statistical analysis</i>	85
3.3.	Results.....	85
3.3.1.	<i>Backbone Polymers</i>	85
3.3.2.	<i>Base Polymers</i>	87
3.3.3.	<i>Targeting Polymers</i>	94
3.3.4.	<i>Imaging Polymers</i>	100
3.3.5.	<i>Complex Polymers</i>	105
3.3.6.	<i>Polymers as Drug Delivery Vehicles</i>	106
3.4.	Discussion.....	115
3.5.	References.....	118
Chapter 4. Evaluation of Cellular Uptake of Alternating Copolymers <i>In Vitro</i>		121
4.1.	Introduction.....	121
4.2.	Methods.....	124
4.2.1.	<i>Materials and reagents</i>	124
4.2.2.	<i>Cell lines and culture</i>	125
4.2.3.	<i>Confocal microscopy</i>	125
4.2.4.	<i>Radioactive uptake assay</i>	126
4.2.5.	<i>Cell counting</i>	128
4.2.6.	<i>Dynamic Light Scattering (DLS)</i>	128
4.2.7.	<i>Statistical analysis</i>	129
4.3.	Results.....	129
4.3.1.	<i>Cellular uptake of non-targeted polymers</i>	129
4.3.2.	<i>Theoretical Design of Targeting Polymers</i>	135
4.3.3.	<i>Cellular uptake of targeted polymers with EPPT by labeling with ¹²⁵I</i> <i>146</i>	
4.3.4.	<i>Cellular uptake of targeted polymers with folate by labeling with ¹²⁵I</i> <i>and ³H</i> <i>155</i>	
4.3.5.	<i>In-depth analysis of polymer cell-association</i>	172
4.3.6.	<i>Size measurement of polymer and free folate in folate-free media by</i> <i>DLS</i> <i>182</i>	
4.3.7.	<i>Comparison of theoretical calculations to experimental uptake results</i> <i>186</i>	
4.3.8.	<i>Cellular uptake of free ¹²⁵I</i>	186
4.4.	Discussion.....	189
4.5.	References.....	193

Chapter 5. Initial Biodistribution Studies of Alternating Copolymers <i>In Vivo</i>	201
5.1. Introduction.....	201
5.2. Methods.....	203
5.2.1. <i>Materials and reagents</i>	203
5.2.2. <i>Cell lines and culture</i>	203
5.2.3. <i>Cell counting</i>	204
5.2.4. <i>Tumor induction by subcutaneous injection in nu/nu mice</i>	204
5.2.5. <i>Biodistribution</i>	204
5.2.6. <i>Statistical analysis</i>	205
5.3. Results.....	205
5.3.1. <i>Biodistribution of non-targeted polymers in mice with no tumors</i>	205
5.3.2. <i>Biodistribution of targeted polymers in mice with tumors</i>	207
5.4. Discussion.....	210
5.5. References.....	211
Appendix I. Description of Methods for Polymer Synthesis	215
I.i. Synthesis of backbone polymer	215
I.ii. Attachment of hydrocarbon side chains.....	216
I.ii.a. <i>Ether bond</i>	216
I.ii.b. <i>Ester bond</i>	216
I.ii.c. <i>Ether ester bond</i>	217
I.ii.d. <i>Amide bond</i>	217
I.iii. Attachment of perfluorocarbon side chains	217
I.iii.a. <i>Ether ester bond</i>	217
I.iii.b. <i>Amide bond</i>	218
I.iv. Attachment of fluorescent labels	218
I.iv.a. <i>Rhodamine B</i>	218
I.iv.b. <i>Fluorescein isothiocyanate (FITC)</i>	219
I.iv.c. <i>Cy 5.5</i>	219
I.v. Attachment of targeting ligands.....	219
I.v.a. <i>EPPT with triethylene glycol spacer</i>	219
I.vi. Radiolabeling of polymers.....	221
I.vi.a. <i>Iodination with ¹²⁵I</i>	221
I.vi.b. <i>Methylation with ³H</i>	221
I.vii. Encapsulation of chemotherapeutic drugs in polymer micelles	222
I.vii.a. <i>Doxorubicin</i>	222
I.vii.b. <i>Paclitaxel</i>	222
I.viii. References.....	223

Appendix II. Table of Polymers.....	225
Appendix III. Cell Counting by Flow Cytometry.....	235
III.i. Methods.....	235
III.i.a. Materials and reagents	235
III.i.b. Cell lines and culture.....	235
III.i.c. Seeding of cells and solution make up	236
III.i.d. Cell counting.....	236
III.ii. Results and Discussion	236
Appendix IV. Validation of Scintillation Counting Sample Preparation 239	
IV.i. Methods.....	239
IV.i.a. Materials and reagents	239
IV.i.b. Cell lines and culture.....	239
IV.i.c. Validation of scintillation counting sample preparation.....	240
IV.i.d. Statistical analysis	240
IV.ii. Results and Discussion	241
Appendix V. Detailed Calculations for Theoretical Design of Targeting Polymers.....	243
V.i. Calculations for EPPT.....	243
V.i.a. Cooperativity polyvalency calculations.....	243
V.i.b. Structural polyvalency calculations.....	244
V.ii. Calculations for Folate.....	245
V.ii.a. Cooperativity polyvalency estimates.....	245
V.ii.b. Structural polyvalency estimates	246
V.ii.c. Ligand tether length calculations	247
V.iii. Comparison to experimental data in literature.....	250
V.iv. References.....	251
Appendix VI. Theoretical Modeling of Cellular Uptake	253
VI.i. Analysis of EPPT cellular uptake	253
VI.i.a. Calculation of experimental specific uptake.....	253
VI.i.b. Kinetic parameters for uptake model.....	254
VI.i.c. Theoretical model of EPPT cellular uptake.....	257
VI.ii. Analysis of folate cellular uptake	261
VI.ii.a. Scatchard analysis from experimental data.....	261
VI.ii.b. Theoretical model of folate cellular uptake.....	262
VI.iii. References.....	266

Appendix VII. Kinetic Analysis of Experimental Uptake of EPPT and EPPT-Containing Polymer 267

 VII.i. Analysis of kinetics of cellular uptake..... 267

 VII.i.a. Separation of internalized and surface bound material 267

 VII.i.b. Comparison of internalized and surface bound material for EPPT peptide and EPPT-containing polymer..... 269

-Intentionally Left Blank-

List of Figures

Figure 2.1. Examples of bulk polyesterification of a diester with diol using Novozyme-435 under mild reaction conditions, where R = -CH=CH ₂ [10], -H [11]. ...	66
Figure 2.2. Chemo-enzymatic condensation using Novozyme-435 of a diester and diol to form a polyester.	66
Figure 2.3. Backbone polymer synthesis using two linker molecules with distinct functionality.	68
Figure 2.4. Formation of self-assembling alternating copolymer micelles.	69
Figure 2.5. Hydrocarbon side chain attachment via the ether bond.	70
Figure 2.6. Hydrocarbon side chain attachment via the ester bond.	70
Figure 2.7. Attachment of perfluorinated sidechains to the backbone polymer for potential use in ¹⁹ F MRI imaging applications.	71
Figure 2.8. Attachment of the fluorescent dye, FITC, to the amine functionality of the backbone polymer.	72
Figure 2.9. Attachment of targeting peptide, EPPT, via triethylene glycol.	74
Figure 3.1. Cytotoxicity of the individual polymer components poly-ethylene glycol (PEG-900), 5-methyl hydroxyl isophthalate, and 5-methyl amino isophthalate at 1 g/L in uMUC1- (U87) and uMUC1+ (BT-20) cells (n=3).	86
Figure 3.2. Cytotoxicity of backbone polymers with various linkers: 100% 5-methyl hydroxyl isophthalate (#23), 100% 5-methyl amino isophthalate (#32), and 95% 5-methyl hydroxyl isophthalate plus 5% 5-methyl amino isophthalate (#24) at 1 g/L in uMUC1- (U87) and uMUC1+ (BT-20) cells (n=3).	87
Figure 3.3. Cytotoxicity due to residual TEA: polymers synthesized in the presence of TEA (#22) were cytotoxic, while those synthesized in the absence of TEA (#27) at 1 g/L in uMUC1- (U87) and uMUC1+ (BT-20) cells (n=3).	88
Figure 3.4. Example of aggregation of polymers synthesized in the presence of TEA (#22) when in solution at 1 g/L at 37°C over the course of 48 hours.	89
Figure 3.5. Effect of PEG length on cytotoxicity: polymer with PEG-600 (#52), PEG-900 (#53), or PEG-1500 (#54) in the backbone at = 1 g/L in FR- (HT-1080) and FR+ (KB) cells (n=3).	90

LIST OF FIGURES

- Figure 3.6. Effect of side chain bond type on cytotoxicity: polymer with attachment of the side chain to the backbone at the linker molecule using ether (#26), ester (#27), or ester and amide (#25) bond at 1 g/L in uMUC1- (U87) and uMUC1+ (BT-20) cells (n=3). 91
- Figure 3.7. Effect of side chain bond type on cytotoxicity: polymer with attachment of the side chain to the backbone at the linker molecule using amide (#53) and ether-ester (#57) bond at 1 g/L in FR- (HT-1080) and FR+ (KB) cells (n=3). 91
- Figure 3.8. Effect of side chain length when attached by ether bond: polymer with hydrocarbon side chains attached by ether bonds containing 9 carbons (#34) or 10 carbons (#26) at 1 g/L in uMUC1- (U87) and uMUC1+ (BT-20) cells (n=3). 93
- Figure 3.9. Effect of side chain length when attached by ester bond: polymer with hydrocarbon side chains attached by ester bonds containing 9 carbons (#27) or 10 carbons (#31) at 1 g/L in uMUC1- (U87) and uMUC1+ (BT-20) cells (n=3). 93
- Figure 3.10. Effect of side chain length when attached by ether-ester bond: polymer with hydrocarbon side chains attached by ether-ester bonds containing 6 carbons (#58), 8 carbons (#57), or 12 carbons (#62) at 1 g/L in FR- (HT-1080) and FR+ (KB) cells (n=3). 94
- Figure 3.11. Cytotoxicity of EPPT-containing polymers: polymer with 5% of the linkers having TEG-EPPT attached and the remaining 95% of the linkers having hydrocarbon side chains (#37), polymer with 5% of the linkers having TEG-EPPT attached and the remaining 95% of the linkers having no side chains (#33), polymer with 7% of the linkers having TEG-EPPT attached and no other side chains (#42) and polymer with 34% of the linkers having TEG-EPPT attached and no other side chains (#44) at 1 g/L in uMUC1- (U87) and uMUC1+ (BT-20) cells (n=3). 95
- Figure 3.12. Cytotoxicity of EPPT-containing polymer: polymer containing EPPT attached by PEG-3400 (#65) at 1 g/L in FR- (HT-1080) and FR+ (KB) cells (n=3). 96
- Figure 3.13. Cytotoxicity of folate-containing polymers with folate attached to backbone: polymer with 10% of the linkers having folate attached and no other side chains (#50) and polymer with 10% of the linkers having folate attached and the remaining 90% of the linkers having hydrocarbon side chains attached (#51) at 1 g/L in FR- (HT-1080) and FR+ (KB) cells (n=3). 98

-
- Figure 3.14. Cytotoxicity of folate-containing polymers with folate attached at end of polymer chain: polymer with PEG-3400-folate attached at the end of the polymer chain with hydrocarbon side chains (#59) and polymer with PEG-3400-folate attached at the end of the polymer chain without side chains (#56) at 1 g/L in FR- (HT-1080) and FR+ (KB) cells (n=3). 98
- Figure 3.15. Cytotoxicity of folate-containing polymers with folate attached by PEG-3400: polymer with 25% of the linkers having PEG-3400-folate attached and no other side chains (#60) at 1 g/L, polymer with 25% of the linkers having PEG-3400-folate attached and the remaining 75% of the linkers having hydrocarbon side chains attached (#61) at 0.5 g/L, and polymer with 100% of the linkers having PEG-3400-folate attached (#64) at 1 g/L in FR- (HT-1080) and FR+ (KB) cells (n=3). 99
- Figure 3.16. Cytotoxicity of folate-containing polymers at lower concentrations: polymer with 10% of the linkers having folate attached and the remaining 90% having hydrocarbon side chains attached (#51) at 0.5 g/L and 0.1 g/L and polymer with 25% of the linkers having PEG-3400-folate attached and the remaining 75% having hydrocarbon side chains attached (#61) at 0.1 g/L in FR- (HT-1080) and FR+ (KB) cells (n=3). 100
- Figure 3.17. Effect of bond type and number of carbons in side chain on cytotoxicity of PFC-containing polymers: polymer with 12-carbon PFC side chains attached by ether-ester bonds (#8), polymer with 10-carbon PFC side chains attached by ether-ester bonds (#9), and polymer with 7-carbon PFC side chains attached by amide bonds (#12) at 1 g/L in INS-1 cells (n=3). 101
- Figure 3.18. Effect of PEG length in backbone on cytotoxicity of PFC-containing polymer: PFC-containing polymer with PEG-600 in the backbone (#9) and PFC-containing polymer with PEG-900 in the backbone (#10) at 1 g/L in INS-1 cells (n=3). 102
- Figure 3.19. Effect of PEG length in backbone on cytotoxicity of PFC-containing polymers: PFC-containing polymer with PEG-1500 in the backbone (#41) and PFC-containing polymer with PEG-600 in the backbone (#43) at 1 g/L in uMUC1- (U87) and uMUC1+ (BT-20) cells (n=3). 102
- Figure 3.20. Cytotoxicity of Rhodamine B: free Rhodamine B and polymer with 10% Rhodamine B attached and 90% hydrocarbon side chains (#4) at 1 g/L in INS-1 cells (n=3). 104
- Figure 3.21. Cytotoxicity of FITC: free FITC, polymer with 5% FITC and 95% no side chains (#40), and polymer with 5% FITC and 95% hydrocarbon side chains (#28) at 1 g/L in uMUC1- (U87) and uMUC1+ (BT-20) cells (n=3). 104
- Figure 3.22. Cytotoxicity of Cy 5.5: polymer containing 5% Cy 5.5 and 95% hydrocarbon side chains (#17) at 1 g/L in uMUC1- (U87) and uMUC1+ (BT-20) cells (n=3). 105
-

LIST OF FIGURES

- Figure 3.23. Cytotoxicity of complex polymers: polymer with 5% FITC and 95% PFC (#13), polymer with 5% EPPT, 5% FITC, and 90% PFC (#29), polymer with 5% EPPT and 95% PFC (#36) and polymer with 5% EPPT, 5% FITC, and 90% no side chains (#39) at 1 g/L in uMUC1- (U87) and uMUC1+ (BT-20) cells (n=3)..... 106
- Figure 3.24. Untargeted drug delivery of DOX in polymer containing hydrocarbon side chains: polymer containing hydrocarbon side chains with (#14) and without (#26) encapsulated DOX in uMUC1- (U87) cells (n=3)..... 107
- Figure 3.25. Untargeted drug delivery of DOX in polymer containing PFC side chains: polymer containing PFC side chains with (#15) and without (#43) encapsulated DOX in uMUC1- (U87) cells (n=3). 108
- Figure 3.26 Cell death due to encapsulated DOX: polymer with ester-linked hydrocarbon side chains with (#38) and without (#35) EPPT peptide at a polymer concentration of 1 g/L and DOX concentration of 0.02 g/L in uMUC1- (U87) and uMUC1+ (BT-20) cells (n=3). A and B are for polymer in solution for two days, while C and D are for polymer in solution for two weeks..... 110
- Figure 3.27. Comparison of cell death due to various forms of polymer and DOX: polymer with ester-linked hydrocarbon side chains with (#38) and without (#35) EPPT peptide at a polymer concentration of 1 g/L and DOX concentration of 0.02 g/L in uMUC1+ (BT-20) cells (n=3). 111
- Figure 3.28. Encapsulation of DOX by dialysis, changing dialysate throughout, starting with 5 mg DOX and 200 mg polymer in 20 mL water. 113
- Figure 3.29. Encapsulation of DOX by dialysis, without changing dialysate, starting with 5 mg DOX and 200 mg polymer in 20 mL water. 113
- Figure 3.30. Cell death due to encapsulated PAC: encapsulated PAC in polymer with ester-linked hydrocarbon side chains without peptide (#49), polymer with ester-linked hydrocarbon side chains without peptide (#27), and free PAC at a polymer concentration of 1 g/L, encapsulated PAC concentration of 0.02 g/L, and free PAC concentration of 0.0003 g/L in uMUC1+ (BT-20) cells (n=3)..... 114
- Figure 4.1. Confocal microscopy images of cellular uptake of polymer with FITC and PFC (#13) at 1 g/L in INS-1 cells, free doxorubicin at 0.02 g/L in U87 cells, and doxorubicin encapsulated in polymer (#14) at 1 g/L polymer and 0.02 g/L doxorubicin in U87 cell. Note: Top image is fluorescent image, bottom image is fluorescent image merged with optical image. 130

LIST OF FIGURES

- Figure 4.2. Cellular uptake of non-targeted polymer with 100% of the linkers having ester-linked hydrocarbon side chains (#27) at 1 g/L in uMUC1- (U87) and uMUC1+ (BT-20) cells and non-targeted polymer with 100% of the linkers having PFC side chains (#10) at 1 g/L in uMUC1- (MRC-5) and uMUC1+ (BT-20) cells (n=3)..... 132
- Figure 4.3. Cellular uptake of non-targeted polymer with 100% of the linkers having ether-ester-linked hydrocarbon side chains (#58) at 0.1 g/L in FR- (HT-1080) and FR+ (KB) cells (n=3). 132
- Figure 4.4. Effect of polymer concentration on the cellular uptake of non-targeted polymer with 100% of the linkers having ester-linked hydrocarbon side chains (#27) in uMUC1- (U87) and uMUC1+ (BT-20) cells as a function of time (n=3). C and D are magnified versions of A and B, respectively. 134
- Figure 4.5. Effect of polymer concentration on the cellular uptake of non-targeted polymer with 100% of the linkers having ester-linked hydrocarbon side chains (#27) in uMUC1- (U87) and uMUC1+ (BT-20) cells as a function of polymer concentration (n=3). C and D are magnified versions of A and B, respectively..... 135
- Figure 4.6. Affinity of polymer drug delivery vehicles targeted with EPPT based on number of available ligand sites..... 140
- Figure 4.7. Affinity of polymer drug delivery vehicles targeted with folate based on number of available ligand sites..... 141
- Figure 4.8. Schematic of parameters used for ligand tether length calculations adapted from [70]. 143
- Figure 4.9. Effect of PEG tether molecular weight on the active fractional area of the carrier. 144
- Figure 4.10. Theoretical affinity of particles targeted with EPPT ligands as compared to experimental data from the literature. 146
- Figure 4.11. Cellular uptake of EPPT peptide at 0.1 g/L in uMUC1- (MRC-5) and uMUC1+ (BT-20) cells (n=3). 147
- Figure 4.12. Cellular uptake of non-targeted polymer with 100% of the linkers having ester-linked hydrocarbon side chains (#27) and targeted polymer with 5% of the linkers having EPPT attached by a TEG spacer and the remaining 95% of the linkers having ester-linked hydrocarbon side chains (#37) at 1 g/L in uMUC1- (U87) and uMUC1+ (BT-20) cells (n=3). 148

LIST OF FIGURES

- Figure 4.13. Effect of amount of EPPT peptide on cellular uptake of targeted polymers: polymer with 7% of the linkers having TEG-EPPT attached and the remaining 93% of the linkers having no side chains (#42) at 1 g/L in uMUC1- (MRC-5) and uMUC1+ (BT-20) cells, polymer with 34% of the linkers having TEG-EPPT attached and the remaining 66% of the linkers having no side chains (#44) at 1 g/L in uMUC1- (MRC-5) and uMUC1+ (BT-20) cells, and polymer with 100% of the linkers having EPPT attached by a PEG-3400 spacer (#65) at 1 g/L in uMUC1- (MRC-5) and uMUC1+ (LS174T) cells (n=3). 150
- Figure 4.14. Cellular uptake of imaging polymer with 100% of the linkers having PFC chains attached (#10) at 1 g/L in uMUC1- (MRC-5) and uMUC1+ (BT-20) cells and imaging polymer with 5% of the linkers having EPPT attached by HEG, 5% of the linkers having FITC attached, and 90% of the linkers having no side chain (#39) at 1 g/L in uMUC1- (U87) and uMUC1+ (BT-20) cells (n=3). 151
- Figure 4.15. Effect of polymer concentration on cellular uptake of polymer with 100% of the linkers having ester-linked hydrocarbon side chains (#27) and polymer with 5% of the linkers having TEG-EPPT attached and the remaining 95% of the linkers having ester-linked hydrocarbon side chains (#37) in uMUC1- (U87) and uMUC1+ (BT-20) cells as a function of time (n=3). C and D are magnified versions of A and B, respectively. 153
- Figure 4.16. Effect of polymer concentration on cellular uptake of polymer with 100% of the linkers having ester-linked hydrocarbon side chains (#27) and polymer with 5% of the linkers having TEG-EPPT attached and the remaining 95% of the linkers having ester-linked hydrocarbon side chains (#37) in uMUC1- (U87) and uMUC1+ (BT-20) cells as a function of concentration (n=3). C and D are magnified versions of A and B, respectively. 154
- Figure 4.17. Cellular uptake of ³H-folate at 50 nM in FR+ (KB) cells under various conditions (excess unlabeled folate concentration = 100 μM) (n=3). 157
- Figure 4.18. Cellular uptake of ³H-folate at 50 nM in FR- (HT-1080) and FR+ (KB) cells (n=3). 158
- Figure 4.19. Cellular uptake of ³H-folate at 50 nM in FR+ (KB) cells under conditions affecting the regulation of the FR (n=3). 160
- Figure 4.20. Cellular uptake of ³H-folate in FR+ (KB) cells at various concentrations (n=3). 161

-
- Figure 4.21. Cellular uptake of polymers with folate attached directly to the linkers: polymer with 10% of the linkers having folate attached without a spacer and the remaining 90% of the linkers having no side chains (#50) at 1 g/L and polymer with 10% of the linkers having folate attached without a spacer and the remaining 90% of the linkers having ether-linked hydrocarbon side chains (#51) at 0.1 g/L in FR- (HT-1080) and FR+ (KB) cells (n=3)..... 162
- Figure 4.22. Cellular uptake of polymer with PEG-3400-folate at the end of the polymer chain: polymer with PEG-3400-folate attached at the end of the polymer chain and no side chains (#56) at 1 g/L, polymer with PEG-3400-folate attached at the end of the polymer chain and ether-ester-linked hydrocarbon side chains (#59) at 0.1 g/L, and polymer without folate and with ether-ester-linked hydrocarbon side chains (#58) at 0.1 g/L in FR- (HT-1080) and FR+ (KB) cells (n=3). 164
- Figure 4.23. Cellular uptake of polymers with PEG-3400-folate attached: polymer with 25% of the linkers having PEG-3400-folate attached and the remaining 75% of the linkers having no side chains (#60) at 0.1 g/L, polymer with 25% of the linkers having PEG-3400-folate attached and the remaining 75% of the linkers having ether-ester-linked hydrocarbon side chains (#61) at 0.1 g/L, and polymer with 100% of the linkers having PEG-3400-folate attached (#64) at 1 g/L in FR- (HT-1080) and FR+ (KB) cells (n=3)..... 166
- Figure 4.24. Competitive inhibition of the uptake of ^3H -folate at 50 nM by an excess of folate-containing polymers at 100 μM in FR+ (KB) cells: polymer with 10% of the linkers having folate attached without a spacer and the remaining 90% of the linkers having no side chains (#50), polymer with 10% of the linkers having folate attached without a spacer and the remaining 90% of the linkers having ether-linked hydrocarbon side chains (#51), polymer with PEG-3400-folate attached at the end of the polymer chain and no side chains (#56), polymer with PEG-3400-folate attached at the end of the polymer chain and ether-ester-linked hydrocarbon side chains (#59), polymer with 25% of the linkers having PEG-3400-folate attached and the remaining 75% of the linkers having no side chains (#60), polymer with 25% of the linkers having PEG-3400-folate attached and the remaining 75% of the linkers having ether-ester-linked hydrocarbon side chains (#61), and polymer with 100% of the linkers having PEG-3400-folate attached (#64) (n=3). 168
- Figure 4.25. Competitive inhibition of the uptake of ^3H -folate at 50 nM by an excess of polymers without folate at 100 μM in FR+ (KB) cells: polymer with no folate and no side chains (#24), polymer with methyl groups attached to the linkers (#66), polymer with PEG-3400-COOH attached to the linkers (#67), and PEG-900 (n=3). 169
-

LIST OF FIGURES

- Figure 4.26. Cellular uptake of tritiated folate-containing polymer with 98% of the linkers having PEG-3400-folate attached and the remaining 2% of the linkers having methyl groups containing ^3H attached (#71) at various concentrations in FR- (HT-1080) and FR+ (KB) cells as a function of time (n=3). 171
- Figure 4.27. Cellular uptake of tritiated folate-containing polymer with 98% of the linkers having PEG-3400-folate attached and the remaining 2% of the linkers having methyl groups containing ^3H attached (#71) at various concentrations (50 nM, 500 nM, and 5 μM) in FR+ (KB) cells under conditions affecting the regulation of the FR (n=3). 174
- Figure 4.28. Comparison of cellular uptake of ^3H -folate or polymer with 98% of the linkers having PEG-3400-folate attached and the remaining 2% of the linkers having methyl groups containing ^3H attached (#71) in folate-free media in FR+ (KB) cells as a function of time (Left axis = 10^8 , Right axis = 10^7) (n=3). 176
- Figure 4.29. Comparison of surface bound ^3H -folate or polymer with 98% of the linkers having PEG-3400-folate attached and the remaining 2% of the linkers having methyl groups containing ^3H attached (#71) in FR+ (KB) cells as a function of time (n=3). 176
- Figure 4.30. Comparison of uptake of ^3H -folate or polymer with 98% of the linkers having PEG-3400-folate attached and the remaining 2% of the linkers having methyl groups containing ^3H attached (#71) in folate-free media in FR+ (KB) cells as a function of concentration (Left axis = 10^8 , Right axis = 10^7) (n=3). 177
- Figure 4.31. Comparison of surface bound ^3H -folate or polymer with 98% of the linkers having PEG-3400-folate attached and the remaining 2% of the linkers having methyl groups containing ^3H attached (#71) in FR+ (KB) cells as a function of concentration (n=3). 178
- Figure 4.32. Comparison of normalized cellular uptake of ^3H -folate or polymer with 98% of the linkers having PEG-3400-folate attached and the remaining 2% of the linkers having methyl groups containing ^3H attached (#71) in folate-free media in FR+ (KB) cells as a function of time (Left axis = 10^5 , Right axis = 10^4) (n=3). 179
- Figure 4.33. Comparison of normalized surface bound ^3H -folate or polymer with 98% of the linkers having PEG-3400-folate attached and the remaining 2% of the linkers having methyl groups containing ^3H attached (#71) in FR+ (KB) cells as a function of time (Left axis = 10^5 , Right axis = 10^4) (n=3). 180
-

LIST OF FIGURES

Figure 4.34. Comparison of normalized non-specific cellular uptake of ^3H -folate or polymer with 98% of the linkers having PEG-3400-folate attached and the remaining 2% of the linkers having methyl groups containing ^3H attached (#71) in FR+ (KB) cells as a function of time (n=3).....	180
Figure 4.35. Comparison of normalized cellular uptake in folate-free media and surface bound ^3H -folate or polymer with 98% of the linkers having PEG-3400-folate attached and the remaining 2% of the linkers having methyl groups containing ^3H attached (#71) in FR+ (KB) cells as a function of concentration (n=3).	181
Figure 4.36. Cellular uptake of free iodine at levels mimicking residual free iodine remaining after polymer labeling in uMUC1+ (BT-20) cells (n=3).	188
Figure 4.37. Cellular uptake of free iodine as compared to polymer with 100% of the linkers having ester-linked hydrocarbon side chains (#27) and polymer with 5% of the linkers having TEG-EPPT and the remaining 95% of the linkers having ester-linked hydrocarbon side chains (#37) in uMUC1+ (BT-20) cells (n=3).....	188
Figure 5.1. Biodistribution and blood circulation of non-targeted polymer with 100% of the linkers having ester-linked hydrocarbon side chains (#27) labeled with ^{125}I injected retro-orbitally in <i>nu/nu</i> mice.	207
Figure 5.2. Biodistribution and blood circulation of targeted polymer with 100% of the linkers having PEG-3400-folate attached (#64) labeled with ^{125}I injected retro-orbitally in <i>nu/nu</i> mice.	208
Figure 5.3. Biodistribution and blood circulation of targeted polymer with 100% of the linkers having PEG-3400-folate attached (#64) labeled with ^{125}I injected via the tail vein in <i>nu/nu</i> mice.	209
Figure III.1. Cell counting during incubation with cell media (control) or a 1 g/L solution of polymer with 100% of the linkers having ether-ester linked hydrocarbon side chains (#57) in FR- (HT-1080) and FR+ (KB) cells (n=3).....	237
Figure IV.i. Validation of scintillation counting preparation method using 50 nM ^3H -folate.....	242
Figure IV.ii. Validation of scintillation counting preparation method using 50 nM, 500 nM, and 5 μM ^3H -polymer.....	242
Figure V.i. Schematic of parameters used for ligand tether length calculations adapted from [8].	248
Figure VI.i. Calculation of specific uptake from total uptake in uMUC1+ cells and non-specific uptake in uMUC1- cells.	253

LIST OF FIGURES

Figure VI.ii. Scatchard plot analysis using data from Moore et al. [1]..... 255

Figure VI.iii. Estimation of kinetic parameters from experimental uptake data. 257

Figure VI.iv. Theoretical model of EPPT uptake compared to experimental data..... 258

Figure VI.v. Scatchard plot analysis using experimental data of folate uptake..... 261

Figure VI.vi. Theoretical model of folate uptake compared to experimental data..... 263

Figure VII.i. Separation of surface bound and internalized EPPT peptide..... 268

Figure VII.ii. Separation of surface bound and internalized polymer with 5% EPPT (#37).
..... 268

Figure VII.iii. Separation of surface bound and internalized polymer with 5% EPPT and
5% FITC (#39). 269

Figure VII.iv. Comparison of surface bound and internalized EPPT peptide, polymer with
5% EPPT (#37), and polymer with 5% EPPT and 5% FITC (#39). 270

List of Tables

Table 1.1. Targeting pairs in cancer.....	34
Table 1.2. Chemotherapy drugs and their mode of action.....	42
Table 4.1. Measurement of intensity averaged diameter of polymer with 100% of the linkers having PEG-3400-folate attached (#64), polymer with PEG-3400-COOH attached to the linkers (#67), polymer with 25% of the linkers having PEG-3400-folate attached and the remaining 75% of the linkers having ether-ester-linked hydrocarbon side chains (#61), polymer with no folate and no side chains (#24), and free folate in folate-free media with no serum by DLS (n=3).....	185
Table V.i. Calculated apparent dissociation constant, $K_{D,Apparent}$, for EPPT-containing particles from the cooperativity model.....	244
Table V.ii. Calculated apparent dissociation constant, $K_{D,Apparent}$, for EPPT-containing particles from the structural model.....	245
Table V.iii. Calculated apparent dissociation constant, $K_{D,Apparent}$, for folate-containing particles from the cooperativity model.....	246
Table V.iv. Calculated apparent dissociation constant, $K_{D,Apparent}$, for folate-containing particles from the structural model.....	247

-Intentionally Left Blank-

Chapter 1. Introduction

1.1. Cancer

Cancer is the collective group of diseases distinguished by uninhibited growth and spread of abnormal cells. It often results in death if the spread is not controlled. Cancer is second only to heart disease as the leading cause of death in the United States. It is estimated that 565,650 people in the United States died of cancer in 2008 and that the overall costs for cancer in the year 2007 were \$219.2 billion [1]. Most cancers are treated by surgery, radiation, chemotherapy, hormones, or immunotherapy. However, currently there are many issues with these forms of treatment, namely the lack of ability to consistently remove the entire tumor and the side effect of killing normal cells during the treatment process. Therefore there has been an increased interest in targeted drug delivery to tumors to specifically kill cancer cells.

1.2. Circulating delivery systems

In response to this clear need for efficient and selective drug transport to primary tumors and their metastases, many circulating delivery systems have been created. There are three common types of circulating delivery systems, liposomes, dendrimers, and polymeric micelles [2], which are described in more detail below. Many of these systems are able to effectively circulate in the bloodstream by the addition of poly(ethylene glycol) (PEG) either by adsorption or chemical attachment. Addition of PEG to a delivery vehicle creates a dense ‘conformational cloud’ on the exterior conferring the property of

stealth to the particle [3]. It is proposed that both the hydrophilic nature and the chain flexibility of PEG are necessary to avoid opsonization by plasma proteins and subsequent macrophage attack [4]. Interestingly, PEG often serves a dual purpose in polymeric micelles, providing the hydrophilic ‘head-group’ necessary for micellization.

1.2.1. Liposomes

Liposomes are desirable as drug carriers due to their biocompatibility since they are typically constructed either using biological materials like phospholipids or made stealth via conjugation to PEG [5]. They form from closed bilayer structures when in aqueous solution [6]. Moreover, liposomes can carry both hydrophobic and hydrophilic materials and be varied in size and surface properties by careful preparation. The design of stealth liposomes (liposomes covered with PEG) targeted to colon cancer cells was investigated and it was demonstrated that these liposomes bind to colon cancer cells in a specific manner and are internalized through receptor-mediated endocytosis, indicating potential to deliver a therapeutic load directly to colon cancer cells in an efficient and specific manner [7]. Liposomes are, however, limited by issues of size since macrophage recognition and subsequent clearance occurs for particles above ~200 nm. Conjugation to PEG does slow macrophage detection, however this retarding effect decreases as liposome size increases [8]. Other issues include low stability, non-sterility, and poor encapsulation efficiency [9].

Polymersomes are an emerging subclass of liposomes. These bilayer structures are self-assembled from synthetic polymers rather than natural polymers. The hydrophobic blocks of each molecule tend to associate with each other to minimize direct exposure to water, whereas the more hydrophilic blocks face the inner core of the particle

and the outer solution and thereby delimit the two interfaces of a typical bilayer membrane [10, 11]. Some polymer-based shells have exploited a thick hydrophobic membrane and a hydrophilic core to efficiently carry both hydrophobic and hydrophilic drugs, respectively paclitaxel and doxorubicin [12]. These polymersomes caused two-fold higher cell death in tumors than free drug suggesting promise for multi-drug delivery.

1.2.2. Dendrimers

Dendrimers are highly branched macromolecules synthesized by either divergent or convergent methods [13] yielding highly monodisperse particles with a high number of surface units per area as well as an adaptable internal environment [14]. Although dendrimeric drug delivery systems have achieved successes in *in vitro* studies [15], the time-consuming and expensive methods required to synthesize dendrimers does not lead to a process scaleable to industrial production. In spite of these constraints, James Baker's group at the University of Michigan has published quite promising *in vivo* results using a PAMAM dendrimeric system targeted to the folic acid receptor overexpressed in the KB human cancer cell line [16]. In this work, the chemotherapeutic methotrexate was delivered to mice bearing KB tumor xenografts. The dendrimers were covalently attached to both fluorescein-5-isothiocyanate (FITC) and tritium for post-experiment histological assays. Their delivery system reduced methotrexate toxicity ten-fold and nearly doubled survival time in the methotrexate-treated group in comparison to controls. Additionally, current work in Paula Hammond's lab at the Massachusetts Institute of Technology has focused on linear dendritic block copolymer micelles as targeted delivery systems [17].

In this system, the linear block can be chosen to improve encapsulation, while the dendritic exterior provides many surface groups for addition of targeting capability.

1.2.3. Polymeric micelles

Polymeric micelles [18-21] are amphiphilic colloids that spontaneously form aggregates composed of several amphiphilic molecules at concentrations and temperatures conducive for doing so. The critical micelle concentration (CMC) is the concentration above which micelle formation begins at a particular temperature. Below the CMC, the amphiphilic sub-units remain solubilized in the solvent. The resulting particles are typically ~5-100 nm in diameter and are usually spherical in morphology.

Polymeric micelles are composed of two major components. The interior, hydrophobic core is a hospitable environment for hydrophobic molecules, such as many contrast and therapeutic agents. The solubilization properties of this internal environment may be tailored to encapsulate these poorly soluble molecules, sheltering the molecule from biological degradation. The second major component is the hydrophilic corona that surrounds the hydrophobic core. As previously described, this corona is often PEG, a molecule that gives a 'stealth' property to a circulating particle [19].

According to Torchilin, the ideal polymeric micelle system would have a diameter between 5 and 100 nm, demonstrate stability both *in vitro* and *in vivo* (low CMC and stability until reaching the desired destination), disintegrate into biocompatible materials after delivery, and encapsulate the desired agent in sufficient quantities [18]. The upper limit of the size recommendation is necessary in order to avoid clearance by the macrophages of the reticuloendothelial system (RES). The lower limit ensures that the delivery vehicle avoids rapid clearance by renal exclusion and that it takes advantage of

the enhanced permeability and retention (EPR) effect where passive targeting is possible due to the ‘leaky’ vasculature often encountered in tumors [22-26], as described in more detail below. Acknowledging the tremendous advantages in size, stability, biocompatibility, and adaptability attributed to polymeric micelles, the next step is to endeavor to construct delivery systems with the most ideal biodistribution and pharmacokinetic characteristics.

There has been a great deal of activity in the field of polymeric micelle drug delivery systems, particularly within the last 10-15 years. The most extensive achievement in polymeric micelle delivery has been by Kazunori Kataoka’s group at the University of Tokyo. Their work began with poly(ethylene glycol)-poly(aspartic acid) block copolymers [PEG-PAsp] [27] and has since expanded to include other block copolymers (including PEG-poly(D,L-lactide) [PEG-PLA]), as well as polyion complex (PIC) micelles [20]. Most, if not all, of Kataoka’s initial work does not include any targeting, instead relying on passive uptake via the EPR effect. The original PEG-PAsp system was chemically conjugated to the chemotherapeutic agent, doxorubicin, and this system is currently in clinical trials in Japan [28]. Other investigators have explored solubilization of aromatic molecules in poly(ethylene oxide)-poly(propylene oxide) block copolymer [PEO-PPO] micelles measuring various solute partition coefficients [29], while others have examined the cellular distribution of a PEO-poly(caprolactone) block copolymer showing accumulation in the cytoplasm and mitochondria, but not in the nucleus using a triple-staining technique [30].

Recent work using paclitaxel-loaded poly(DL-lactide-co-glycolide) [PLGA] block copolymer nanoparticles showed successful increase of tumor doubling time from 11

days in control animals to greater than 25 days for treated animals [31]. These PLGA nanoparticles, which included an isopropyl myristate release modifier, were targeted to the wheat germ agglutinin receptor. Other researchers have employed a poly(γ -glutamic acid)-*b*-poly(lactide) [PG-PLA] block copolymer conjugated with Rhodamine-123 targeted to the ASGP receptor using galactosamine [32]. Their results have shown a linear uptake profile in time, suggesting ligand-mediated particle internalization as a potential mechanism. Most recently, Farokhzad and Langer have developed PLGA-*b*-PEG block copolymer nanoparticles encapsulating docetaxel bioconjugated to an aptamer targeted to the prostate-specific membrane antigen [33]. Aptamers are oligonucleotides that fold into conformations that bind to targets with high affinity and specificity [34]. The treatment group receiving the targeted, drug-loaded nanoparticles had 100% survival with 5 of 7 animals having complete tumor regression, whereas only 20% or less of the control group mice survived during the 109 day experiment [33].

A number of shell cross-linked polymer micelle systems (SCKs) have been developed [35] in an attempt to improve micelle stability in the dilute conditions encountered upon injection *in vivo*. These SCKs are typically block copolymer micelles that include polyion metal complex cores that may be chemically induced to form cross-links [36]. Moreover, these SCK systems have been used to try to alter the delivery pharmacokinetics. The Karen Wooley group at Washington University has developed SCK micelles that may be used for controlled release via thermolytic cleavage of the cross-linking bonds [37]. The Kazumori Kataoka group has developed an SCK-like system whose disulfide cross-linked stabilization is sensitive to glutathione concentration, the most abundant reducing agent present in the cytoplasm [38].

1.3. Alternating copolymer micelle nanoparticles

Supramolecular assemblies can be made to form nanospherical structures for drug delivery or carrying contrast agent, such as liposomes [39-41] and polymer micelles [19, 42-45]. Polymeric micelles have previously been prepared from block copolymers containing hydrophobic and hydrophilic segments that aggregate in aqueous solution to form a nanoparticle with a hydrophobic cavity and the hydrophilic segments often forming part of the surface of the aggregate. To make the nanoparticles more biocompatible and nonimmunogenic, polyethylene glycol (PEG) is grafted to the aggregate or is one of the blocks.

The amphiphilic alternating copolymer system used in this work was first described in August, 2004 [46]. The alternating copolymer chains, which self-assemble into nanospheres, offer a number of advantages over both liposomes and block copolymer micelles as a result of their unique chemical structure. The fundamental units are a hydrophilic segment, typically PEG (MW 600-1,500 Da) and a trifunctional, hydrophobic linker molecule. These base units are polymerized to yield the base polymer (MW 5,000-20,000 Da). Hydrophobic side chains, such as hydrocarbons or perfluorocarbons, can be attached to the functional group of the linkers. For targeting purposes, ligands can be coupled to the free PEG hydroxyls at the ends of each base polymer chain or attached to the functional group of the linkers. When dissolved in water above the critical micelle concentration, about 8 to 12 polymer chains self assemble into a spherical micelle consisting of a compact core of hydrophobic side chains covered by linkers with an external corona of deformable PEG loops. Additional agents can be encapsulated in the core, for example, by dissolving the polymer and agent in a solvent,

evaporating the solvent, and dissolving the resulting viscous mixture in water. The structure is stabilized by the water-soluble PEG at the exterior surface and by hydrophobic interactions between the linkers, side chains, and agents. Depending upon chemical composition, the micelles have a molecular weight of about 100-200,000 Da.

Through the use of various PEG lengths, linkers, side chains, and ligands, great flexibility in chemical composition, size, structure, and function can be obtained. Conceptually, this kind of functionality might be achieved with conventional chemistry only by use of complex and time-consuming multiple-step reaction pathways that involve synthesis of a suitable monomer with a protected functional group prior to the polymerization step, followed by deprotection. Fortunately, the development of these alternating copolymer structures is carried out with a novel and straight-forward chemo-enzymatic approach [46, 47] that makes synthesis of these nanoparticles feasible from a practical standpoint. Details of the synthesis and physical characterization of the polymers used in this study are given in Chapter 2.

1.4. Targeting of tumor cells

1.4.1. Passive targeting by the enhanced permeability and retention (EPR) effect

The increased accumulation of soluble macromolecules, such as liposomes, polymer-conjugated drugs, and proteins, in solid tumors as compared to normal tissue has been well documented [48-55]. This phenomenon, described as the “enhanced permeability and retention (EPR) effect” [56-58], is attributed to pathophysiological characteristics of solid tumors that are not observed in normal tissue. These characteristics include defective tumor blood vessel architecture (often termed “leaky

vasculature”), defective lymphatic drainage system, and increased production of permeability mediators [22, 24]. It has been reported that particles >5 nm in diameter get trapped in the tumor tissue [18, 23], but tumors exhibit a characteristic pore cutoff size ranging from 200 nm to $1.2\ \mu\text{m}$ [25]. Drug delivery particles in the 5-200 nm size range should benefit from the EPR effect.

1.4.2. Active targeting with ligand/antigen pairs

Targeting the polymer micelles to a tumor cell is necessary in drug delivery in order to kill the cancerous cells without damaging normal cells. There are many technologies which are being used to target molecules to tumor cells. Often, a monoclonal antibody, a peptide fragment, or a small molecule is used as the targeting agent. Typically these targeting agents form a ligand/antigen pair with the target found on the tumor cell surface. It is desirable for the target antigen to be over expressed on the tumor cells, be vital to tumor progression so that expression is not downregulated during the life of the tumor, and have limited shedding. The targeting ligand should have a high specific affinity for the target antigen, have low immunogenicity *in vivo*, and be efficiently internalized after binding to the antigen.

One of the most difficult aspects of tumor cell targeting is that each type of cancer must often be targeted in its own way since different proteins are over expressed on various cancer cells. The table below shows some examples of ligand/antigen pairs and the type of cancer in which the antigen is over expressed. The most commonly studied targeting pairs are epidermal growth factor (EGF)/EGF receptor and the folate/folate receptor.

Table 1.1. Targeting pairs in cancer.

Targeting Agent	Target	Type of Cancer	Ref
Lipid	Low-Density Lipoprotein Receptor	Most human cancers	[59]
Epidermal Growth Factor (EGF)	EGF Receptor	Most human cancers	[41]
Transferrin	Transferrin Receptor	Malignant gliomas	[60, 61]
EPPT/alpha-M2	uMUC1	Human epithelial cell adenocarcinomas	[62]
Vitamin B-12 (cobalamin)	Transcobalamin and B-12 Receptor	Most human cancers	[63]
Folate	Folate Receptor	Epithelial malignancies	[64]
Bombesin (BN)/Gastrin Releasing Peptide (GRP)	BN/GRP Receptor	Small cell lung cancer	[65]
Anti-Carcinoembryonic Antigen (CEA) antibody	CEA	Colorectal cancer	[66]
Telomerase Inhibitor	Telomerase	90% of all malignant human cancers	[67]

1.4.2.1. EPPT as a targeting ligand to MUC1

A successful *in vivo* drug carrier for cancer therapy needs (1) to be highly specific for tumor marker(s) and not normal tissues and (2) to display a high affinity for its molecular target. Conversely, the target for the drug carrier should be (1) present on a wide range of human cancers, (2) abundantly expressed on tumor cells but not on normal cells, and (3) indispensable for tumor survival and hence always present, showing nonvariable, high-level tumoral expression. As a suitable target, mucin-1 (MUC1), a transmembrane molecule, expressed by most glandular epithelial cells [68, 69] was selected. Several important features make mucin-1 an attractive target:

1. MUC1 is overexpressed on the cell surface and in intracellular compartments of almost all human epithelial cell adenocarcinomas, including more than 90% of human

breast cancers [70-73], ovarian [74-76], pancreatic [77], colorectal [78], lung [79, 80], prostate [81], colon [77, 82] and gastric carcinomas [83, 84], and expression has been demonstrated in non-epithelial cancer cell lines (astrocytoma, melanoma, and neuroblastoma [82]), as well as in hematological malignancies such as multiple myeloma and some B-cell non-Hodgkin lymphomas [85-88], constituting more than 50% of all cancers in humans [89].

2. In adenocarcinomatous tissue, the ordered architecture of the gland is lost, and basolateral and apical cell surfaces are not distinct. As a result, MUC1 is ubiquitously expressed all over the cell surface [90]. Because of its rod-like structure, the molecule extends more than 100-200 nm above the surface, which is 5-10 fold longer than most membrane molecules [91]. This feature makes MUC1 an accessible target for drug delivery nanospheres.
3. MUC1 is heavily glycosylated (50-90% of its molecular mass is due to carbohydrates) in normal tissues but underglycosylated in neoplastic tissues. The biochemical basis of underglycosylated mucin-1 in tumors (uMUC1) has been well investigated. Normal MUC1 consists of a tandemly repeated 20-amino acid sequence found in the extracellular portion of the molecule and present in 30-90 copies. Within each repeat sequence, there are five potential glycosylation sites. However, in the malignant state, the oligosaccharide chains are prematurely terminated by the addition of sialic acids, which limit their branching potential[90]. Reduced glycosylation permits the immune system to access the epitopes of the peptide core of the tumor-associated uMUC1 [92] that are masked by oligosaccharides in the normal cells, making it possible to design

probes with discriminating capacity between normal cells and adenocarcinoma cells [93].

4. The extracellular domain of uMUC1 defined by the presence of a PDTRP sequence extends above the cell surface, thus interfering with the interaction between adhesion molecules on the tumor cell surface and their ligands on lymphocytes and aiding in the inaccessibility of tumor epitopes to immune recognition [94-100]. Therefore, there is little or no response to immunotherapy and, hence, no tumor antigen downregulation. The expression of uMUC1 on tumor cells of epithelial cell adenocarcinomas remains homogeneously upregulated during the life of the tumor [101]. Furthermore, uMUC1 antigen is found both in primary tumors and tumor metastasis [73]. These features are important in designing the drug carriers for different stages of tumor progression.
5. uMUC1 undergoes rapid turnover. It is internalized in clathrin-coated pits, which bud to form coated vesicles at a rate twice that of normal MUC1, trafficks through intracellular compartments including lysosomes, and recycles to the plasma membrane [102] in a process akin to receptor recycling in receptor-mediated endocytosis [103]. The total intracellular residence time is 66 minutes in human mammary carcinoma cells [104]. This rapid turnover continuously brings new uMUC1 to the cell surface, which would be beneficial to the targeting process.

It is important to note, however, that there is one significant disadvantage to using mucin-1 as a target. It has been determined that the extracellular domain of mucin-1 undergoes a proteolytic cleavage early in its processing. The extracellular subunit remains associated with the transmembrane region and cytoplasmic tail, via a

noncovalent bond, throughout intracellular processing and transport to the cell surface [105-107]. Despite the strong association of the noncovalent bond between the subunits, soluble forms of the extracellular region have been found in the media of cultured cells and in sera from cancer patients [107]. There have been numerous instances of MUC1 shedding recently observed [108-111], but it remains to be seen whether or not this will affect the use of mucin-1 as the target *in vivo*.

There are several cell lines that have been shown in the literature to be uMUC1-positive or uMUC1-negative. Examples of uMUC1-positive cell lines include a human breast carcinoma cell line, BT-20, and a human colorectal adenocarcinoma, LS174T [62]. Examples of uMUC1-negative cell lines include a human glioblastoma cell line, U87, and a human lung fibroblast cell line, MRC-5 [62, 112].

Several investigations have examined uMUC1 as a target for immunotherapy. Multiple monoclonal antibodies have been produced to the PDTRP sequence of the tandem repeat since its protrusion property is the basis for its exclusive immunogenicity [101, 113-118]. However, when antibodies were used as targeting molecules, the immunogenicity and long plasma half-life of these proteins were detrimental [119]. Consequently, the use of small peptides instead may eliminate these shortcomings because peptide ligands are nonimmunogenic and have high affinity and selectivity for receptors. In this study it is proposed to use the synthetic peptide EPPT (YCAREPPTRTFAYWG), also known as alpha-M2 peptide, derived from the CDR3 V_h region of a monoclonal antibody (ASM2) raised against human epithelial cancer cells [113, 120]. Previously, this peptide has been labeled with (^{99m}Tc) and used to image breast carcinomas *in vivo* [120]. The peptide structure revealed a β -strand type of

sequence as the active binding site [121]. The EPPT synthetic peptide has significant affinity, $K_D=2.5 \times 10^{-5}$ M, for the uMUC1-derived peptide PDTRP, although not as high as the affinity of the parent monoclonal antibody, $K_D=2 \times 10^{-8}$ M [120]. The EPPT peptide was identified as the smallest possible molecule that could be derived from the original antibody while still retaining its specificity for the uMUC1 antigen. Six anti-uMUC1 single-chain antibody fragments with binding affinities in the range of 1 to 12.5 nM have been characterized [122]. While these peptides had affinities comparable to the parent monoclonal antibody, they are substantially larger than the 15-amino acid EPPT. Although the EPPT affinity is modest, both the targeted nanoparticle and uMUC1 antigen are multivalent, increasing the effective affinity of the particles for uMUC1. All the features of the uMUC1 protein listed above (overexpression throughout the cytoplasm and the cell surface, aberrant glycosylation exclusively on tumor cells, stability of the protein core, clathrin-mediated endocytosis), as well as those characteristics of EPPT mentioned here, make this receptor/ligand pair an ideal candidate for targeted drug delivery.

1.4.2.2. Folate as a targeting ligand to the folate receptor

The folate receptor, which can be targeted with folate, was chosen as a model target since it has been described extensively in the literature [123-126]. This model targeting system was used for two reasons: 1) to decrease costs associated with polymer synthesis during the probing phase of the project and 2) to verify the targeting ability of the polymer system in an extensively studied system.

The folate receptor (FR) is a membrane bound protein that recycles between the cell surface and intracellular compartments, internalizing folate and folate conjugates

through receptor-mediated endocytosis [123, 127-129]. FR is a high affinity receptor for the small molecule folate, or folic acid, with a dissociation constant, K_D , for this binding event of 1×10^{-10} M [124, 126, 130]. Its expression is often elevated on the surface of many human tumor cells, such as ovarian, lung, breast, brain, endometrial, renal, and colon cancers and it is up-regulated in more than 90% of non-mucinous ovarian carcinomas [131-135]. The high affinity for this targeting pair and the increased expression in malignant tissue makes FR an advantageous target.

The human nasopharyngeal epidermoid carcinoma cell line, KB, is commonly used as the FR-positive cell line for *in vitro* studies in the literature [136-139]. The uptake of folate in KB cells was determined to be $\sim 1 \times 10^7$ molecules per cell [140]. The human fibrosarcoma cell line, HT-1080, is often used as the FR-negative cell line and studies have shown essentially no uptake of folate in these cells [137, 138].

Many studies have used folate and FR for targeted drug delivery and imaging in cancer diagnosis and treatment [141, 142]. *In vitro* experiments have investigated the binding to and uptake in FR-positive cells of folate-targeted delivery vehicles such as dendrimers [143], liposomes [144, 145], micelles [146-149], nanocapsules [150], or other nanoparticles [135]. One study demonstrated a 5-10 fold increase in cell binding of liposomes containing PEG-folate conjugates over PEG-folate conjugates not incorporated into liposomes [145]. This increase is likely due to the multivalent nature of the liposome-bound folate. Other studies have demonstrated the ability of folate-conjugated micelles encapsulating the chemotherapeutic drug doxorubicin to be more effective in tumor cell killing as compared to micelles without folate due to the folate receptor-mediated uptake of the targeted micelles in tumor cells [146, 147, 149]. Uptake of folate-

PEG conjugated superparamagnetic iron oxide nanoparticles was found to be 12-fold higher than the untargeted nanoparticles, showing promise as a magnetic resonance imaging (MRI) contrast agent [135].

Several investigations have examined the effect of folate-targeting on therapeutic response *in vivo*. Two groups have demonstrated that tumor volumes in mice treated with doxorubicin loaded, folate conjugated nanoparticles were significantly less than in mice treated with free doxorubicin or non-targeted nanoparticles [148, 151]. It has also been shown in biodistribution studies that dendrimers conjugated to folate and coupled to the chemotherapeutic drug methotrexate concentrated in the tumor tissue [16]. Further, these targeted dendrimers increased therapeutic efficacy by decreasing tumor volumes and also increasing the survival time of the mice as compared to the free drug and non-targeted dendrimers. The overexpression of FR in tumor cells, the high affinity of FR for folate, and the extensive number of published studies on targeting FR with folate make this targeting pair an excellent model for our system.

1.5. Chemotherapy

Chemotherapy is a systemic therapy in which the anti-cancer drug is circulated throughout the entire body. These chemotherapy drugs prevent cells from replicating in the typical, out-of-control manner in which cancer cells divide. In addition, since they are circulated through the entire body, these drugs can be effective in treating metastases. However, there are other cells in the body which undergo constant and rapid division, such as cells in the blood, mouth, intestinal tract, nose, nails, and hair. The growth and division of these cells is also slowed by the chemotherapy drugs, thus causing unwanted

side effects. Chemotherapy drugs are divided into several categories based on how they affect specific chemical substances within cancer cells, which cellular activities or processes the drug interferes with, and which specific phases of the cell cycle the drug affects. Table 1.2 outlines these categories and includes examples of chemotherapy drugs from each group [152].

Table 1.2. Chemotherapy drugs and their mode of action.

	Mode of Action	Cell Cycle Phase	Examples
Alkylating agents	work directly on DNA to prevent the cancer cell from reproducing	not phase-specific	busulfan, cisplatin, carboplatin, chlorambucil, cyclophosphamide, ifosfamide, dacarbazine (DTIC), mechlorethamine (nitrogen mustard), and melphalan
Nitrosoureas	interfere with enzymes that help repair DNA	not phase-specific	Carmustine (BCNU) and lomustine (CCNU)
Antimetabolites	interfere with DNA and RNA growth	S phase	5-fluorouracil, capecitabine, methotrexate, gemcitabine, cytarabine (ara-C), and fludarabine
Antitumor antibiotics	interfere with DNA by stopping enzymes and mitosis or altering the membranes that surround cells	not phase-specific	dactinomycin, daunorubicin, doxorubicin (Adriamycin), idarubicin, and mitoxantrone
Mitotic inhibitors	inhibit, or stop, mitosis or inhibit enzymes for making proteins needed for reproduction of the cell	M phase	paclitaxel , docetaxel, etoposide (VP-16), vinblastine, vincristine, and vinorelbine
Corticosteroid hormones	used to kill cancer cells or slow their growth	not phase-specific	Prednisone and dexamethasone
Sex hormones	slow the growth of breast, prostate, and endometrial cancers	not phase-specific	anti-estrogens (tamoxifen, fulvestrant), aromatase inhibitors (anastrozole, letrozole), progestins (megestrol acetate), anti-androgens (bicalutamide, flutamide), and LHRH agonists (leuprolide, goserelin)
Immunotherapy	stimulate the immune system to more effectively recognize and attack cancer cells	-	-
Other	-	-	L-asparaginase and tretinoin

1.5.1. Doxorubicin

Doxorubicin ($C_{27}H_{29}NO_{11}$) was chosen as one of the chemotherapy drugs to be used in this project. Doxorubicin hydrochloride, or adriamycin, is approved by the FDA for cancer treatment. As shown in the table above, it belongs to the group of chemotherapy drugs known as antitumor antibiotics or anthracycline antibiotics. It is used to treat non-Hodgkin's lymphoma, multiple myeloma, acute leukemias, and cancers of the breast, adrenal cortex, endometrium, lung, and ovary [153]. In the form of the hydrochloride salt, doxorubicin is given by intravenous injection over about 15 minutes. An alternative form of this drug is the doxorubicin hydrochloride liposome injection, also known as Doxil, in which the active pharmaceutical ingredient, doxorubicin, is encapsulated in a liposome coated with polyethylene glycol (PEG) to protect it from being damaged by the immune system [154, 155]. This form is given by injection in a vein over 1 hour [156]. However, in treatment using either of these forms of doxorubicin, normal cells are affected and side effects are experienced.

One way to decrease the effect on normal cells is to target the chemotherapy drug to the cancer cells. A study was recently carried out in which PEG-coated liposomal doxorubicin was targeted to breast cancer cells using a monoclonal antibody, B27.29, against the uMUC1 antigen [157]. Two models of breast cancer, pseudometastatic and metastatic, were examined in mice. In the pseudometastatic model, tumor cells were injected into the mouse and metastases were studied in the absence of a primary tumor. In this case, survival time was used as the main criterion for determining treatment efficacy. When the mice were treated with targeted liposomal doxorubicin, the mean survival time was increased from 36.8 days for free doxorubicin and 46.2 days for liposomal

doxorubicin to 62.4 days. In the metastatic model, a primary tumor was implanted in the fatpad of immunodeficient mice. The therapeutic efficacy was determined by observing the growth of the primary tumor by measuring the tumor diameter using calipers. It was shown that targeted liposomal doxorubicin and non-targeted liposomal doxorubicin were equally effective in preventing growth of the primary tumor, while free doxorubicin was ineffective, however, the study was limited by the inability to completely remove the primary tumor and therefore the effect on the metastases could not be observed in this model. The liposomes used in this study were 90-120 nm in diameter, by dynamic light scattering. It is likely that these drug carriers were too large, causing transport issues to and throughout the tumors. However, these results are promising for the future of targeted anti-cancer drug delivery.

1.5.2. Paclitaxel

Paclitaxel ($C_{47}H_{51}NO_{14}$) was also chosen as one of the chemotherapy drugs to be used in this project. Paclitaxel, or taxol, is a mitotic inhibitor, as shown in Table 1.2. It was discovered in 1967 when it was isolated from the bark of the Pacific yew tree. Paclitaxel is also available commercially under the name Abraxane, in which the paclitaxel is bound to albumin as the delivery agent. Paclitaxel interferes with the normal function of microtubules, arresting their function by hyper-stabilizing their structure [158]. This destroys the cell's ability to use its cytoskeleton in a flexible manner. Specifically, paclitaxel binds to the β subunit of tubulin, the "building block" of microtubules. The resulting microtubule/paclitaxel complex does not have the ability to disassemble. This adversely affects cell function because the shortening and lengthening of microtubules (termed dynamic instability) is necessary for their function as a

mechanism to transport other cellular components, such as the chromosomes during mitosis. Paclitaxel is approved by the Food and Drug Administration (FDA) to treat ovarian and breast cancer, and AIDS-related Kaposi sarcoma. It is also approved to be used together with cisplatin, a chemotherapeutic drug, to treat advanced ovarian cancer and non-small cell lung cancer (NSCLC) [159]. Paclitaxel has very low water solubility (1.5 $\mu\text{g/mL}$). As a result, this agent already requires administration with a surfactant carrier. Currently, the clinically approved carrier to solubilize the drug is Cremophor® EL, a polyethylene glycol modified castor oil. Though useful in drug administration, the delivery agent itself has negative side effects therefore, an alternate delivery system using PEG-PLA micelles, Genexol-PM, has been developed [160].

Several groups have used paclitaxel as the therapeutic agent in studies of drug delivery systems in order to enhance the solubility of paclitaxel, increasing the drug payload that can be delivered to tumor cells. Paclitaxel-entrapped polymeric micelles, based on amphiphilic block copolymers of poly(2-ethyl-2-oxazoline) (PEtOz) and poly(ϵ -caprolactone) (PCL), exhibited comparable activity to that observed with the clinically used formulation of Cremophore EL-based paclitaxel in inhibiting the growth of KB cells [161]. Paclitaxel-loaded nanoparticles of poly(D,L-lactide)/methoxy poly(ethylene glycol)-poly(D,L-lactide) (PLA/MPEG-PLA) blends were formulated by the nanoprecipitation method for controlled release of paclitaxel [162]. The formulation of these nanoparticles could be tailored to achieve a desired release rate of the drug. Others have extended this research, using paclitaxel in targeted drug delivery systems, in order to increase the selective killing of tumor cells while decreasing the effect on normal cells. In one study, self-assembled nanoparticles were composed of block copolymers

synthesized by poly(γ -glutamic acid) and poly(lactide) loaded with paclitaxel and conjugated to galactosamine for the potential targeting of liver cancer cells [163, 164]. In the *in vitro* studies, it was found that the nanoparticles had similar release and cytotoxicity profiles to paclitaxel. The biodistribution and anti-tumor efficacy of the prepared nanoparticles were studied in hepatoma-tumor-bearing nude mice and it was found that the group injected with the galactosamine conjugated, paclitaxel loaded nanoparticles appeared to have the most significant efficacy in the reduction of the size of the tumor. Several groups have used folate, mentioned in the targeting of tumor cells section above, as a targeting agent for paclitaxel delivery. PEO-PPO-PEO/PEG shell cross-linked nanocapsules encapsulating an oil phase in their nanoreservoir structure and further conjugated with folate were developed as a target-specific carrier for paclitaxel to achieve folate receptor targeted delivery [150]. Confocal microscopy and flow cytometric analysis revealed that folate-mediated targeting significantly enhanced the cellular uptake and apoptotic effect against cancer cells overexpressing the folate receptor. In addition, cholesterol-grafted poly(N-isopropylacrylamide-co-N,N-dimethylacrylamide-co-undecenoic acid) was synthesized and folate was subsequently attached to the hydrophilic segment of the polymer [165]. Using a membrane dialysis method, the polymer was then self-assembled into micelles whose hydrophobic cores could be utilized to encapsulate paclitaxel. *In vitro* cytotoxicity assays performed against KB cells then provided concluding evidence of selective cell death due to a receptor-assisted endocytosis process.

1.6. Objectives

In order to improve cancer treatment by selectively killing tumor cells while leaving normal cells unaffected, new drug delivery systems specifically targeting tumors are necessary. The central hypothesis of this thesis is that targeting PEG-based alternating copolymer nanoparticles to tumor cells will increase the cellular uptake of these nanoparticles, thereby enhancing the therapeutic efficacy of these nanoparticles when used as drug delivery vehicles. I have studied the *in vitro* cytotoxicity of these particles, with or without targeting ligands and containing or not containing chemotherapeutic drugs, at relevant dose levels. In addition I have investigated the cellular uptake of the nanoparticles to determine the selectivity of these particles for the targeted cells. A comprehensive description of the synthesis of the copolymer nanoparticles and details of the experimental studies are found in the subsequent chapters.

1.7. Overview

Chapter 2: Synthesis of Alternating Copolymer Structures

This chapter describes the methods that were used by Professor Arthur Watterson's group at the University of Massachusetts, Lowell, to synthesize all of the polymers employed in this work and the rationale for designing each of these polymers. First, the methods by which the backbone polymers were produced are explained. Next, I describe the addition of the ligands to the polymers. Then the techniques to attach a variety of side chains and radioactive labels are discussed. The procedures used to encapsulate material in the polymer micelles are reported. Finally, a review of the physical characterization is given.

Chapter 3: In Vitro Cytotoxicity of Alternating Copolymers as Drug Delivery Vehicles

This chapter discusses the cytotoxic effects of the alternating copolymer structures *in vitro*. Cell death is assessed by mitochondrial function using the tetrazolium salt MTS assay. Studies examining the cytotoxicity of the polymers without chemotherapeutic drugs are reported. *In vitro* culture experiments were also carried out to assess therapeutic efficacy of the alternating copolymers encapsulating chemotherapeutic drugs.

Chapter 4: Evaluation of the Cellular Uptake of Alternating Copolymers In Vitro

This chapter reports on the assessment of the binding and internalization of the alternating copolymers with tumor cells. The selectivity of the polymers for the targeted cells was evaluated using target-positive and target-negative cell lines as well as polymers containing the targeting ligand and those not containing the targeting ligand. Cellular association was determined by radioactive labeling of the polymer with ^{125}I , ^{14}C , or ^3H , or by competitive inhibition of radioactively labeled ligand. Theoretical modeling, including polyvalency estimates and ligand tether length calculations, was used to direct the design of the targeting polymers, as well as compliment the experimental results.

Chapter 5: Initial Results on the Pharmacokinetics of Alternating Copolymers In Vivo

This chapter describes the *in vivo* experimental work that was done in collaboration with Kevin Brower from the Colton Lab in the Department of Chemical Engineering at the Massachusetts Institute of Technology. Preliminary pharmacokinetic

studies were performed to examine the biodistribution and blood-half lives of the alternating copolymers in xenograft models of human tumors in nude mice using radioactively labeled polymers. Results were obtained by collecting blood samples and harvesting organs at specified time points and measuring the radioactivity of these samples.

1.8. References

1. Cancer facts & figures 2008, A.C. Society, Editor. 2008, American Cancer Society: Atlanta.
2. Sahoo, S.K., Labhasetwar, V., Nanotech approaches to drug delivery and imaging. *Drug Discovery Today*, 2003. 8(24): p. 1112-1120.
3. Torchilin, V.P., Trubetskoy, V. S., Which polymers can make nanoparticulate drug carries long-circulating? *Adv Drug Delivery Rev*, 1995. 16: p. 141-155.
4. Gref, R., Domb, A., Quellec, P., Blunk, T., Muller, R. H., Verbavatz, J. M., Langer, R., The controlled intravenous delivery of drugs using peg-coated sterically stabilized nanospheres. *Adv Drug Delivery Rev*, 1995. 16: p. 215-233.
5. Gabizon, A., Goren, D., Horowitz, A. T., Tzemach, D., Lossos, A., Siegal, T., Long-circulating liposomes for drug delivery in cancer therapy: A review of biodistribution studies in tumor-bearing animals. *Adv Drug Delivery Rev*, 1997. 24(2-3): p. 337-344.
6. Torchilin, V.P., Recent advances with liposomes as pharmaceutical carriers. *Nature Reviews*, 2005. 4: p. 145-160.
7. Garg, A., A.W. Tisdale, E. Haidari, and E. Kokkoli, Targeting colon cancer cells using pegylated liposomes modified with a fibronectin-mimetic peptide. *International Journal of Pharmaceutics*, 2009. 366(1-2): p. 201-210.
8. Klibanov, A.L., Maruyama, K., Beckerleg, A. M., Torchilin, V. P., Huang, L., Acitivity of ahipathic poly(ethylene glycol) 5000 to prolong the circulation time of liposomes depnds on the liposome size and is unfavorable for immunoliposome binding to target. *Biochimica et Biophysica Acta*, 1991. 1062: p. 142-148.
9. Sharma, A., Sharma, U. S., Liposomes in drug delivery: Progress and limitations. *International J Pharmaceutics*, 1997. 154: p. 123-140.
10. Discher, D.E. and F. Ahmed, Polymersomes. *Annual Review of Biomedical Engineering*, 2006. 8: p. 323-341.
11. Hammer, D.A., M.J. Therien, P.P. Ghoroghchian, N.A. Christian, J.A. Silas, P.R. Frail, F.S. Bates, and G.Z. Li, Targeting and imaging with polymersomes. *Abstracts of Papers of the American Chemical Society*, 2006. 231: p. 121-COLL.
12. Ahmed, F., R.I. Pakunlu, A. Brannan, F. Bates, T. Minko, and D.E. Discher, Biodegradable polymersomes loaded with both paclitaxel and doxorubicin

- permeate and shrink tumors, inducing apoptosis in proportion to accumulated drug. *Journal of Controlled Release*, 2006. 116(2): p. 150-158.
13. Tomalia, D.A., Frechet, J. M., Discovery of dendrimers and dendritic polymers: A brief historical perspective. *J Polymer Science: Part A: Polymer Chemistry*, 2001. 40: p. 2719-2728.
 14. Ambabe, A.V., Savariar, E. N., Thayumanavan, S., Dendrimeric micelles for controlled drug release and targeted delivery. *Molecular Pharmaceutics*, 2005. 2(4): p. 264-272.
 15. Thomas, T.P., Patri, A. K., Myc, A., Myaing M. T., Ye, J. Y., Norris, T. B., Baker Jr., J. R., *In vitro* targeting of synthesized antibody-conjugated dendrimer nanoparticles. *Biomacromolecules*, 2004. 5: p. 2269-2274.
 16. Kukowska-Latallo, J., Candido, KA, Cao, Z, Nigavekar, SS, Majoros, IJ, Thomas, TP, Balogh, LP, Khan, MK, Baker, JR Jr, Nanoparticle targeting of anticancer drug improves therapeutic response in animal model of human epithelial cancer. *Cancer Res.*, 2005. 65(12): p. 5317-24.
 17. Wood, K.C., S.R. Little, R. Langer, and P.T. Hammond, A family of hierarchically self-assembling linear-dendritic hybrid polymers for highly efficient targeted gene delivery, in *Angew. Chem. Int. Ed.* 2005. p. 6704-6708.
 18. Torchilin, V.P., Structure and design of polymeric surfactant-based drug delivery systems. *J Controlled Release*, 2001. 73: p. 137-172.
 19. Allen, C., D. Maysinger, and A. Eisenberg, Nano-engineering block copolymer aggregates for drug delivery. *Colloids and Surfaces B: Biointerfaces*, 1999. 16: p. 3-27.
 20. Kataoka, K., Harada, A., Nagasaki, Y., Block copolymer micelles for drug delivery: Design, characterization and biological significance. *Adv Drug Delivery Rev*, 2001. 47: p. 113-131.
 21. Rosler, A., Vandermeulen, G. W. M., Klok, H-A., Advanced drug delivery devices via self-assembly of amphiphilic block copolymers. *Adv Drug Delivery Rev*, 2001. 53: p. 95-108.
 22. Maeda, H., Wu, J., Sawa, T., Matsumura, Y., Hori, K., Tumor vascular permeability and the epr effect in macromolecular therapeutics: A review. *J Controlled Release*, 2000. 65: p. 271-284.
 23. Maeda, H., The enhanced permeability and retention (epr) effect in tumor vasculature: The key role of tumor-selective macromolecular drug targeting. *Adv Enzyme Regul*, 2001. 41: p. 189-207.

24. Noguchi, Y., Wu, J., Duncan, R., Strohal, J., Ulbrich, K., Akaike, T., Maeda, H., Early phase tumor accumulation of macromolecules: A great difference in clearance rate between tumor and normal tissues. *Jpn J Cancer Res*, 1998. 89: p. 307-314.
25. Hobbs, S.K., Monsky, W. L., Yuan, F., Roberts, W. G., Griffith, L., Torchilin, V. P., Jain, R. K., Regulation of transport pathways in tumor vessels: Role of tumor type and microenvironment. *PNAS*, 1998. 95: p. 4607-4612.
26. Maeda, H., The enhanced permeability and retention (epr) effect in tumor vasculature: The key role of tumor-selective macromolecular drug targeting, in *Advan Enzyme Regul.* 2001. p. 189-207.
27. Yokoyama, M., Lnoue, S., Kataoka, K., Yui, N., Sakurai, Y., Preparation of adriamycin-conjugated poly(ethylene glycol)-poly(aspartic acid) block copolymer: A new type of polymeric anticancer agent. *Macromol Rapid Commun*, 1987. 8: p. 431-435.
28. Yokoyama, M., Fukushima, S., Uehara, R., Okamoto, K., Kataoka, K., Sakurai, Y., Okano, T., Characterization of physical entrapment and chemical conjugation of adriamycin in polymeric micelles and their design for in vivo delivery to a solid tumor. *J Controlled Release*, 1998. 50: p. 79-92.
29. Gadelle, F., Koros, W. J., Schechter, R. S., Solubilization of aromatic solutes in block copolymers. *Macromolecules*, 1995. 28: p. 4883-4892.
30. Savic, R., Luo, L., Eisenberg, A., Maysinger, D., Micellar nanocontainers distribute to defined cytoplasmic organelles. *Science*, 2003. 300: p. 615-618.
31. Mo, Y., Lim, L-Y., Paclitaxel-loaded plga nanoparticles: Potentiation of anticancer activity by surface conjugation with wheat germ agglutinin. *J Controlled Release*, 2005. 108: p. 244-262.
32. Liang, H.-F., Yang, T-F., Huang, C-T., Chen, M-C., Sung, H-W., Preparation of nanoparticles composed of poly(glutamic acid)-poly(lactide) block copolymers and evaluation of their uptake by hepg2 cells. *J Controlled Release*, 2005. 105: p. 213-225.
33. Farokhzad, O.C., Cheng, J., Teply, B. A., Sherifi, I., Jon, S., Kantoff, P. W., Richie, J. P., Langer, R., Targeted nanoparticle-aptamer bioconjugates for cancer chemotherapy in vivo. *PNAS*, 2006. 103(16): p. 6315-6320.
34. Ellington, A.D., Szostak, J. W., In vitro selection of rna molecules that bind specific ligands. *Nature*, 1990. 346(6287): p. 818-822.
35. Liu, J., Zhang, Q., Remsen, E., Wooley, K., Nanostructured materials designed for cell binding and transduction. *Biomacromolecules*, 2001. 2: p. 362-368.

36. Bronich, T.K., Keifer, P. A., Shlyakhtenko, L. S., Kabanov, A. V., Polymer micelle with cross-linked ionic core. *JACS*, 2005. 127: p. 8236-8237.
37. Murthy, K.S., Ma, Q., Clark, Jr., C. G., Remsen, E. E., Wooley, K., L., Fundamental design aspects of amphiphilic shell-crosslinked nanoparticles for controlled release applications. *Chem Commun*, 2001: p. 773-774.
38. Kakizawa, Y., Harada, A., Kataoka, K., Glutathione-sensitive stabilization of block copolymer micelles composed of antisense DNA and thiolated poly(ethylene glycol)-*block*-poly(l-lysine): A potential carrier for systemic delivery of antisense DNA. *Biomacromolecules*, 2001. 2: p. 491-497.
39. Caride, V.J., Liposomes as carriers of imaging agents. *Critical Reviews in Therapeutic Drug Carrier Systems*, 1985. 1: p. 121-153.
40. Phillips, W.T., Delivery of gamma-imaging agents by liposomes. *Advanced Drug Delivery Reviews*, 1999. 37: p. 13-32.
41. Kullberg, E.B., M. Nestor, and L. Gedda, Tumor-cell targeted epidermal growth factor liposomes loaded with boronated acridine: Uptake and processing. *Pharmaceutical Research*, 2003. 20(2): p. 229-236.
42. Van Domeselaar, G.H., G.S. Kwon, L.C. Andrew, and D.S. Wishart, Application of solid phase peptide synthesis to engineering peo-peptide block copolymers for drug delivery. *Colloids and Surfaces B: Biointerfaces*, 2003. 30: p. 323-334.
43. Trubetskoy, V.S., Polymeric micelles as carriers of diagnostic agents. *Advanced Drug Delivery Reviews*, 1999. 37: p. 81-88.
44. Torchilin, V.P., Peg-based micelles as carriers of contrast agents for different imaging modalities. *Advanced Drug Delivery Reviews*, 2002. 54: p. 235-252.
45. Lavasanifar, A., J. Samuel, and G.S. Kwon, Poly(ethylene oxide)-*block*-poly(l-amino acid) micelles for drug delivery. *Advanced Drug Delivery Reviews*, 2002. 54: p. 169-190.
46. Kumar, R., M.H. Chen, V.S. Parmar, L.A. Samuelson, J. Kumar, R.A. Nicolosi, S. Yoganathan, and A.C. Watterson, Supramolecular assemblies based on copolymers of peg600 and functionalized aromatic diesters for drug delivery applications. *Journal of the American Chemical Society*, 2004. 126(34): p. 10640-10644.
47. Kumar, R., N.A. Shakil, M.-H. Chen, V.S. Parmar, L.A. Samuelson, J. Kumar, and A.C. Watterson, Chemo-enzymatic synthesis and characterization of novel functionalized amphiphilic polymers. *Journal of Macromolecular Science*, 2002. A39(10): p. 1137-1149.

48. Konno, T., Maeda, H., Iwai, K., Tashiro, S., Maki, S., Morinaga, T., Mochinaga, M., Hiraoka, T. and Yokoyama, I., Effect of arterial administration of high molecular weight anticancer agent smancs with lipid lymphographic agent on hepatoma: A preliminary report. *Eur. J. Cancer Clin. Oncol.*, 1983. 19: p. 1053–1065.
49. Iwai, K., Maeda, H. and Konno, T., Use of oily contrast medium for selective drug targeting to tumor: Enhanced therapeutic effect and x-ray image. *Cancer Research*, 1984. 44: p. 2115–2121.
50. Konno, T., Maeda, H., Iwai, K., Maki, S., Tashiro, S., Uchida, M. and Miyauchi, Y., Selective targeting of anticancer drug and simultaneous image enhancement in solid tumors by arterially administered lipid contrast medium. *Cancer*, 1983. 54: p. 2367–2374.
51. Iwai, K., Maeda, H., Konno, T., Matsumura, Y., Yamashita, R., Yamasaki, K., Hirayama, S. and Miyauchi, Y., Tumor targeting by arterial administration of lipids: Rabbit model with vx2 carcinoma in the liver. *Anticancer Res*, 1987. 7: p. 321–328.
52. Seymour, L.W., Ulbrich, K., Steyger, P. S., Brereton, M., Subr, V., Strohalm, J. and Duncan, R., Tumour tropism and anticancer efficacy of polymer-based doxorubicin prodrugs in the treatment of subcutaneous murine b16 f10 melanoma. *Br. J. Cancer*, 1994. 70: p. 636–641.
53. Sinn, H., Shrenk, H. H., Fredrich, E. A., Schilling, U. and Maier-Borst, W. A. A., Design of compounds having an increased tumour uptake: Using serum albumin as carrier. Part 1. *Nucl. Med. Biol.*, 1990. 17: p. 819–827.
54. Wu, N.Z., Da, D., Rudoll, T. L., Needham, D., Whorton, A. R. and Dewhirst, M. W., Increased microvascular permeability contributes to preferential accumulation of stealth liposomes in tumor tissue. *Cancer Res.*, 1993. 53: p. 3765–3770.
55. Yuan, F., Dellian, M., Fukumura, D., Leunig, M., Berk, D. A., Torchilin, V. P. and Jain, R. K., Vascular permeability in a human tumour xenograft: Molecular size dependence and cutoff size. *Cancer Res.*, 1995. 55: p. 3752–3756.
56. Matsumura, Y.a.M., H., A new concept for macromolecular therapeutics in cancer therapy: Mechanism of tumoritropic accumulation of proteins and the antitumor agents smancs. *Cancer Res.*, 1986. 46: p. 6387–6392.
57. Maeda, H.a.M., Y., Tumoritropic and lymphotropic principles of macromolecular drugs. *Crit. Rev. Ther. Drug Carrier Syst.*, 1989. 6: p. 193–210.
58. Maeda, H., Smancs and polymer-conjugated macromolecular drugs: Advantages in cancer chemotherapy. *Adv. Drug Delivery Rev.*, 1991. 6: p. 181–202.

59. Maletinska, L., E.A. Blakely, K.A. Bjornstad, D.F. Deen, L.J. Knoff, and T.M. Forte, Human glioblastoma cell lines: Levels of low-density lipoprotein receptor and low-density lipoprotein receptor-related protein. *Cancer Research*, 2000. 60: p. 2300-2303.
60. Weaver, M. and D.W. Laske, Transferrin receptor ligand-targeted toxin conjugate (tf-crm107) for therapy of malignant gliomas. *Journal of Neuro-Oncology*, 2003. 65: p. 3-13.
61. Sutherland, R., D. Delia, C. Schneider, R. Newman, J. Kemshead, and M. Greaves, Ubiquitous cell-surface glycoprotein on tumor cells is proliferation-associated receptor for transferrin. *Proceedings of the National Academy of Sciences of the United States of America*, 1981. 78(7): p. 4515-4519.
62. Moore, A., Z. Medarova, A. Potthast, and G. Dai, In vivo targeting of underglycosylated muc-1 tumor antigen using a multimodal imaging probe. *Cancer Research*, 2004. 64: p. 1821-1827.
63. Bauer, J.A., B.H. Morrison, R.W. Grane, B.S. Jacobs, S. Dabney, A.M. Gamero, K.A. Carnevale, D.J. Smith, J. Drazba, B. Seetharam, and D.J. Lindner, Effects of interferon beta on transcobalamin ii-receptor expression and antitumor activity of nitrosylcobalamin. *Journal of the National Cancer Institute*, 2002. 94(13): p. 1010-1019.
64. Lu, Y., E. Segal, C.P. Leamon, and P.S. Low, Folate receptor-targeted immunotherapy of cancer: Mechanism and therapeutic potential. *Advanced Drug Delivery Reviews*, 2004. 56: p. 1161-1176.
65. Zhou, J. and J. Chen, Bombesin/gastrin-releasing peptide receptor: A potential target for antibody-mediated therapy of small cell lung cancer. *Clinical Cancer Research*, 2003. 9: p. 4953-4960.
66. Azria, D., M. Dorvillius, S. Gourgou, P. Martineau, B. Robert, M. Pugnieri, R. Delard, M. Ychou, J.-B. Dubois, and A. Pelegrin, Enhancement of radiation therapy by tumor necrosis factor alpha in human colon cancer using a bispecific antibody. *International Journal of Radiation Oncology, Biology, Physics*, 2003. 55(5): p. 1363-1373.
67. Elmore, L.W. and S.E. Holt, Diagnosis and treatment of human disease using telomerase as a novel target, in *Drug delivery systems in cancer therapy*, D.M. Brown, Editor. 2004, Humana Press: Totowa, New Jersey. p. 361-376.
68. Allen, A., Mucus - a protective secretion of complexity. *Trends in Biochemical Sciences*, 1983. 8: p. 169-173.
69. Zotter, S., Hageman, P., Lossnitzer, A., Mooi, W., and Hilgers, J., Tissue and tumour distribution of human polymorphic epithelial mucin. *Cancer Review*, 1988. 11-12: p. 55.

70. Xing, P., J. Tjandra, S. Stacker, J. Teh, C. Thompson, P. McLaughlin, and I. McKenzie, Monoclonal antibodies reactive with mucin expressed in breast cancer. *Immunology & Cell Biology*, 1989. 67 (Pt 3): p. 183-195.
71. Hayes, D., R. Mesa-Tejada, L. Papsidero, G. Croghan, A. Korzun, L. Norton, W. Wood, J. Strauchen, M. Grimes, R. Weiss, H. Ree, A. Thor, F. Koerner, M. Rice, M. Barcos, and D. Kufe, Prediction of prognosis in primary breast cancer by detection of a high molecular weight mucin-like antigen using monoclonal antibodies df3, f36/22, and cu18: A cancer and leukemia group b study. *Journal of Clinical Oncology*, 1991. 9: p. 1113-1123.
72. Perey, L., Hayes, D., Maimonis, P., Abe, M., O'Hara, C., and Kufe, D., Tumor-specific reactivity of a monoclonal antibody prepared against a recombinant peptide derived from the d3 human breast carcinoma-associated antigen. *Cancer Research*, 1992. 52: p. 2563-2568.
73. Nacht, M., A.T. Ferguson, W. Zhang, J.M. Petroziello, B.P. Cook, Y.H. Gao, S. Maguire, D. Riley, G. Coppola, G.M. Landes, S.L. Madden, and S. Sukumar, Combining serial analysis of gene expression and array technologies to identify genes differentially expressed in breast cancer. *Cancer Research*, 1999. 59: p. 5464-5470.
74. van Hof, A., C. Molthoff, Q. Davies, A. Perkins, R. Verheijen, P. Kenemans, W. den Hollander, A. Wilhelm, T. Baker, M. Sopwith, M. Frier, E. Symonds, and J. Roos, Biodistribution of (111)indium-labeled engineered human antibody ctmo1 in ovarian cancer patients: Influence of protein dose. *Cancer Research*, 1996. 56: p. 5179-5185.
75. Avichezer, D., J. Taylor-Papadimitriou, and R. Arnon, A short synthetic peptide (dtrpap) induces anti-mucin (muc-1) antibody, which is reactive with human ovarian and breast cancer cells. *Cancer Biochemistry Biophysics*, 1998. 16: p. 113-128.
76. Hough, C.D., C.A. Sherman-Baust, E.S. Pizer, F.J. Montz, D.D. Im, N.B. Rosenshein, K.R. Cho, G.J. Riggins, and P.J. Morin, Large-scale serial analysis of gene expression reveals genes differentially expressed in ovarian cancer. *Cancer Research*, 2000. 60: p. 6281-6287.
77. Burdick, M.D., A. Harris, C.J. Reid, T. Iwamura, and M.A. Hollingsworth, Oligosaccharides expressed on muc1 produced by pancreatic and colon tumor cell lines. *Journal of Biological Chemistry*, 1997. 272(39): p. 24198-24202.
78. Aoki, R., S. Tanaka, K. Haruma, M. Yoshihara, K. Sumii, G. Kajiyama, F. Shimamoto, and N. Kohno, Muc-1 expression as a predictor of the curative endoscopic treatment of submucosally invasive colorectal carcinoma. *Diseases of the Colon and Rectum*, 1998. 41: p. 1262-1272.

79. Willsher, P., P. Xing, C. Clarke, D. Ho, and I. McKenzie, Mucin 1 antigens in the serum and bronchial lavage fluid of patients with lung cancer. *Cancer*, 1993. 72: p. 2936-2942.
 80. Maeshima, A., A. Miyagi, T. Hirai, and T. Nakajima, Mucin-producing adenocarcinoma of the lung, with special reference to goblet cell type adenocarcinoma: Immunohistochemical observation and ki-ras gene mutation. *Pathology International*, 1997. 47: p. 454-460.
 81. Zhang, S., S. Zhang, V. Reuter, S. Slovin, H. Scher, and P. Livingston, Expression of potential target antigens for immunotherapy on primary and metastatic prostate cancers. *Clinical Cancer Research*, 1998. 4: p. 295-302.
 82. Oosterkamp, H.M., L. Scheiner, M.C. Stefanova, K.O. Lloyd, and C.L. Finstad, Comparison of muc-1 mucin expression in epithelial and non-epithelial cancer cell lines and demonstration of a new short variant form (muc-1/z). *International Journal of Cancer*, 1997. 72: p. 87-94.
 83. Strous, G. and J. Dekker, Mucin-like glycoproteins. *Critical Reviews in Biochemistry and Molecular Biology*, 1992. 27: p. 57-92.
 84. Medina, M., D. Velez, J.A. Asenjo, G. Egea, F.X. Real, J. Gil, and J.L. Subiza, Human colon adenocarcinomas express a muc1-associated novel carbohydrate epitope on core mucin glycans defined by a monoclonal antibody (a10) raised against murine ehrlich tumor cells. *Cancer Research*, 1999. 59: p. 1061-1070.
 85. Brossart, P., A. Schneider, P. Dill, T. Schammann, F. Grunebach, S. Wirths, L. Kanz, H.-J. Buhring, and W. Brugger, The epithelial tumor antigen muc1 is expressed in hematological malignancies and is recognized by muc1-specific cytotoxic t-lymphocytes. *Cancer Research*, 2001. 61: p. 6846-6850.
 86. Burton, J., D. Mishina, T. Cardillo, K. Lew, A. Rubin, D. Goldenberg, and D. Gold, Epithelial mucin-1 (muc1) expression and ma5 anti-muc1 monoclonal antibody targeting in multiple myeloma. *Clinical Cancer Research*, 1999. 5(10 Suppl): p. 3065s-3072s.
 87. Treon, S.P., J.A. Mollick, M. Urashima, G. Teoh, D. Chauhan, A. Ogata, N. Raje, J.H.M. Hilgers, L. Nadler, A.R. Belch, L.M. Pilarski, and K.C. Anderson, Muc-1 core protein is expressed on multiple myeloma cells and is induced by dexamethasone. *Blood*, 1999. 93(4): p. 1287-1298.
 88. Dyomin, V.G., N. Palanisamy, K.O. Lloyd, K. Dyomina, S.C. Jhanwar, J. Houldsworth, and R.S.K. Chaganti, Muc1 is activated in a b-cell lymphoma by the t(1;14)(q21;q32) translocation and is rearranged and amplified in b-cell lymphoma subsets. *Blood*, 2000. 95(8): p. 2666-2671.
 89. Greenlee, R.T., T. Murray, S. Bolden, and P.A. Wingo, Cancer statistics, 2000. *CA: A Cancer Journal for Clinicians*, 2000. 50: p. 7-33.
-

90. Barratt-Boyes, S.M., Making the most of mucin: A novel target for tumor immunotherapy. *Cancer Immunology, Immunotherapy*, 1996. 43: p. 142-151.
91. Taylor-Papadimitriou, J., J. Burchell, D.W. Miles, and M. Dalziel, Muc1 and cancer. *Biochimica et Biophysica Acta*, 1999. 1455: p. 301-313.
92. Burchell, J. and J. Taylor-Papadimitrou, Effect of modification of carbohydrate side chains on the reactivity of antibodies with core-protein epitopes of the muc1 gene product. *Epithelial Cell Biology*, 1993. 2: p. 155-162.
93. Spicer, A., G. Rowse, T. Lidner, and S. Gendler, Delayed mammary tumor progression in muc-1 null mice. *The Journal of Biological Chemistry*, 1995. 270(50): p. 30093-30101.
94. Jentoft, N., Why are proteins o-glycosylated? *Trends in Biochemical Sciences*, 1990. 15: p. 291-294.
95. Apostolopoulos, V. and I. McKenzie, Cellular mucins: Targets for immunotherapy. *Critical Reviews in Immunology*, 1994. 14: p. 293-309.
96. Finn, O., K. Jerome, R. Henderson, G. Pecher, N. Domenech, J. Magarian-Blander, and S. Barratt-Boyes, Muc-1 epithelial tumor mucin-based immunity and cancer vaccines. *Immunological Reviews*, 1995. 145: p. 61-89.
97. Barnd, D., M. Lan, R. Metzgar, and F. OJ, Specific, major histocompatibility complex-unrestricted recognition of tumor-associated mucins by human cytotoxic t cells. *Proceedings of the National Academy of Sciences of the United States of America*, 1989. 86: p. 7159-7163.
98. Takahashi, T., Y. Makiguchi, Y. Hinoda, H. Kakiuchi, N. Nakagawa, K. Imai, and A. Yachi, Expression of muc1 on myeloma cells and induction of hla-unrestricted ctl against muc1 from a multiple myeloma patient. *Journal of Immunology*, 1994. 153: p. 2102-2109.
99. Noto, H., T. Takahashi, Y. Makiguchi, T. Hayashi, Y. Hinoda, and K. Imai, Cytotoxic t lymphocytes derived from bone marrow mononuclear cells of multiple myeloma patients recognize an underglycosylated form of muc1 mucin. *International Immunology*, 1997. 9: p. 791-798.
100. Dove, A., Cell-based therapies go live. *Nature Biotechnology*, 2002. 20: p. 339-343.
101. Peterson, J.A., E.W. Blank, and R.L. Ceriani, Effect of multiple, repeated doses of radioimmunotherapy on target antigen expression (breast muc-1 mucin) in breast carcinomas. *Cancer Research*, 1997. 57(6): p. 1103-8.

102. Altschuler, Y., C.L. Kinlough, P.A. Poland, J.B. Bruns, G. Apodaca, O.A. Weisz, and R.P. Hughey, Clathrin-mediated endocytosis of muc1 is modulated by its glycosylation state. *Molecular Biology of the Cell*, 2000. 11: p. 819-831.
103. Lauffenburger, D.A. and J.J. Linderman, *Receptors: Models for binding, trafficking, and signaling*. 1993, New York: Oxford University Press. 365.
104. Litvinov, S.V. and J. Hilkens, The ipethelial sialomucin, episialin, is sialylated during recycling. *Journal of Biological Chemistry*, 1993. 268: p. 21364-21371.
105. Ligtenberg, M.J.L., L. Kruijshaar, F. Buijs, M. van Meijer, S.V. Litvinov, and J. Hilkens, Cell-associated episialin is a complex containing two proteins derived from a common precursor. *Journal of Biological Chemistry*, 1992. 267(9): p. 6171-6177.
106. Parry, S., H.S. Silverman, K. McDermott, A. Willis, M.A. Hollingsworth, and A. Harris, Identification of muc1 proteolytic cleavage sites *in vivo*. *Biochemical and Biophysical Research Communications*, 2001. 283: p. 715-720.
107. Lillehoj, E.P., F. Han, and K.C. Kim, Mutagenesis of a gly-ser cleavage site in mic1 inhibits ectodomain shedding. *Biochemical and Biophysical Research Communications*, 2003. 307: p. 743-749.
108. Porowska, H., A. Paszkiewicz-Gadez, T. Anchim, S. Wolczynski, and A. Gindzienski, Inhibition of the o-glycan elongation limits muc1 incorporation to cell membrane of human endometrial carcinoma cells. *International Journal of Molecular Medicine*, 2004. 13: p. 459-464.
109. Thathiah, A., C.P. Blobel, and D.D. Carson, Tumor necrosis factor-alpha converting enzyme/adam 17 mediates muc1 shedding. *Journal of Biological Chemistry*, 2003. 278(5): p. 3386-3394.
110. Thathiah, A. and D.D. Carson, Mt1-mmp mediates muc1 shedding independent of tace/adam17. *Biochemical Journal*, 2004. 382: p. 363-373.
111. Schuhmacher, J., S. Kaul, G. Klivenyi, H. Junkermann, A. Magener, M. Henze, J. Doll, U. Haberkorn, F. Amelung, and G. Bastert, Immunoscintigraphy with positron emission tomography: Gallium-68 chelate imaging of breast cancer pretargeted with bispecific anti-muc1/anti-ga chelate antibodies. *Cancer Research*, 2001. 61: p. 3712-3717.
112. Okarvi, S., Synthesis, radiolabeling and in vitro and in vivo characterization of a technetium-99m-labeled alpha-m2 peptide as a tumor imaging agent. *J Pept Res*, 2004. 63(6): p. 460-8.
113. Hussain, R., N. Courtenay-Luck, and G. Siligardi, Structure-function correlation and biostability of antibody cdr-derived peptides as tumor imaging agents. *Biomedical Peptides, Proteins & Nucleic Acids*, 1996. 2: p. 67-70.

114. Pietersz, G.A., L. Wenjun, K. Krauer, T. Baker, D. Wreschner, and I.F.C. McKenzie, Comparison of the biological properties of two anti-mucin-1 prepared for imaging and therapy. *Cancer Immunology, Immunotherapy*, 1997. 44: p. 323-328.
115. Winthrop, M., S. DeNardo, and G. DeNardo, Development of a hyperimmune anti-muc-1 single chain antibody fragments phage display library for targeting breast cancer. *Clinical Cancer Research*, 1999. 5 (10 Suppl): p. 3088s-3094s.
116. Wong, C., R. Waibel, M. Sheets, j.-P. Mach, and R. Finnern, Human scfv antibody fragments specific for the epithelial tumour marker muc-1, selected by phage display on living cells. *Cancer Immunology, Immunotherapy*, 2001. 50: p. 93-101.
117. Moller, H., N. Serttas, H. Paulsen, J.M. Burchell, J. Taylor-Papadimitriou, and B. Meyer, Nmr-based determination of the binding epitope and conformational analysis of muc-1 glycopeptides and peptides bound to the breast cancer-selective monoclonal antibody sm3. *European Journal of Biochemistry*, 2002. 269: p. 1444-1455.
118. Burchell, J., S. Gendler, J. Taylor-Papadimitriou, A. Girling, A. Lewis, R. Millis, and D. Lampion, Development and characterization of breast cancer reactive monoclonal antibodies directed to the core protein of the human milk mucin. *Cancer Research*, 1987. 47(20): p. 5476-82.
119. Goldsmith, S.J., Receptor imaging: Competitive or complementary to antibody imaging? *Seminars in Nuclear Medicine*, 1997. 27: p. 85-93.
120. Sivolapenko, G.B., V. Douli, D. Pectasides, D. Skarlos, G. Sirmalis, R. Hussain, J. Cook, N.S. Courtenay-Luck, E. Merkouri, K. Konstantinides, and A.A. Epenetos, . Breast cancer imaging with radiolabelled peptide from complementarity-determining region of antitumour antibody. *Lancet*, 1995. 346: p. 1662-1666.
121. Hussain, R., G. Siligardi, S. Adebakin, J.A. Cook, A. George, A. Drake, and N. Courtney-Luck. Tumour-imaging peptides: Conformation-activity relationship by cd spectroscopy. in *Peptides: Chemistry, Structure, and Biology. Proceedings of the 14th American Peptide Symposium*. 1996. England: Mayflower Scientific Ltd.
122. Bremer, C., C. Tung, and R. Weissleder, In vivo molecular target assessment of matrix metalloproteinase inhibition. *Nature Medicine*, 2001. 7: p. 743-748.
123. Lee, R.a.L., PS, Delivery of liposomes into cultured kb cells via folate receptor-mediated endocytosis. *J. Biol. Chem*, 1994. 269: p. 3198-3204.
124. Leamon, C., Low, PS, Folate-mediated targeting: From diagnostics to drug and gene delivery. *Drug Discov Today*, 2001. 6(1): p. 44-51.

125. Low, P., Antony, AC, Folate receptor-targeted drugs for cancer and inflammatory diseases. *Adv Drug Deliv Rev*, 2004. 56(8): p. 1055-8.
126. Low, P., Henne, WA, Doorneweerd, DD, Discovery and development of folic-acid-based receptor targeting for imaging and therapy of cancer and inflammatory diseases. *Acc Chem Res*, 2008. 41(1): p. 120-9.
127. Leamon, C.P., Low, P. S., Delivery of macromolecules into living cells: A method that exploits folate receptor endocytosis. *Proceedings of the National Academy of Sciences of the United States of America*, 1991. 88: p. 5572-5576.
128. Elnakat, H., Ratnam, M, Distribution, functionality and gene regulation of folate receptor isoforms: Implications in targeted therapy. *Adv Drug Deliv Rev*, 2004. 56(8): p. 1067-84.
129. Sabharanjak, S., Mayor, S, Folate receptor endocytosis and trafficking. *Adv Drug Deliv Rev*, 2004. 56(8): p. 1099-109.
130. Kamen, B.A., Capdevila, A., Receptor-mediated folate accumulation is regulated by the cellular folate content. *PNAS*, 1986. 83: p. 5983-5987.
131. Weitman, S., Lark, RH, Coney, LR, Fort, DW, Frasca, V, Zurawski, VR Jr, Kamen, BA, Distribution of the folate receptor gp38 in normal and malignant cell lines and tissues. *Cancer Research*, 1992. 52(12): p. 3396-401.
132. Ross, J., Chaudhuri, PK, Ratnam, M, Differential regulation of folate receptor isoforms in normal and malignant tissues in vivo and in established cell lines. Physiologic and clinical implications. *Cancer*, 1994. 73(9): p. 2432-43.
133. Lu, Y., Low, PS, Immunotherapy of folate receptor-expressing tumors: Review of recent advances and future prospects. *J Control Release*, 2003. 91(1-2): p. 17-29.
134. Kamen, B.A., Smith, A. K., A review of folate receptor alpha cycling and 5-methyltetrahydrofolate accumulation with an emphasis on cell models in vitro. *Adv Drug Delivery Rev*, 2004. 56: p. 1085-1097.
135. Sun, C., Sze, R, Zhang, M, Folic acid-peg conjugated superparamagnetic nanoparticles for targeted cellular uptake and detection by mri. *J Biomed Mater Res A*, 2006. 78(3): p. 550-7.
136. Paulos, C., Reddy, JA, Leamon, CP, Turk, MJ, Low, PS, Ligand binding and kinetics of folate receptor recycling in vivo: Impact on receptor-mediated drug delivery. *Mol Pharmacol*, 2004. 66(6): p. 1406-14.
137. Moon, W., Lin, Y, O'Loughlin, T, Tang, Y, Kim, DE, Weissleder, R, Tung, CH, Enhanced tumor detection using a folate receptor-targeted near-infrared fluorochrome conjugate. *Bioconjug Chem*, 2003. 14(3): p. 539-45.

138. Zheng, G., Chen, J, Li, H, Glickson, JD, Rerouting lipoprotein nanoparticles to selected alternate receptors for the targeted delivery of cancer diagnostic and therapeutic agents. *Proceedings of the National Academy of Sciences of the United States of America*, 2005. 102(49): p. 17757-62.
139. Sudimack, J., Lee, RJ, Targeted drug delivery via the folate receptor. *Adv Drug Deliv Rev*, 2000. 41(2): p. 147-62.
140. Paulos, C., Turk, MJ, Breur, GJ, Low, PS, Folate receptor-mediated targeting of therapeutic and imaging agents to activated macrophages in rheumatoid arthritis. *Adv Drug Deliv Rev*, 2004. 56(8): p. 1205-17.
141. Leamon, C.P., Reddy, J. A., Folate-targeted chemotherapy. *Adv Drug Delivery Rev*, 2004. 56: p. 1127-1141.
142. Ke, C., Mathias, CJ, Green, MA, Folate-receptor-targeted radionuclide imaging agents. *Adv Drug Deliv Rev*, 2004. 56(8): p. 1143-60.
143. Hong, S., Leroueil, PR, Majoros, IJ, Orr, BG, Baker, JR Jr, Banaszak Holl, MM, The binding avidity of a nanoparticle-based multivalent targeted drug delivery platform. *Chem Biol*, 2007. 14(1): p. 107-15.
144. Saul, J., Annapragada, A, Natarajan, JV, Bellamkonda, RV, Controlled targeting of liposomal doxorubicin via the folate receptor in vitro. *J Control Release*, 2003. 92(1-2): p. 49-67.
145. Gabizon, A., Horowitz, AT, Goren, D, Tzemach, D, Mandelbaum-Shavit, F, Qazen, MM, Zalipsky, S, Targeting folate receptor with folate linked to extremities of poly(ethylene glycol)-grafted liposomes: In vitro studies. *Bioconjug Chem*, 1999. 10(2): p. 289-98.
146. Lee, E., Na, K, Bae, YH, Polymeric micelle for tumor ph and folate-mediated targeting. *J Control Release*, 2003. 91(1-2): p. 103-13.
147. Bae, Y., Jang, WD, Nishiyama, N, Fukushima, S, Kataoka, K, Multifunctional polymeric micelles with folate-mediated cancer cell targeting and ph-triggered drug releasing properties for active intracellular drug delivery. *Mol Biosyst*, 2005. 1(3): p. 242-50.
148. Yoo, H., Park, TG, Folate-receptor-targeted delivery of doxorubicin nano-aggregates stabilized by doxorubicin-peg-folate conjugate. *J Control Release*, 2004. 100(2): p. 247-56.
149. Yoo, H., Park, TG, Folate receptor targeted biodegradable polymeric doxorubicin micelles. *J Control Release*, 2004. 96(2): p. 273-83.

150. Bae, K.H., Y. Lee, and T.G. Park, Oil-encapsulating peo-ppo-peo/peg shell cross-linked nanocapsules for target-specific delivery of paclitaxel. *Biomacromolecules*, 2007. 8: p. 650-656.
151. Lee, E., Na, K, Bae, YH, Doxorubicin loaded ph-sensitive polymeric micelles for reversal of resistant mcf-7 tumor. *J Control Release*, 2005. 103(2): p. 405-18.
152. What are the different types of chemotherapy drugs? 2004, American Cancer Society.
153. Cancer drug guide: Doxorubicin hydrochloride. 2004.
154. Sparano, J.A., U. Malik, L. Rajdev, C. Sarta, U. Hopkins, and A.C. Wolff, Phase I trial of pegylated liposomal doxorubicin and docetaxel in advanced breast cancer. *Journal of Clinical Oncology*, 2001. 19(12): p. 3117-3125.
155. Tardi, P.G., N.L. Boman, and P.R. Cullis, Liposomal doxorubicin. *Journal of Drug Targeting*, 1996. 4(3): p. 129-140.
156. Cancer drug guide: Doxorubicin hydrochloride liposome injection. 2004.
157. Moase, E.H., W. Qi, T. Ishida, Z. Gabos, B.M. Longenecker, G.L. Zimmerman, L. Ding, M. Krantz, and T.M. Allen, Anti-muc-1 immunoliposomal doxorubicin in the treatment of murine models of metastatic breast cancer. *Biochimica et Biophysica Acta*, 2001. 1510: p. 43-55.
158. Kumar, N., Taxol-induced polymerization of purified tubulin. *The Journal of Biological Chemistry*, 1981. 256(20): p. 10435-10441.
159. National Cancer Institute. Drug information: Paclitaxel, 2008.
<http://www.cancer.gov/cancertopics/druginfo/paclitaxel>
160. Sutton, D., N. Nasongkla, E. Blanco, and J. Gao, Functionalized micellar systems for cancer targeted drug delivery. *Pharmaceutical Research*, 2007. 24(6): p. 1029-1046.
161. Lee, S.C., C. Kim, I.C. Kwon, H. Chung, and S.Y. Jeong, Polymeric micelles of poly(2-ethyl-2-oxazoline)-block-poly(ϵ -caprolactone) copolymer as a carrier for paclitaxel. *Journal of Controlled Release*, 2003. 89: p. 437-446.
162. Dong, Y. and S.-S. Feng, Nanoparticles of poly(d,l-lactide)/methoxy poly(ethylene glycol)-poly(d,l-lactide) blends for controlled release of paclitaxel. *Inc. J Biomed Mater Res*, 2006. 78A: p. 12-19.
163. Liang, H.-F., S.-C. Chen, M.-C. Chen, P.-W. Lee, C.-T. Chen, and H.-W. Sung, Paclitaxel-loaded poly(γ -glutamic acid)-poly(lactide) nanoparticles as a targeted drug delivery system against cultured hepg2 cells. *Bioconjugate Chemistry*, 2006. 17: p. 291-299.

164. Liang, H.-F., C.-T. Chen, S.-C. Chen, A.R. Kulkarni, Y.-L. Chiu, M.-C. Chen, and H.-W. Sung, Paclitaxel-loaded poly(g-glutamic acid)-poly(lactide) nanoparticles as a targeted drug delivery system for the treatment of liver cancer. *Biomaterials*, 2006. 27: p. 2051-2059.
165. Seow, W.Y., J.M. Xue, and Y.-Y. Yang, Targeted and intracellular delivery of paclitaxel using multi-functional polymeric micelles. *Biomaterials*, 2007. 28: p. 1730-1740.

Chapter 2. Synthesis of Alternating Copolymer Structures

The syntheses of all polymers used in this project were carried out by Dr. Rahul Tyagi, Dr. Mukesh Pandey, and Bhavna Gupta in Prof. Arthur Watterson's group at the University of Massachusetts, Lowell (UML). The radioiodination of these polymers was performed by Kevin Brower in Professor Clark Colton's group at the Massachusetts Institute of Technology (MIT). The physical characterization was performed by Dr. Jin Zhou Dawson in Prof. Clark Colton's group at MIT. The following descriptions are based on papers published (or to be published) by the Watterson group and the Colton Group, the doctoral thesis of Rahul Tyagi, and the doctoral thesis of Jin Zhou Dawson [1-7]. A detailed description of each synthesis protocol can be found in Appendix I and a list of all polymer structures used in this project is given in Appendix II.

2.1. Enzymatic polymerization

Recent investigation has demonstrated the utility of employing enzymes to perform traditional chemical polymerizations in a more efficient and selective manner [8, 9]. In particular, immobilized *Candida antarctica* Lipase B (Novozyme-435) for organic synthesis overcomes a number of problems traditionally encountered in polyester chemistry. The high enantio- and regiospecificity of the enzyme in the condensation reaction of diacids/diesters with diols to form polyesters is desirable since protection and deprotection steps may be avoided while attaining a high molecular weight linear polymerization product with very little branching. An additional benefit is that the chemistry can proceed without a solvent due to the solubility, albeit to a limited extent, of

diacids in diols. The polymerization, therefore, is an example of a ‘green chemistry’ [3]. The immobilized lipase has been used in various polyesterifications, two of which are presented as examples in Figure 2.1 and Figure 2.2.

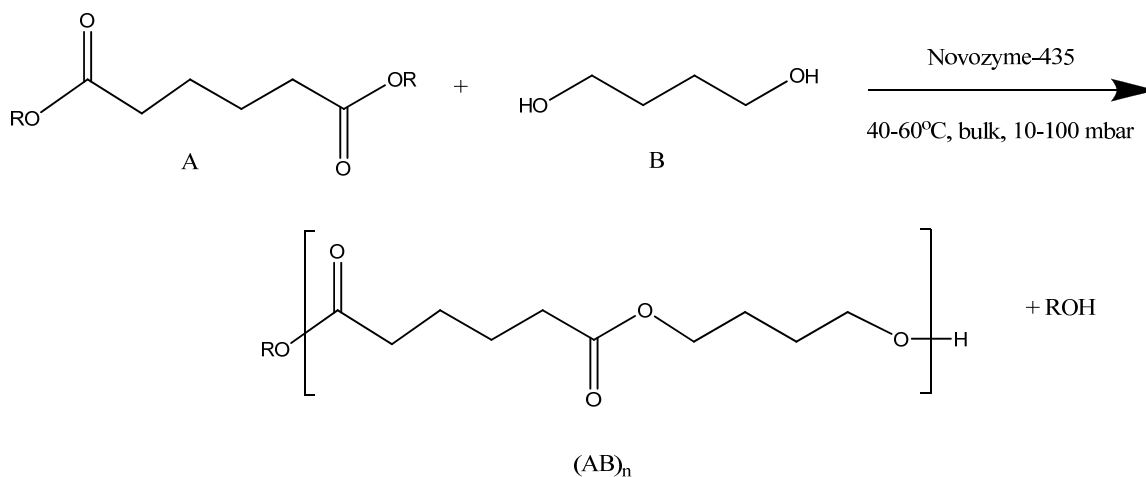


Figure 2.1. Examples of bulk polyesterification of a diester with diol using Novozyme-435 under mild reaction conditions, where R = -CH=CH₂ [10], -H [11].

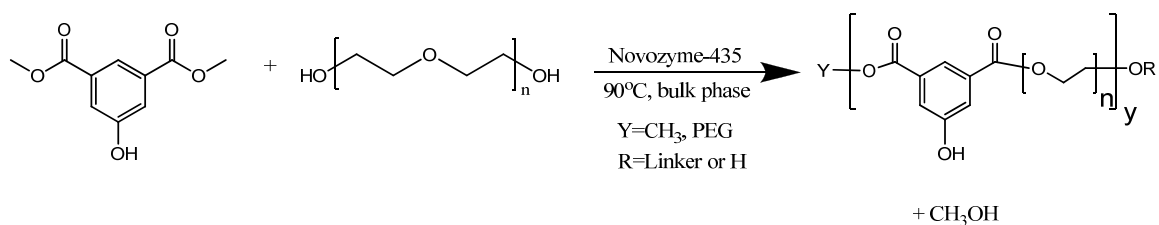


Figure 2.2. Chemo-enzymatic condensation using Novozyme-435 of a diester and diol to form a polyester.

A critical factor in achieving a high molecular weight product is the removal of the condensation byproduct, ROH, such as water (Figure 2.1) or methanol (Figure 2.2), or the vinyl alcohol byproduct, acetaldehyde (CH₃CHO) (Figure 2.1) [10, 11]. Continual removal of the byproduct shifts the equilibrium towards the polymer product.

The mechanism for the polymerization by Novozyme-435 has been investigated by Binns et. al. by performing GPC analysis of the oligomers present during the reaction using synthesized low molecular weight intermediates for comparison [11]. In the proposed mechanism, shown in Figure 2.2, the enzyme forms an active complex by acylating the diacid (or diester), A, which then reacts with the diol, B, to form the intermediate, AB. The enzyme then acylates the second acid site forming an activated Enz-AB complex for addition to a $B(AB)_n$ oligomer. Essentially, in the acylation step, the enzyme attaches itself to the oligomer via a ‘pseudo-ester bond’ forming a highly reactive intermediate where the enzyme itself is the leaving group in the subsequent reaction. This step-wise mechanism was also reported during investigation of polyesterification using *Aspergillus niger* lipase [12].

A reaction scheme has been developed by Watterson and colleagues at UML [1-4, 13] that utilizes Novozyme-435 to synthesize the backbone polymer as the first step in the production of amphiphilic alternating copolymers with potential application in the field of imaging and drug delivery. It is presented in Figure 2.2. For this reaction, dimethyl 5-hydroxyisophthalate participates as the diester while poly(ethylene glycol-900) (PEG-900) is the diol. The product is the polyester poly[poly(oxyethylene-900)-oxy-5-hydroxyisophthaloyl]. The condensation byproduct, methanol, is removed from the reacting mixture by vacuum. The condensation product is the ‘backbone polymer.’ Application of a suitably low vacuum to remove the methanol is necessary to shift the equilibrium towards the polymer product since the reaction energetics alone are not favorable enough to achieve sufficiently high molecular weights.

In the attachment via the ester linkage, the highly reactive acid chloride terminus of the nonanoyl chloride reacts with the many free hydroxyl groups on the backbone. The acid chloride is so reactive that it is likely that it also reacts with the free hydroxyl group on the end of the polymer backbone. During the development of this project, the cytotoxicity of the polymers formed by hydrocarbon attachment via each of these bonds was investigated. These results are discussed in Chapter 3. Different bonds were used throughout the project depending on the desired properties of the polymer.

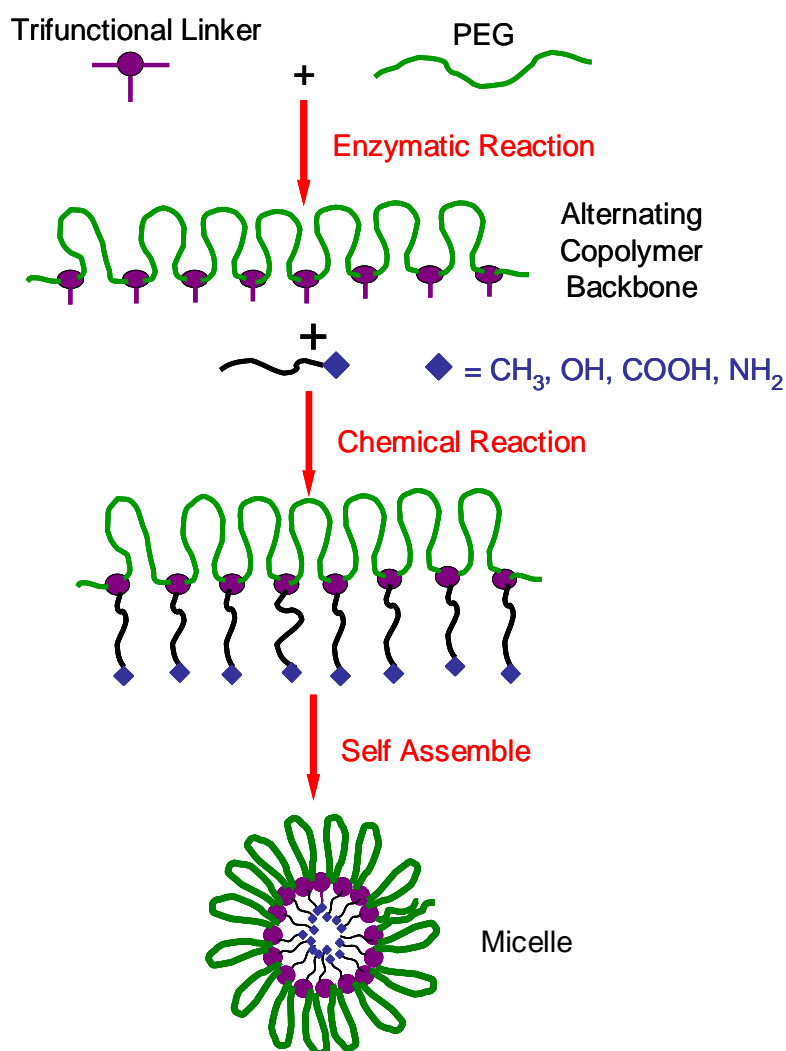


Figure 2.4. Formation of self-assembling alternating copolymer micelles.

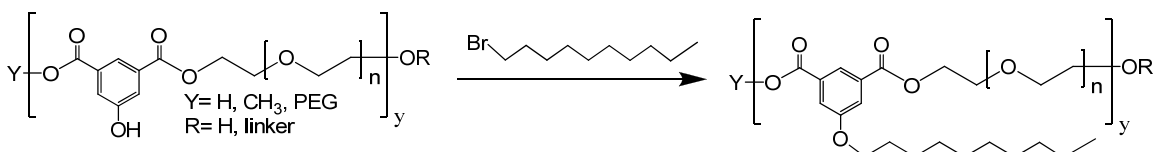


Figure 2.5. Hydrocarbon side chain attachment via the ether bond.

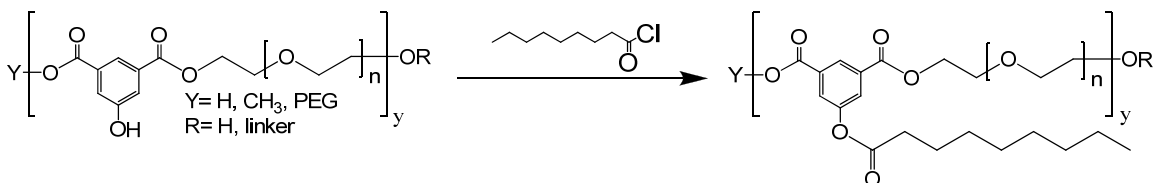


Figure 2.6. Hydrocarbon side chain attachment via the ester bond.

2.3. Attachment of perfluorocarbon side chains

A synthetic method was also developed for the attachment of perfluorinated side chains. These side chains serve a dual purpose in that they not only act as a contrast agent in ^{19}F -MRI but are also extremely hydrophobic thereby imparting amphiphilicity to the resulting polymer. Thus, these perfluorocarbon (PFC) side chains can replace the need for hydrocarbon side chains in the self-assembly mechanism for micelle formation. PFC side chains have been attached by an ether ester bond to the hydroxyl linkers (shown in Figure 2.7) or by an amide bond to the amino linkers. To accomplish the attachment through an ether ester bond, a perfluorinated alcohol is converted into a perfluorinated bromoester by addition of bromoacetic acid in the presence of the lipase Novozyme-435 under vacuum. This activated perfluorocarbon is then added to the linker hydroxyl group on the backbone polymer in acetonitrile with potassium carbonate to produce polymer having perfluorinated side chains [4]. To accomplish the attachment through an amide bond, the

acid chloride of the PFC was reacted with the backbone polymer containing free amino groups on the linkers, giving the desired polymer with perfluorinated side chains.

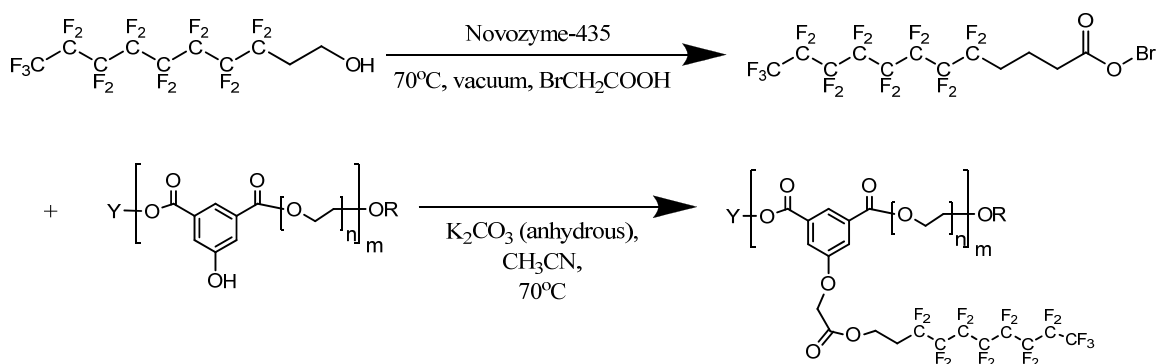


Figure 2.7. Attachment of perfluorinated sidechains to the backbone polymer for potential use in ^{19}F MRI imaging applications.

2.4. Attachment of fluorescent labels

Fluorescent labels were attached to the studied polymers for two purposes. First, the labeled polymers could be observed *in vitro* experiments by confocal microscopy to provide insight into the interaction of these polymers with cells. In addition, the attachment of some fluorescent labels, for example Cy 5.5, offers the potential for these labeled polymers to be used for near infrared fluorescence (NIRF) imaging. The amino group on the linker can be used as an attachment point for fluorescent dyes including FITC and Cy 5.5. The attachment of the former is demonstrated in Figure 2.8 where the amine group on the backbone polymer readily reacts with the isothiocyanate group (NCS) on FITC to produce the labeled polymer, which can be functionalized as desired [5].

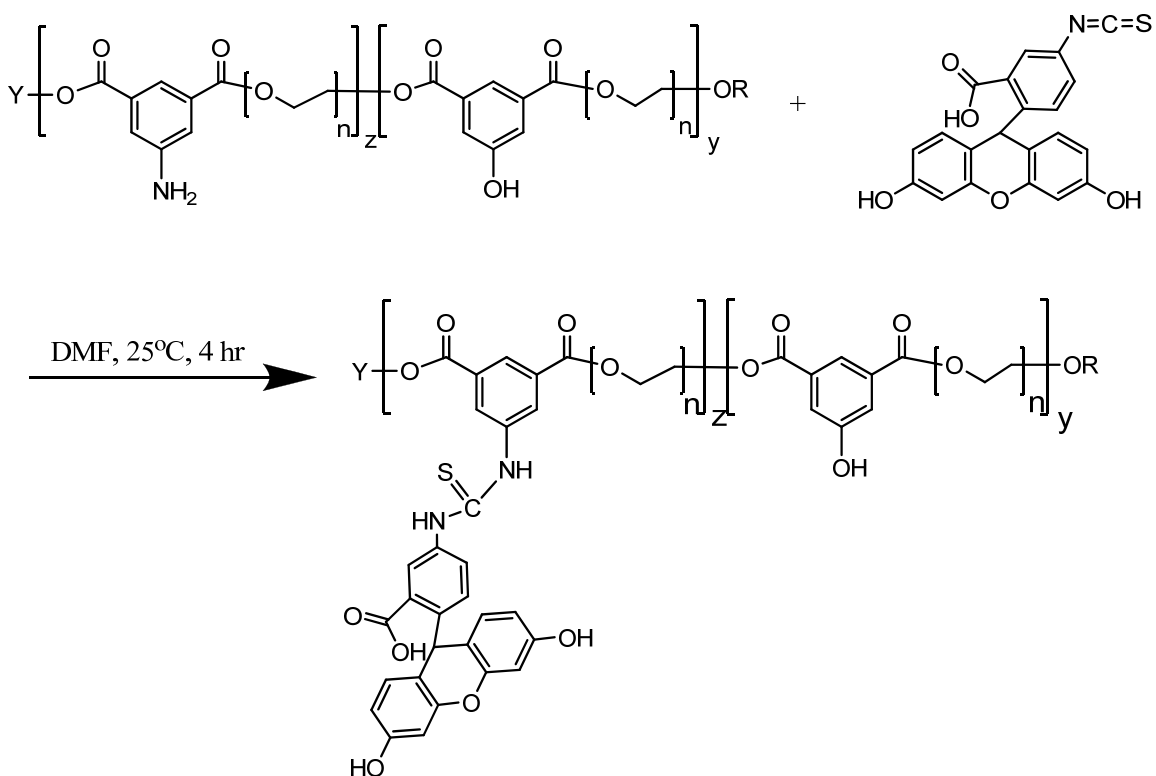


Figure 2.8. Attachment of the fluorescent dye, FITC, to the amine functionality of the backbone polymer.

2.5. Attachment of targeting ligands

2.5.1. EPPT

Our collaborators at UML successfully attached the targeting peptide, EPPT, via two synthetic routes. The first synthetic route, shown in Figure 2.9, attached the EPPT via the spacer triethylene glycol (TEG). The first step involved the attachment of the small hydrophilic spacer molecule to the polymer at the hydroxyl groups of the linkers. The quantity of triethylene glycol added to the reaction mixture determined the percent of side chains in the final product that were devoted to the peptide. Next, the hydroxyl group of the hydrophilic spacer was activated by the addition of disuccinimidyl carbonate. The entire EPPT molecule (Ahx-AREPPTRTFAYWG) consists of a short polypeptide

terminated by an aminohexanoyl (Ahx) group. The Ahx group provided both a reaction site in the amine group as well as an additional spacer between the peptide and reaction site [14]. To complete the attachment, EPPT was reacted with the activated group on the spacer to produce the targeted polymer. The combined hydrophilic nature of both the spacer and the targeting peptide itself are believed to cause the peptide side chains to present themselves on the micelle exterior upon self-assembly.

As will be discussed in Chapter 4, it was determined through experiments and modeling that the triethylene glycol spacer used to attach the EPPT to the polymer in the first synthetic scheme may not be long enough to allow free binding with no steric hindrances. Because of this, a second synthetic route was established by our collaborators using bifunctional PEG-3400 as the peptide attachment spacer. The first step of this synthetic route involved the protection of the hydroxyl group on the PEG-3400, followed by activation of the carboxyl group on the PEG-3400. This activated hydrophilic spacer molecule was reacted with the hydroxyl group of the linkers on the polymer backbone. Again, the quantity of spacer added to the reaction mixture determines the percent of side chains in the final product that will be devoted to the peptide. Next, the end of the hydrophilic spacer was deprotected and activated and EPPT was reacted with this activated group on to produce the targeted polymer with a longer spacer. Again, the combined hydrophilic nature of both the spacer and the targeting peptide should cause the peptide side chains to present themselves on the micelle exterior upon self-assembly.

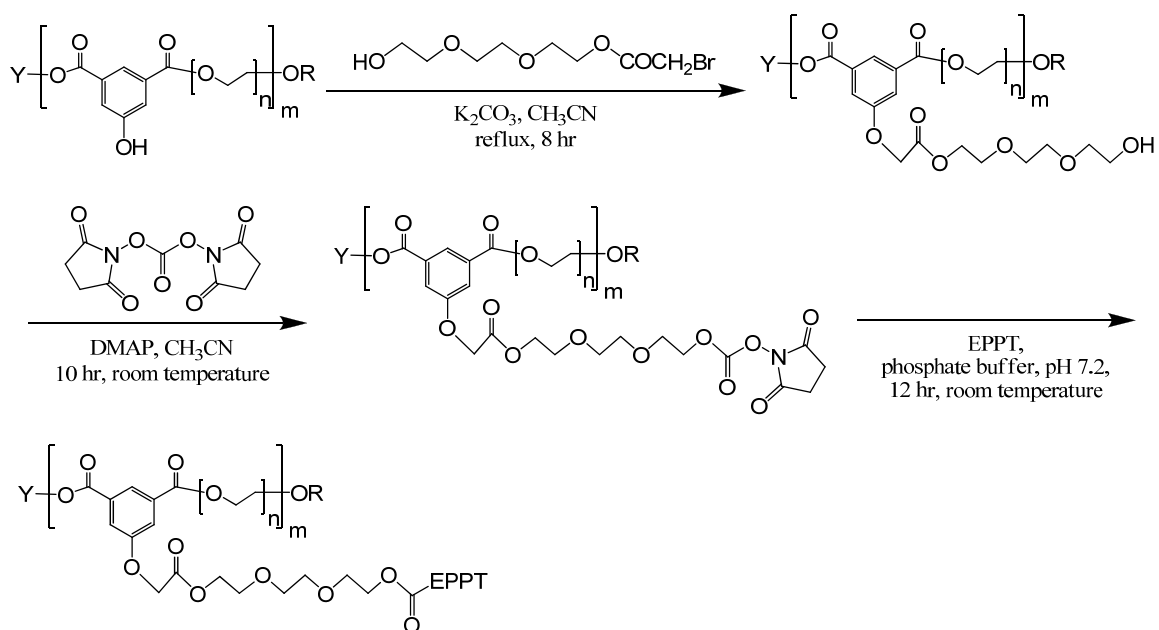


Figure 2.9. Attachment of targeting peptide, EPPT, via triethylene glycol.

2.5.2. Folate

In addition to EPPT, folate, which targets the folate receptor, was chosen as a model target. This targeting system was used for two reasons: 1) to decrease costs associated with polymer synthesis during the probing phase of the project and 2) to verify the targeting ability of the polymer system in an extensively studied system, as targeting with folate has been described at length in the literature (see Chapter 1). Our collaborators at UML successfully attached folate via two synthetic routes. In the first synthetic route, folate was attached directly to the backbone polymer via the hydroxyl groups on the linkers. The folate was first activated and then directly reacted with the backbone polymer. The hydrophilic nature of the targeting ligand will allow for the folate to present itself on the micelle exterior upon self-assembly.

As mentioned above, it was determined through experiments and modeling that a long spacer may be needed in order to allow free binding of the targeting ligand with the

target, avoiding steric hindrances. As with EPPT, a second synthetic route was established by our collaborators using bifunctional PEG-3400 as the spacer to attach folate. The first step of this synthetic route involved the protection of the hydroxyl group on the PEG-3400, followed by activation of the carboxyl group on the PEG-3400. This activated hydrophilic spacer molecule was reacted with the hydroxyl group of the linkers on the polymer backbone. The end of the hydrophilic spacer was deprotected and activated and folate was reacted with this activated group on the spacer to produce the targeted polymer with a long spacer. Again, the combined hydrophilic nature of both the spacer and the targeting peptide should cause the peptide side chains to present themselves on the micelle exterior upon self-assembly.

2.6. Radiolabeling of polymers

As with the attachment of PFC side chains and fluorescent labels, radiolabeling of polymers has two intentions. Labeling of the polymer with ^{125}I , ^{14}C , or ^3H allow for measurement of cellular uptake of these polymers *in vitro*. Results obtained from these measurements are discussed in Chapter 4. The same labeling techniques can be used to attach ^{124}I to the polymer, allowing for positron emission tomography (PET) imaging.

Radioiodine can be added via exchange with the aromatic hydrogens that are present on the linker molecule as well as with the tyrosine, phenylalanine, and tryptophan molecules on the EPPT peptide. There are a number of methods available to perform the exchange reaction, including the iodogen and iodobead methods [15]. In the iodobead method the targeted polymer is added to a vial containing a single iodobead along with Na^{125}I . The iodobead is conjugated to a molecule that catalyzes the iodine substitution

labeling. All radioiodinations were performed by Kevin Brower in the Colton group at MIT. Polymers labeled with ^{125}I can be quantified using a gamma counter.

Labeling of polymers with ^{14}C is easily accomplished through methylation. A methyl group containing ^{14}C can react by nucleophilic substitution at a hydroxyl group, such as the hydroxyl group on the linker, thereby labeling the polymer with ^{14}C .

Alternatively, ^3H is added to the polymer by using commercially available ^3H -folate in the targeting ligand attachment step. For this project, polymers containing folate were the only ones labeled with ^3H . Polymers labeled with ^{14}C or ^3H can be quantified using a scintillation counter.

2.7. Encapsulation of chemotherapeutic drugs in polymer micelles

It has been demonstrated that a variety of small molecules including drugs (aspirin, naproxen) may be encapsulated by the self-assembly process described above [3, 16]. Larger molecules such as proteins (insulin) and polysaccharides (inulin) have also been encapsulated since the nanospheres can adjust to the size of the encapsulant molecule in the self-assembly process. For use in this study, a hydrophilic chemotherapeutic drug, doxorubicin, was encapsulated in the form of its hydrochloride salt. All encapsulations were performed by our collaborators in Professor Arthur Watterson's lab at UML, as described in Appendix I. To encapsulate doxorubicin, the polymer and drug were each dissolved in water, the solutions were mixed, and then dialyzed against water to remove unencapsulated drug. During the study, it was determined that this procedure may not be reliable or reproducible, as discussed in Chapter 3. In order to use a more reliable procedure, a hydrophobic chemotherapeutic

drug, paclitaxel, was used. To encapsulate paclitaxel, the polymer and drug were dissolved in a solvent, such as chloroform or methanol, the solvent was evaporated, and the viscous mixture was dissolved in water to allow for formation of the encapsulating micelles. The structure of the micelles is stabilized by the water-soluble PEG at the exterior surface and by hydrophobic interactions between the linkers, side chains and encapsulated drug.

2.8. Physical Characterization

The physical characterization of the polymers was the focus of the doctoral thesis of Jin Zhou Dawson in the Colton group at MIT [7]. The size and morphology of the nanoparticles was characterized by dynamic light scattering, transmission electron microscopy (TEM), cryo-TEM, and small angle neutron scattering (SANS). It was determined that micelles formed from the polymers described above are spheroidal with a radius of about 4-5 nm with hydrocarbon side chains, 8-9 nm with PFC side chains, and 11 nm with PFC side chains and encapsulated PFC. The hydrodynamic radius of micelles did not change with polymer concentration, PEG length, sample preparation method, or time after sample preparation. The polymers were found to form two populations of particles – small micelles and large secondary aggregates. The large secondary aggregates were most likely compound micelles. The sample preparation method, polymer molecular weight, and time after sample preparation could change the proportion of micelles versus aggregates.

The critical micelle concentration (CMC) was determined by surface tension measurements. The CMC was measured as 12 μM for polymers with hydrocarbon side

chains and 2 μM for polymers with PFC side chains. The PFC side chains may be useful when it is desired to keep the micelle intact at low concentration.

Preliminary studies of the polymers with PFC side chains by ^{19}F -MRI were performed to investigate the use of the polymers as imaging agents. Micellization of these polymers caused the spectral lines, as measured by ^{19}F -NMR, to broaden indicating a reduction in the signal-to-noise ratio (SNR). Consequently, it is difficult to utilize ^{19}F -NMR to measure biological samples loaded with polymers with PFC side chains *in vitro* because the SNR is too low.

2.9. References

1. Kumar, R., N.A. Shakil, M.-H. Chen, V.S. Parmar, L.A. Samuelson, J. Kumar, and A.C. Watterson, Chemo-enzymatic synthesis and characterization of novel functionalized amphiphilic polymers. *Journal of Macromolecular Science*, 2002. A39(10): p. 1137-1149.
2. Kumar, R., Tyagi, R., Parmar, V. S., Samuelson, L. A., Watterson, A. C., Kumar, J., *Candida antarctica* lipase b catalyzed copolymerizations of non-poteinogenic amino acids and poly(ethylene glycol) to generate novel functionalized polyesters. *J Macromolecular Science*, 2003. A40(12): p. 1283-1293.
3. Kumar, R., M.H. Chen, V.S. Parmar, L.A. Samuelson, J. Kumar, R.A. Nicolosi, S. Yoganathan, and A.C. Watterson, Supramolecular assemblies based on copolymers of peg600 and functionalized aromatic diesters for drug delivery applications. *Journal of the American Chemical Society*, 2004. 126(34): p. 10640-10644.
4. Kumar, R., Tyagi, R., Parmar, V. S., Watterson, A. C., Kumar, J., Zhou, J., Hardiman, M., Fisher, R., Colton, C. K., Perfluorinated amphiphilic polymers as nano probes for imaging and delivery of therapeutics for cancer. *Polymer Preprints*, 2005.
5. Pandey, M.K., Tyagi, Rahul, Kumar, Rajesh, Parmar, Virinder S., Watterson, Arthur C., Kumar, Jayant, Hardiman, Michelle T. Zhou, Jin, Brower, Kevin P., Fisher, Robert J., Colton, Clark K., Design and synthesis of novel amphiphilic polymers for mri and selective targeting in cancer diagnosis / therapy. *Polymeric Materials: Science and Engineering*, 2007. 96: p. 855-6.
6. Tyagi, R., Unknown title, in Department of Chemistry. 2008, University of Massachusetts, Lowell: Lowell, MA. p. 1-163.
7. Dawson, J.Z., Physicochemical characterization of peg-based comb-like amphiphilic copolymer structures for possible imaging and therapeutic applications, in Department of Chemical Engineering. 2008, Massachusetts Institute of Technology: Cambridge, MA. p. 1-267.
8. Roberts, S.M., Preparative biotransformations. *J Chem Soc, Perkin Trans 1*, 2001: p. 1475-1499.
9. Kobayashi, S., Uyama, H., Kimura, S., Enzymatic polymerization. *Chem Rev*, 2001. 101: p. 3793-3818.
10. Chaudhary, A.K., Lopez, J., Beckman, E. J., Russell, A. J., Biocatalytic solvent-free polymerization to produce high molecular weight polyesters. *Biotechnol Prog*, 1997. 13: p. 318-325.

11. Binns, F., Harffey, P., Roberts, S. M., Taylor, A., Studies of lipase-catalyzed polyesterification of an unactivated diacid/diol system. *J Polymer Science: Part A: Polymer Chemistry*, 1998. 36: p. 2069-2080.
12. Okumura, S., Iwai, M., Tominaga, Y., *Agric Biol Chem*, 1994. 48: p. 2805.
13. Sharma, S.K., Sharma, A. K., Kumar, R., Parmar, V. S., Samuelson, L. A., Kumar, J., Watterson, A. C., Synthesis of amino functionalized amphiphilic copolymers as potential gene delivery carriers. *Polymer Preprints*, 2003. 44(2): p. 791-792.
14. Pham, W., Discussion of eppt1 synthesis and subsequent reaction capabilities, K. Brower, Editor. 2006.
15. Seevers, R.H., Counsell, R. E., Radioiodination techniques for small organic molecules. *Chem Rev*, 1982. 82: p. 575-590.
16. Sharma, S.K., R. Kumar, S. Kumar, R. Mosurkal, V.S. Parmar, L.A. Samuelson, A.C. Watterson, and J. Kumar, Influence of eda-pi interactions in drug encapsulation using nanospheres. *Chemical Communication*, 2004. 23: p. 2689-2691.

Chapter 3. *In Vitro* Cytotoxicity of Polymers as Drug Delivery Vehicles

3.1. Introduction

Polymeric micelle-based carriers have been developed by many groups and are currently under investigation for drug and imaging agent delivery [1-20]. Polymeric micelles, with various drugs incorporated into the inner core by chemical conjugation or physical entrapment, are expected to increase the accumulation of those drugs in tumor tissues by using passive and active targeting. Targeted micelles are selective for tumor cells, allowing for reduced incidence of the adverse side effects of chemotherapeutic drugs. Several polymeric micelle systems, for which clinical trials are now underway, have been reviewed [21].

One of the essential requirements for drug and imaging agent carriers is that they have no inherent cytotoxicity [22-25]. In the present study, we investigated the toxic effects of a variety of alternating copolymers using cell culture systems. In addition, we examined the use of these carriers as drug delivery vehicles when loaded with chemotherapeutic drugs. Cytotoxicity was assessed by measuring the mitochondrial function of the cells being tested. The MTS assay tests the reduction of the tetrazolium salt MTS by mitochondrial reactions to form a dye molecule with an absorbance spectrum different from the parent dye [26-28]. The measurement of absorbance over time is correlated to the viability of the cells. We selected five types of cultured cells (BT-20 (uMUC1+), U87 (uMUC1-), KB (FR+), HT-1080 (FR-), and INS-1), applicable to the uptake studies discussed in Chapter 4, for use in these cytotoxicity studies.

This chapter clarifies the effect of the structure of the alternating copolymer, including linker type, PEG length, side chain type, side chain bond type, side chain length, ligand type, ligand spacer type, and imaging agent type, on the degree of toxicity in cultured cells and establishes the drug delivery capabilities of these alternating copolymers. A detailed description of the synthesis protocol for each polymer can be found in Appendix I. A list of all polymer structures used in this study is given in Appendix II. The numbers referred to throughout the text correspond to polymer structures in the table in Appendix II.

3.2. Methods

3.2.1. Materials and reagents

All polymers were provided by our collaborators in Professor Arthur Watterson's lab at the University of Massachusetts, Lowell. All reagents were obtained from commercial sources. Poly-ethylene glycol (PEG-900), 5-methyl hydroxyl isophthalate, 5-methyl amino isophthalate, and β -mercaptoethanol were obtained from Sigma Aldrich. Dulbecco's phosphate buffered saline (DPBS) and distilled deionized sterile water, trypsin EDTA (1X, 0.25% trypsin/0.53 mM EDTA in HBSS), penicillin-streptomycin solution, RPMI, D-glucose, L-glutamine, sodium pyruvate, and fetal bovine serum (FBS) were purchased from Mediatech, Inc. Minimum essential media, Eagle, with 2 mM L-glutamine and Earle's BSS adjusted to contain 1.5 g/L sodium bicarbonate, 0.1 mM non-essential amino acids, and 1.0 mM sodium pyruvate (EMEM) was purchased from ATCC. CellTiter 96® Aqueous Non-Radioactive Cell Proliferation Assay kits (for MTS) were purchased from Promega. Fluorescein-5-isothiocyanate (FITC) was purchased from

American Peptide. Rhodamine B was purchased from EMD Chemicals. Doxorubicin (DOX) and paclitaxel (PAC) were purchased from EMD Biosciences.

3.2.2. Cell lines and culture

BT-20 cells (human breast carcinoma; uMUC1+), U87 cells (human brain glioblastoma; uMUC1-), MRC-5 cells (human lung fibroblast; uMUC1-), KB cells (human epidermoid carcinoma; FR+), and HT-1080 cells (human fibrosarcoma; FR-) were purchased from American Type Culture Collection and INS-1 cells (rat insulinoma) were a gift from Chris Newgard at Duke University. BT-20, U87, MRC-5, KB, and HT-1080 cells were all cultured in EMEM supplemented with 10% FBS and 1% penicillin–streptomycin solution. INS-1 cells were cultured in RPMI supplemented with 11.1 mM D-glucose, 1% penicillin–streptomycin solution, 2 mM L-glutamine, 1 mM sodium pyruvate, 50 μ M β -mercaptoethanol, and 10% FBS. All cells were grown under sterile conditions at 37°C in a humidified atmosphere containing 5% CO₂.

3.2.3. Cytotoxicity assay

The MTS-based *in vitro* cytotoxicity assay was performed to determine the effects of polymers against relevant cell lines. Reduction of a water soluble tetrazolium compound, 3-(4,5-dimethylthiazol-2-yl)-5-(3-carboxymethoxyphenyl)-2-(4-sulfophenyl)-2H-tetraolium, inner salt (MTS), by cells was measured using the CellTiter 96® Aqueous Non-Radioactive Cell Proliferation Assay kit. The cells growing as a mono-layer were harvested with trypsin EDTA (1X, 0.25% trypsin/0.53 mM EDTA in HBSS). Each cell line was seeded on a 96-well plate at a cell density of 2×10^5 cells/mL 16 hours before the start of the test. Solutions were made by dissolving polymer (0.1-13.2 g/L; 1 g/L

unless otherwise noted), polymer component (1 g/L), or drug (0.0003-0.02 g/L) in cell media and sterile filtering through a 0.2 μm filter. Cells were incubated with the test solution under sterile conditions at 37°C in a humidified atmosphere containing 5% CO_2 . At each time point (0, 2, 6, 24, and 48 hr), the cell media (for control cells) or polymer solution (for test cells) was removed from each well of the 96-well plate. The combined electron coupling reagent phenazine methosulfate and MTS solution (MTS/PMS) and 25 mM glucose in DPBS are premixed in a ration of 1:5. For each well, 120 μL of the premixed solution are added. The same amount of this solution is also added to three empty wells to be used as background readings. The absorbance is measured at 490 nm at 10 min intervals for 60 min in a plate reader (FLUOstar/POLARstar Galaxy, BMG LABTECH, Durham, NC). The slope (rate of increase of absorbance with time), determined by linear least squares regression, is proportional to the number of viable cells. The fraction of viable cells was calculated relative to control cells, thus accounting for normal cell population growth.

3.2.4. Imaging of aggregation

Polymer solutions in cell media (100 μL) were pipetted into a 96-well plate. At each time point, the polymer solution was observed under an optical light microscope and photographs of each were taken. Polymer solutions were observed for various times (0-48 hours) at several concentrations (1-10 g/L) to determine the time- and concentration-dependent aggregation of polymer.

3.2.5. Encapsulation of drug

Separate solutions were made of 200 mg polymer (any polymer containing hydrophobic side chains which can form a micelle) in 5 mL distilled deionized sterile water and 5 mg DOX in 5 mL distilled deionized sterile water. The two solutions were mixed together and further diluted to make a resultant solution of 20 mL. The mixture was dialyzed against distilled deionized sterile water (100 mL) using a MWCO 1000 membrane. The dialysate water was changed frequently. Dialysis was continued while the DOX content of the dialysate was analyzed in a fluorescence plate reader (FLUOstar/POLARstar Galaxy, BMG LABTECH, Durham, NC) with excitation at 480 nm and emission at 590 nm.

3.2.6. Statistical analysis

All data were represented as mean \pm standard deviation.

3.3. Results

3.3.1. Backbone Polymers

The cytotoxicity of each of the three major components that make up the polymer backbone, poly-ethylene glycol (PEG-900), 5-methyl hydroxyl isophthalate, and 5-methyl amino isophthalate, was established using the MTS assay. A solution of each polymer component in cell media was prepared at a concentration of 1 g/L. Each of these reagents showed no cytotoxicity in uMUC1- (U87) cells over 48 hours. However, in uMUC1+ (BT-20) cells some mild toxicity was observed for the amino isophthalate and a significant amount of toxicity was measured for the hydroxyl isophthalate (Figure 3.1).

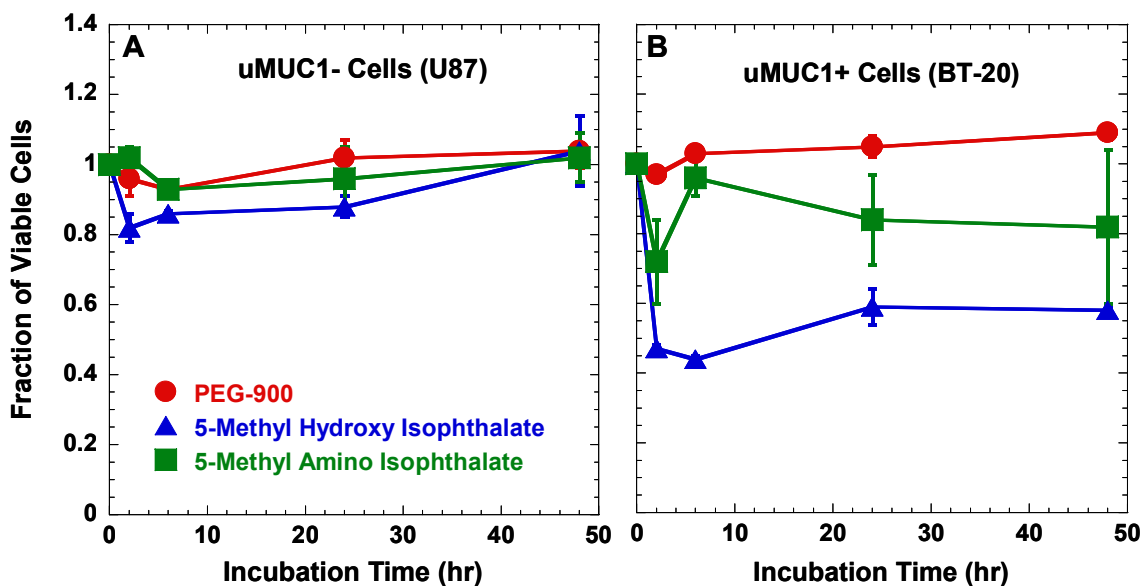


Figure 3.1. Cytotoxicity of the individual polymer components poly-ethylene glycol (PEG-900), 5-methyl hydroxyl isophthalate, and 5-methyl amino isophthalate at 1 g/L in uMUC1- (U87) and uMUC1+ (BT-20) cells (n=3).

The backbone of the polymer was produced using three variations of linker molecules: 100% 5-methyl hydroxyl isophthalate (#23), 100% 5-methyl amino isophthalate (#32), and 95% 5-methyl hydroxyl isophthalate plus 5% 5-methyl amino isophthalate (#24). The cytotoxicity of each backbone polymer was determined at a concentration of 1 g/L using the MTS assay. All three backbone polymers were non-toxic to both the uMUC1- (U87) and uMUC1+ (BT-20) cells (Figure 3.2).

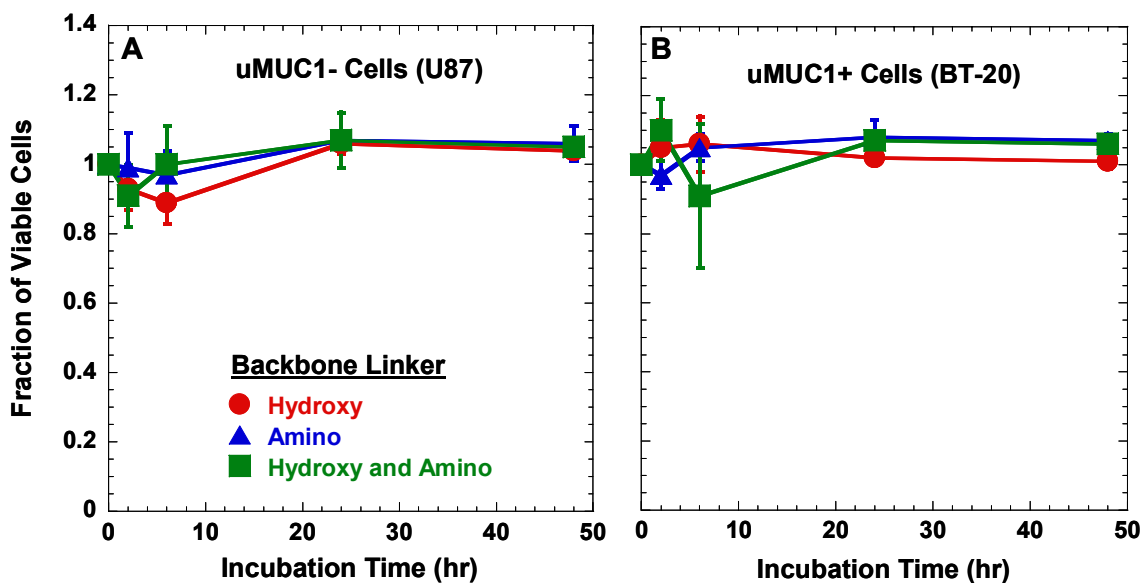


Figure 3.2. Cytotoxicity of backbone polymers with various linkers: 100% 5-methyl hydroxyl isophthalate (#23), 100% 5-methyl amino isophthalate (#32), and 95% 5-methyl hydroxyl isophthalate plus 5% 5-methyl amino isophthalate (#24) at 1 g/L in uMUC1- (U87) and uMUC1+ (BT-20) cells (n=3).

3.3.2. Base Polymers

Some polymers with only hydrocarbon side chains, which were expected to have no cytotoxicity, exhibited some toxicity *in vitro*. It was hypothesized that residual triethylamine (TEA), a reagent used in the hydrocarbon side chain attachment reaction, caused the toxicity. When TEA was replaced by potassium bromide (KBr) as the base in the attachment step, *in vitro* experiments did not indicate cytotoxicity. This confirms that polymers synthesized in the presence of TEA (#22) were cytotoxic, while those synthesized in the absence of TEA (#27) were not (Figure 3.3).

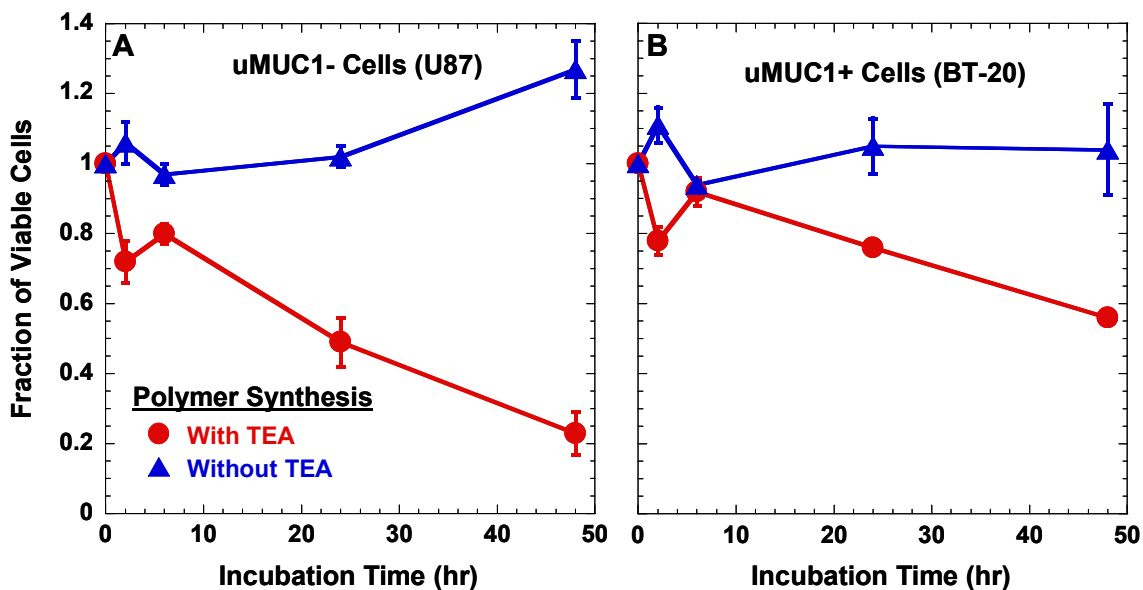


Figure 3.3. Cytotoxicity due to residual TEA: polymers synthesized in the presence of TEA (#22) were cytotoxic, while those synthesized in the absence of TEA (#27) at 1 g/L in uMUC1- (U87) and uMUC1+ (BT-20) cells (n=3).

Polymers synthesized in the presence of TEA (#22) also aggregated when in solution at a concentration of 1 g/L at 37°C over the course of 48 hours. Examples of this aggregation are shown in the time-course optical microscope images in Figure 3.4. Perhaps this aggregation resulted in the observed cytotoxicity of these polymers. When the synthesis was altered to avoid the use of TEA, the aggregation was no longer observed.

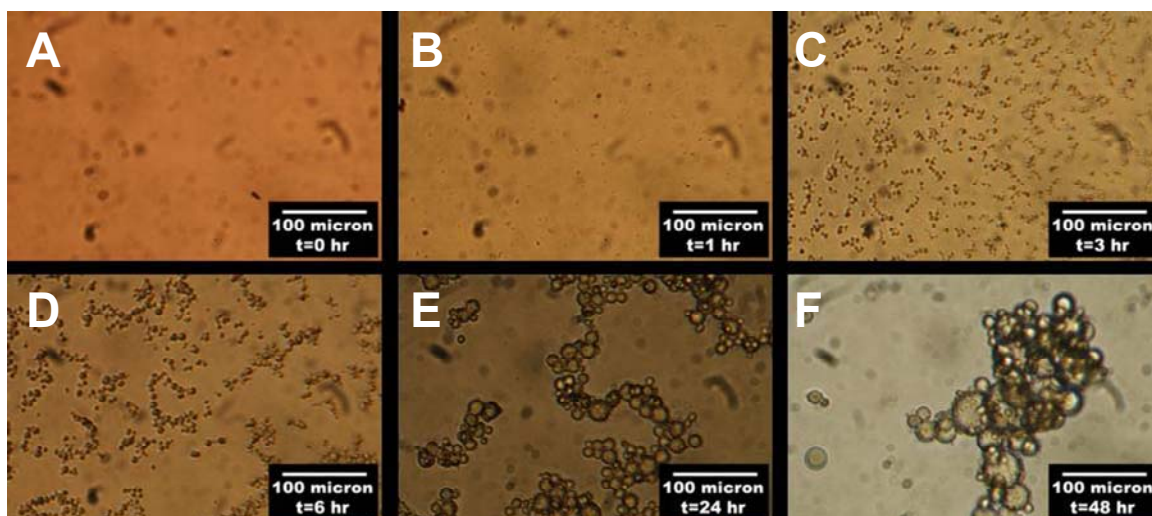


Figure 3.4. Example of aggregation of polymers synthesized in the presence of TEA (#22) when in solution at 1 g/L at 37°C over the course of 48 hours.

Base polymers were also synthesized using backbone polymer containing different PEG lengths. Figure 3.5 shows the cytotoxicity results for three base polymers with hydrocarbon side chains attached via an amide bond. Each polymer differed in the length of the PEG that was used to synthesize the backbone polymer: PEG-600 (#52), PEG-900 (#53), or PEG-1500 (#54). The polymer containing PEG-600 in the backbone demonstrated toxic effects in the FR- cells (HT-1080), but not in the FR+ cells (KB). Otherwise, no differences in cytotoxicity were observed due to PEG length.

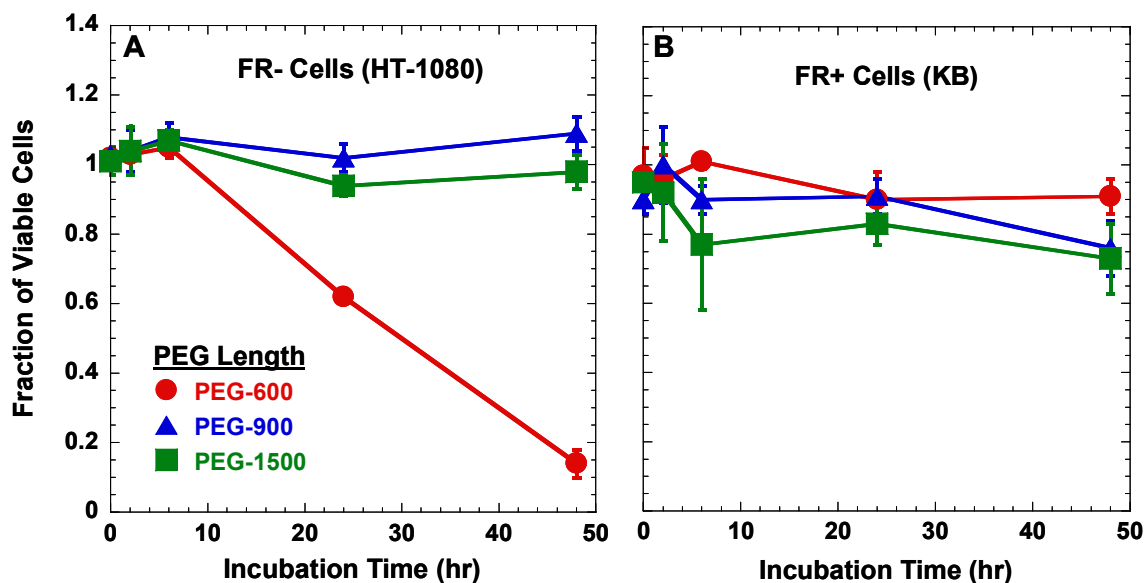


Figure 3.5. Effect of PEG length on cytotoxicity: polymer with PEG-600 (#52), PEG-900 (#53), or PEG-1500 (#54) in the backbone at = 1 g/L in FR- (HT-1080) and FR+ (KB) cells (n=3).

The effects of five different hydrocarbon side chain bond types were explored. The attachment of the side chain to the backbone at the linker molecule was accomplished using ether (#26), ester (#27), ester and amide (#25), amide (#53), and ether-ester (#57) bond types. The toxicity of each was assayed, showing that polymer with side chains attached by ether bonds were cytotoxic in uMUC1- and uMUC1+ cells after 48 hours of incubation, but polymer with side chains attached by ester bonds or by ester and amide bonds were not cytotoxic *in vitro* (Figure 3.6). In addition, polymers with side chains attached by amide bonds were slightly cytotoxic in FR+ cells at 48 hours, but not in FR- cells, and polymers with side chains attached by ether-ester bonds were not cytotoxic (Figure 3.7). All bond types were not tested in all cell types due to cell line availability issues and material limitations.

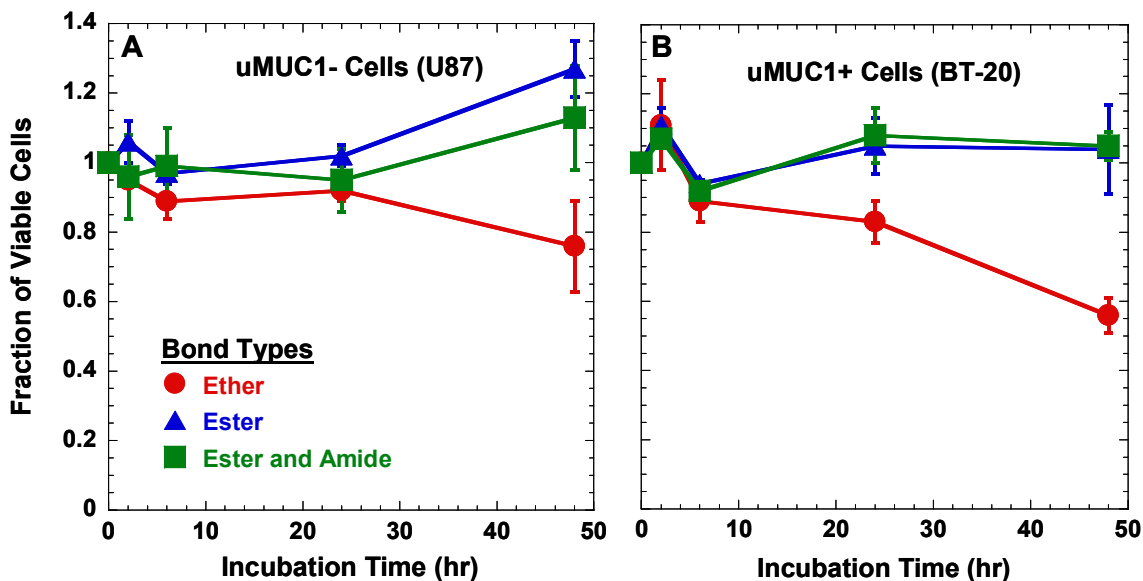


Figure 3.6. Effect of side chain bond type on cytotoxicity: polymer with attachment of the side chain to the backbone at the linker molecule using ether (#26), ester (#27), or ester and amide (#25) bond at 1 g/L in uMUC1- (U87) and uMUC1+ (BT-20) cells (n=3).

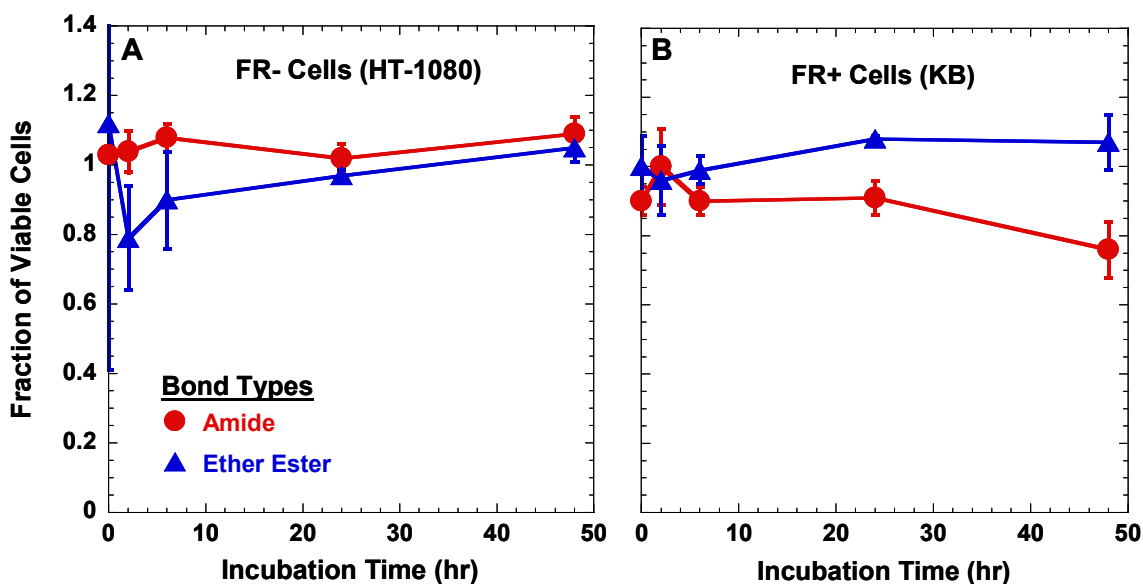


Figure 3.7. Effect of side chain bond type on cytotoxicity: polymer with attachment of the side chain to the backbone at the linker molecule using amide (#53) and ether-ester (#57) bond at 1 g/L in FR- (HT-1080) and FR+ (KB) cells (n=3).

In the study of the effect of bond types, the ether bond was used to attach a 9 carbon side chain, the ester bond was used to attach a 10 carbon side chain, and the ether-ester bond was used to attach an 8 carbon side chain. Therefore, it was unclear whether the side chain length or the bond type was responsible for the toxicity. It was hypothesized that the number of carbons in the hydrocarbon side chain could affect the toxicity, either by affecting the length of the side chain or by determining the odd or even numbered nature of the side chain. The results of the cytotoxicity of polymers with hydrocarbon side chains, containing 9 carbons (#34) or 10 carbons (#26), attached by ether bonds are shown in Figure 3.8. Both polymers were cytotoxic, however, the polymer with 9-carbon side chains caused more cell death. In Figure 3.9, toxicity results are shown for polymers with hydrocarbon side chains attached by ester bonds, again with either 9 carbons (#27) or 10 carbons (#31). No cytotoxicity was observed for either polymer with ester bonds. Figure 3.10 exhibits the toxicity results for polymers with hydrocarbon side chains, with 6 (#58), 8 (#57), or 12 (#62) carbons, attached by ether-ester bonds. The polymer with 6-carbon side chains was cytotoxic in FR- cells, but the cells revived by the 48 hour time point. It was not cytotoxic in FR+ cells. The polymers with 8-carbon and 12-carbon side chains were not cytotoxic. This study confirms that the cytotoxic effects observed with polymers with ether-linked side chain are due to the bond type and not the number of carbons in the side chains.

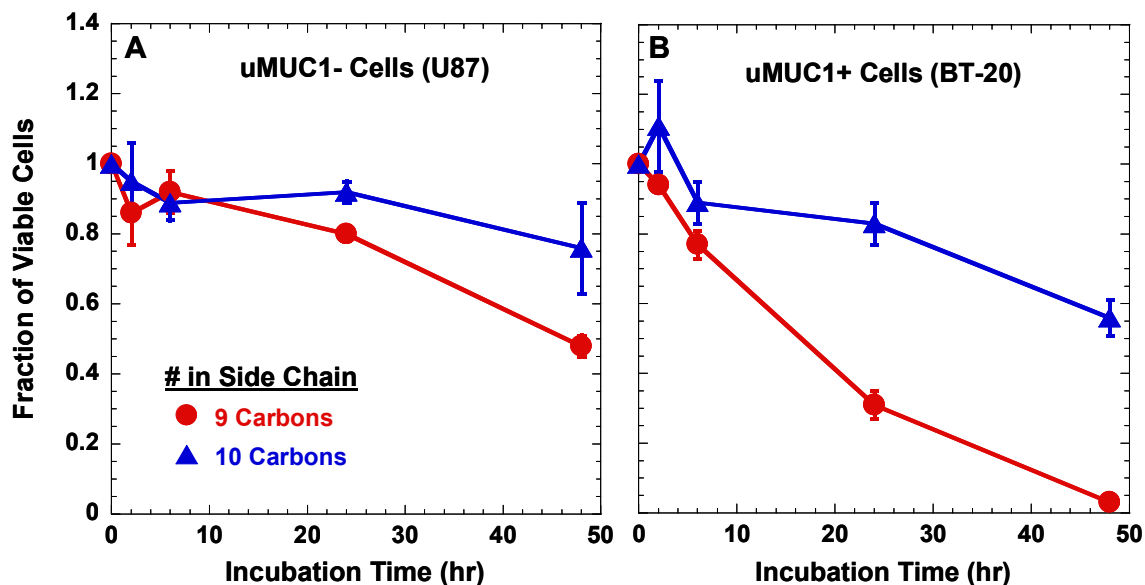


Figure 3.8. Effect of side chain length when attached by ether bond: polymer with hydrocarbon side chains attached by ether bonds containing 9 carbons (#34) or 10 carbons (#26) at 1 g/L in uMUC1- (U87) and uMUC1+ (BT-20) cells (n=3).

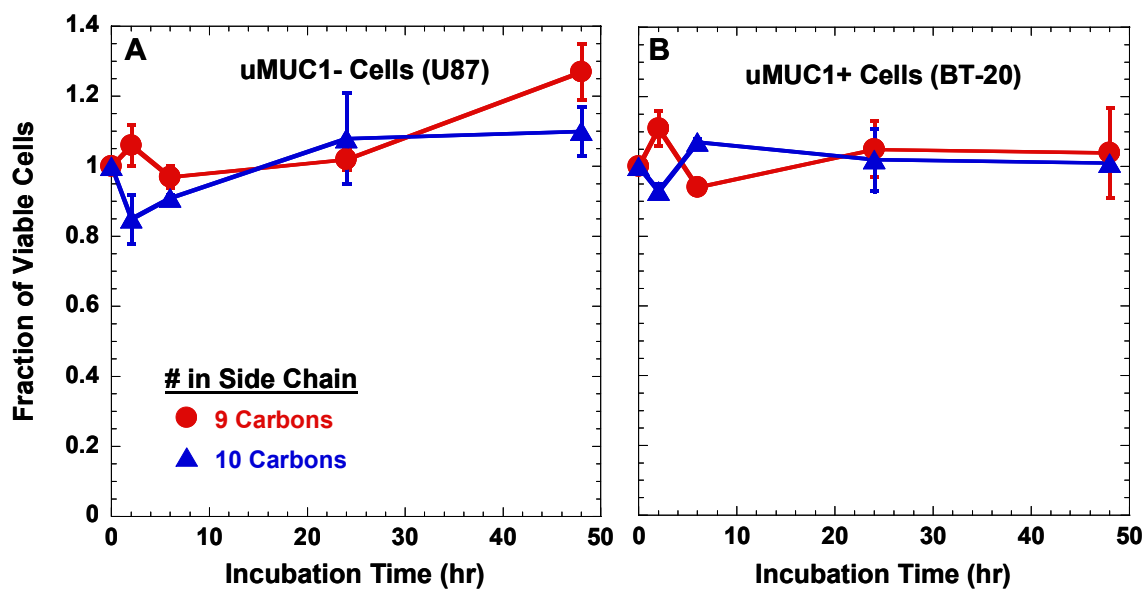


Figure 3.9. Effect of side chain length when attached by ester bond: polymer with hydrocarbon side chains attached by ester bonds containing 9 carbons (#27) or 10 carbons (#31) at 1 g/L in uMUC1- (U87) and uMUC1+ (BT-20) cells (n=3).

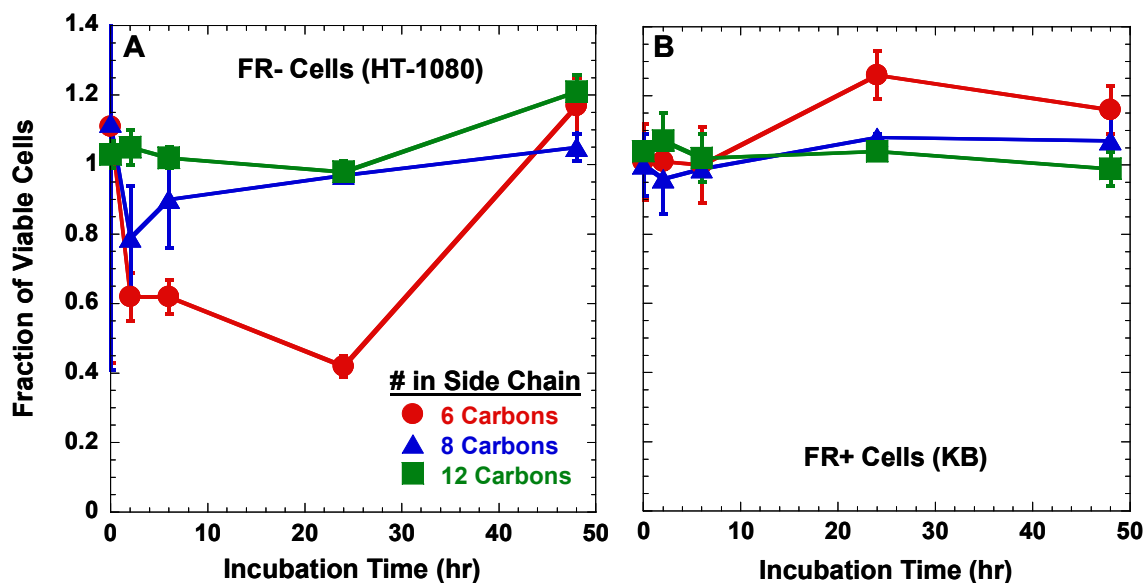


Figure 3.10. Effect of side chain length when attached by ether-ester bond: polymer with hydrocarbon side chains attached by ether-ester bonds containing 6 carbons (#58), 8 carbons (#57), or 12 carbons (#62) at 1 g/L in FR- (HT-1080) and FR+ (KB) cells (n=3).

3.3.3. Targeting Polymers

3.3.3.1. EPPT ligand

The targeting ligand EPPT has been attached to our polymer by two different attachment methods and in variable amounts. The cytotoxicity results for all polymers containing EPPT attached by triethylene glycol (TEG) are shown in Figure 3.11. Polymer with 5% of the linkers having TEG-EPPT attached and the remaining 95% of the linkers having either hydrocarbon side chains (#37) or no side chains (#33) were completely non-toxic *in vitro* up to 48 hours. Polymer with 7% of the linkers having TEG-EPPT attached and no other side chains (#42) was mildly toxic in uMUC1+ cells at 24 hours, but non-toxic in uMUC1- cells. Polymer with 34% of the linkers having TEG-EPPT attached and no other side chains (#44) was mildly toxic in uMUC1- cells at 48 hours,

but very toxic in uMUC1+ cells. This trend implies increased cytotoxicity with increased percent of targeting peptide, possibly due to increased cellular uptake of the polymers with increased percent of EPPT. Figure 3.12 shows the cytotoxicity results for polymer containing EPPT attached by PEG-3400 (#65). This polymer demonstrated no cytotoxicity *in vitro* over the 48 hour assay time period. Consequently, these results were used in planning the uptake experiments described in Chapter 4.

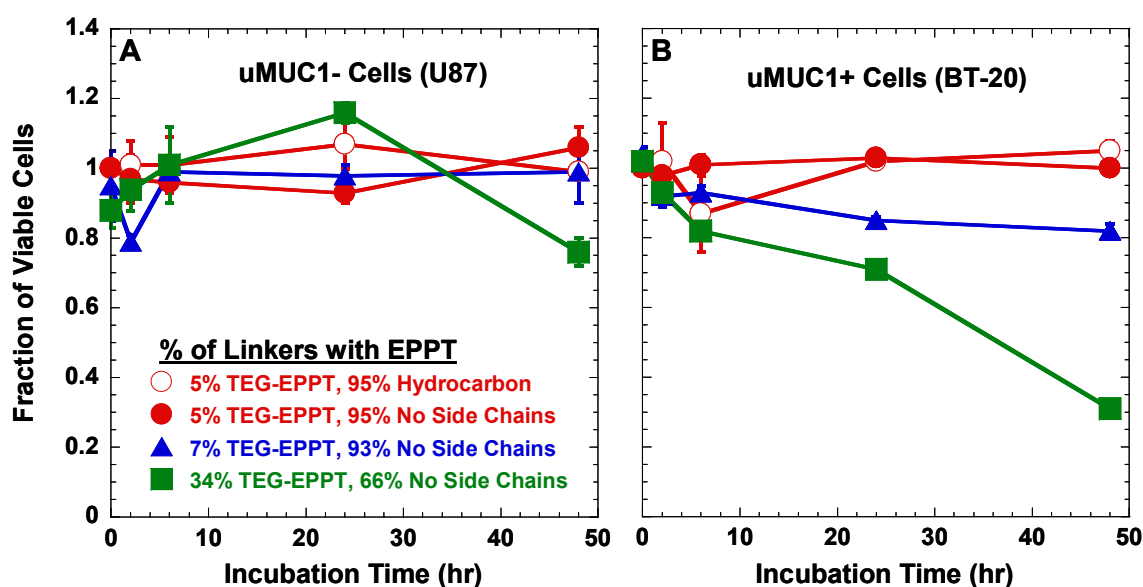


Figure 3.11. Cytotoxicity of EPPT-containing polymers: polymer with 5% of the linkers having TEG-EPPT attached and the remaining 95% of the linkers having hydrocarbon side chains (#37), polymer with 5% of the linkers having TEG-EPPT attached and the remaining 95% of the linkers having no side chains (#33), polymer with 7% of the linkers having TEG-EPPT attached and no other side chains (#42) and polymer with 34% of the linkers having TEG-EPPT attached and no other side chains (#44) at 1 g/L in uMUC1- (U87) and uMUC1+ (BT-20) cells (n=3).

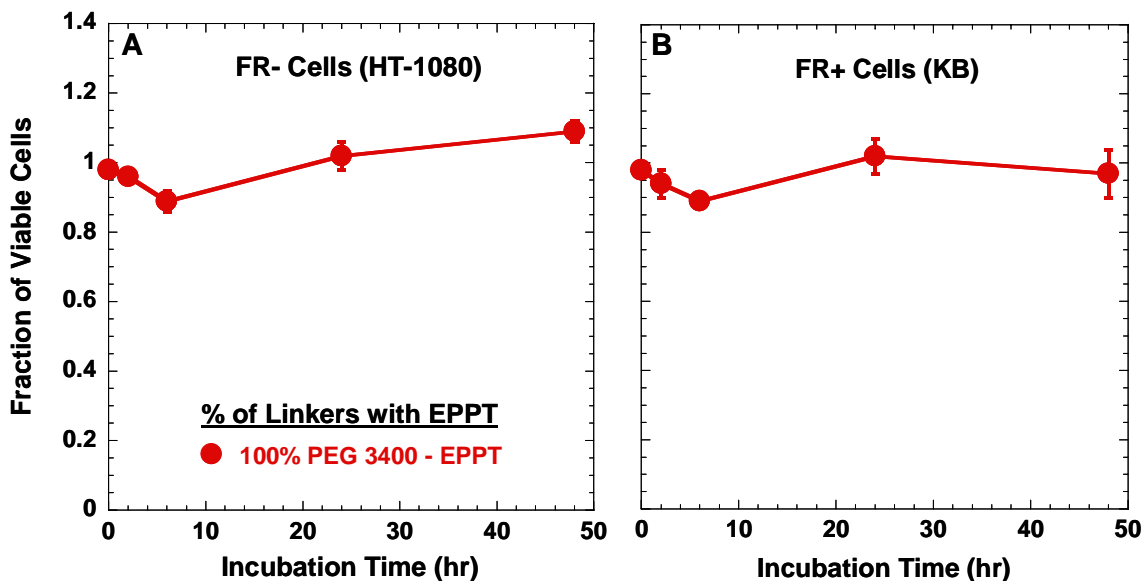


Figure 3.12. Cytotoxicity of EPPT-containing polymer: polymer containing EPPT attached by PEG-3400 (#65) at 1 g/L in FR- (HT-1080) and FR+ (KB) cells (n=3).

3.3.3.2. Folate ligand

Varying amounts of the targeting ligand folate has been covalently bound to our polymer by three different methods. Figure 3.13 illustrates the cytotoxicity results for two polymers that contain folate attached directly to the backbone via the isophthalate linker at a concentration of 1 g/L. Polymer with 10% of the linkers having folate attached and no other side chains (#50) was not toxic *in vitro*, but when the remaining 90% of the linkers had hydrocarbon side chains attached (#51), the polymer was cytotoxic to both FR- and FR+ cells over 48 hours. Folate was also attached to the polymer via a PEG-3400 spacer at one end of the polymer chain. The cytotoxicity data for two polymers containing folate attached in this manner are shown in Figure 3.14. Polymer with PEG-3400-folate attached at the end of the polymer chain, either with (#59) or without (#56) side chains, gave no cytotoxic response with the FR- or FR+ cells.

Polymers were also synthesized with folate attached via a PEG-3400 spacer to the linker molecule in the backbone and the cytotoxicity results of these polymers are shown in Figure 3.15. Polymer with 25% of the linkers having PEG-3400-folate attached and no other side chains (#60) was not toxic in either cell line, whereas with the remaining 75% of the linkers having hydrocarbon side chains attached (#61), mild toxicity was observed only in the FR+ cells. Finally, polymer with 100% of the linkers having PEG-3400-folate attached (#64) demonstrated no cytotoxicity. These results indicate that adding hydrocarbon side chains to any of the polymers containing folate increases cytotoxicity at this higher polymer concentration.

The cytotoxicity assay was performed at lower concentrations for the two folate-containing polymers that included hydrocarbon side chains to assess possible dose effects. Polymer with 10% of the linkers having folate attached and the remaining 90% having hydrocarbon side chains attached (#51) and polymer with 25% of the linkers having PEG-3400-folate attached and the remaining 75% having hydrocarbon side chains attached (#61) were both not toxic at 0.1 g/L (Figure 3.16). This concentration was used in planning the uptake experiments described in Chapter 4.

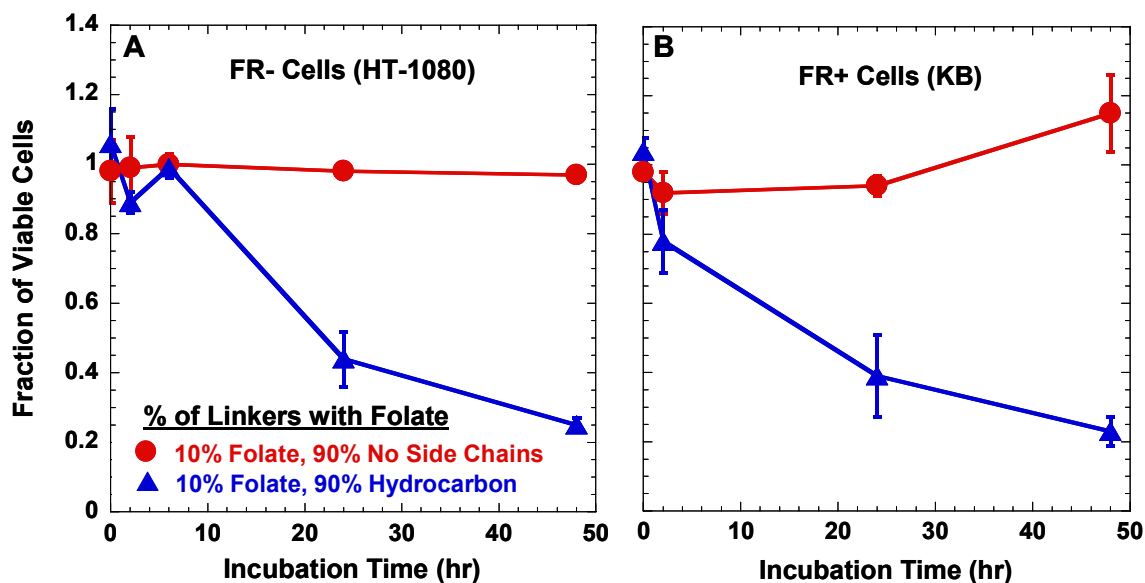


Figure 3.13. Cytotoxicity of folate-containing polymers with folate attached to backbone: polymer with 10% of the linkers having folate attached and no other side chains (#50) and polymer with 10% of the linkers having folate attached and the remaining 90% of the linkers having hydrocarbon side chains attached (#51) at 1 g/L in FR- (HT-1080) and FR+ (KB) cells (n=3).

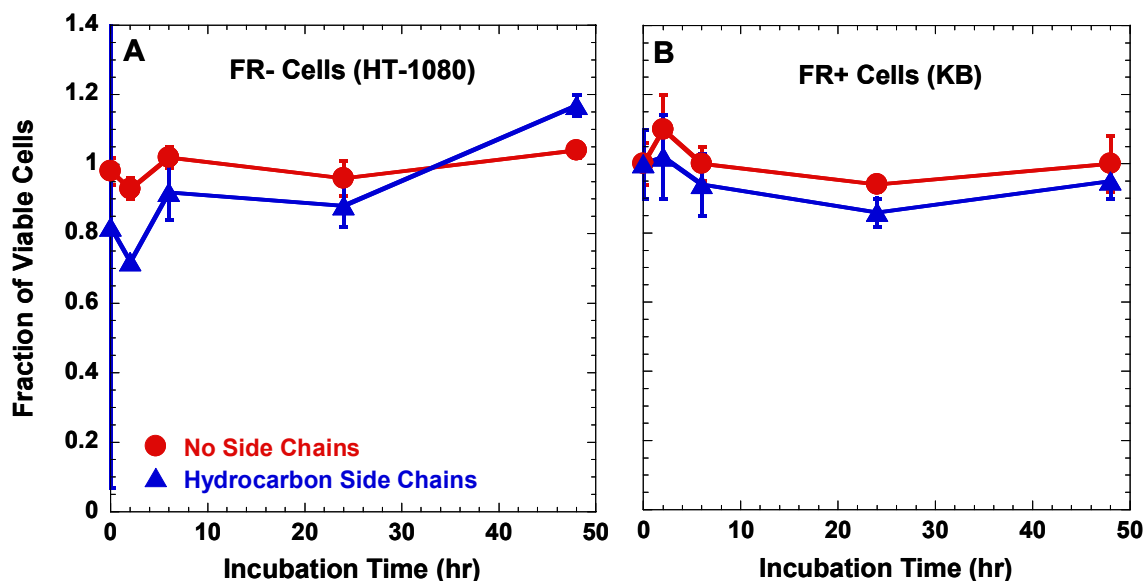


Figure 3.14. Cytotoxicity of folate-containing polymers with folate attached at end of polymer chain: polymer with PEG-3400-folate attached at the end of the polymer chain with hydrocarbon side chains (#59) and polymer with PEG-3400-folate attached at the end of the polymer chain without side chains (#56) at 1 g/L in FR- (HT-1080) and FR+ (KB) cells (n=3).

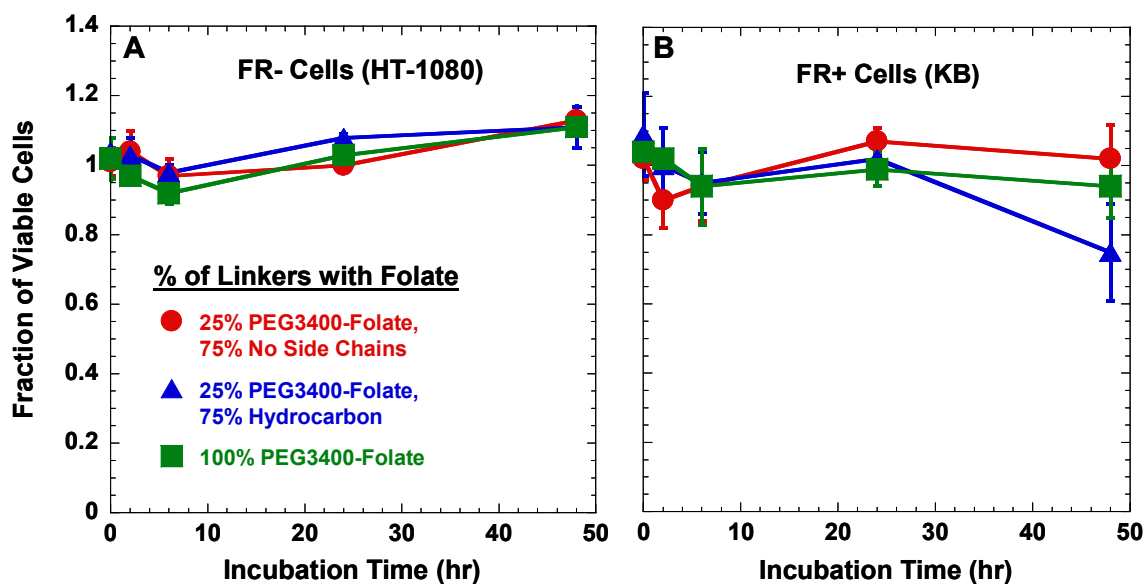


Figure 3.15. Cytotoxicity of folate-containing polymers with folate attached by PEG-3400: polymer with 25% of the linkers having PEG-3400-folate attached and no other side chains (#60) at 1 g/L, polymer with 25% of the linkers having PEG-3400-folate attached and the remaining 75% of the linkers having hydrocarbon side chains attached (#61) at 0.5 g/L, and polymer with 100% of the linkers having PEG-3400-folate attached (#64) at 1 g/L in FR- (HT-1080) and FR+ (KB) cells (n=3).

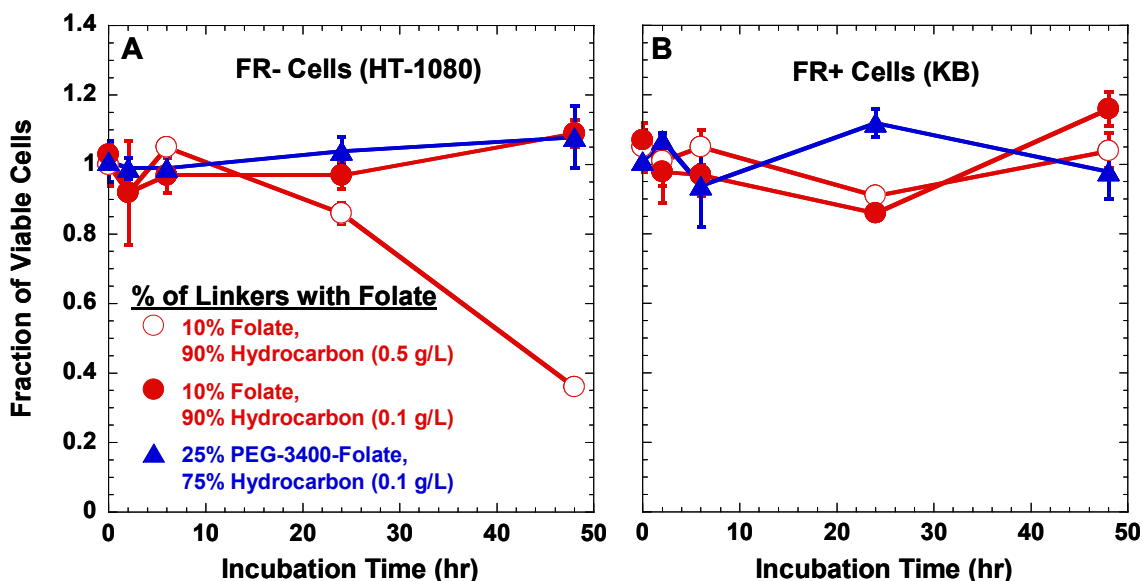


Figure 3.16. Cytotoxicity of folate-containing polymers at lower concentrations: polymer with 10% of the linkers having folate attached and the remaining 90% having hydrocarbon side chains attached (#51) at 0.5 g/L and 0.1 g/L and polymer with 25% of the linkers having PEG-3400-folate attached and the remaining 75% having hydrocarbon side chains attached (#61) at 0.1 g/L in FR- (HT-1080) and FR+ (KB) cells (n=3).

3.3.4. Imaging Polymers

Perfluorocarbon (PFC) was attached to the polymer for the investigation of ^{19}F -MRI applications by Dr. Jin Zhou Dawson, as mentioned in Chapter 2. The cytotoxicity of these polymers was measured *in vitro*. Polymer with 12-carbon PFC side chains attached by ether-ester bonds (#8), polymer with 10-carbon PFC side chains attached by ether-ester bonds (#9), and polymer with 7-carbon PFC side chains attached by amide bonds (#12) all showed no cytotoxicity in INS-1 cells (Figure 3.17). This implies that there is no toxic effect of bond type or number of carbons with PFC side chains. Also, PFC-containing polymer with PEG-600 in the backbone (#9) and PFC-containing polymer with PEG-900 in the backbone (#10) were both not toxic to INS-1 cells (Figure

3.18). The effect on cytotoxicity of PEG length in the backbone of PFC-containing polymers was also considered. The PFC-containing polymer with PEG-1500 in the backbone (#41) showed no toxic response. However, PFC-containing polymer with PEG-600 in the backbone (#43) demonstrated toxicity in uMUC1+ cells, but not in uMUC1- cells (Figure 3.19). These results imply a correlation between decreased PEG length in the backbone and increased cytotoxicity, as also observed with hydrocarbon side chains.

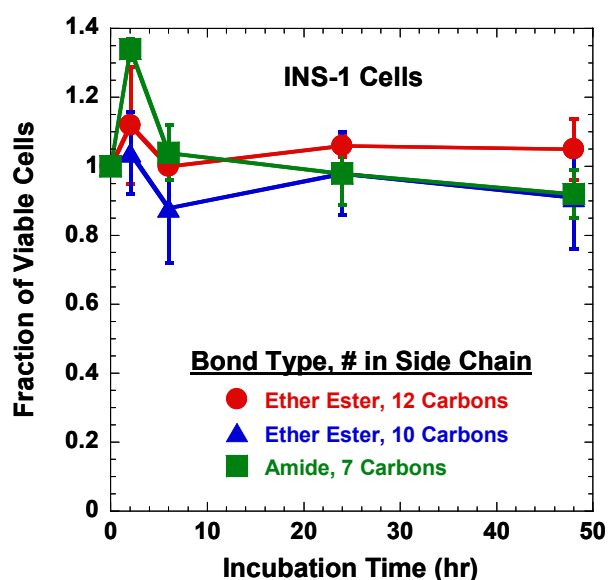


Figure 3.17. Effect of bond type and number of carbons in side chain on cytotoxicity of PFC-containing polymers: polymer with 12-carbon PFC side chains attached by ether-ester bonds (#8), polymer with 10-carbon PFC side chains attached by ether-ester bonds (#9), and polymer with 7-carbon PFC side chains attached by amide bonds (#12) at 1 g/L in INS-1 cells (n=3).

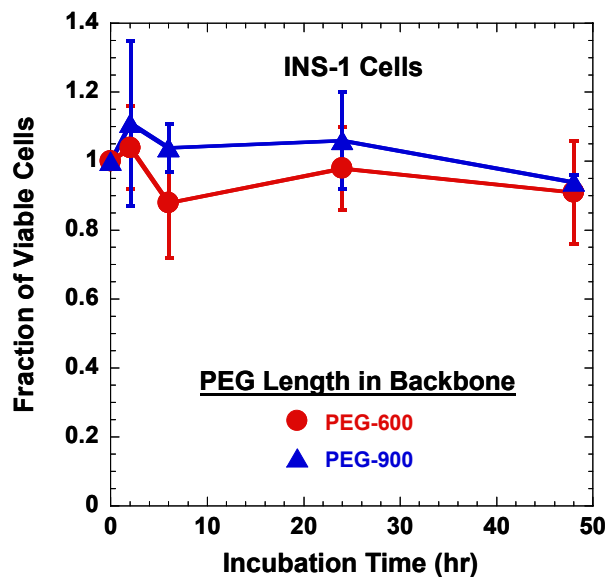


Figure 3.18. Effect of PEG length in backbone on cytotoxicity of PFC-containing polymer: PFC-containing polymer with PEG-600 in the backbone (#9) and PFC-containing polymer with PEG-900 in the backbone (#10) at 1 g/L in INS-1 cells (n=3).

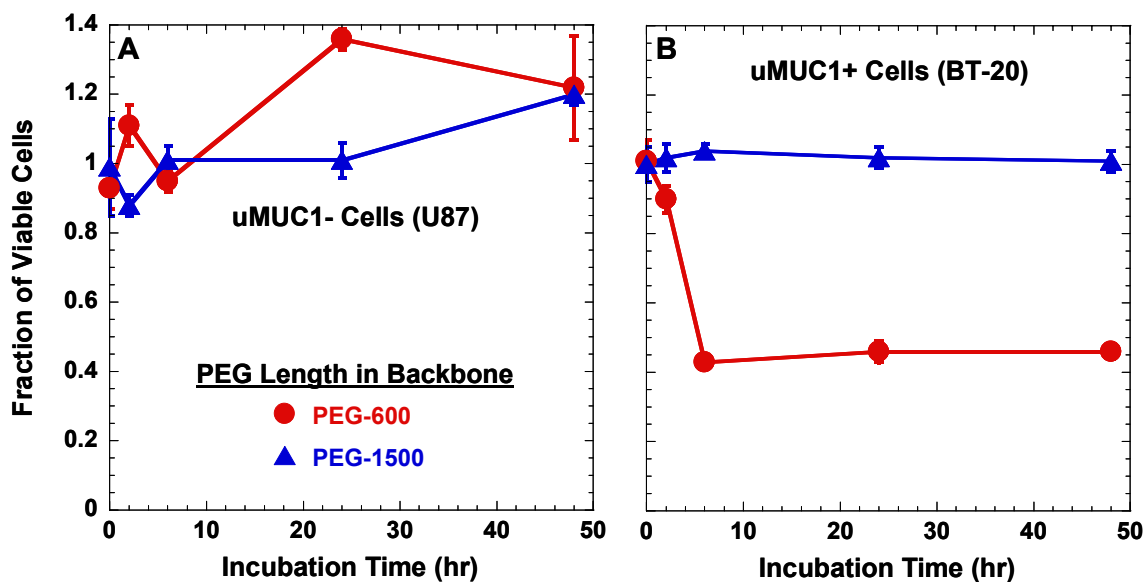


Figure 3.19. Effect of PEG length in backbone on cytotoxicity of PFC-containing polymers: PFC-containing polymer with PEG-1500 in the backbone (#41) and PFC-containing polymer with PEG-600 in the backbone (#43) at 1 g/L in uMUC1- (U87) and uMUC1+ (BT-20) cells (n=3).

Rhodamine B was the first fluorescent dye that was attached to the linker molecules in the polymer. As seen in Figure 3.20, polymer with 10% Rhodamine B attached and 90% hydrocarbon side chains (#4) was cytotoxic. This cytotoxic effect was due to the presence of Rhodamine B, as evidenced by the toxic effect of free Rhodamine B. Our collaborators at UML replaced Rhodamine B with FITC as the fluorescent dye in the polymer synthesis. Figure 3.21 shows the cytotoxicity data of free FITC, polymer with 5% FITC and 95% no side chains (#40), and polymer with 5% FITC and 95% hydrocarbon side chains (#28). No cytotoxicity was observed with free FITC or polymer with 5% FITC and no other side chains. Some cytotoxicity was seen for polymer with 5% FITC and 95% hydrocarbon side chains at the 48 hour time point. Since the hydrocarbon side chains were attached by ether bonds, this results was not surprising. The cytotoxicity of these hydrocarbon bonds was observed without FITC present, as discussed previously. Figure 3.22 shows the cytotoxicity results for polymer containing 5% Cy 5.5 and 95% hydrocarbon side chains (#17). Cytotoxicity was observed, however this is probably the effect of TEA since this polymer was synthesized before TEA was removed from that procedure.

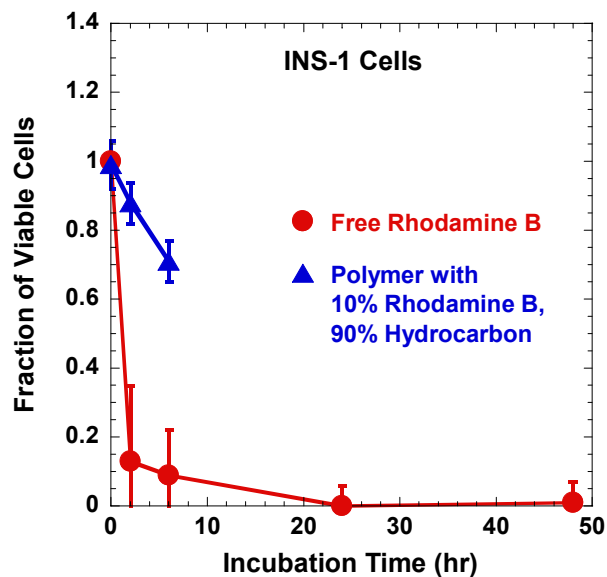


Figure 3.20. Cytotoxicity of Rhodamine B: free Rhodamine B and polymer with 10% Rhodamine B attached and 90% hydrocarbon side chains (#4) at 1 g/L in INS-1 cells (n=3).

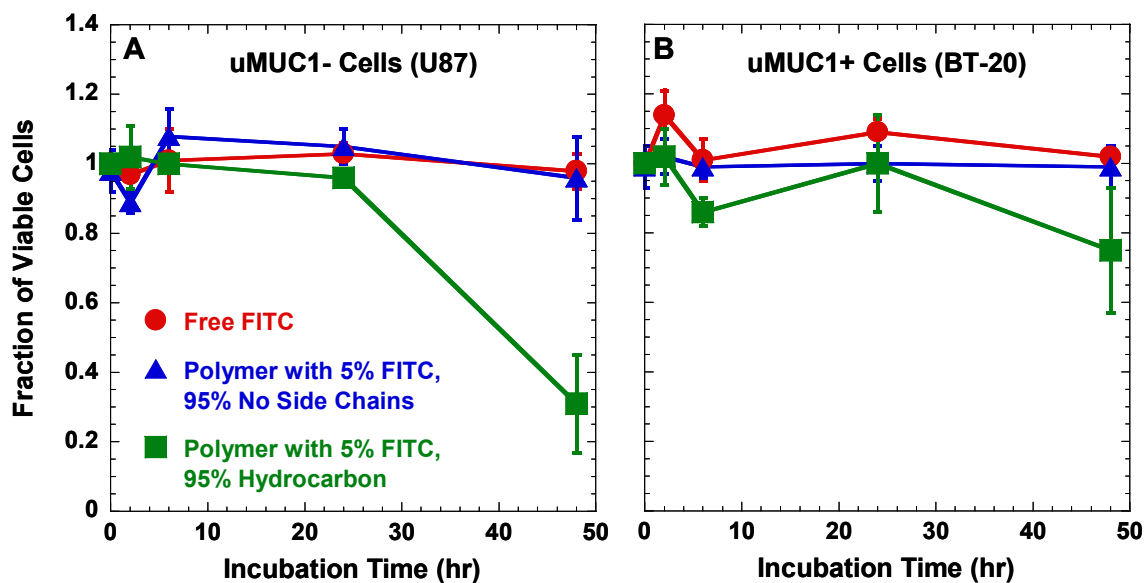


Figure 3.21. Cytotoxicity of FITC: free FITC, polymer with 5% FITC and 95% no side chains (#40), and polymer with 5% FITC and 95% hydrocarbon side chains (#28) at 1 g/L in uMUC1- (U87) and uMUC1+ (BT-20) cells (n=3).

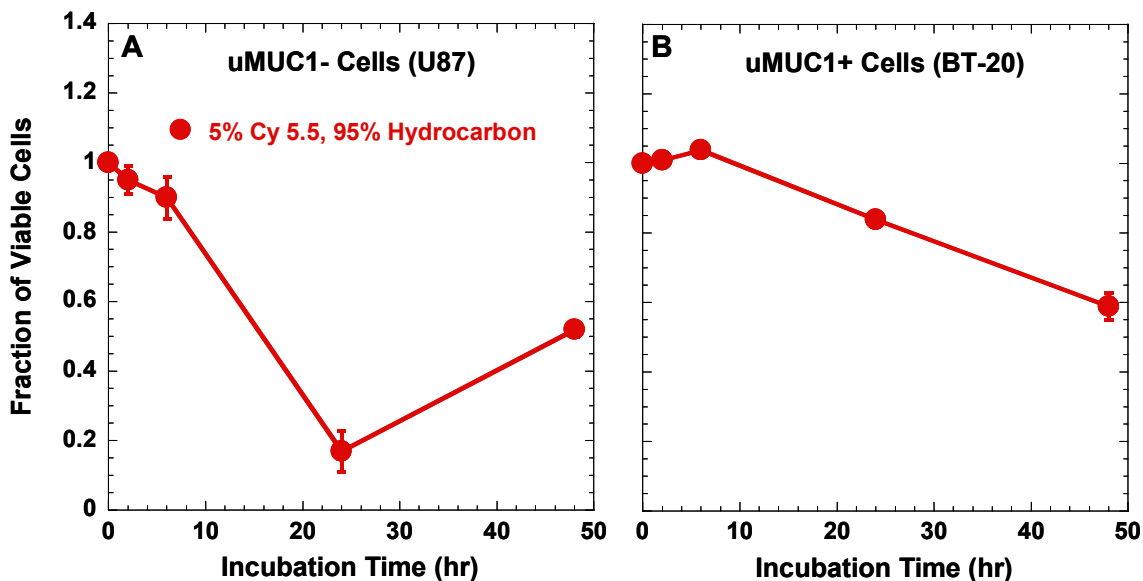


Figure 3.22. Cytotoxicity of Cy 5.5: polymer containing 5% Cy 5.5 and 95% hydrocarbon side chains (#17) at 1 g/L in uMUC1- (U87) and uMUC1+ (BT-20) cells (n=3).

3.3.5. Complex Polymers

Several complex polymers were synthesized containing FITC, PFC, and EPPT in various combinations and amounts. Figure 3.23 shows the cytotoxicity results of these complex polymers. Polymer with 5% FITC and 95% PFC (#13) showed no cytotoxicity. Polymer with 5% EPPT, 5% FITC, and 90% PFC (#29) was slightly cytotoxic *in vitro* at the 48 hour time point. Polymer with 5% EPPT and 95% PFC (#36) and polymer with 5% EPPT, 5% FITC, and 90% no side chains (#39) were both cytotoxic. It was hypothesized that the harsher conditions of multiple processing steps may have left impurities which caused cytotoxicity of these complex polymers.

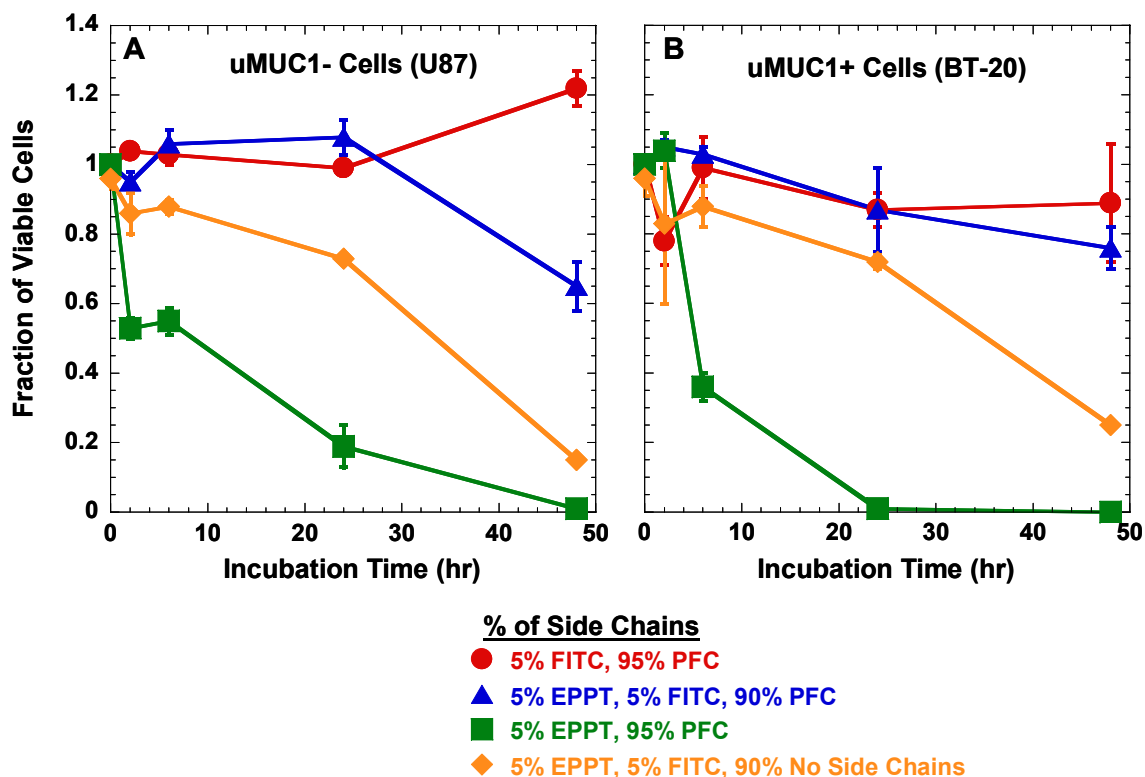


Figure 3.23. Cytotoxicity of complex polymers: polymer with 5% FITC and 95% PFC (#13), polymer with 5% EPPT, 5% FITC, and 90% PFC (#29), polymer with 5% EPPT and 95% PFC (#36) and polymer with 5% EPPT, 5% FITC, and 90% no side chains (#39) at 1 g/L in uMUC1- (U87) and uMUC1+ (BT-20) cells (n=3).

3.3.6. Polymers as Drug Delivery Vehicles

Initial drug delivery experiments used untargeted polymers with encapsulated doxorubicin (DOX). All *in vitro* drug delivery experiments were performed using material encapsulated by our collaborators in Professor Arthur Watterson's lab at UML, as described in Appendix I. *In vitro* cell death was measured in order to assess the drug delivery capability of these polymers. Figure 3.24 shows the drug delivery data for polymer containing hydrocarbon side chains with (#14) and without (#26) encapsulated DOX. The polymer without encapsulated DOX showed no toxicity, however the polymer

with encapsulated DOX showed significant cell death within 24 hours, regardless of polymer concentration. The drug delivery data for polymer containing PFC side chains with (#15) and without (#43) encapsulated DOX is shown in Figure 3.25. Again, the polymer without encapsulated DOX showed no toxicity. However, the polymer with encapsulated DOX also did not show toxicity. One possibility is that the PFC side chains are more hydrophobic than hydrocarbon side chains, creating a more stable cargo-loaded vesicle that does not easily release drug. Another explanation is that the encapsulation procedure itself was not successful; the possibility of which is described below.

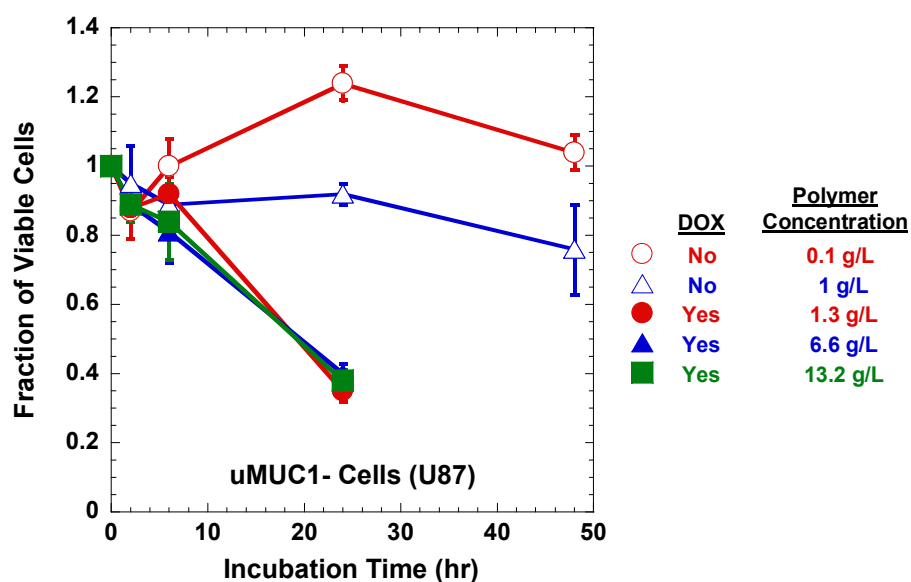


Figure 3.24. Untargeted drug delivery of DOX in polymer containing hydrocarbon side chains: polymer containing hydrocarbon side chains with (#14) and without (#26) encapsulated DOX in uMUC1- (U87) cells (n=3).

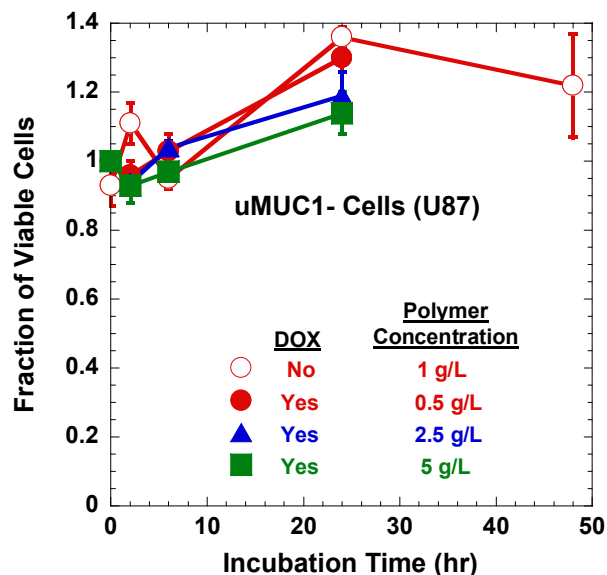


Figure 3.25. Untargeted drug delivery of DOX in polymer containing PFC side chains: polymer containing PFC side chains with (#15) and without (#43) encapsulated DOX in uMUC1- (U87) cells (n=3).

Once the synthetic approach for attaching targeting ligand was developed by our collaborators, cytotoxicity experiments were performed to compare cell death in uMUC1- and uMUC1+ cells by DOX encapsulated in polymer with and without targeting peptide. All experiments used concentrations of 1 g/L polymer and/or 0.02 g/L DOX. Drug delivery experiments using DOX encapsulated in polymer with ester-linked hydrocarbon side chains with (#38) and without (#35) EPPT peptide were inconclusive due to reproducibility issues (Figure 3.26). Two batches of each polymer encapsulating DOX were made. Each batch was tested at two days in solution and two weeks in solution. Batch 1 of each polymer showed no toxicity in either cell line after two days in solution. However, after two weeks in solution, batch 1 of both polymers demonstrated toxicity in uMUC1+ cells. Batch 2 of each polymer shows no toxicity in either cell line after two days or two weeks in solution, thus exhibiting a lack of reproducibility. In addition, the

uMUC1- cell line showed resistance to free DOX, which was later verified in the literature [29].

Figure 3.27 compares the positive case of cell death due to encapsulated DOX in polymer with (#38) and without peptide (#35) from Figure 3.26 with free DOX, the same polymers not encapsulating DOX (#37 and #27), and the same polymers in solution with free DOX. There was no cell death due to polymer with or without peptide when no DOX was encapsulated. In addition, solutions of polymer and free DOX mimic the cell death effect of free DOX without polymer. However, loss of viability due to DOX increases with encapsulation and increases slightly more with addition of targeting ligand. This indicates that the cell death observed in Figure 3.26 can not be explained as DOX having been released from the polymer micelles over the two weeks in solution. Encouragingly, the greatest loss of viability occurs in uMUC-1+ cells exposed to polymer with peptide encapsulating DOX.

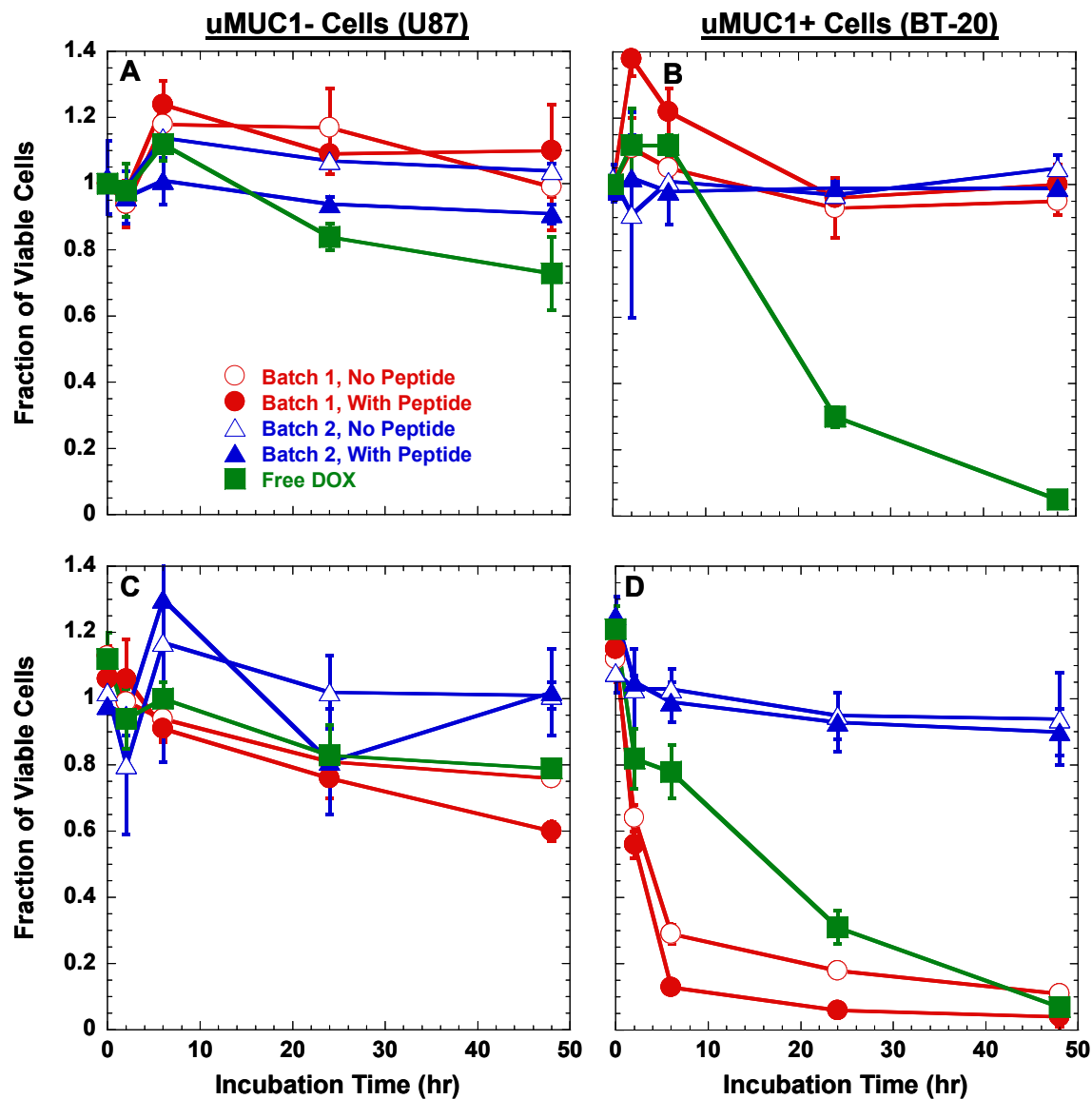


Figure 3.26 Cell death due to encapsulated DOX: polymer with ester-linked hydrocarbon side chains with (#38) and without (#35) EPPT peptide at a polymer concentration of 1 g/L and DOX concentration of 0.02 g/L in uMUC1- (U87) and uMUC1+ (BT-20) cells (n=3). A and B are for polymer in solution for two days, while C and D are for polymer in solution for two weeks.

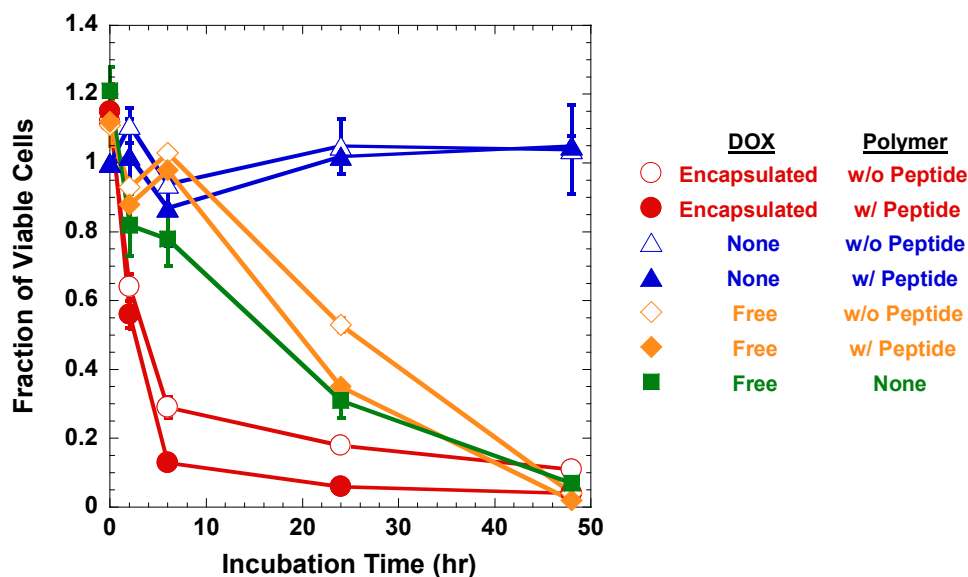


Figure 3.27. Comparison of cell death due to various forms of polymer and DOX: polymer with ester-linked hydrocarbon side chains with (#38) and without (#35) EPPT peptide at a polymer concentration of 1 g/L and DOX concentration of 0.02 g/L in uMUC1+ (BT-20) cells (n=3).

Due to the lack of reproducibility in the drug delivery of encapsulated DOX, the encapsulation method used by our collaborators at UML was questioned. Experiments were initiated to investigate the kinetics of encapsulation and release of DOX from micelles of polymer with ester-linked hydrocarbon side chains (#27). All *in vitro* drug delivery data discussed above was performed using material encapsulated by our collaborators in Professor Arthur Watterson's lab at UML, as described in Appendix I. For these kinetic experiments, the same method of encapsulation was used, but the DOX content of the dialysate was measured by fluorescence plate reader. In the first experiment, the dialysate was changed every 24-72 hours and the DOX content of the dialysate was measured each time it was changed. The results of this experiment are shown in Figure 3.28 as total percent of DOX removed by dialysis as a function of time. Throughout the 266 hour time course of this experiment, the percent of DOX removed in

the dialysate continued to increase. Since no plateau was reached, it appears that equilibrium was not attained. This indicates that the previous encapsulations likely resulted in different amounts of encapsulated DOX, as the dialysis was terminated at various times, making the results difficult to compare between polymer batches. A second experiment was performed at three different temperatures. The dialysate at each temperature was not changed at all during the experiment. Figure 3.29 shows the results for this experiment, again as total percent of DOX removed by dialysis as a function of time. The amount of DOX removed increased with increasing temperature, possibly because the higher temperature increases the solubility of DOX in water. A plateau is reached at both 25°C and 37°C within 60 hours. However, this merely indicates that the solubility limit for DOX in water was reached, since the dialysate was not changed. There is no evidence that DOX is actually encapsulated and that no free DOX remains in the polymer solution.

DOX, in the form of its hydrochloride salt, is hydrophilic, leading to the water-based encapsulation method used here. It was hypothesized that the lack of reproducibility in the encapsulation was due to this hydrophilic encapsulation method. This DOX encapsulation method used by UML was examined in our lab and found to be faulty. Therefore, the project shifted to using the chemotherapeutic drug paclitaxel (PAC), a highly hydrophobic drug, such that a well-established hydrophobic encapsulation method, described in Appendix I, could be used.

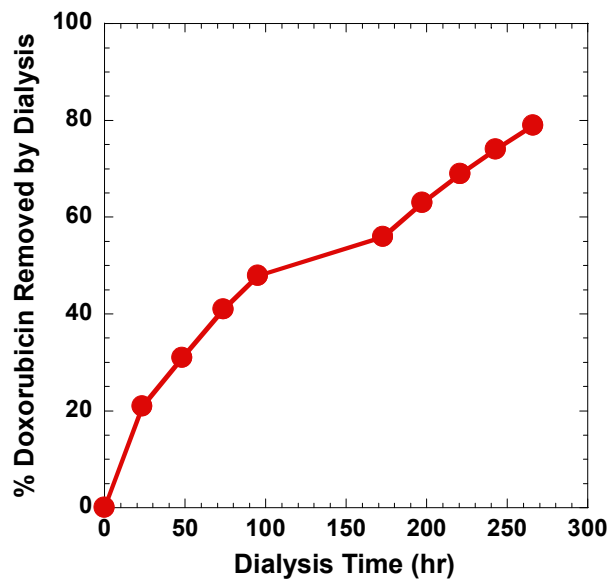


Figure 3.28. Encapsulation of DOX by dialysis, changing dialysate throughout, starting with 5 mg DOX and 200 mg polymer in 20 mL water.

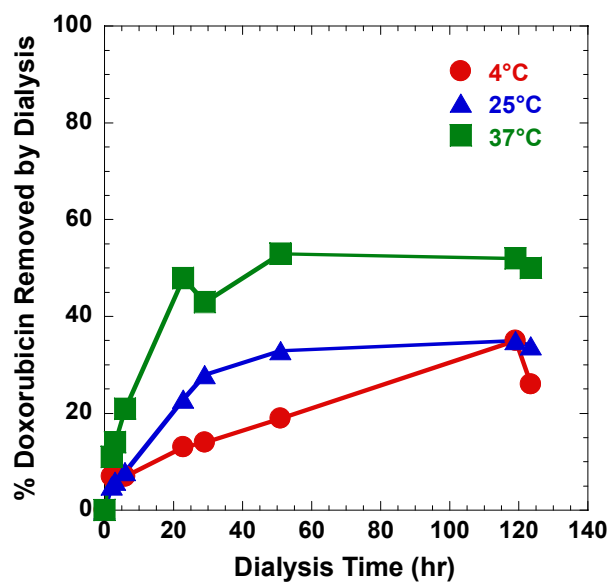


Figure 3.29. Encapsulation of DOX by dialysis, without changing dialysate, starting with 5 mg DOX and 200 mg polymer in 20 mL water.

Drug delivery experiments were performed with encapsulated PAC in polymer with ester-linked hydrocarbon side chains. Figure 3.30 shows the cytotoxicity results for

encapsulated PAC in polymer with ester-linked hydrocarbon side chains without peptide (#49), polymer with ester-linked hydrocarbon side chains without peptide not encapsulating PAC (#27), and free PAC. The polymer concentration was 1 g/L. When PAC was encapsulated in polymer it resulted in a concentration of 0.02 g/L, however, the concentration of free PAC was 0.0003 g/L, the maximum allowed by the solubility limit of PAC in water. Merely by encapsulating the drug in polymer, the solubility, and thereby the deliverable dose, was increased. Again, the polymer not encapsulating drug is not toxic. Encapsulating PAC in polymer increased cell death versus free PAC, however, this is likely due to the increased deliverable dose.

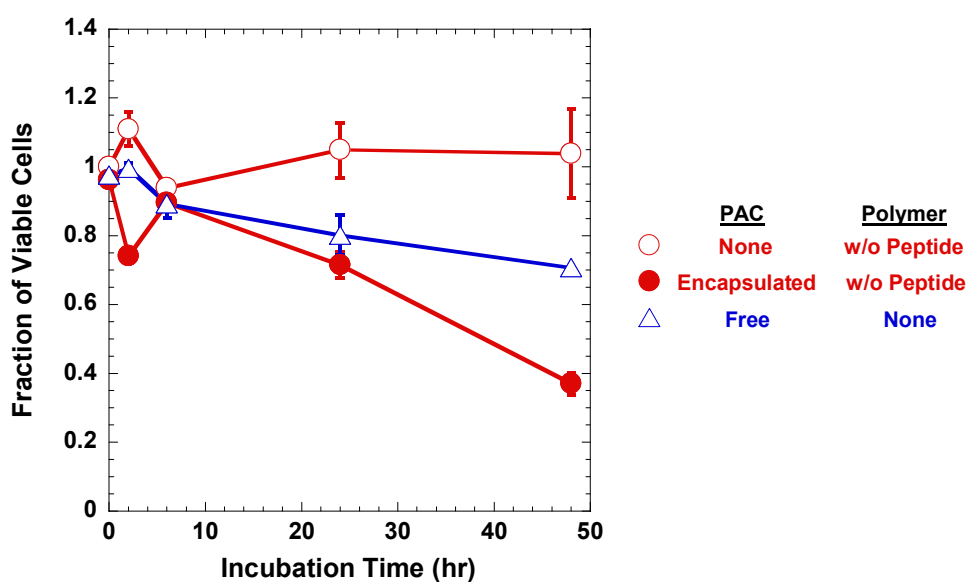


Figure 3.30. Cell death due to encapsulated PAC: encapsulated PAC in polymer with ester-linked hydrocarbon side chains without peptide (#49), polymer with ester-linked hydrocarbon side chains without peptide (#27), and free PAC at a polymer concentration of 1 g/L, encapsulated PAC concentration of 0.02 g/L, and free PAC concentration of 0.0003 g/L in uMUC1+ (BT-20) cells (n=3).

3.4. Discussion

Overall the polymers used in this study were largely non-toxic when studied *in vitro*. This characteristic enhances the appeal of using these polymers as drug delivery vehicles. Given the mild toxicity of the isophthalate linkers, there could be concern if the polymers break down *in vivo*. However, the lack of toxicity of the backbone polymers indicates that this will not be a problem. Trace amounts of one reagent, TEA, caused toxicity, but changing the reagent resolved the toxicity problem. PEG-600 in the backbone caused slight toxicity, but polymers with PEG-900 or PEG-1500 were not toxic. Polymers with hydrocarbon side chains attached by ether linkage were toxic and polymers with hydrocarbon side chains attached by amide linker were slightly toxic, but polymers with ester, ester and amide, and ether-ester linkages were not. In polymers with ester-linked hydrocarbon side chains, the length of the side chains did not affect toxicity. In polymers with ether-linked and ether-ester-linked hydrocarbon side chains, toxicity increased with decreasing side chain length.

Polymers with EPPT attached by triethylene glycol increased in toxicity with increasing percent substitution with EPPT. However, polymers with EPPT attached by PEG-3400 were not toxic, even with 100% of the side chains substituted with PEG-3400-EPPT. Polymer containing folate attached directly to the backbone and no side chains was not toxic, but it was toxic with hydrocarbon side chains. Polymers containing folate attached at the end of the polymer chain were not toxic. Polymers with folate attached to the backbone by PEG-3400 were not toxic except for some mild toxicity when the polymer also contained hydrocarbon side chains. All folate-containing polymers were not

toxic at lower concentrations, more indicative of the concentrations used in the uptake experiments discussed in Chapter 4.

Polymers containing PFC were not toxic regardless of bond type attaching the PFC side chains or the length of those side chains. However, as with polymers with hydrocarbon side chains, PEG-600 in the backbone of PFC-containing polymer caused toxicity, but polymers with PEG-900 or PEG-1500 were not toxic. Polymer with Rhodamine B was very toxic, but it was later determined that free Rhodamine B was toxic. Free FITC and polymer with FITC were not cytotoxic, unless the polymer also contained hydrocarbon side chains. Polymer with Cy 5.5 was toxic, but the polymer also contained hydrocarbon side chains. Polymer containing both FITC and PFC was not toxic and polymer containing FITC, PFC and EPPT only showed slight cytotoxicity. However, polymer with EPPT and FITC and polymer with EPPT and PFC were both toxic. It appears that simple imaging polymers only containing the imaging agent on the backbone polymer are not toxic, but further investigation of imaging agents in more complex polymers is necessary.

Drug delivery experiments were performed using polymer encapsulating DOX or PAC. DOX encapsulated in polymer containing hydrocarbon side chains demonstrated cell death. However, when DOX was encapsulated in polymer containing PFC side chains, there was no cell death. It was hypothesized that the higher hydrophobicity of PFC side chains may have led to more stable cargo-loaded vesicles that do not easily release drug or that drug was not actually encapsulated in this case. Cell death due to DOX increased with encapsulation and increased slightly more with the addition of targeting ligand to the encapsulating polymer. However, cell death due to DOX

encapsulated in polymer with and without polymer was not reproducible. This lack of reproducibility was likely due to the poor encapsulation method used by our collaborators at UML, leading to variation in the amount of DOX encapsulated. Finally, encapsulating PAC in polymer increased cell death as compared to free PAC, probably due to the increased deliverable dose allowed by encapsulation in polymer. These results demonstrate that these alternating copolymers have had some success as drug delivery vehicles *in vitro* and should be further tested as delivery platforms *in vitro* and *in vivo*.

3.5. References

1. Torchilin, V.P., Structure and design of polymeric surfactant-based drug delivery systems. *J Controlled Release*, 2001. 73: p. 137-172.
2. Allen, C., D. Maysinger, and A. Eisenberg, Nano-engineering block copolymer aggregates for drug delivery. *Colloids and Surfaces B: Biointerfaces*, 1999. 16: p. 3-27.
3. Kataoka, K., Harada, A., Nagasaki, Y., Block copolymer micelles for drug delivery: Design, characterization and biological significance. *Adv Drug Delivery Rev*, 2001. 47: p. 113-131.
4. Rosler, A., Vandermeulen, G. W. M., Klok, H-A., Advanced drug delivery devices via self-assembly of amphiphilic block copolymers. *Adv Drug Delivery Rev*, 2001. 53: p. 95-108.
5. Yokoyama, M., Lnoue, S., Kataoka, K., Yui, N., Sakurai, Y., Preparation of adriamycin-conjugated poly(ethylene glycol)-poly(aspartic acid) block copolymer: A new type of polymeric anticancer agent. *Macromol Rapid Commun*, 1987. 8: p. 431-435.
6. Yokoyama, M., Fukushima, S., Uehara, R., Okamoto, K., Kataoka, K., Sakurai, Y., Okano, T., Characterization of physical entrapment and chemical conjugation of adriamycin in polymeric micelles and their design for in vivo delivery to a solid tumor. *J Controlled Release*, 1998. 50: p. 79-92.
7. Gadelle, F., Koros, W. J., Schechter, R. S., Solubilization of aromatic solutes in block copolymers. *Macromolecules*, 1995. 28: p. 4883-4892.
8. Savic, R., Luo, L., Eisenberg, A., Maysinger, D., Micellar nanocontainers distribute to defined cytoplasmic organelles. *Science*, 2003. 300: p. 615-618.
9. Mo, Y., Lim, L-Y., Paclitaxel-loaded plga nanoparticles: Potentiation of anticancer activity by surface conjugation with wheat germ agglutinin. *J Controlled Release*, 2005. 108: p. 244-262.
10. Liang, H.-F., Yang, T-F., Huang, C-T., Chen, M-C., Sung, H-W., Preparation of nanoparticles composed of poly(glutamic acid)-poly(lactide) block copolymers

- and evaluation of their uptake by hepg2 cells. *J Controlled Release*, 2005. 105: p. 213-225.
11. Farokhzad, O.C., Cheng, J., Teply, B. A., Sherifi, I., Jon, S., Kantoff, P. W., Richie, J. P., Langer, R., Targeted nanoparticle-aptamer bioconjugates for cancer chemotherapy in vivo. *PNAS*, 2006. 103(16): p. 6315-6320.
 12. Ellington, A.D., Szostak, J. W., In vitro selection of rna molecules that bind specific ligands. *Nature*, 1990. 346(6287): p. 818-822.
 13. Liu, J., Zhang, Q., Remsen, E., Wooley, K., Nanostructured materials designed for cell binding and transduction. *Biomacromolecules*, 2001. 2: p. 362-368.
 14. Bronich, T.K., Keifer, P. A., Shlyakhtenko, L. S., Kabanov, A. V., Polymer micelle with cross-linked ionic core. *JACS*, 2005. 127: p. 8236-8237.
 15. Murthy, K.S., Ma, Q., Clark, Jr., C. G., Remsen, E. E., Wooley, K., L., Fundamental design aspects of amphiphilic shell-crosslinked nanoparticles for controlled release applications. *Chem Commun*, 2001: p. 773-774.
 16. Kakizawa, Y., Harada, A., Kataoka, K., Glutathione-sensitive stabilization of block copolymer micelles composed of antisense DNA and thiolated poly(ethylene glycol)-*block*-poly(l-lysine): A potential carrier for systemic delivery of antisense DNA. *Biomacromolecules*, 2001. 2: p. 491-497.
 17. Van Domeselaar, G.H., G.S. Kwon, L.C. Andrew, and D.S. Wishart, Application of solid phase peptide synthesis to engineering peo-peptide block copolymers for drug delivery. *Colloids and Surfaces B: Biointerfaces*, 2003. 30: p. 323-334.
 18. Trubetskoy, V.S., Polymeric micelles as carriers of diagnostic agents. *Advanced Drug Delivery Reviews*, 1999. 37: p. 81-88.
 19. Torchilin, V.P., Peg-based micelles as carriers of contrast agents for different imaging modalities. *Advanced Drug Delivery Reviews*, 2002. 54: p. 235-252.
 20. Lavasanifar, A., J. Samuel, and G.S. Kwon, Poly(ethylene oxide)-*block*-poly(l-amino acid) micelles for drug delivery. *Advanced Drug Delivery Reviews*, 2002. 54: p. 169-190.
 21. Matsumura, Y., Polymeric micellar delivery systems in oncology. *Jpn J Clin Oncol*, 2008. 38(12): p. 793-802.
 22. Sezaki, H. and M. Hashida, Macromolecule-drug conjugates in targeted cancer chemotherapy. *CRC Crit. Rev. Ther. Drug Carrier Syst.*, 1984. 1: p. 1-38.
 23. Choksakulnimitr, S., S. Masuda, H. Tokuda, Y. Takakura, and M. Hashida, In vitro cytotoxicity of macromolecules in different cell culture systems. *Journal of Controlled Release*, 1995. 34: p. 233-241.
-

24. Fischer, D., Y. Li, B. Ahlemeyer, J. Kriegelsteinc, and T. Kissel, In vitro cytotoxicity testing of polycations: Influence of polymer structure on cell viability and hemolysis. *Biomaterials*, 2003. 24: p. 1121–1131.
25. Lee, E., Na, K, Bae, YH, Polymeric micelle for tumor ph and folate-mediated targeting. *J Control Release*, 2003. 91(1-2): p. 103-13.
26. Mosmann, T., Rapid colorimetric assay for cellular growth and survival: Application to proliferation and cytotoxicity assays. *Journal of Immunological Methods*, 1983. 65(1-2): p. 55-63.
27. Cory, A.H., T.C. Owen, J.A. Bartlop, and J.G. Cory, Use of an aqueous soluble tetrazolium/formazan assay for cell growth assays. *Cancer Commun*, 1991. 3: p. 207–212.
28. Riss, T.L. and R.A. Moravec, Comparison of mtt, xtt, and a novel tetrazolium compound mts for in vitro proliferation and chemosensitivity assays. *Mol. Biol. Cell*, 1992. 3: p. 184a.
29. Le Jeune, N., N. Perek, D. Denoyer, and F. Dubois, Study of monogluthionyl conjugates tc-99m-sestamibi and tc-99m-tetrofosmin transport mediated by the multidrug resistance–associated protein isoform 1 in glioma cells. *Cancer Biotherapy & Radiopharmaceuticals*, 2005. 20(3): p. 249-259.

Chapter 4. Evaluation of Cellular Uptake of Alternating Copolymers *In Vitro*

4.1. Introduction

During the past quarter century there has been a steady increase in the number of nanoparticles being developed for use as therapeutics, many as anti-cancer therapeutics [1-5]. Liposomes, dendrimers, and polymer micelles are all being exploited as platforms for nanoparticle drug delivery. Several drug delivery platforms have been approved for clinical use [6] and others are showing significant potential in clinical trials [7, 8]. Specifically, polymeric micelle-based drug carriers have been developed by many groups and are currently under investigation for drug and imaging agent delivery [9-13].

Some investigations focus on using polymeric micelles to incorporate various drugs into the inner core by chemical conjugation or physical entrapment, using the nanoparticles as carriers, or chaperones, for the drug [14-32]. This scheme can increase the dose of the drug, by increasing the solubility of very hydrophobic drugs. Alternatively, the nanoparticles can protect the drug from destruction under *in vivo* conditions.

Nanoparticles may be preferentially concentrated at tumor sites through strategic targeting. For instance, the phenomenon described as the “enhanced permeability and retention (EPR) effect” [33-35], in which nanoparticles accumulate in solid tumors in increased amounts as compared to normal tissue has been well documented [36-43] and is attributed to pathophysiological characteristics of solid tumors that are not observed in

normal tissue. These characteristics include defective tumor blood vessel architecture (often termed “leaky vasculature”), defective lymphatic drainage system, and increased production of permeability mediators [44, 45]. It has been reported that particles >5 nm in diameter get trapped in the tumor tissue [9, 46], but tumors also exhibit a characteristic pore cutoff size of 200 nm or greater [47]. Therefore drug delivery particles in the 5-200 nm size range should passively target tumors due to the EPR effect. It was determined that micelles formed from our alternating copolymers are 8-22 nm in diameter [48], therefore these particles are in the size range for passive targeting *in vivo*.

In addition to passive targeting, nanoparticles can be actively targeted to a tumor cell in order to kill the cancerous cells without damaging normal cells. There are many technologies which are being used to specifically target molecules or particles to tumor cells [49-62]. Often, a monoclonal antibody, a peptide fragment, or a small molecule is used as the targeting agent. Typically these targeting agents form a binding pair with the target found on the tumor cell surface. Selectivity of the nanoparticles for specific cancer cells by targeting allows for reduced incidence of the adverse side effects of the chemotherapeutic drugs, however this comes at the expense of adding complexity to the nanoparticle preparation, potentially increasing particle size, and the risk of adverse biological reactions with the targeting agent. It is desirable for the target biomarker to (1) be over-expressed on the tumor cells, (2) be vital to tumor progression so that expression is not down-regulated during the life of the tumor, and (3) have limited shedding. The targeting ligand should (1) have a high specific affinity for the target antigen, (2) have low immunogenicity *in vivo*, and (3) be efficiently internalized after binding to the

antigen. The targeting pairs chosen for this study, as discussed in Chapter 1, are EPPT/underglycosylated mucin-1 (uMUC1) and folate/folate receptor (FR).

The physical characterization of our alternating copolymers was the focus of the doctoral thesis of Jin Zhou Dawson in the Colton group at MIT [48]. The critical micelle concentration (CMC) was determined by surface tension measurements to be 12 μM (0.07 g/L) for polymer with 100% of the linkers having ester-linked hydrocarbon side chains (#27) and 2 μM (0.016 g/L) for polymer with 100% of the linkers having perfluorocarbon (PFC) side chains (#10). The sizes of the micelles were determined by dynamic light scattering. It was found that micelles formed from the polymer with 100% of the linkers having ester-linked hydrocarbon side chains (#27) have a radius of about 4-5 nm and polymer with 100% of the linkers having PFC side chains (#10) have a radius of about 8-9 nm.

This chapter describes the cellular uptake of our alternating copolymer nanoparticles. First, the cellular uptake of the non-targeted polymers is examined experimentally *in vitro*. Next, the rational design of targeted polymers is discussed, with respect to polyvalency and ligand tether length. Then, the experimental results of the *in vitro* cellular uptake of targeted alternating copolymers in tumor cells are given for both the EPPT/uMUC1 and folate/FR targeting systems. The selectivity of the polymers for the targeted cells was evaluated using target-positive and target-negative cell lines as well as competition studies. In all experiments, cellular association was determined by radioactive labeling of the polymer or free ligand with either ^{125}I or ^3H . The chapter concludes with discussions of these results and suggestions for future uses of these copolymers.

4.2. Methods

4.2.1. Materials and reagents

A detailed description of the synthesis protocol for each polymer can be found in Appendix I. A list of all polymer structures used in this study is given in Appendix II. The numbers referred to throughout the remainder of this text correspond to the polymer structures as identified in the table presented in Appendix II.

All polymers were provided by our collaborators in the Arthur Watterson lab at the University of Massachusetts, Lowell. All reagents were obtained from commercial sources. Phosphate buffered saline (PBS), distilled deionized sterile water, trypsin EDTA (1X, 0.25% trypsin/0.53 mM EDTA in HBSS), penicillin-streptomycin solution, RPMI, D-glucose, L-glutamine, sodium pyruvate, and fetal bovine serum (FBS) were purchased from Mediatech, Inc. Minimum essential media, Eagle, with 2 mM L-glutamine and Earle's BSS adjusted to contain 1.5 g/L sodium bicarbonate, 0.1 mM non-essential amino acids, and 1.0 mM sodium pyruvate (EMEM) was purchased from ATCC. RPMI Medium 1640 (without folic acid) was purchased from GIBCO. Guava Viacount assay kit was purchased from Guava Technologies/Millipore. Paraformaldehyde and Triton X-100 lysis buffer were purchased from EMD Chemicals. Folate was purchased from TCI. ³H-folate was purchased from American Radiolabeled Chemicals, Inc. Iodine-125 was purchased as Na¹²⁵I from Perkin Elmer. Doxorubicin was purchased from EMD Biosciences. Phosphatidylinositol-phospholipase C (PI-PLC) was purchased from Sigma-Aldrich.

4.2.2. Cell lines and culture

BT-20 cells (human breast carcinoma; uMUC1+), LS174T cells (human colon carcinoma; uMUC1+), U87 cells (human brain glioblastoma; uMUC1-), MRC-5 cells (human lung fibroblast; uMUC1-), KB cells (human epidermoid carcinoma; FR+), HT-1080 cells (human fibrosarcoma; FR-) were purchased from the American Type Culture Collection and INS-1 cells (rat insulinoma) were a gift from Chris Newgard at Duke University. BT-20, LS174T, U87, MRC-5, KB, and HT-1080 cells were all cultured in EMEM supplemented with 10% FBS and 1% penicillin–streptomycin solution. INS-1 cells were cultured in RPMI supplemented with 11.1 mM D-glucose, 1% penicillin–streptomycin solution, 2 mM L-glutamine, 1 mM sodium pyruvate, 50 μ M β -mercaptoethanol, and 10% FBS. All cells were grown at 37°C in a humidified atmosphere containing 5% CO₂.

4.2.3. Confocal microscopy

Cells were seeded in six-well plates containing 22 mm-diameter glass cover slips at a density of 1.5×10^5 cell/mL and incubated with polymer nanoparticles. The specific polymers used are described in section 4.3 (Results) and detailed in Appendices I and II. Cells were incubated with 1 g/L polymer or 0.2 g/L free or encapsulated doxorubicin at 37°C. After incubating for 14 hours in the case of INS-1 cells or 5 hours in the case of U87 cells, the cells were washed 3 times with PBS. The cells were then fixed to the slides with 4% paraformaldehyde and examined with a Zeiss LSM 510 Meta high resolution laser scanning confocal microscope equipped with a 100X oil emersion objective lens at

the W.M. Keck Foundation Biological Imaging Facility located at the Whitehead Institute. Image analysis was performed using Zeiss LSM software.

4.2.4. Radioactive uptake assay

In the experiments using folate to target, cells were grown in RPMI Medium 1640 (without folic acid) supplemented with 10% FBS and 1% penicillin–streptomycin solution for 2 days before the experiment. Otherwise cells were grown continually in EMEM supplemented with 10% FBS and 1% penicillin–streptomycin solution. Cells growing as a mono-layer were harvested with trypsin and seeded at a concentration of 1×10^6 cells/mL 1 day before the start of the experiment. Cells were incubated with various amounts of polymer (0.001-1 g/L), EPPT (0.1 g/L) or folate (0.00002-0.002 g/L) labeled with a radioactive atom (^{125}I or ^3H) at 37°C in a humidified 5% CO_2 atmosphere. The specific polymers used are described in the Results section and detailed in Appendices I and II. At each time point, the cells were washed three times with 100 μL PBS. When samples contained ^{125}I , cells were harvested with 100 μL trypsin and the cell suspensions were analyzed in a gamma counter (Packard COBRA II Auto-Gamma). When samples contained ^3H , cells were harvested with 100 μL lysis buffer, 400 μL of deionized water and 3.5 mL of scintillation cocktail (Ultima Gold XR) were added, the samples were vortexed, and the samples were analyzed in a scintillation counter (Beckman Coulter LS6500 Multipurpose Scintillation Counter). The validation of this sample preparation procedure for scintillation counting is shown in Appendix IV. All experiments were performed in triplicate. The activity of each sample, measured as counts per minute (CPM), was compared to the activity measurements of solutions of known concentrations to calculate the amount of polymer taken up.

More specifically, the polymer solution used in each experiment was diluted to various concentrations and the activity, as CPM, was measured for each sample. For scintillation counting, polymer solutions were made with cellular debris present in lysis buffer. A calibration curve was prepared by plotting each activity (CPM) as a function of mass of polymer in grams (g). The slope of the calibration curve has units of g/CPM. This slope is used as a calibration factor to convert the activity for each uptake experiment sample measured in CPM to mass of polymer in g by the equation

$$\text{mass of polymer (g)} = \text{measured sample activity (CPM)} \times \text{calibration factor (g/CPM)} \quad (4.1)$$

For each sample, the mass of polymer (g) is converted to number of polymer chains (no. of polymer chains) using the calculated molecular weight (MW) of the polymer, shown in Appendix II, by the equation

$$\text{No. of polymer chains} = \frac{\text{mass of polymer (g)}}{\text{MW (g/mol)}} \times N_A \quad (4.2)$$

where N_A is Avogadro's number (6.022×10^{23} molecules/mol). The no. of polymer chains is converted to number of polymer chains per cell (no. of polymer chains/cell) by dividing by the number of cells in each well (no. of cells).

$$\text{no. of polymer chains/cell} = \frac{\text{no. of polymer chains}}{\text{no. of cells}} \quad (4.3)$$

Data is reported as no. of polymer chains/cell.

For competitive inhibition studies, cells were incubated with labeled folate or polymer and an excess (100 μM) of unlabeled folate or polymer at 37°C in a humidified CO₂ atmosphere. For saturation of the FR, cells were incubated with unlabeled free folate for 3 hours at 37°C prior to performing the experiment. For acid wash treatment to remove surface bound material and determine the internalized material, at each time point

each well was washed twice with PBS followed by one wash with acidified saline (pH 3) [58, 63]. To determine the surface bound material, endocytosis was inhibited by incubating the cells at 4°C. For treatment of cells with phosphatidylinositol-phospholipase C (PI-PLC) to cleave the GPI-anchored FR, cells were rinsed twice with folate-free media and incubated for 60 min at 37 °C with 1 unit/mL PI-PLC in folate-free media. Each well was then rinsed twice with folate-free media [58]. In each of these variations, the uptake experiments were otherwise performed as described above.

4.2.5. Cell counting

After cells were detached from the plate with trypsin, cell number was evaluated by staining cells using a Guava Viacount assay solution and acquiring data with a Guava Personal Cell Analysis (PCA) flow cytometer using the Guava Viacount software. Dilution factors and original sample volumes were entered as appropriate for each sample. Each sample was run in triplicate and 1000 events were acquired per sample.

4.2.6. Dynamic Light Scattering (DLS)

Polymer solutions in folate-free media were filtered through 0.45 µm cellulose filters. These studies were conducted using a light scattering apparatus from Brookhaven Instruments, which consists of a motor driven goniometer (BI-200SM), a digital autocorrelator (BI-9000AT), and a photon counter (BI-9025AT). The laser light was provided by an Argon ion laser (Spectra-physics 2017-055) operated at a wavelength of 514 nm, a measurement angle of 90°, and a temperature of 25°C. Results are reported as intensity averaged diameters calculated using the CONTIN method.

4.2.7. Statistical analysis

All data were represented as mean \pm standard deviation. Statistical significance ($p < 0.05$) was determined, where appropriate, by a two-tailed Student t-test.

4.3. Results

4.3.1. Cellular uptake of non-targeted polymers

4.3.1.1. Fluorescence imaging of cellular uptake

Confocal microscopy studies were carried out to determine if the polymer and drug are taken up into cells and the location of the polymer and drug upon uptake into cells. Since doxorubicin is a fluorescent molecule, it could be observed by confocal microscopy. Polymer with 5% of the linkers having the fluorescent dye FITC and 95% of the linkers having perfluorocarbon (PFC) side chains (#13), free doxorubicin, and doxorubicin encapsulated in polymer with hydrocarbon side chains (#14) were all studied *in vitro*. Polymer at this concentration (1 g/L) is in the form of micelles. Images of the fluorescently labeled polymer alone demonstrated that the polymer is likely confined to vesicles within the cytoplasm and it is not found in the nucleus (Figure 4.1). Free and encapsulated doxorubicin were largely confined to the nucleus. Since the polymer does not enter the nucleus, it is likely that the doxorubicin is released from the polymer. However, it was reported in Chapter 3 that cell death due to DOX encapsulated in polymer with and without peptide was not reproducible. This lack of reproducibility was likely due to a poor encapsulation method, leading to variation in the amount of DOX

encapsulated. Therefore, the polymers are taken up by cells, but firm conclusions about the delivery of DOX can not be made.

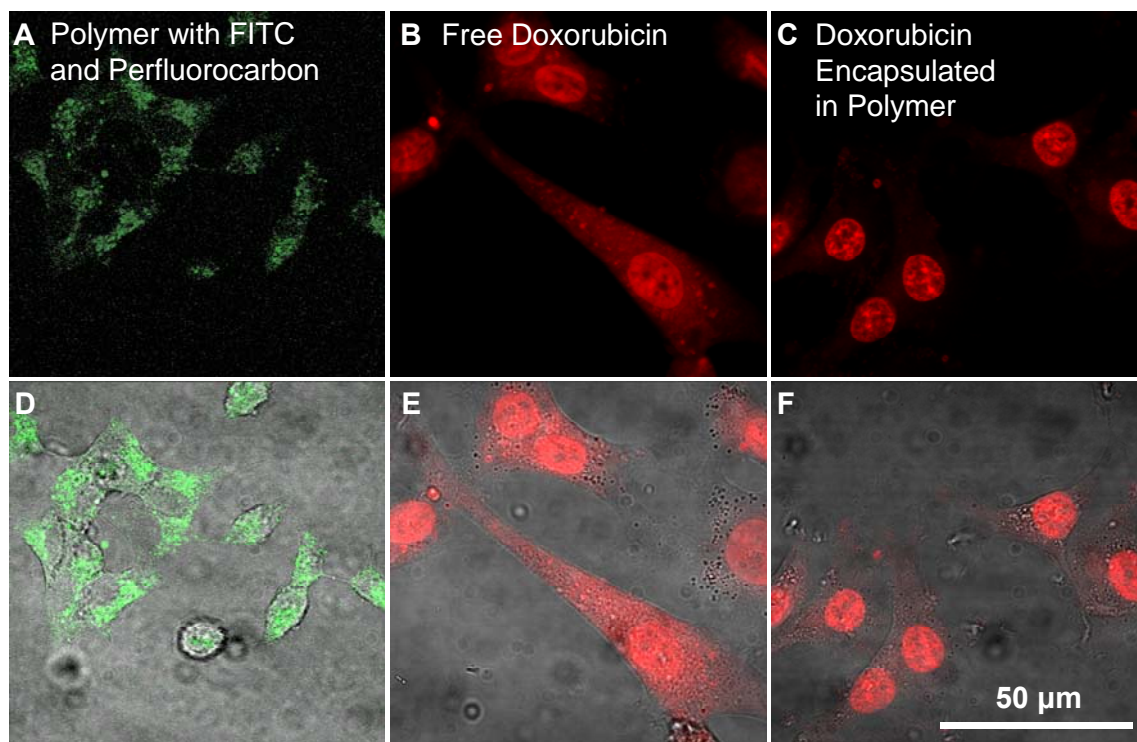


Figure 4.1. Confocal microscopy images of cellular uptake of polymer with FITC and PFC (#13) at 1 g/L in INS-1 cells, free doxorubicin at 0.02 g/L in U87 cells, and doxorubicin encapsulated in polymer (#14) at 1 g/L polymer and 0.02 g/L doxorubicin in U87 cell. Note: Top image is fluorescent image, bottom image is fluorescent image merged with optical image.

4.3.1.2. Cellular uptake by labeling with ^{125}I

Initial *in vitro* experiments focused on the uptake of non-targeted polymers. Each polymer was labeled with ^{125}I . The cellular uptake, presented as number of polymer chains per cell versus time, for polymer with 100% of the linkers having ester-linked hydrocarbon side chains (#27) and polymer with 100% of the linkers having perfluorocarbon (PFC) side chains (#10) is shown in Figure 4.2 for uMUC1+ and

uMUC1- cell lines. Polymer at this concentration (1 g/L) is in the form of micelles. In both uMUC1+ and uMUC1- cells, the uptake is equivalent up to 0.5 hours. After 0.5 hours, the hydrocarbon-containing polymer enters the cells faster, roughly linear with time, but the uptake of the perfluorocarbon-containing polymer levels off. In addition, the results for polymer with 100% of the linkers having ether-ester-linked hydrocarbon side chains (#58) are shown in Figure 4.3 for FR+ and FR- cell lines. Polymer at this concentration (0.1 g/L) is in the form of micelles. The uptake of this polymer in FR+ and FR- cells is much lower than either polymer in uMUC1+ or uMUC1- cells, but the concentration was lower by a factor of 10 in the study in FR+ and FR- cells. With all three polymers, there was significant cellular uptake into all cell lines, on the order of 1×10^7 to 1×10^9 polymer chains taken up per cell. However, the non-targeted uptake rate for each polymer is similar in both positive and negative cells. Since the polymers do enter cells, drug or imaging agent that is covalently bound to or encapsulated in the polymer will also enter cells. It should be noted that across all uptake data discussed in this chapter, the uptake at early time points (0.25 and 0.5 hours) often appear aberrant. An explanation for this irregular data is not clear, although it is possibly due to inconsistent lengths of time at room temperature during the preparation of the experiment.

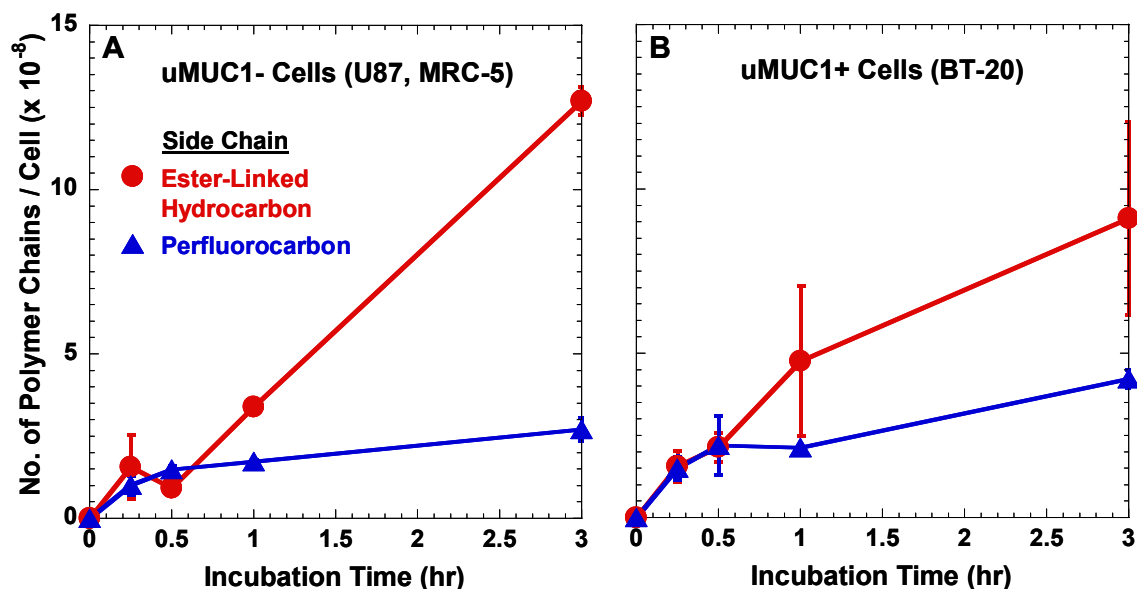


Figure 4.2. Cellular uptake of non-targeted polymer with 100% of the linkers having ester-linked hydrocarbon side chains (#27) at 1 g/L in uMUC1- (U87) and uMUC1+ (BT-20) cells and non-targeted polymer with 100% of the linkers having PFC side chains (#10) at 1 g/L in uMUC1- (MRC-5) and uMUC1+ (BT-20) cells (n=3).

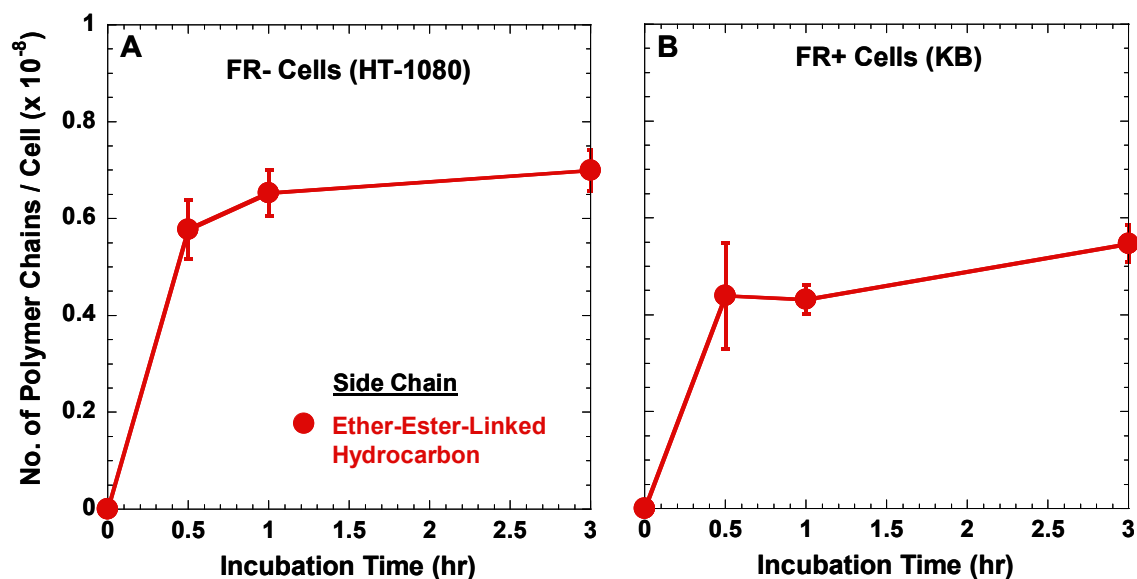


Figure 4.3. Cellular uptake of non-targeted polymer with 100% of the linkers having ether-ester-linked hydrocarbon side chains (#58) at 0.1 g/L in FR- (HT-1080) and FR+ (KB) cells (n=3).

The polymer solution concentration was examined as a factor affecting the uptake of the non-targeted polymers. The cellular uptake of polymer with 100% of the linkers having ester-linked hydrocarbon side chains (#27) at three concentrations is shown in Figure 4.4 as a function of incubation time. The data plotted for 1 g/L polymer is the same as that in Figure 4.2. Data in panels A and B is replotted with an expanded scale in panels C and D, respectively. Polymer is in the form of micelles at concentrations of 1 g/L and 0.1 g/L, but not at 0.01 g/L. The uptake in both cell lines is similar at each concentration. In addition, there is a direct correlation between increased polymer concentration in solution and increased cellular uptake. The same data plotted as a function of polymer concentration is shown in Figure 4.5. Again, data in panels A and B is replotted with an expanded scale in panels C and D, respectively. This figure shows that the uptake at each time point greater than 0.25 hours is nearly linear in polymer concentration, as expected for passive uptake.

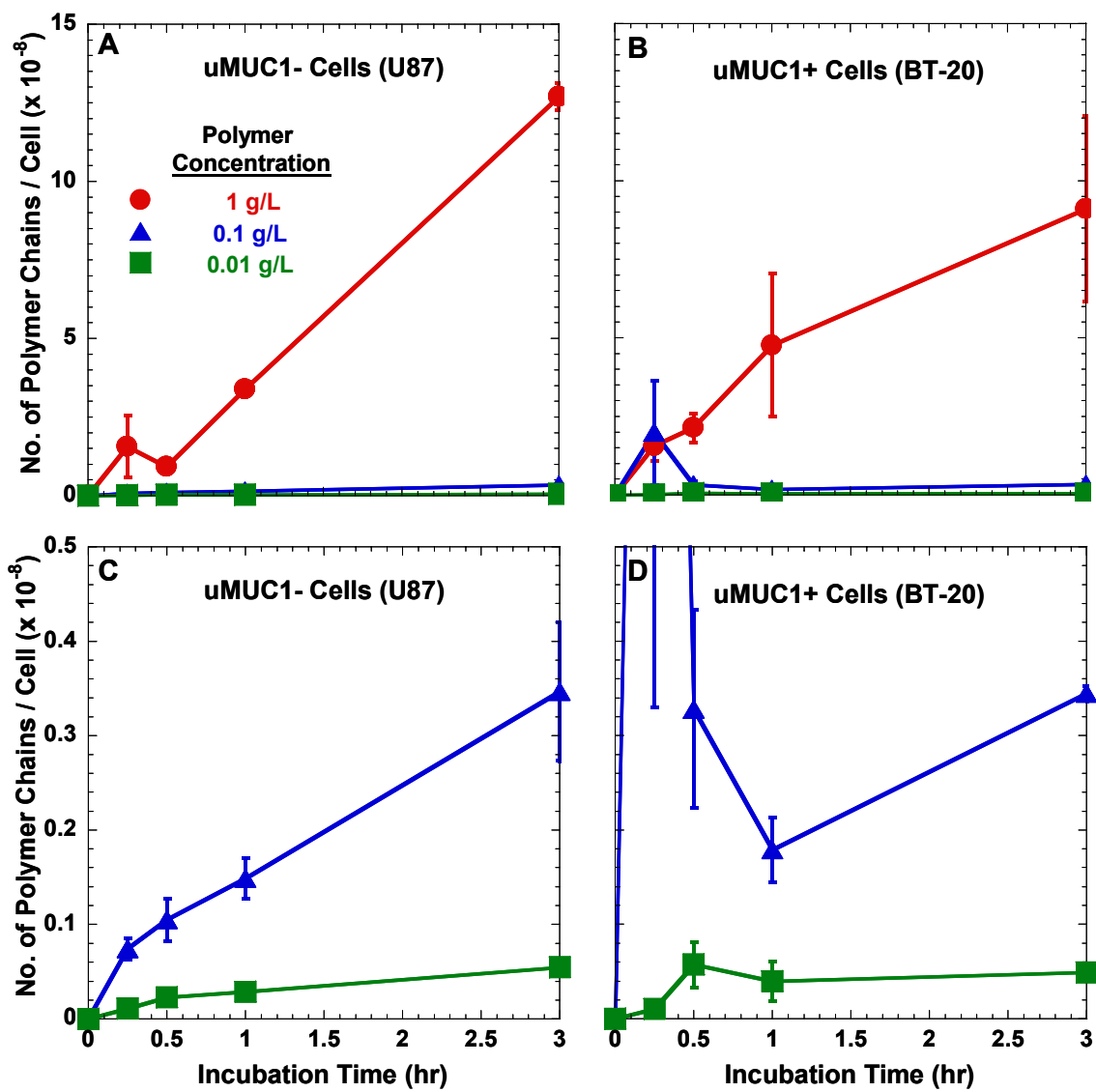


Figure 4.4. Effect of polymer concentration on the cellular uptake of non-targeted polymer with 100% of the linkers having ester-linked hydrocarbon side chains (#27) in uMUC1- (U87) and uMUC1+ (BT-20) cells as a function of time (n=3). C and D are magnified versions of A and B, respectively.

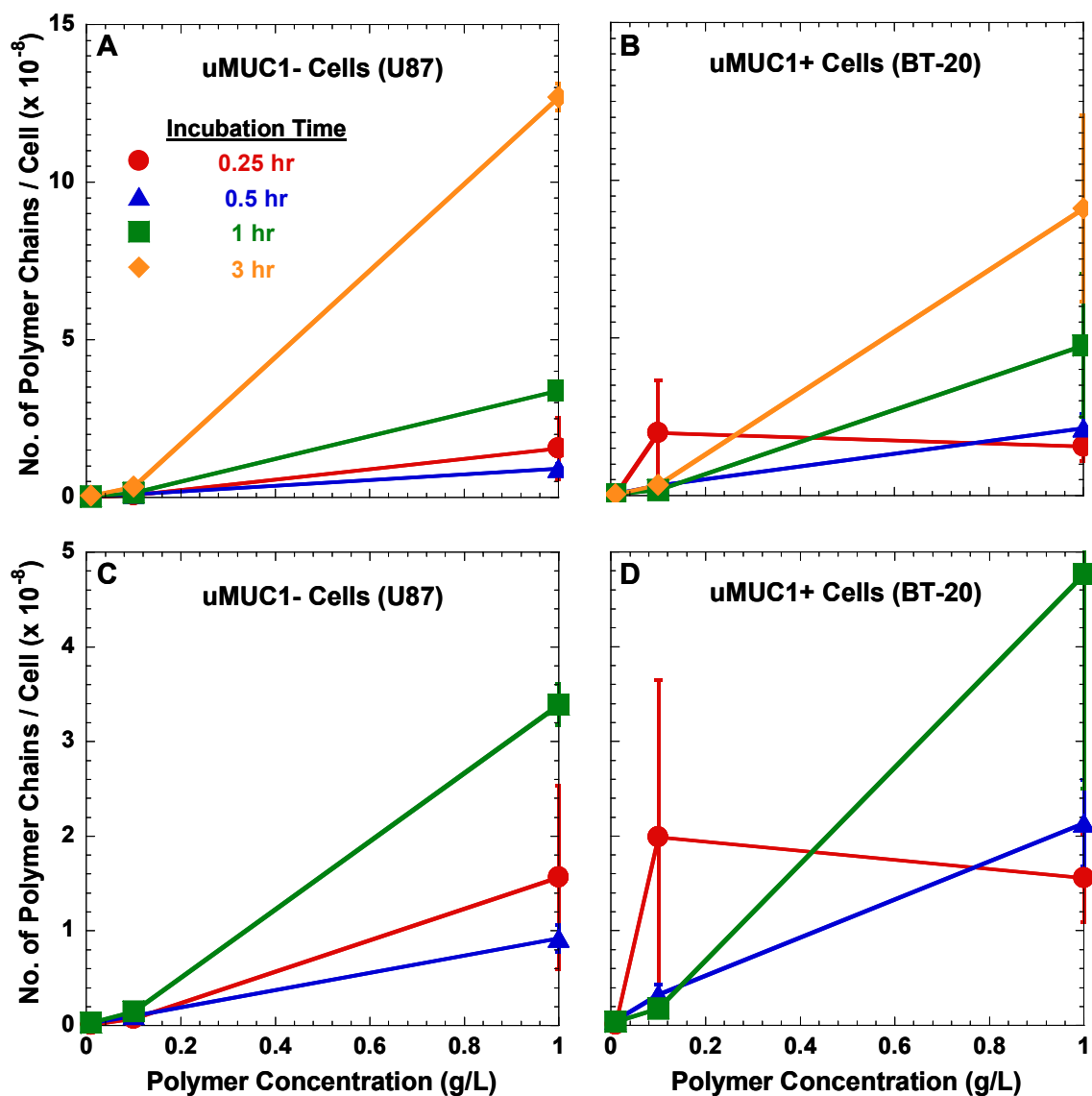


Figure 4.5. Effect of polymer concentration on the cellular uptake of non-targeted polymer with 100% of the linkers having ester-linked hydrocarbon side chains (#27) in uMUC1- (U87) and uMUC1+ (BT-20) cells as a function of polymer concentration ($n=3$). C and D are magnified versions of A and B, respectively.

4.3.2. Theoretical Design of Targeting Polymers

After demonstrating that these non-targeted polymers were taken up into cells, it was desired to investigate the use of these polymers as targeted delivery vehicles. In order to rationally design our alternating copolymers for use as targeted drug delivery

vehicles, several theoretical calculations were performed to determine the requisite properties and characteristics of the desired copolymers. These properties included the minimum number of ligands required per particle to achieve the desired polyvalency and the length of the ligand spacer essential for ligand binding. In order to investigate the minimum number of ligands required per particle to achieve the desired polyvalency, the affinity or avidity of each particle for the targeted receptors needed to be calculated. In general, a higher number of ligands on a multivalent particle leads to more ligand-receptor interactions and a higher avidity of the particle for the receptors. Descriptions of the models used along with the interpretation of the results of these calculations are given in this section, whereas the detailed calculations are given in Appendix V. The results from these calculations guided the synthesis of the targeting polymers used in the uptake studies described in sections 4.3.3 and 4.3.4.

4.3.2.1. Polyvalency estimates

In biological systems, the weak binding of a ligand to its receptor is often enhanced through multivalent interactions. Multivalency, also known as polyvalency, occurs when an entity with multiple ligands or binding sites binds to another entity with multiple receptors or binding sites, creating numerous ligand-receptor pairs and thus a stronger interaction. Two models from the literature were used to analyze the advantage of polyvalency for targeted delivery. The avidity of the targeted polymers for the target cells was calculated based on the affinity of one ligand for one receptor.

Cooperativity Model

The first model that was considered is based on the cooperativity of multiple ligands present on one polymer delivery vehicle [56]. This cooperativity model is derived by equating the total Gibbs free energy (ΔG^{total}) of binding to the sum of the Gibbs free energies for individual binding events (ΔG^i).

$$\Delta G^{\text{total}} = \Delta G^1 + \Delta G^2 \dots + \Delta G^N \quad (4.4)$$

where N is the number of ligands per particle. The association constant, K_A , is related to the Gibbs free energy of binding by

$$\Delta G = -RT \ln K_A \quad (4.5)$$

where R is the gas constant and T is the temperature. Substituting equation (4.5) into equation (4.4) gives

$$-RT \ln K_{A,\text{Apparent}} = \left[-RT \ln K_{A,1} \right] + \left[-RT \ln K_{A,2} \right] \dots + \left[-RT \ln K_{A,N} \right] \quad (4.6)$$

where $K_{A,\text{Apparent}}$ is the apparent association constant for the polyvalent particle and $K_{A,i}$ is the association constant for the i^{th} binding event. Canceling and rearranging gives

$$K_{A,\text{Apparent}} = K_{A,1} K_{A,2} \dots K_{A,N} \quad (4.7)$$

If it is assumed that each individual binding event is not affected by any other binding event (non-cooperativity), the association constants for all binding events are equal.

Substituting gives

$$K_{A,\text{Apparent}} = (K_A)^N \quad (4.8)$$

However, since these individual binding events may be positively or negatively affected by the previous binding events, a degree of cooperativity between ligands, α , can be included in the equation giving

$$K_{A,Apparent} = (K_A)^{\alpha N} \quad (4.9)$$

For positive cooperativity, non-cooperativity, and negative cooperativity, α is greater than 1, equal to 1, and less than 1, respectively. For the calculations shown below, we used α values of 2, 1, and 0.5. The dissociation constant, K_D , is the reciprocal of the association constant and is often used as a metric for the affinity, or avidity, of a binding interaction. Therefore, in this model, the apparent dissociation constant of the polymer particle was calculated from the equation

$$K_{D,Apparent} = (K_D)^{\alpha N} \quad (4.10)$$

This model is often used due to its simplicity and is powerful if information can be obtained for the degree of cooperativity between ligands.

Structural Model

The second model uses a structural argument to calculate the binding enhancement due to multivalency [64]. Gargano et al. developed the model for a bivalent ligand consisting of two ligand binding sites attached by a polymer linker, accounting for statistical factors representing the number of permutations that can lead to binding of a ligand divided by the number of permutations that can lead to unbinding of a ligand and the effective concentration of one polymer end at a given distance from the other bound end when the two polymer ends are a set distance apart. This model was then extrapolated to a general solution for higher order systems. The apparent dissociation constant of the polymer particle was calculated from the equations

$$K_{D,Apparent} = K_D (nBE)^{-1} \quad (4.11)$$

$$BE = F \left[s K_D^{-1} (10^{-2}) \right]^{n-1} \quad (4.12)$$

where K_D is the dissociation constant for the ligand, BE is defined as the binding enhancement per ligand, F is a system-specific statistical factor, s is 30 divided by the distance between binding sites on the receptor, in Å, and n is the lesser of the number of binding sites on the receptor or the number of ligands or binding sites on the particle. The factor 10^{-2} is due to the inclusion of the maximum effective concentration of a second ligand once a first is bound. The statistical factor, F, was assumed to be 1 based on the literature [64]. This general solution is applicable assuming that (1) the binding sites are equivalent, (2) there is no cooperative binding between ligands, (3) all ligand sites are available for binding, and (4) there are no polymer-receptor interactions. These two models were used to analyze the polyvalency in both the EPPT/uMUC1 and folate/FR systems.

First, the advantage of polyvalency was examined in the EPPT/uMUC1 system. The EPPT synthetic peptide has significant affinity, $K_D=2.5 \times 10^{-5}$ M, for the uMUC1-derived PDTRP epitope, although much lower than the affinity of the parent monoclonal antibody, $K_D=2 \times 10^{-8}$ M [52]. Assuming 100% underglycosylation of the mucin-1 protein, the distance between PDTRP binding sequences was calculated as 90 Å, using known bond lengths and angles (see Appendix V). Since there are 30-90 repeats of the PDTRP sequence on a mucin-1 and this is greater than the number of ligands on the polymer, n was always the number of ligands on the polymer carrier. The calculated affinity of the targeted alternating copolymer particles with varying numbers of EPPT peptides attached is shown for both models in Figure 4.6. The dashed line indicates the K_D value for the parent monoclonal antibody. If three to four ligands per particle are

available for binding, a $K_{D,Apparent}$ equivalent to or lower than the K_D for the monoclonal antibody is achieved, even for the worst case model. Since three or four ligands need to be available for binding, not simply attached to the particle, it was necessary to determine how the length of the tether connecting the ligand to the polymer affects the percent of ligands on the particle that are available to the surface of the cell. This is discussed in section 4.3.2.2.

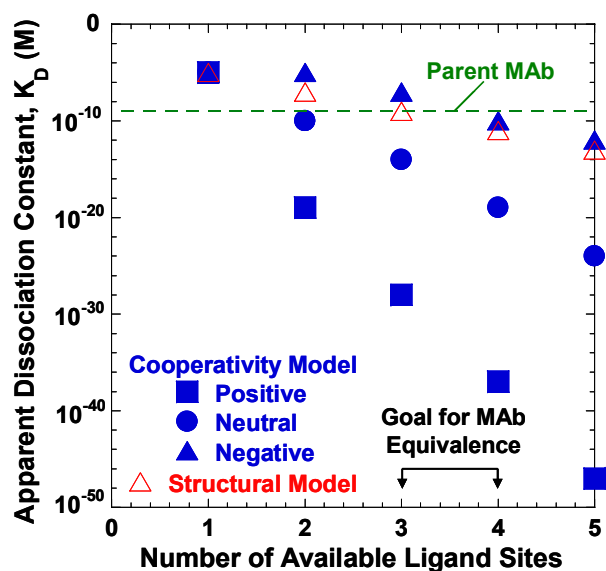


Figure 4.6. Affinity of polymer drug delivery vehicles targeted with EPPT based on number of available ligand sites.

With respect to the folate/FR system, polyvalency may not be a significant issue. The FR is a high affinity receptor for the small molecule folate, or folic acid, with a dissociation constant, K_D , for this binding event of 1×10^{-10} M [65-67]. This affinity is even greater (5X) than the parent monoclonal antibody from which EPPT was derived in the uMUC1 targeting system discussed above. Even though polyvalency may not be necessary in this system, calculations for the apparent dissociation constant were

performed. GPI-anchored FR are clustered in microdomains of around 70 nm in size containing approximately 50 FR, therefore they are an average of 100 Å apart [68]. The calculated affinity of the targeted alternating copolymer particles with varying numbers of folate ligands attached is shown in Figure 4.7. The dashed line indicates the K_D value for one isolated binding event. The analysis magnifies the point that a polymer with only one folate molecule attached will match the affinity of a free folate molecule. However, it is clear that increasing the number of folates per particle will only enhance the overall affinity of our particles for the target cells. Since the FR is internalized, along with any particle bound to the FR, it must be considered that an extremely low $K_{D,Apparent}$ value, indicating a very high affinity, may hinder the release of the particle from the FR once the complex is internalized into a cell. However, it has been shown in the literature that folate readily dissociates from the FR in the acidic environment of an endosome, therefore a multivalent particle will likely dissociate in the endosome as well [58].

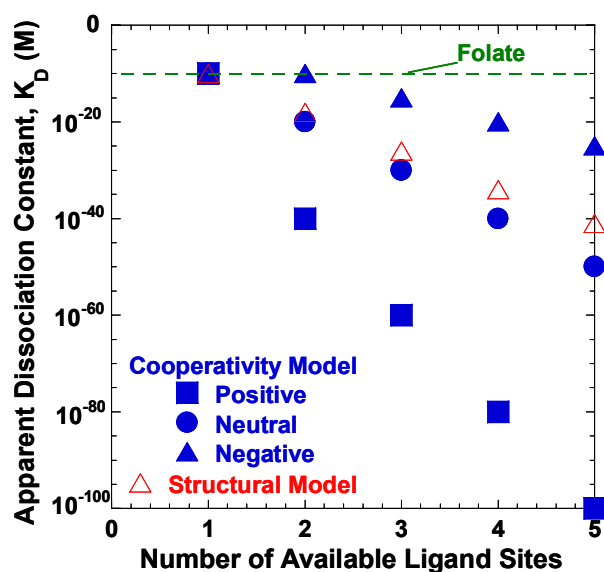


Figure 4.7. Affinity of polymer drug delivery vehicles targeted with folate based on number of available ligand sites.

4.3.2.2. Ligand tether length calculations

Calculations were also made to determine the length of the tether attaching the ligand to the polymer particles that is necessary to allow for polyvalency. Several other researchers have found that attaching the ligand by a tether greatly increases the cellular uptake [67, 69]. A geometric model was used, assuming spherical particles, to calculate the fraction of the surface area of the particle able to bind to the surface of the cell for a given tether length [70]. The active fractional area of the polymer carrier is described as the fraction of carrier surface that is available for binding to the cell. It has been shown to be dependent on tether length, ligand size and carrier size. A schematic depicting the geometrical arrangement and parameters used in this model is shown in Figure 4.8.

Assuming that the tether is in a fully extended conformation and using simple geometry, the active fractional area of the carrier is given by

$$A = \frac{2\pi RH}{4\pi R^2} = \frac{H}{2R} \quad (4.13)$$

where R is the radius of the carrier and H is given by $L-d_B$ when $L \leq R+d_B$. Here, L is the sum of the ligand length and the maximum extended length of the tether and d_B is the binding distance of the ligand and the receptor. As two entities approach each other, the total free energy of the system decreases and at a critical distance the total free energy of the system reaches a minimum. It has been shown that for a binding pair having a high affinity, the majority of ligand–receptor bond formation will occur at this critical distance, also defined as the binding distance. Varying the tether length alters the binding distance between the carrier and cell surface receptors since binding distance is a function

of tether length. The effect of tether length on binding distance was determined, as reported in the literature, by using a combination of Monte Carlo simulations, diffusion reaction theory, and surface force measurements [71]. When $L > R + d_B$, H becomes $R + x$, where x is the vertical distance above the horizontal line passing through the center of the carrier, indicating the position of the fully extended tether on the carrier surface that is tangent to the surface of the carrier and reaching the cell surface.

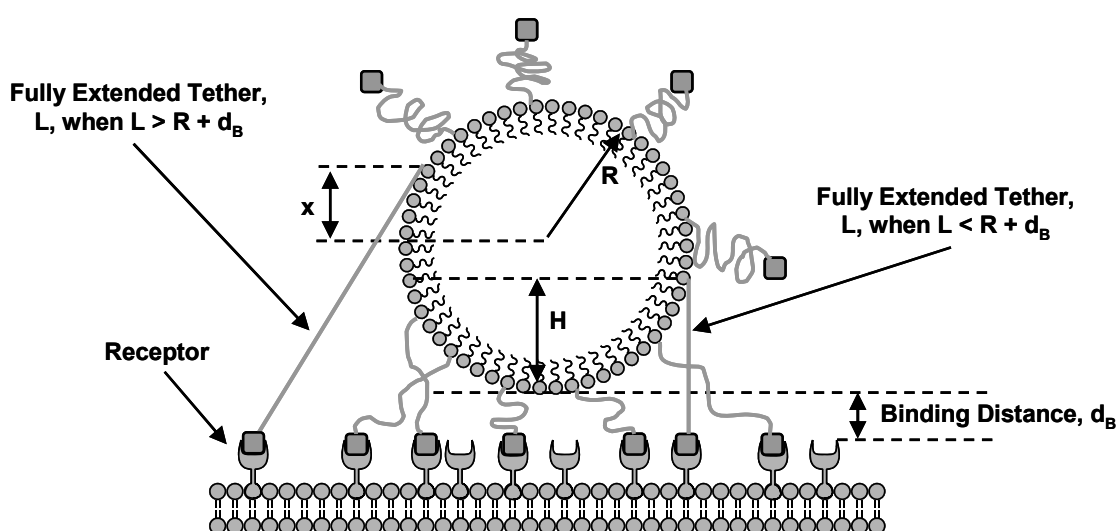


Figure 4.8. Schematic of parameters used for ligand tether length calculations adapted from [70].

This study was performed for PEG ranging in molecular weight from 900 to 10,000 and carrier diameters ranging from 10 nm to 150 nm. The tether length was calculated from the PEG molecular weight based on a molecular weight of 44 and a length of 350 pm for each PEG repeat unit [70]. The analysis showed that, for our particle size of ~ 10 nm in diameter [48], increasing the tether length by using PEG-3400 as the spacer would increase the fraction of the surface area of the particle able to bind to $\sim 75\%$ (Figure 4.9). Assuming there is at least one ligand on every other polymer chain and at

least eight polymer chains aggregate to form one micelle, this ligand tether length would allow for three ligands available for binding to the cell per drug carrier. The availability of three ligands for binding satisfies the requirements determined by the polyvalency estimates discussed earlier.

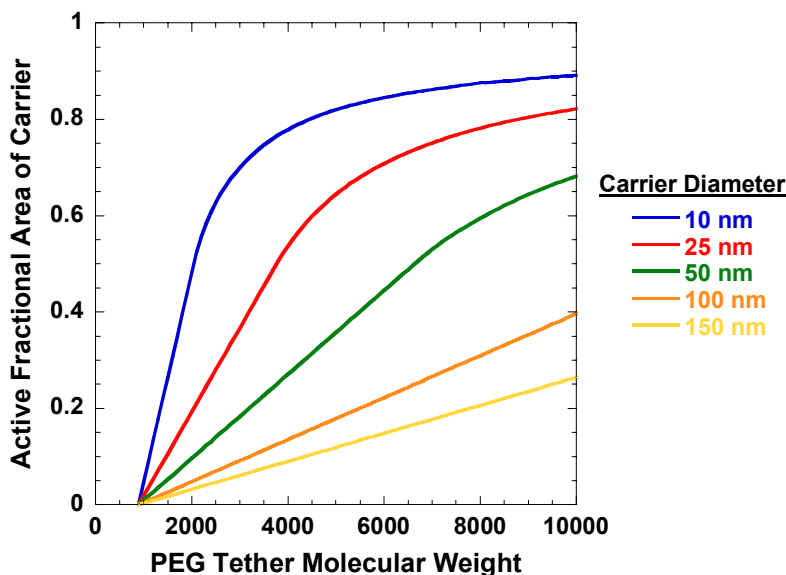


Figure 4.9. Effect of PEG tether molecular weight on the active fractional area of the carrier.

The major assumption of this model is that the tether is in a fully extended conformation. It is unlikely that a PEG tether would be fully extended in an aqueous environment, therefore this model over-estimates the active fractional area of the carrier. Future, more rigorous models could potentially provide more accurate estimates of PEG chain length using various available models (ie. random coil, etc.) to estimate the end-to-end distance of the tether. The purpose of this exercise was to determine the accessibility of the ligand attached to the carrier to the receptors on the cell surface. However, another assumption of this model is that all ligands are available for binding, ie. not internalized

into the particle. Further improvements to this model could account for the availability of the ligands based on steric arguments and polymer shielding.

4.3.2.3. Comparison to experimental data in literature

The validity of the theoretical calculations discussed earlier, both polyvalency estimates and ligand tether length calculations, was tested by using experimental data from the literature. Moore et al. investigated the *in vitro* uptake of cross-linked iron oxide nanoparticles modified with Cy5.5 dye and carrying EPPT peptides attached to the dextran coat of the nanoparticles [53]. The structural properties of these nanoparticles reported in the literature (ie. 35.8 nm in size, 14 EPPT per particle) were used to calculate the active fractional area of the particle. It was calculated that the active fractional area of the particles was ~10% of the surface, therefore ~1.4 EPPT were accessible per particle. See Appendix V for the details of these calculations. Concurrently a Scatchard plot analysis was performed on the experimental data from this paper to determine the apparent K_D of these particles, as shown in Appendix VI. The apparent K_D of these iron oxide particles was found experimentally to be 8×10^{-9} M. Figure 4.10 demonstrates that the apparent K_D for the particles of Moore et al. matches well with the predicted apparent K_D values from the theoretical neutral cooperativity model. Note that the ligands were not attached to the particles by a tether, removing the necessity of the fully extended conformation assumption. These results validate the use of these theoretical calculations for rationally designing our alternating copolymers for use as targeted drug delivery vehicles.

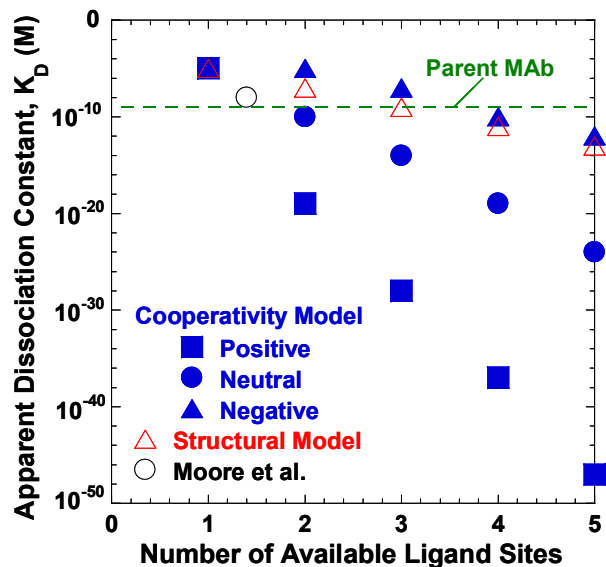


Figure 4.10. Theoretical affinity of particles targeted with EPPT ligands as compared to experimental data from the literature.

4.3.3. Cellular uptake of targeted polymers with EPPT by labeling with ¹²⁵I

In order to gain insight into the uptake of EPPT in uMUC1+ and uMUC1- cell lines, experiments were performed with free EPPT labeled with ¹²⁵I. The uptake of EPPT in uMUC1+ cells was twice the uptake in uMUC1- cells (Figure 4.11). Since the uMUC1 protein is not expressed on the surface of the MRC-5 cells, the uptake in those cells is non-specific. However, the uptake in BT-20 cells likely includes both specific and non-specific uptake since the uMUC1 protein is present in that cell line. In order to increase the specific uptake, multivalency is necessary, as described earlier. Appendix VI contains an analysis of the kinetic parameters that can be obtained from this data as well as a comparison of this data to a theoretical model of EPPT uptake. The experimental data for uptake of EPPT was used to estimate the forward reaction rate of the binding event, k_f , as $1.4 \times 10^{-4} \text{ M}^{-1} \text{ hr}^{-1}$ and the reverse reaction rate, k_r , as $3.4 \times 10^{-9} \text{ hr}^{-1}$. Using these kinetic parameters, the simplest theoretical model, considering one binding event and no

internalization, agrees well with the experimental data ($\sim 2 \times 10^8$ EPPT per cell) when 7-10 particles bind per uMUC1 (Figure V.iv in Appendix VI).

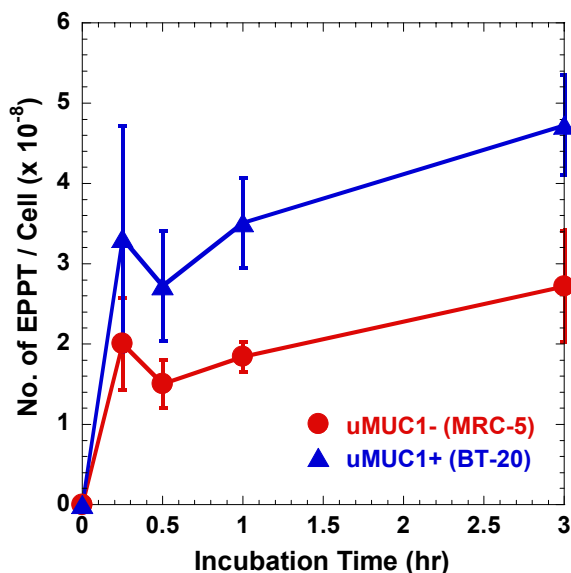


Figure 4.11. Cellular uptake of EPPT peptide at 0.1 g/L in uMUC1- (MRC-5) and uMUC1+ (BT-20) cells (n=3).

Early experiments focused on the uptake of ^{125}I -labeled polymers with and without the EPPT peptide. The cellular uptake for polymer with 100% of the linkers having ester-linked hydrocarbon side chains (#27) and polymer with 5% of the linkers having EPPT attached by a triethylene glycol (TEG) spacer and the remaining 95% of the linkers having ester-linked hydrocarbon side chains (#37) is shown in Figure 4.12.

Polymer at this concentration (1 g/L) is in the form of micelles. The data for polymer with 100% of the linkers having ester-linked hydrocarbon side chains is the same as that in Figure 4.4 for 1 g/L. In the uMUC1- cell line, there is little overall difference in the cellular uptake between the targeted and non-targeted polymers, although the targeted polymer is slightly higher at earlier times. However, the cellular uptake of the targeted

polymer is twice that of the non-targeted polymer in the uMUC1+ cells. This indicates that our polymer nanoparticles may be targeted to cells using the EPPT peptide.

Interestingly, the total uptake at 3 hours in the uMUC1- cells is similar to the uptake of the targeted polymer in the uMUC1+ cells. The non-specific uptake of our nanoparticles in uMUC1- cells is higher than the non-specific uptake in uMUC1+ cells. This data can also be compared to that for uptake of free EPPT shown in Figure 4.11. At the same molar concentration in uMUC1+ cells, $\sim 5 \times 10^8$ EPPT are taken up per cell while $\sim 13 \times 10^8$ polymer chains are taken up per cell for polymer containing EPPT. See Appendix VII for a kinetic analysis of the internalization and surface bound polymer versus EPPT peptide.

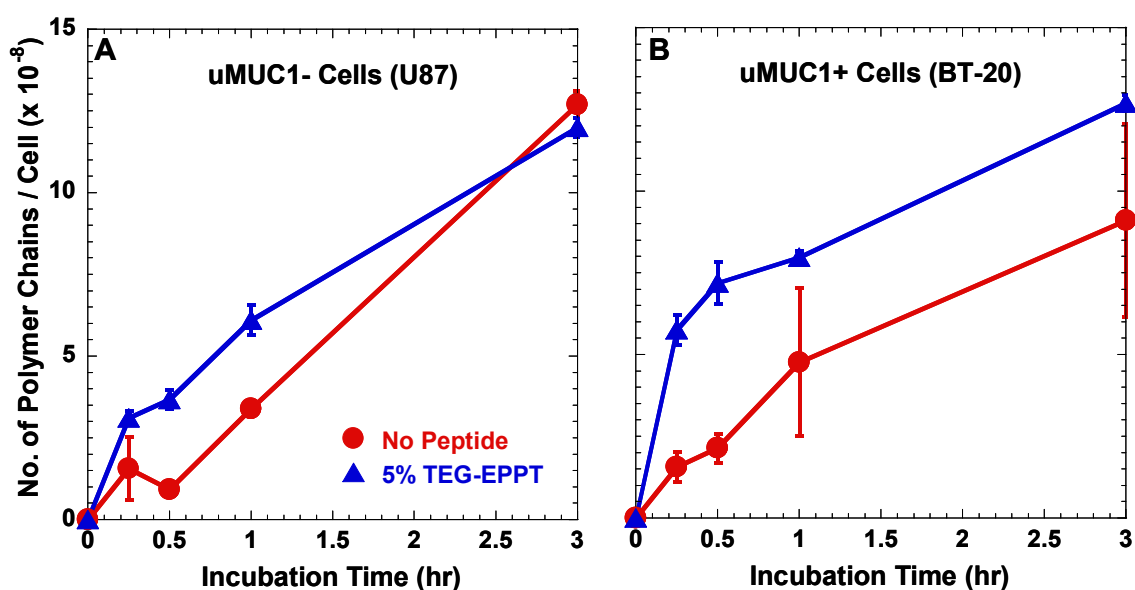


Figure 4.12. Cellular uptake of non-targeted polymer with 100% of the linkers having ester-linked hydrocarbon side chains (#27) and targeted polymer with 5% of the linkers having EPPT attached by a TEG spacer and the remaining 95% of the linkers having ester-linked hydrocarbon side chains (#37) at 1 g/L in uMUC1- (U87) and uMUC1+ (BT-20) cells (n=3).

Next we investigated the effect of increasing the percent of linkers with EPPT attached and increasing the spacer length attaching the EPPT to the linker. The cellular uptake results for experiments using polymer with 7% of the linkers having TEG-EPPT attached and the remaining 93% of the linkers having no side chains (#42), polymer with 34% of the linkers having TEG-EPPT attached and the remaining 66% of the linkers having no side chains (#44), and polymer with 100% of the linkers having EPPT attached by a PEG-3400 spacer (#65) are shown in Figure 4.13. These polymers would not be in the form of micelles since none have hydrocarbon side chains. Again, all polymers were labeled with ^{125}I . In the uMUC1- cell line, the cellular uptake is not greatly affected by the increase in the percent of linkers with EPPT at early times, although at 3 hours the polymer with the highest amount of peptide has the highest uptake. These results indicate that the non-specific uptake of these polymers is quite significant. In the uMUC1+ cells, the highest uptake occurred with the polymer with the lowest amount of EPPT. In addition, lengthening the spacer attaching the EPPT to the polymer, while eliminating the hydrophobic side chains, does not seem to have increased the uptake of the polymer. Comparing these results to Figure 4.12, the uptake is higher when hydrocarbon side chains are attached to the polymer such that micelles can form ($\sim 12 \times 10^8$ polymer chains per cell) than when the amount of peptide attached to the polymer is increased ($\sim 2\text{-}4 \times 10^8$ polymer chains per cell). The formation of micelles due to the presence of hydrophobic side chains and the polyvalent effect of many ligands on each micelle may contribute to the increased cellular uptake.

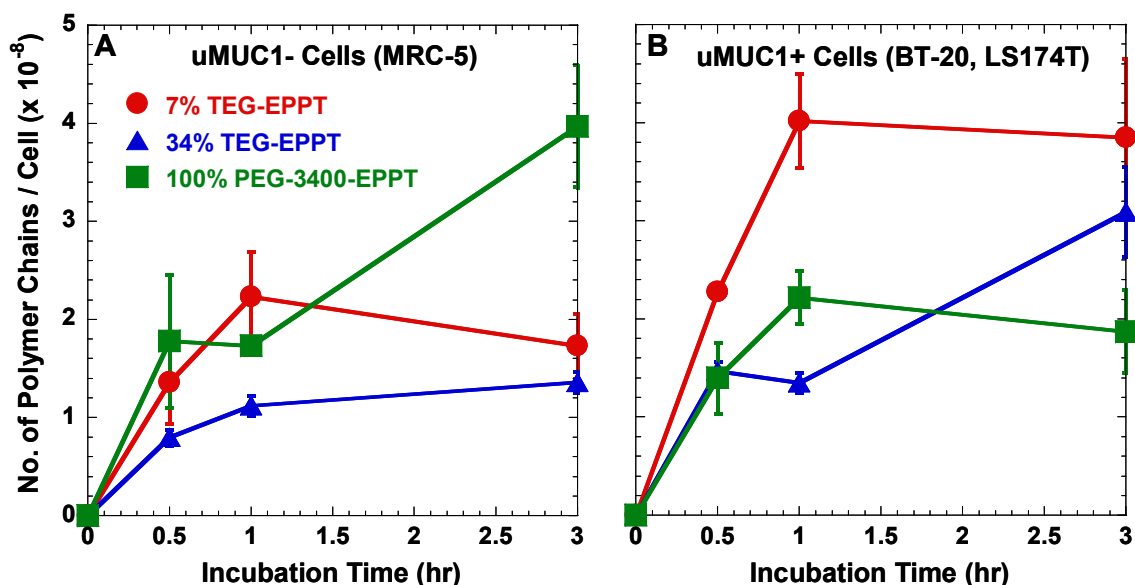


Figure 4.13. Effect of amount of EPPT peptide on cellular uptake of targeted polymers: polymer with 7% of the linkers having TEG-EPPT attached and the remaining 93% of the linkers having no side chains (#42) at 1 g/L in uMUC1- (MRC-5) and uMUC1+ (BT-20) cells, polymer with 34% of the linkers having TEG-EPPT attached and the remaining 66% of the linkers having no side chains (#44) at 1 g/L in uMUC1- (MRC-5) and uMUC1+ (BT-20) cells, and polymer with 100% of the linkers having EPPT attached by a PEG-3400 spacer (#65) at 1 g/L in uMUC1- (MRC-5) and uMUC1+ (LS174T) cells (n=3).

The cellular uptake of two imaging polymers was also investigated in the uMUC1 system. Polymer with 100% of the linkers having PFC chains attached (#10) and polymer with 5% of the linkers having EPPT attached by hexaethylene glycol (HEG), 5% of the linkers having FITC attached, and 90% of the linkers having no side chain (#39) were both labeled with ¹²⁵I. The polymer with PFC chains is in the form of micelles at this concentration (1 g/L), but the polymer with EPPT and FITC is not in the form of micelles since it has no hydrocarbon side chains. Curiously, the polymer with EPPT and FITC was taken up in higher amounts than the polymer with PFC in uMUC1- cells, as shown in Figure 4.14. However, this trend is the same in the uMUC1+ cell lines, possibly indicating the selective advantage of attaching the EPPT peptide or demonstrating higher

non-specific uptake of the polymer with EPPT. See Appendix VII for a kinetic analysis of the internalization and surface bound polymer versus EPPT peptide.

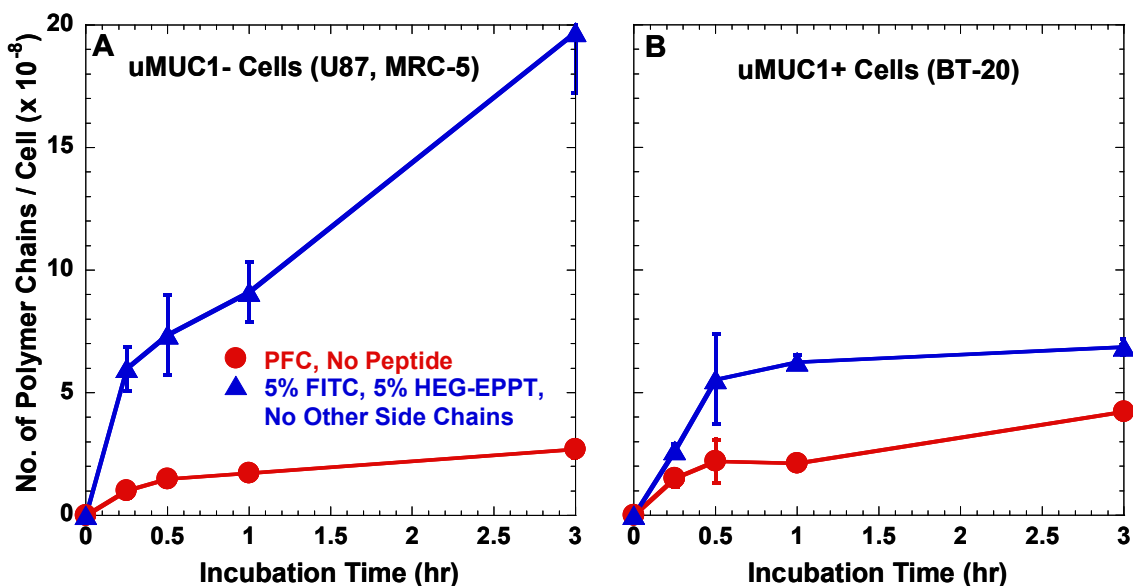


Figure 4.14. Cellular uptake of imaging polymer with 100% of the linkers having PFC chains attached (#10) at 1 g/L in uMUC1- (MRC-5) and uMUC1+ (BT-20) cells and imaging polymer with 5% of the linkers having EPPT attached by HEG, 5% of the linkers having FITC attached, and 90% of the linkers having no side chain (#39) at 1 g/L in uMUC1- (U87) and uMUC1+ (BT-20) cells (n=3).

As shown with the uptake results for non-targeted polymers, the polymer concentration in solution during the incubation can also affect the uptake of polymers. The cellular uptake of polymer with 100% of the linkers having ester-linked hydrocarbon side chains (#27) and polymer with 5% of the linkers having TEG-EPPT attached and the remaining 95% of the linkers having ester-linked hydrocarbon side chains (#37) at three concentrations is shown in Figure 4.15 as a function of incubation time. The data for 1 g/L is the same as that in Figure 4.12. Data in panels A and B is replotted with an expanded scale in panels C and D, respectively. Both polymers are in the form of

micelles at concentrations of 1 g/L and 0.1 g/L, but not at 0.01 g/L. At each concentration, the uptake in the uMUC1- cells is similar to that in the uMUC1+ cells, indicating the high level of non-specific uptake of these particles. In addition, there is a direct correlation between increased polymer concentration in solution and increased cellular uptake. It is clear that, at each concentration, the attachment of the EPPT peptide to the polymer increased the cellular uptake in both cell lines. This observation is logical for the uMUC1+ cells, however, it is curious for the uMUC1- cells, possibly indicating that attaching the EPPT peptide even increases non-specific uptake. The same data plotted as a function of polymer concentration is shown in Figure 4.16. Again, data in panels A and B is replotted with an expanded scale in panels C and D, respectively. This figure shows that the uptake at each time point greater than 0.25 hours is nearly linear in polymer concentration.

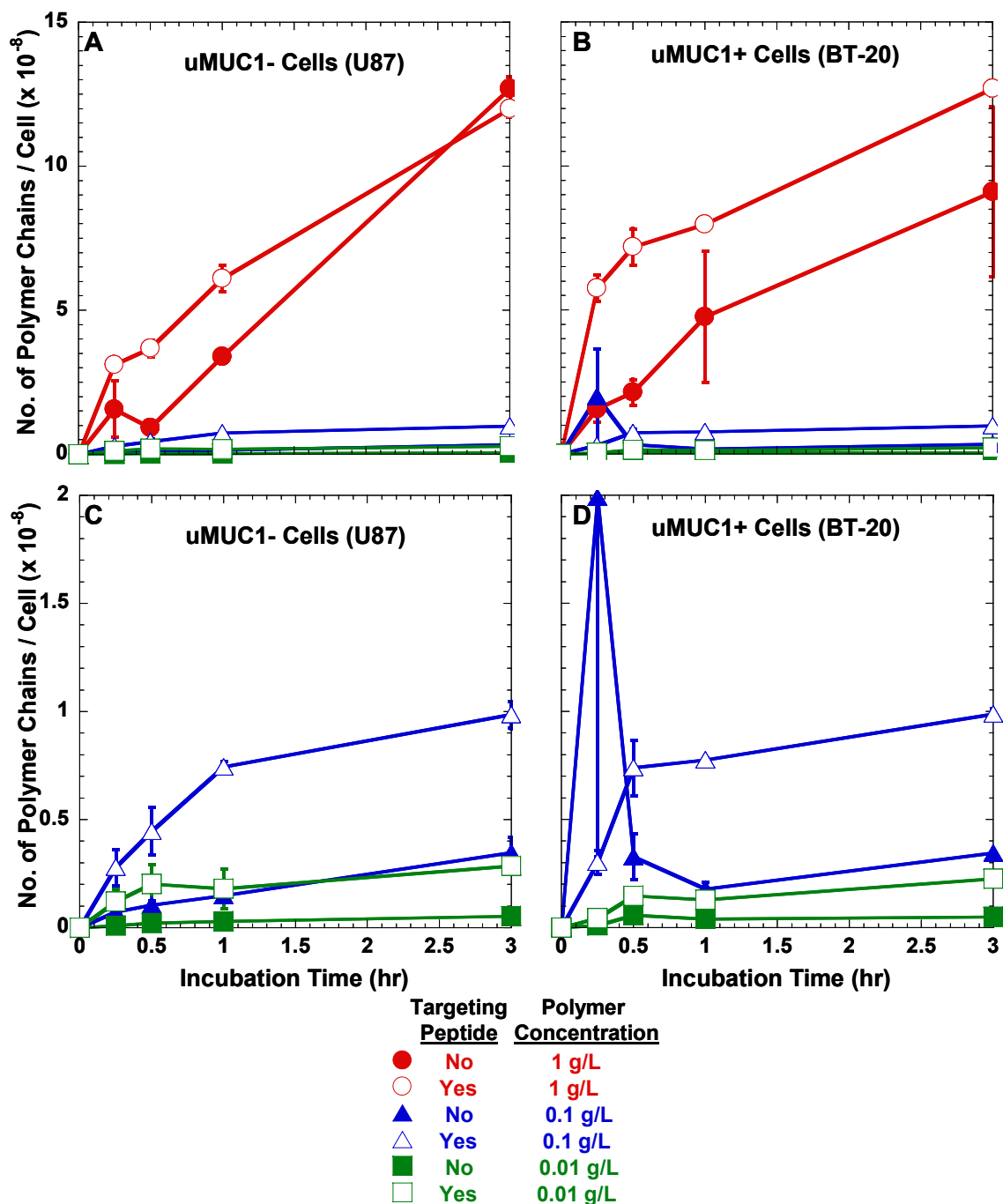


Figure 4.15. Effect of polymer concentration on cellular uptake of polymer with 100% of the linkers having ester-linked hydrocarbon side chains (#27) and polymer with 5% of the linkers having TEG-EPPT attached and the remaining 95% of the linkers having ester-linked hydrocarbon side chains (#37) in uMUC1- (U87) and uMUC1+ (BT-20) cells as a function of time (n=3). C and D are magnified versions of A and B, respectively.

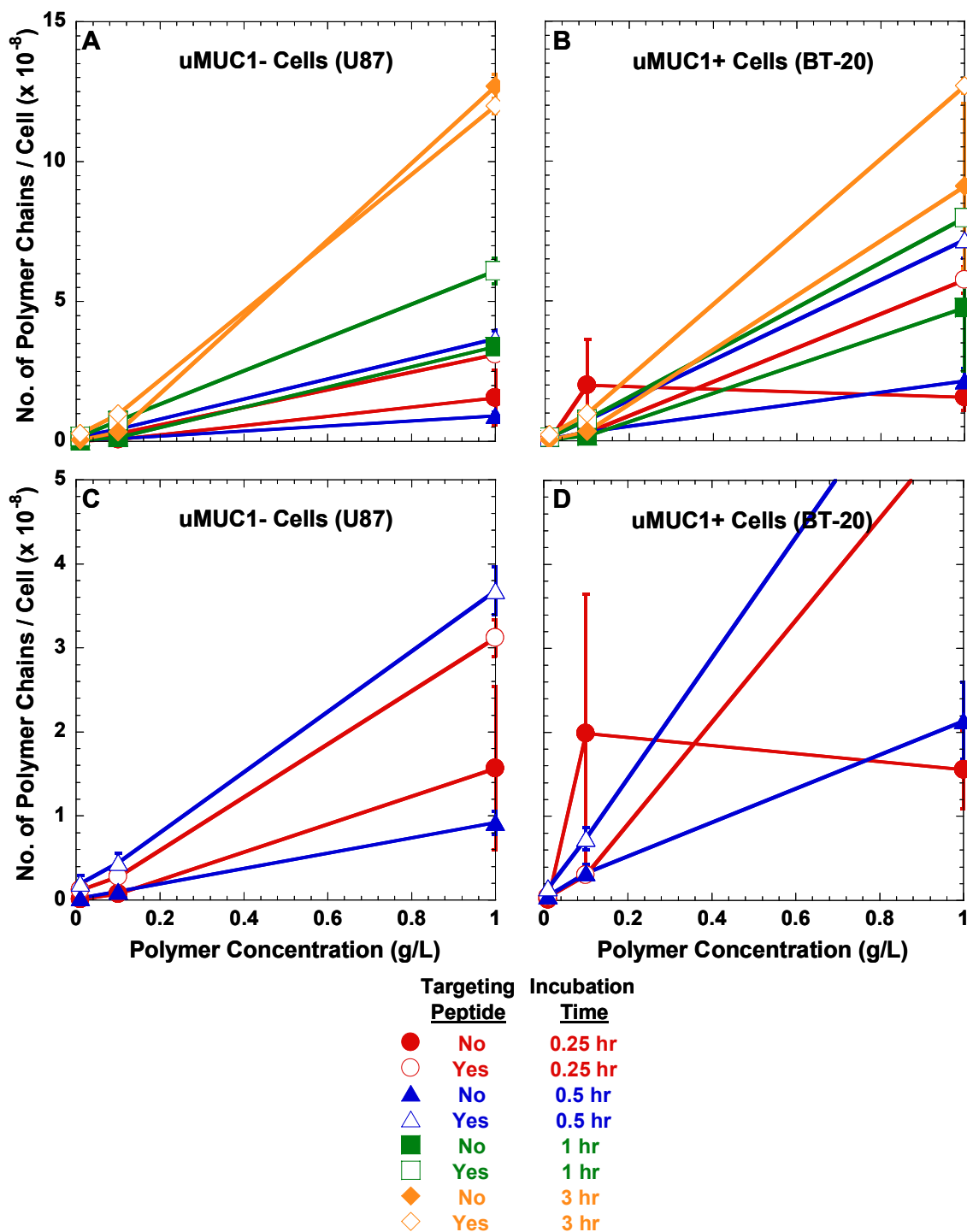


Figure 4.16. Effect of polymer concentration on cellular uptake of polymer with 100% of the linkers having ester-linked hydrocarbon side chains (#27) and polymer with 5% of the linkers having TEG-EPPT attached and the remaining 95% of the linkers having ester-linked hydrocarbon side chains (#37) in uMUC1- (U87) and uMUC1+ (BT-20) cells as a function of concentration (n=3). C and D are magnified versions of A and B, respectively.

Overall, the uptake results in uMUC1- and uMUC1+ cells for polymers containing EPPT did not effectively demonstrate the selectivity of our polymers for the targeted cells. The cellular uptake of polymer with 5% of the linkers having TEG-EPPT attached and the remaining 95% of the linkers having ester-linked hydrocarbon side chains was twice that of polymer with 100% of the linkers having ester-linked hydrocarbon side chains, although the difference was not statistically significant. In addition, increasing the percent of linkers containing the targeting ligand EPPT did not increase the uptake. Therefore, the targeting pair was changed to folate/FR, a model system used often in the literature.

4.3.4. Cellular uptake of targeted polymers with folate by labeling with ^{125}I and ^3H

In order to confirm that our FR+ cells did in fact express the FR, uptake experiments were first performed with ^3H -folate. Studies in the literature reported culturing cells in folate-free media, performing uptake experiments in 24-well plates and collecting cells using lysis buffer. Our previous experiments had used 96-well plates and the cells were removed using trypsin. Therefore, for comparison purposes, these experiments additionally explored the effect of growth media (folate-free versus regular folate-containing media), well size (24-well plates versus 96-well plates), and cellular material removal method (trypsin versus lysis buffer). In each case, the uptake of the labeled ^3H -folate was measured in the absence and presence of an excess of unlabeled folate. If uptake is due to receptor-mediated endocytosis via the FR, an excess of unlabeled folate will compete with the labeled ^3H -folate for the FR, thereby decreasing the measured uptake. The uptake of ^3H -folate dropped significantly in the presence of an

excess of unlabeled folate, regardless of the type of plate, growth media, or cell removal method, as shown Figure 4.17. This confirms that the FR+ cells do express the FR. It was determined that there was no difference in uptake between 24-well plates and 96-well plates, indicating that well size does not affect uptake. The uptake in cells grown in folate-free media for two days before the experiment was ~2.5X higher than that in cells continually grown in regular folate-containing media. This is because depriving the cells of folate causes the up-regulation of the FR. Finally, there was a small difference between collecting the cellular material by trypsin or lysis buffer. In each case, using lysis buffer showed higher uptake. In all subsequent experiments, cells were grown in folate-free media for two days before the experiment and cellular matter was collected using lysis buffer. Additionally, it was confirmed that the FR- cells do not express the FR, since little ³H-folate was taken up in these cells (Figure 4.18). Our results, when cells were grown in folate-free media, are equivalent to those reported in the literature, ~10⁷ ³H-folate per cell taken up over a 3 hour incubation period [63, 72]. Appendix VI contains a comparison of this data to a theoretical model of folate uptake. The simplest theoretical model, considering one binding event and no internalization, agrees well with the experimental data at times greater than 1 hour (Figure V.vi in Appendix VI). The uptake results for free folate can also be compared with the uptake results for free EPPT from Figure 4.11. As mentioned, the number of free folate molecules taken up per cell is on the order of 10⁷, however, the number of free EPPT molecules taken up per cell is on the order of 10⁸.

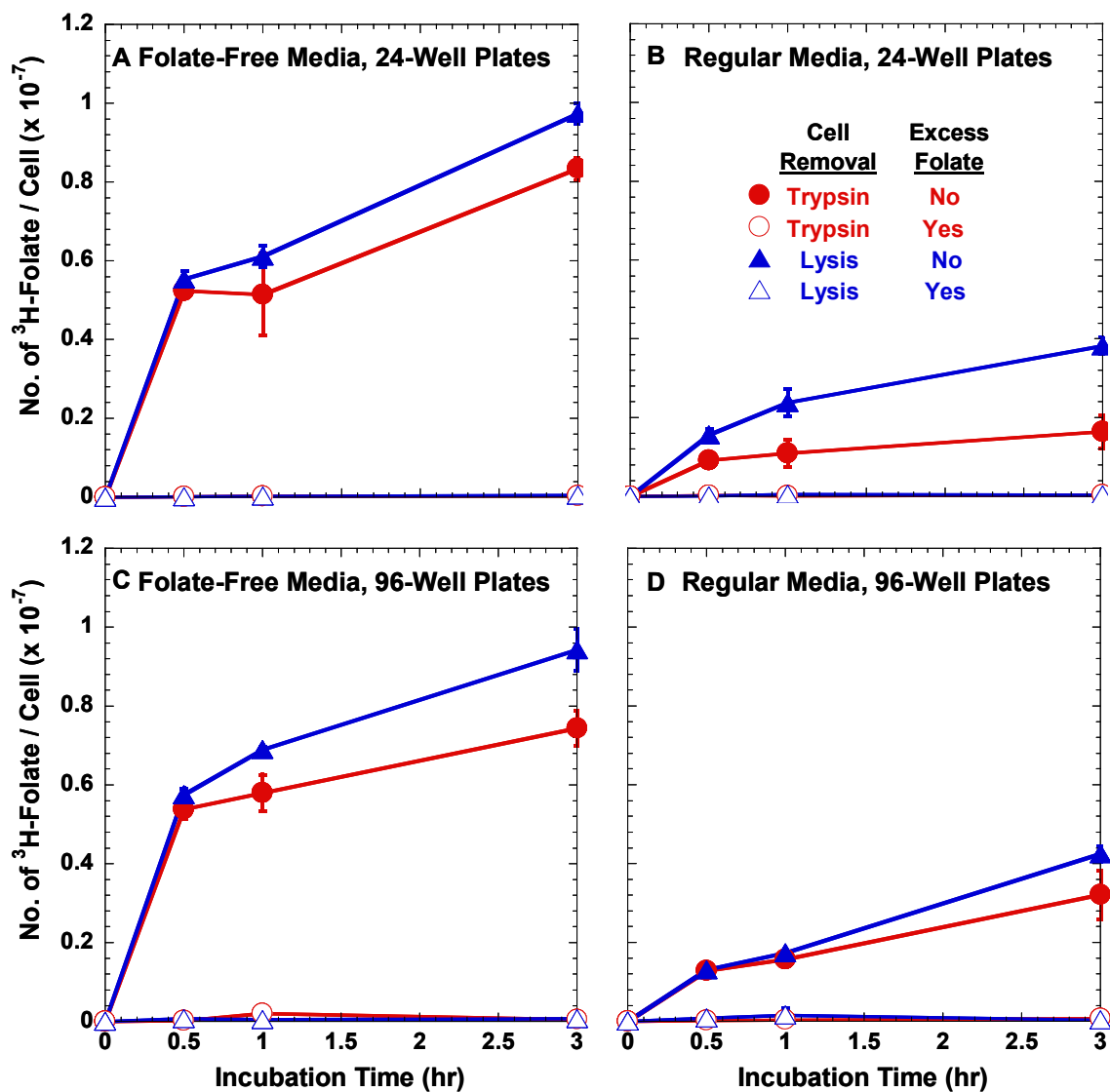


Figure 4.17. Cellular uptake of ^3H -folate at 50 nM in FR+ (KB) cells under various conditions (excess unlabeled folate concentration = 100 μM) (n=3).

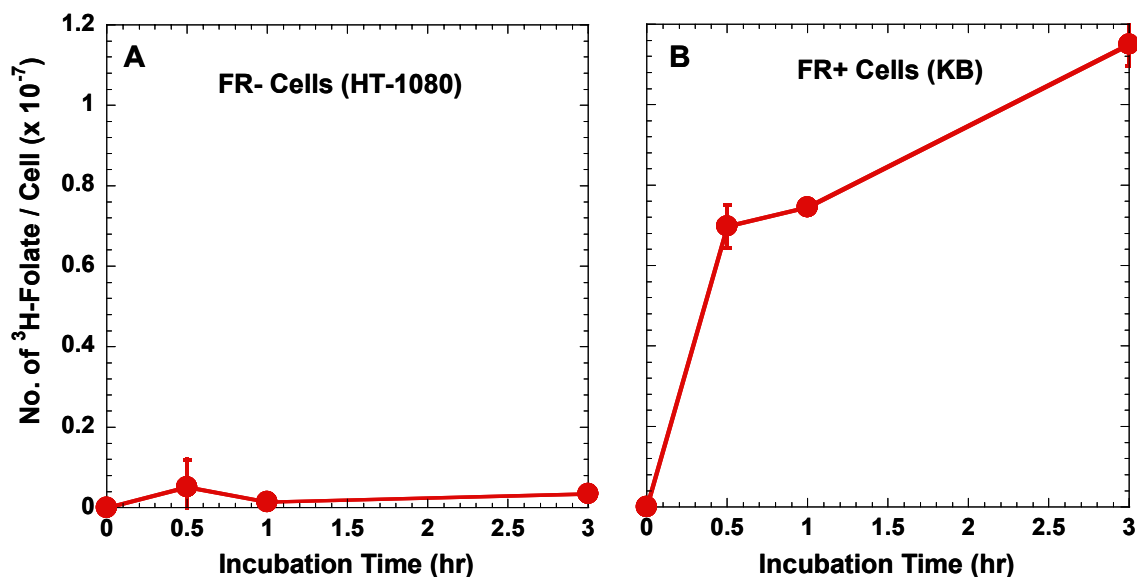


Figure 4.18. Cellular uptake of ^3H -folate at 50 nM in FR- (HT-1080) and FR+ (KB) cells ($n=3$).

Additionally, the amount of cell-associated ^3H -folate was assessed under various conditions affecting the expression of the FR, as shown in Figure 4.19. As mentioned, the uptake of ^3H -folate in cells that had been grown for two days before the experiment in folate-free media (up-regulation) was higher than the uptake in cells that were continuously grown in regular media and demonstrated the highest uptake of ^3H -folate of all conditions investigated here. This is due to the up-regulation of the FR in the cells grown in folate-free media. Furthermore, the uptake of ^3H -folate was investigated in cells that had been grown for two days in folate-free media and then incubated with 100 μM unlabeled free folate for 3 hours immediately before the start of the experiment (down-regulation). The unlabeled free folate acted to saturate and down-regulate the FR. As shown in Figure 4.19, the uptake of ^3H -folate was lower when the cells were saturated with unlabeled free folate before the experiment, as compared to the uptake in cells grown in folate-free media or regular media. These results confirm the effect of the up-

regulation and down-regulation of the FR on the cellular uptake of ^3H -folate by receptor-mediated endocytosis.

Also, as previously discussed, the presence of an excess (100 μM) of unlabeled folate did inhibit uptake of labeled folate. In addition, the cell-associated ^3H -folate after acidic saline wash (internalized) was found to be $\sim 3\text{X}$ lower than the total uptake in folate-free media (up-regulation) and the cell-associated ^3H -folate when the experiment was performed at 4°C (surface bound) was $\sim 2\text{X}$ lower than the total cell-associated ^3H -folate. However, the sum of the surface bound and internalized ^3H -folate is slightly less than the total uptake, which may be explained by the slower binding kinetics at 4°C [73]. Uptake of ^3H -folate, in cells that were pre-treated with PI-PLC to cleave the GPI-anchor attaching the FR to the cell surface (non-specific), is lower than total uptake and slightly lower than internalized folate. This indicates that most of the internalized ^3H -folate is due to non-specific uptake, confirmed in the literature [63, 65]. Finally, when the cells were pre-treated with PI-PLC to cleave the GPI-anchor attaching the FR to the cell surface and then incubated at 4°C (non-specific surface bound), the surface bound folate decreased, confirming the removal of the FR from the surface of the cell.

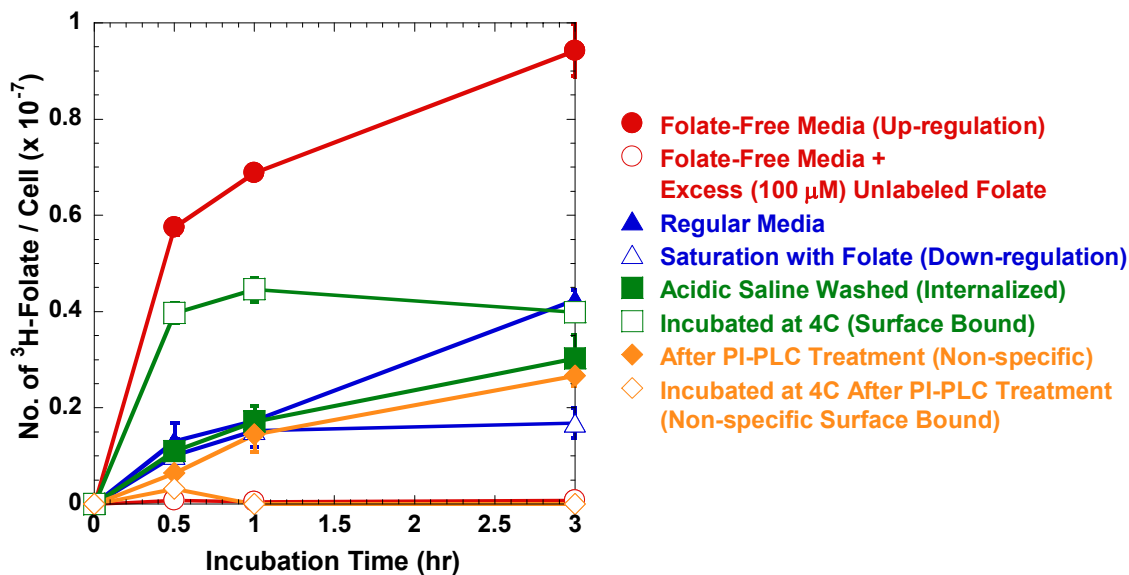


Figure 4.19. Cellular uptake of ^3H -folate at 50 nM in FR+ (KB) cells under conditions affecting the regulation of the FR (n=3).

The effect of varying the concentration on the cellular uptake of ^3H -folate was also explored. The cellular uptake results for ^3H -folate at three concentrations (50 nM, 500 nM, and 5 μM) are shown in Figure 4.20. Increasing the concentration of ^3H -folate did increase the uptake of ^3H -folate at the 3 hour time point, however, when the number of folate molecules per cell was normalized by concentration the uptake was not equivalent for all three concentrations, demonstrating that the uptake of ^3H -folate is not linear with concentration and is likely saturating the FR. It is evident from Figure 4.20 that the uptake of folate is relatively insensitive to concentration in FR+ cells.

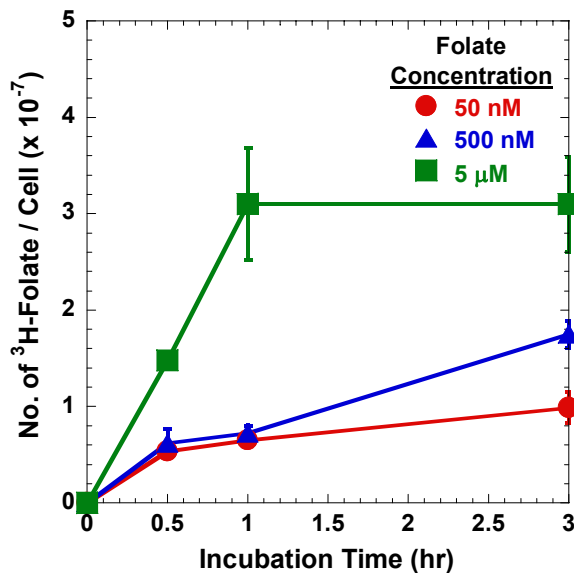


Figure 4.20. Cellular uptake of ³H-folate in FR+ (KB) cells at various concentrations (n=3).

The uptake of several different polymers containing folate was investigated by labeling the polymers with ¹²⁵I. Polymers were synthesized with three different attachment methods for folate. The first series of polymers were produced with folate attached directly to the polymer backbone at the hydroxyl linker. The cellular uptake of polymer with 10% of the linkers having folate attached without a spacer and the remaining 90% of the linkers having no side chains (#50) and polymer with 10% of the linkers having folate attached without a spacer and the remaining 90% of the linkers having ether-linked hydrocarbon side chains (#51) is shown in Figure 4.21. Polymer with hydrocarbon side chains is in the form of micelles at a concentration of 0.1 g/L, but polymer without hydrocarbon side chains is not. For both cell lines the number of polymer chains per cell was higher for polymer without side chains than for that with side chains, however, the concentration used was higher (1 g/L versus 0.1 g/L) for polymer without side chains. In addition, for both polymers, the uptake was the same in both FR-

and FR+ cells and in the absence and presence of an excess of folate, indicating non-specific uptake only.

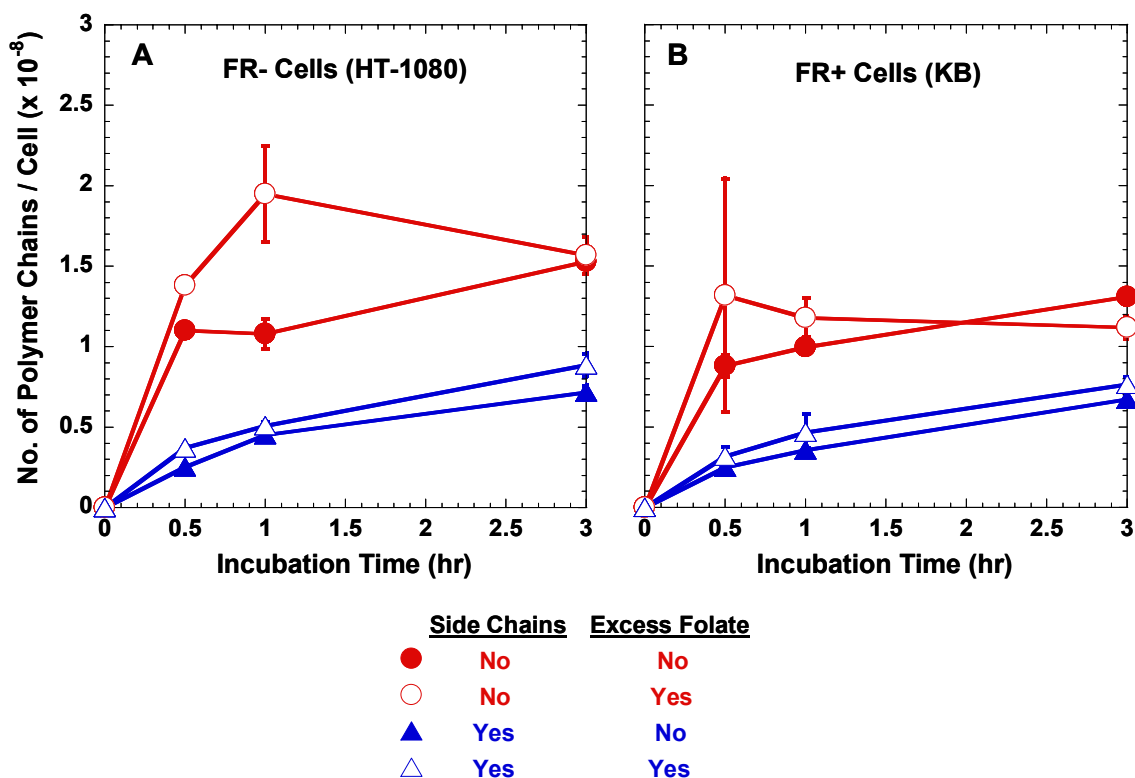


Figure 4.21. Cellular uptake of polymers with folate attached directly to the linkers: polymer with 10% of the linkers having folate attached without a spacer and the remaining 90% of the linkers having no side chains (#50) at 1 g/L and polymer with 10% of the linkers having folate attached without a spacer and the remaining 90% of the linkers having ether-linked hydrocarbon side chains (#51) at 0.1 g/L in FR- (HT-1080) and FR+ (KB) cells (n=3).

The second series of polymers were produced with folate attached to the end of the polymer chain with a PEG-3400 spacer. The spacer was introduced based on the ligand tether length calculations described in Section 4.3.2.2. The cellular uptake of polymer with PEG-3400-folate attached at the end of the polymer chain and no side chains (#56), polymer with PEG-3400-folate attached at the end of the polymer chain and

ether-ester-linked hydrocarbon side chains (#59), and polymer without folate and with ether-ester-linked hydrocarbon side chains (#58) is shown in Figure 4.22. Polymers with hydrocarbon side chains are in the form of micelles at a concentration of 0.1 g/L, but polymer without hydrocarbon side chains is not. As with the previous series of polymers, the number of polymer chains per cell was higher for folate-containing polymer without side chains than for that with side chains in both cell lines, but, again, the concentration used was higher (1 g/L versus 0.1 g/L) for polymer without side chains. In addition, polymer with side chains and no folate was taken up in higher amounts in both cell lines than polymer with side chains and folate, demonstrating no advantage due to the attachment of the targeting ligand. Finally, for all three polymers, the uptake was similar in both FR- and FR+ cells and the uptake was either the same in the absence and presence of an excess of folate or slightly higher in the presence of folate, likely indicative of non-specific uptake only.

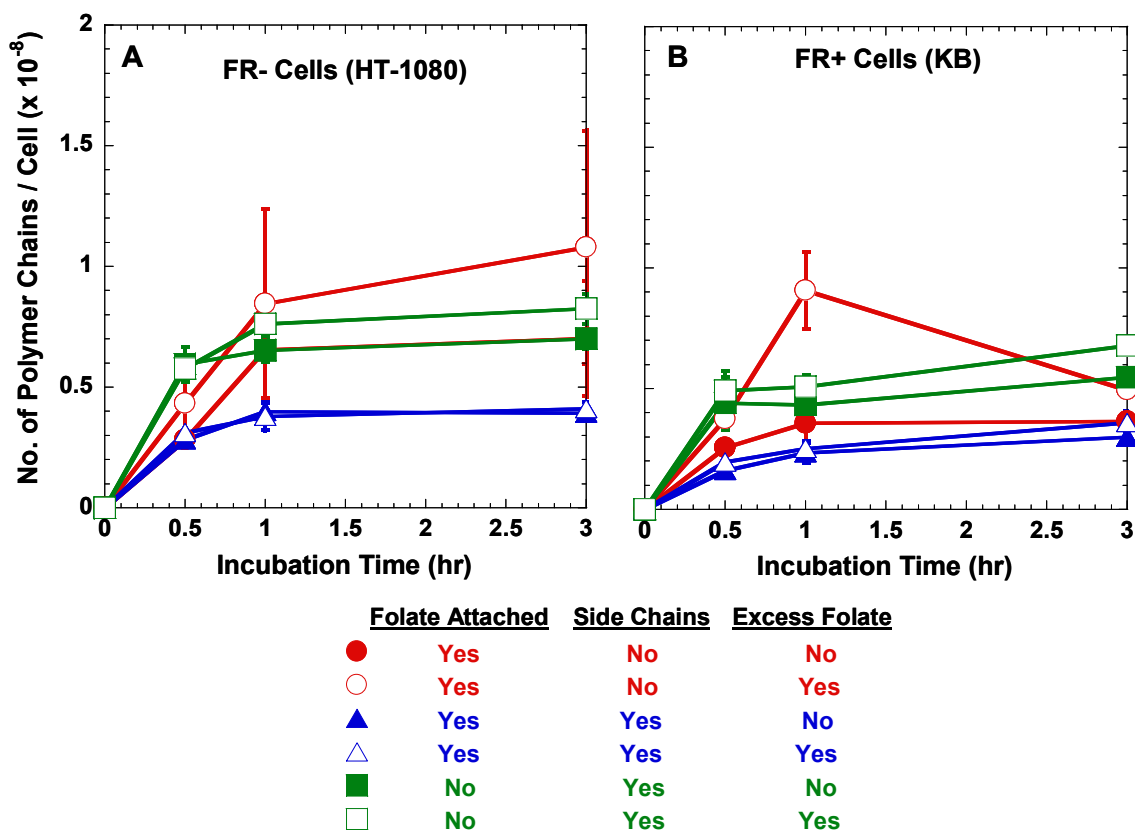


Figure 4.22. Cellular uptake of polymer with PEG-3400-folate at the end of the polymer chain: polymer with PEG-3400-folate attached at the end of the polymer chain and no side chains (#56) at 1 g/L, polymer with PEG-3400-folate attached at the end of the polymer chain and ether-ester-linked hydrocarbon side chains (#59) at 0.1 g/L, and polymer without folate and with ether-ester-linked hydrocarbon side chains (#58) at 0.1 g/L in FR- (HT-1080) and FR+ (KB) cells (n=3).

Finally, the third series contained polymers with PEG-3400-folate attached to the polymer backbone at the hydroxyl linker. Results for polymer with 25% of the linkers having PEG-3400-folate attached and the remaining 75% of the linkers having no side chains (#60), polymer with 25% of the linkers having PEG-3400-folate attached and the remaining 75% of the linkers having ether-ester-linked hydrocarbon side chains (#61), and polymer with 100% of the linkers having PEG-3400-folate attached (#64) is shown in Figure 4.23. Polymer with hydrocarbon side chains is in the form of micelles at a

concentration of 0.1 g/L, but the polymers without hydrocarbon side chains are not. For polymers with 25% of the linkers having PEG-3400-folate, the uptake was higher for polymer with side chains than for that without side chains in both cell lines. The highest number of polymer chains per cell was with polymer with 100% of the linkers having PEG-3400-folate attached, potentially signifying a correlation between increased number of folate per particle and increased uptake. However, the polymer concentration used was higher (1 g/L versus 0.1 g/L) for this polymer. For all three polymers, the uptake was similar in both FR- and FR+ cells and the uptake was the same in the absence and presence of folate, likely indicating non-specific uptake only. Interestingly, if we compare these results to the uptake results for the polymer without folate and with ether-ester-linked hydrocarbon side chains (#58) in Figure 4.22, we see that the uptake was again higher for the polymer with side chains and no folate than for polymer with 25% of the linkers having PEG-3400-folate attached and the remaining 75% of the linkers having the same ether-ester-linked hydrocarbon side chains (#61), confirming the lack of an advantage due to the attachment of the targeting ligand.

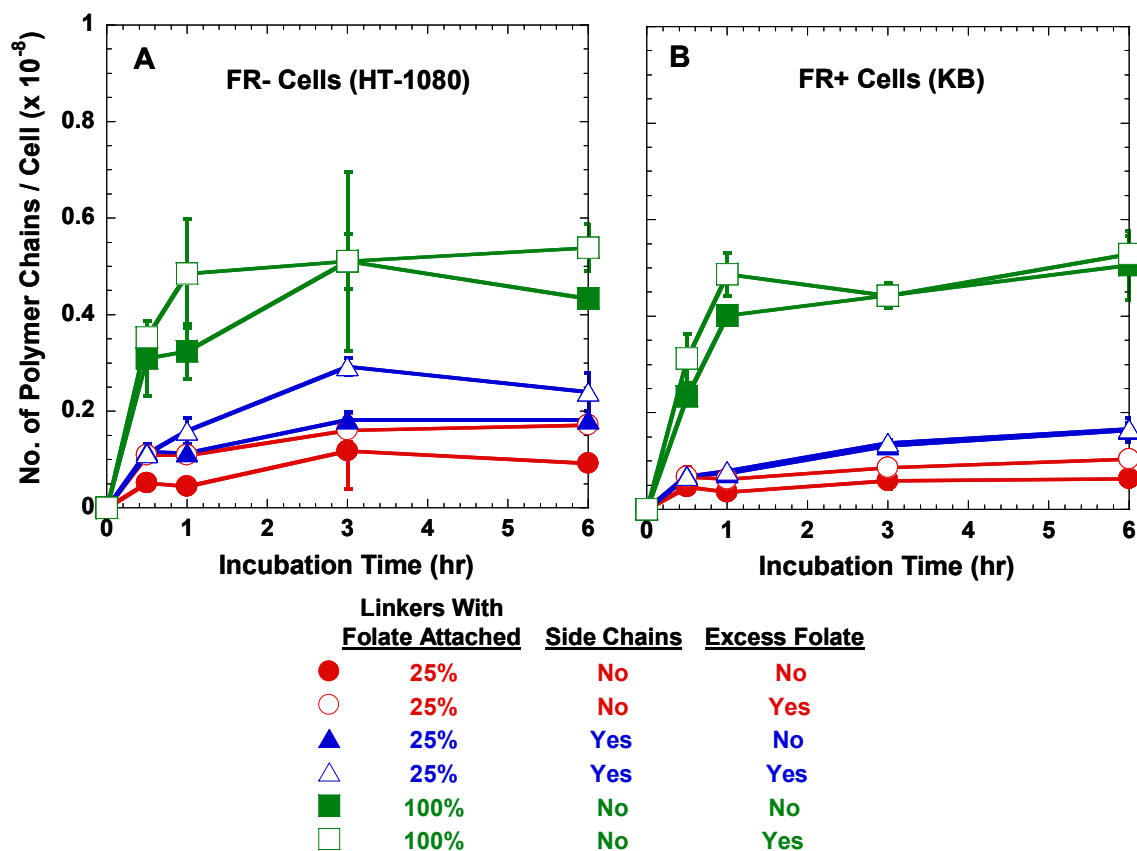


Figure 4.23. Cellular uptake of polymers with PEG-3400-folate attached: polymer with 25% of the linkers having PEG-3400-folate attached and the remaining 75% of the linkers having no side chains (#60) at 0.1 g/L, polymer with 25% of the linkers having PEG-3400-folate attached and the remaining 75% of the linkers having ether-ester-linked hydrocarbon side chains (#61) at 0.1 g/L, and polymer with 100% of the linkers having PEG-3400-folate attached (#64) at 1 g/L in FR- (HT-1080) and FR+ (KB) cells (n=3).

An indirect study of polymer binding was also pursued by analyzing the uptake of ^3H -folate in the presence of an excess of polymer. These competition studies have been used by others in the literature to demonstrate particle binding [58, 72, 74]. If the polymer decreases the uptake of the ^3H -folate, the polymer may be binding to the FR, blocking the ^3H -folate binding. The folate-containing polymers used in the direct studies above were used in this indirect study: polymer with 10% of the linkers having folate attached without a spacer and the remaining 90% of the linkers having no side chains (#50),

polymer with 10% of the linkers having folate attached without a spacer and the remaining 90% of the linkers having ether-linked hydrocarbon side chains (#51), polymer with PEG-3400-folate attached at the end of the polymer chain and no side chains (#56), polymer with PEG-3400-folate attached at the end of the polymer chain and ether-ester-linked hydrocarbon side chains (#59), polymer with 25% of the linkers having PEG-3400-folate attached and the remaining 75% of the linkers having no side chains (#60), polymer with 25% of the linkers having PEG-3400-folate attached and the remaining 75% of the linkers having ether-ester-linked hydrocarbon side chains (#61), and polymer with 100% of the linkers having PEG-3400-folate attached (#64). All polymers with hydrocarbon side chains are in the form of micelles at a concentration of 100 μM , but those polymers without hydrocarbon side chains are not. The results are depicted in Figure 4.24 as number of ^3H -folate per cell versus incubation time on a linear plot (left) and a semi-log plot (right). The two polymers with PEG-3400-folate attached at the end of the polymer chain only inhibited the uptake of ^3H -folate slightly, while all other folate-containing polymers tested inhibited the uptake by 1 or 2 orders of magnitude. Polymer with 100% of the linkers having PEG-3400-folate attached decreased the uptake by 380X. Intriguingly, the polymers with side chains inhibited the uptake less than those with no side chains. It is possible that the formation of micelles decreases the ability to block the binding of the ^3H -folate to the FR. These results suggest that binding of the targeted polymers to the FR may be occurring, thereby blocking the ^3H -folate from binding.

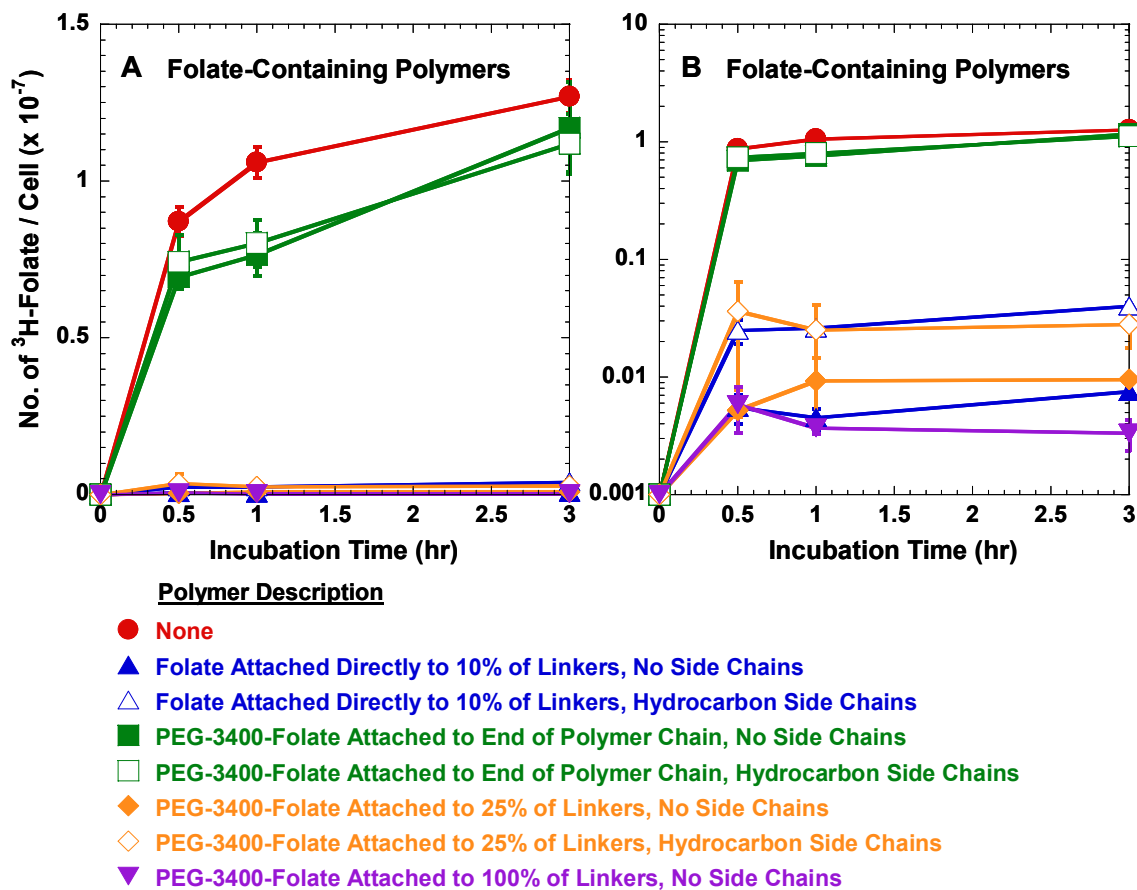


Figure 4.24. Competitive inhibition of the uptake of ^3H -folate at 50 nM by an excess of folate-containing polymers at 100 μM in FR+ (KB) cells: polymer with 10% of the linkers having folate attached without a spacer and the remaining 90% of the linkers having no side chains (#50), polymer with 10% of the linkers having folate attached without a spacer and the remaining 90% of the linkers having ether-linked hydrocarbon side chains (#51), polymer with PEG-3400-folate attached at the end of the polymer chain and no side chains (#56), polymer with PEG-3400-folate attached at the end of the polymer chain and ether-ester-linked hydrocarbon side chains (#59), polymer with 25% of the linkers having PEG-3400-folate attached and the remaining 75% of the linkers having no side chains (#60), polymer with 25% of the linkers having PEG-3400-folate attached and the remaining 75% of the linkers having ether-ester-linked hydrocarbon side chains (#61), and polymer with 100% of the linkers having PEG-3400-folate attached (#64) ($n=3$).

Several non-targeted polymers were used in the same indirect study to compare the inhibition of ^3H -folate to that of targeted polymers: polymer with no folate and no side chains (#24), polymer with methyl groups attached to the linkers (#66), polymer

with PEG-3400-COOH attached to the linkers (#67), and PEG-900. None of these polymers have hydrocarbon side chains, so none would be in the form of micelles. Polymer with methyl groups attached and polymer with PEG-3400-COOH attached did not significantly inhibit the uptake of ^3H -folate as shown in Figure 4.25. PEG-900 decreased the uptake by 2X and backbone polymer with no folate and no side chains decreased the uptake by 15X. This inhibition may be due to possible hydrogen bonding of the polymer and folate or the polymer and FR. However, it seems that the same effect would be observed for all polymers, but it was not.

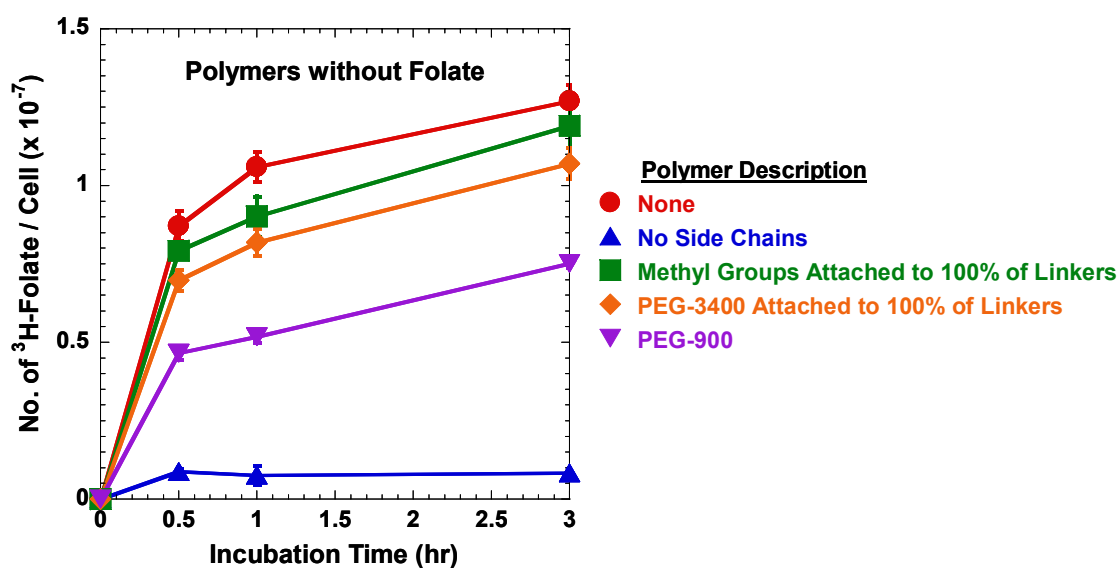


Figure 4.25. Competitive inhibition of the uptake of ^3H -folate at 50 nM by an excess of polymers without folate at 100 μM in FR+ (KB) cells: polymer with no folate and no side chains (#24), polymer with methyl groups attached to the linkers (#66), polymer with PEG-3400-COOH attached to the linkers (#67), and PEG-900 (n=3).

Given that the iodinated polymers did not demonstrate selectivity, but the ^3H -folate uptake studies indicated inhibition of ^3H -folate uptake by the folate-targeted polymers, it was hypothesized that the iodination procedure was negatively impacting the

ability of the targeting polymer to target the appropriate cells. In order to investigate this, polymer was labeled with ^3H . The uptake results for polymer with 98% of the linkers having PEG-3400-folate attached and the remaining 2% of the linkers having methyl groups containing ^3H attached (#71) at three polymer concentrations (50 nM, 500 nM and 5 μM) in the presence and absence of an excess (100 μM) of unlabeled folate are shown in Figure 4.26 plotted on linear plots (top) as well as semi-log plots (bottom). This polymer does not contain hydrocarbon side chains, therefore it is not in the form of micelles. In the FR+ cell line, at each concentration, the uptake is the same in the presence and absence of an excess of unlabeled folate. This indicates that either there is only non-specific uptake since the uptake can not be decreased by competing with unlabeled folate or the specific uptake is insignificant compared to the non-specific uptake. In addition, there is a linear increase in uptake over time at each polymer concentration in both cell lines, and uptake increases with increasing polymer concentration. Finally, the uptake in the FR- cell line is lower than that in the FR+ cell line, which could potentially be construed as demonstrating specificity, but since the presence of an excess of ligand does not alter the amount of uptake, we must conclude that the non-specific uptake is different between these two cell lines. The uptake of ^3H -folate observed in Figure 4.24 and Figure 4.25 ($\sim 10^7$ molecules per cell at 3 hours) was achieved when the cells were incubated in a 50 nM solution of ^3H -folate. From Figure 4.26 we see that the uptake of tritiated polymer at a concentration of 50 nM solution is $\sim 10^6$ polymer chains per cell. Therefore, the ^3H -folate uptake is an order of magnitude higher than that of tritiated polymer at the same concentration. It is likely that this higher uptake of ^3H -folate is due to receptor-mediated endocytosis.

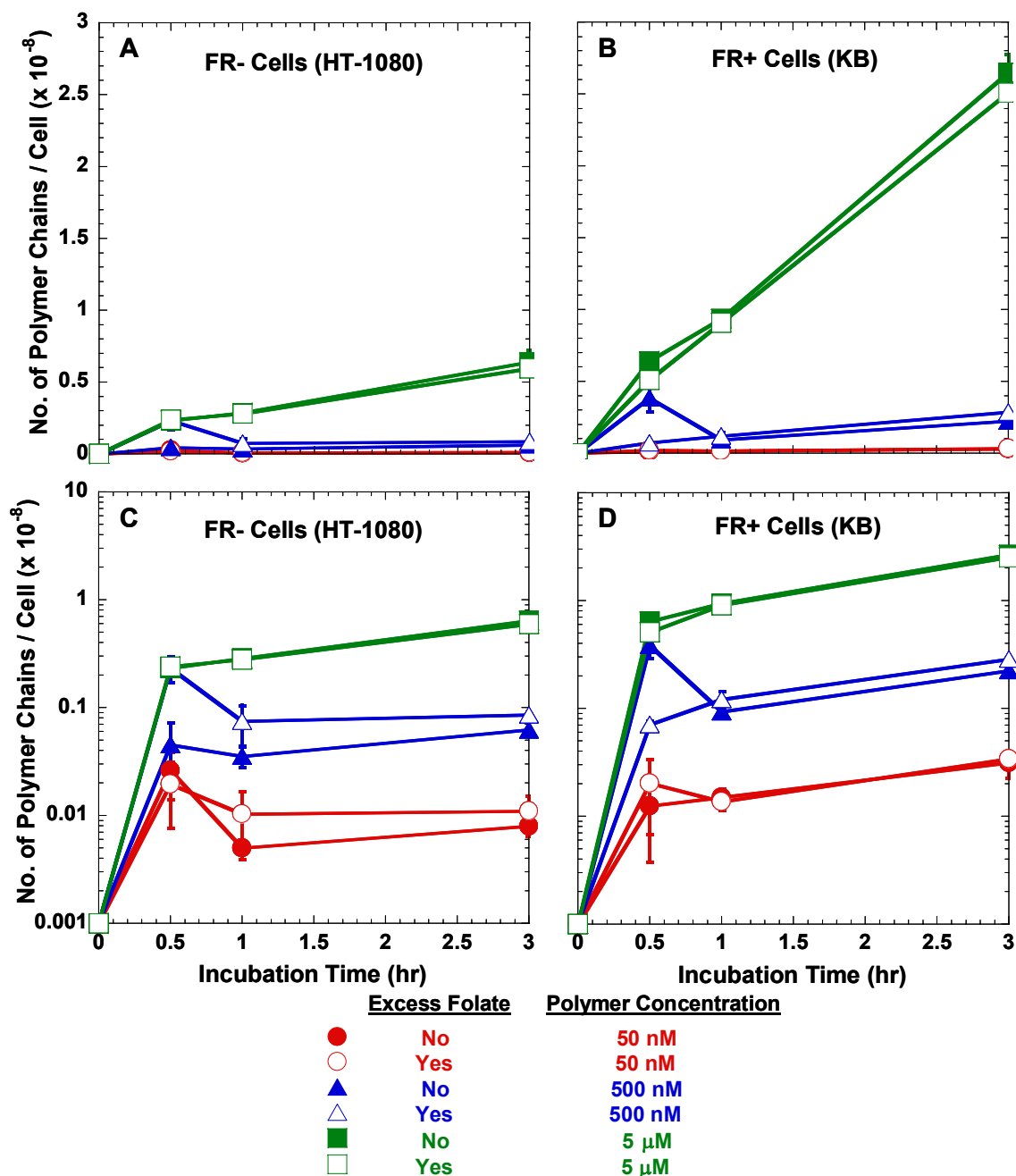


Figure 4.26. Cellular uptake of tritiated folate-containing polymer with 98% of the linkers having PEG-3400-folate attached and the remaining 2% of the linkers having methyl groups containing ^3H attached (#71) at various concentrations in FR- (HT-1080) and FR+ (KB) cells as a function of time ($n=3$).

4.3.5. In-depth analysis of polymer cell-association

In order to determine why our folate-targeted polymers were not behaving as other polymer systems reported in the literature, the amount of cell-associated folate-containing polymer was assessed under various conditions affecting the expression of the FR, as shown in Figure 4.27 for three concentrations of polymer (50 nM, 500 nM, and 5 μ M). First, the uptake of the tritiated folate-containing polymer was observed in cells that had been grown under three conditions which varied the regulation of the FR. The cellular uptake of polymer was examined in cells that had been grown for two days before the experiment in folate-free media to up-regulate the FR, cells that were continuously grown in regular folate-containing media, and cells that had been grown for two days in folate-free media and then incubated with 100 μ M unlabeled free folate for 3 hours immediately before the start of the experiment to saturate and down-regulate the FR. As shown in Figure 4.27, the uptake of tritiated folate-containing polymer was equivalent in all three cases at each polymer concentration and therefore independent of the up-regulation or down-regulation of the FR.

In addition, polymer uptake in the presence of an excess (100 μ M) of unlabeled folate, polymer that was internalized, and non-specific polymer uptake after cells were treated with PI-PLC were all approximately the same as the uptake when the FR was up-regulated or down-regulated. For experiments run at polymer concentrations of 500 nM and 5 μ M, this is easily concluded from Figure 4.27. When the polymer concentration was 50 nM, the trends were the same, but there was more divergence of the data. Small errors in solution makeup could impact this lowest concentration more than the higher concentrations, which may explain this divergence. At all polymer concentrations, the

surface bound polymer, that which was cell-associated when incubated at 4°C, was much lower than the cell-associated polymer under all other conditions. It is likely that the surface bound polymer is the polymer that is bound to the FR. For a polymer concentration of 5 μM, surface bound polymer was ~20X lower than the total uptake in folate-free media. For 500 nM, the surface bound polymer was ~10X lower than the total uptake and for 50 nM, the surface bound polymer was ~4X lower. When the cells were pre-treated with PI-PLC to cleave the GPI-anchor attaching the FR to the cell surface and then incubated at 4°C, the surface bound polymer decreased for all polymer concentrations, confirming that a low level of polymer binds to the FR and that the amount of polymer bound to the FR is masked because it is overwhelmed by the much larger non-specific uptake of the polymer. It is important to note that the non-specific uptake of this polymer in these cells is not unusually high, but rather high when compared to the specific uptake. When compared to non-specific uptake of polymers containing EPPT in uMUC1- and uMUC1+ cells at comparable concentrations, as described in Section 4.3.3, the non-specific uptake of polymer is similar.

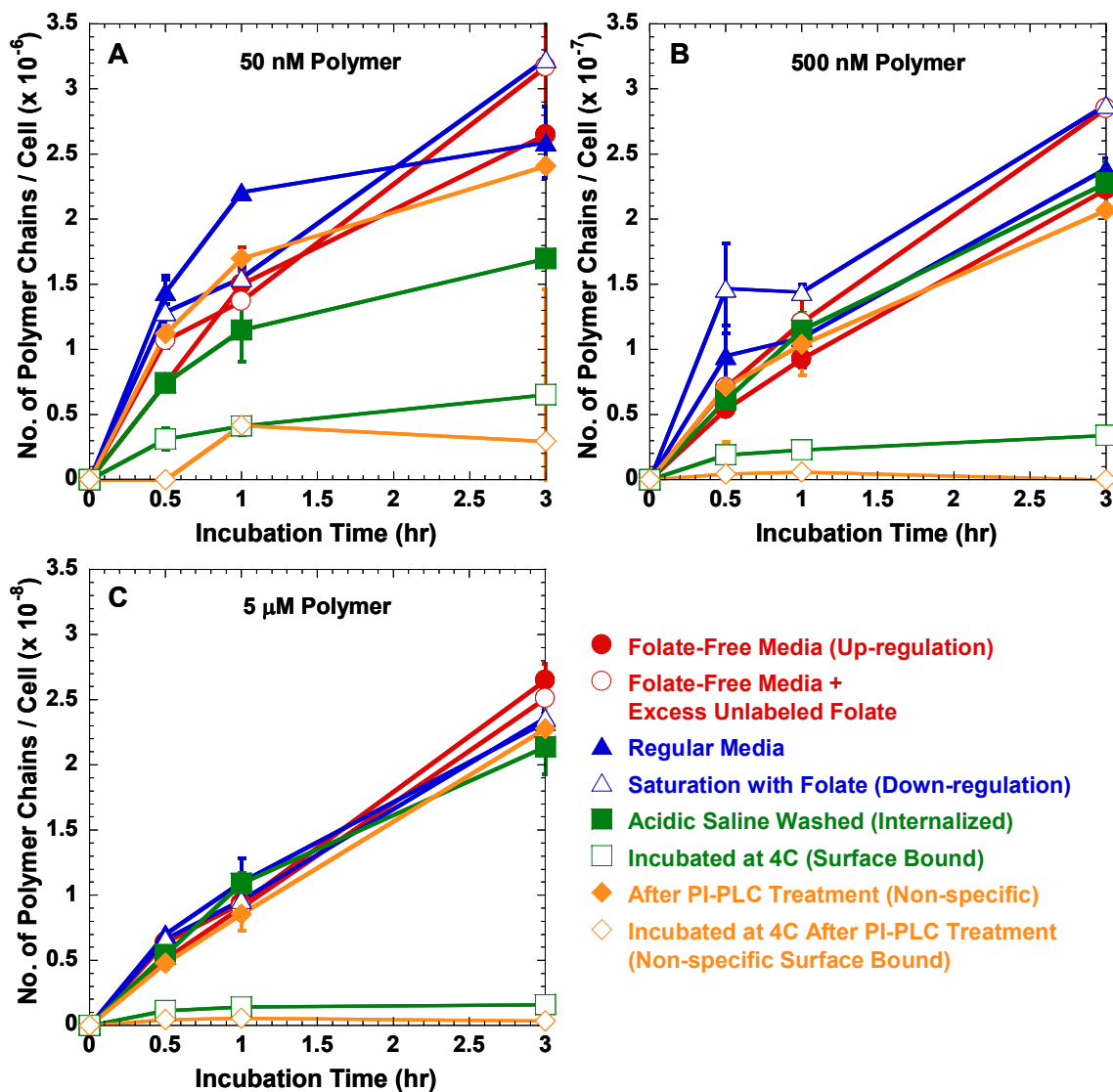


Figure 4.27. Cellular uptake of tritiated folate-containing polymer with 98% of the linkers having PEG-3400-folate attached and the remaining 2% of the linkers having methyl groups containing ^3H attached (#71) at various concentrations (50 nM, 500 nM, and 5 μM) in FR+ (KB) cells under conditions affecting the regulation of the FR ($n=3$).

To facilitate a deeper understanding of the cellular association of the polymer as compared to free folate, it is worthwhile to graph the data in Figure 4.19 and Figure 4.27 by experimental condition. All data for cells grown in folate-free media and incubated with ^3H -folate or folate-containing polymer are shown as a function of incubation time in

Figure 4.28. The graph on the right is an expanded version of the graph on the left. In folate-free media, the uptake of polymer at a concentration of 50 nM was ~4X lower than the uptake of folate at the same concentration, the uptake of polymer at a concentration of 500 nM was about the same as that for folate at the same concentration, and the uptake of polymer at a concentration of 5 μ M was ~10X higher than the uptake of folate at the same concentration. All data for cells grown in folate-free media and incubated at 4°C with 3 H-folate or folate-containing polymer, which limits uptake to surface bound material, are shown as a function of incubation time in Figure 4.29. For a polymer concentration of 50 nM, the surface bound polymer was ~4X lower than that for folate at the same concentration, similar to the results for total uptake in folate-free media. The shape of the curves for 50 nM, 500 nM, and 5 μ M folate-containing polymer indicates saturation of the FR, again indicating that the polymer is bound to the FR at these low levels.

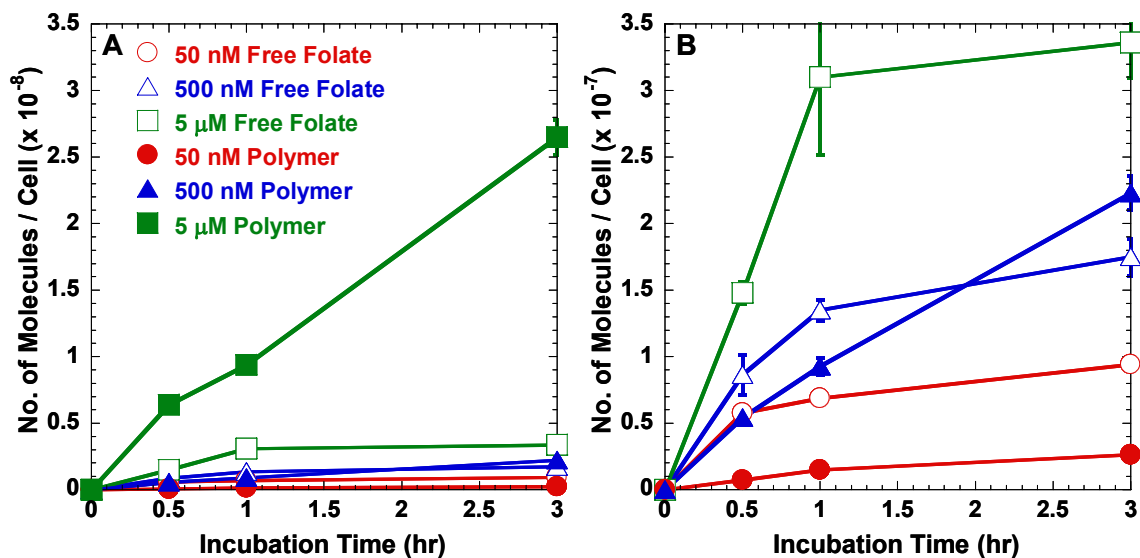


Figure 4.28. Comparison of cellular uptake of ^3H -folate or polymer with 98% of the linkers having PEG-3400-folate attached and the remaining 2% of the linkers having methyl groups containing ^3H attached (#71) in folate-free media in FR+ (KB) cells as a function of time (Left axis = 10^8 , Right axis = 10^7) ($n=3$).

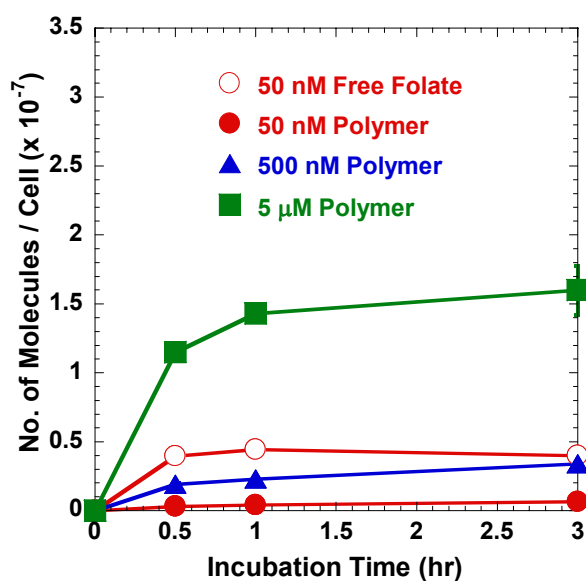


Figure 4.29. Comparison of surface bound ^3H -folate or polymer with 98% of the linkers having PEG-3400-folate attached and the remaining 2% of the linkers having methyl groups containing ^3H attached (#71) in FR+ (KB) cells as a function of time ($n=3$).

The data in Figure 4.28 and Figure 4.29 can also be graphed as a function of concentration. All data for cells grown in folate-free media and incubated with ^3H -folate or folate-containing polymer are shown as a function of concentration in Figure 4.30. Again, the graph on the right is an expanded version of the graph on the left. The uptake of ^3H -folate in folate-free media saturates the FR at all time points, as observed by the curve of the lines with increased concentration. The uptake of folate-containing polymer in folate-free media is linear with concentration, implying non-specific behavior. All data for cells grown in folate-free media and incubated at 4°C with folate-containing polymer, giving the surface bound material, are shown as a function of concentration in Figure 4.31. The surface bound folate-containing polymer is not quite linear with concentration. Perhaps the surface bound polymer starts to saturate the FR at these concentrations, but polymer does not saturate the FR to the extent of free folate.

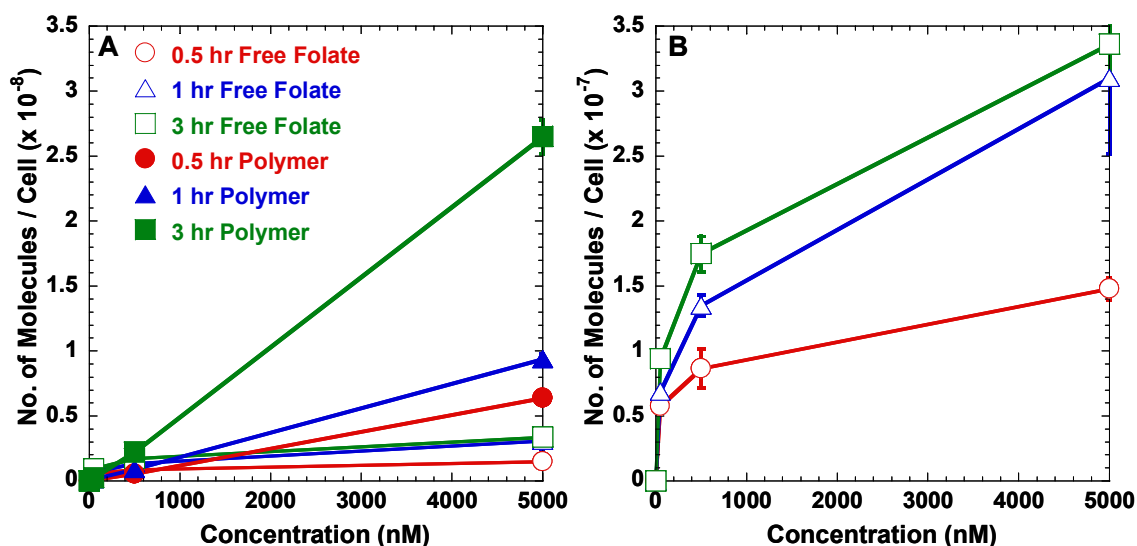


Figure 4.30. Comparison of uptake of ^3H -folate or polymer with 98% of the linkers having PEG-3400-folate attached and the remaining 2% of the linkers having methyl groups containing ^3H attached (#71) in folate-free media in FR+ (KB) cells as a function of concentration (Left axis = 10^8 , Right axis = 10^7) (n=3).

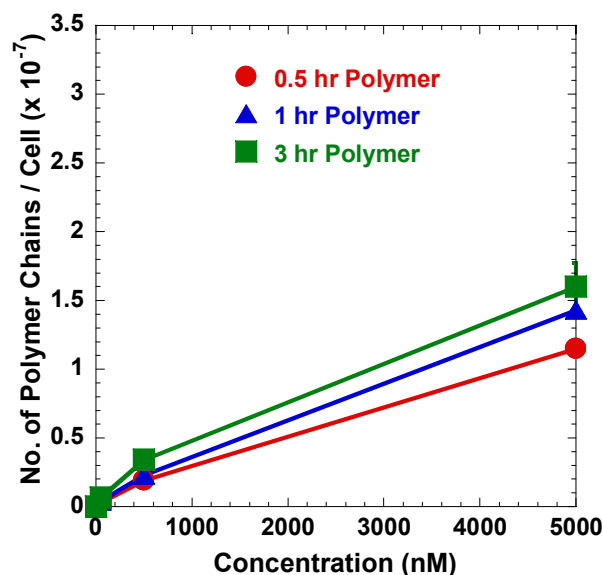


Figure 4.31. Comparison of surface bound ^3H -folate or polymer with 98% of the linkers having PEG-3400-folate attached and the remaining 2% of the linkers having methyl groups containing ^3H attached (#71) in FR+ (KB) cells as a function of concentration ($n=3$).

This cell-association data can also be normalized by the bulk concentration of ^3H -folate or folate-containing polymer (C_{bulk}). The normalized cellular uptake of ^3H -folate and folate-containing polymer is shown in Figure 4.32, again with the graph on the right being an expanded version of the graph on the left. When normalized, the highest uptake of ^3H -folate occurs with the lowest folate concentration. This trend agrees with the point discussed above that the FR is likely saturating with increased concentration. When the uptake of folate-containing polymer is normalized by bulk solution concentration, the results for all three concentrations align, indicative of non-specific behavior. The normalized surface bound ^3H -folate and folate-containing polymer is shown in Figure 4.33, with the expanded graph on the right. The highest normalized surface bound folate-containing polymer occurs with the lowest bulk solution concentration. This behavior is

similar to the behavior of normalized ^3H -folate uptake in folate-free media, again indicating the surface bound polymer is likely bound to the FR. The normalized non-specific uptake of ^3H -folate and folate-containing polymer is shown in Figure 4.34. All non-specific uptake for folate and folate-containing polymer become similar when normalized. This level of uptake is indicative of the non-specific uptake for this cell line.

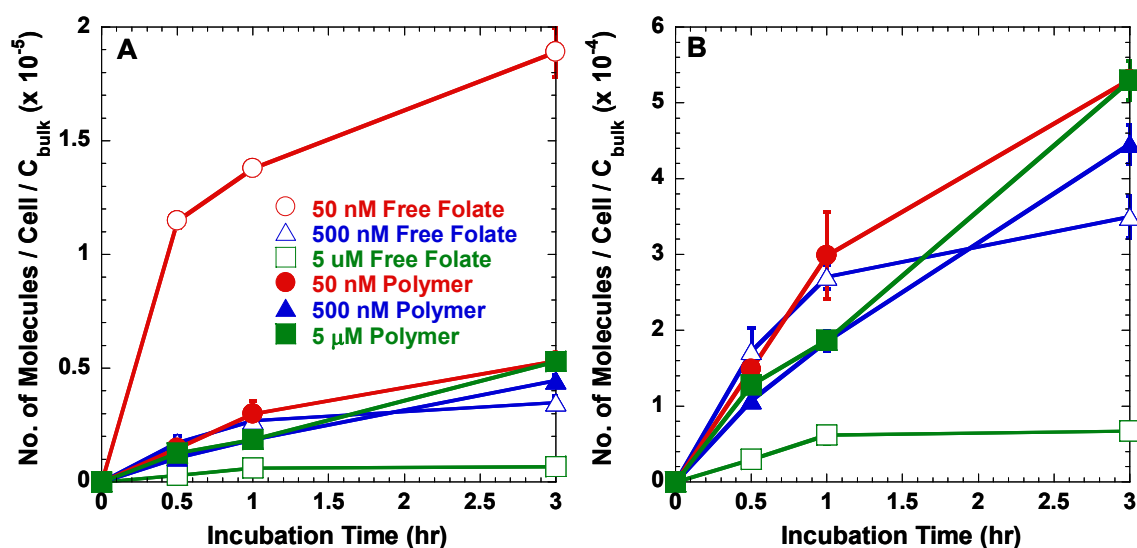


Figure 4.32. Comparison of normalized cellular uptake of ^3H -folate or polymer with 98% of the linkers having PEG-3400-folate attached and the remaining 2% of the linkers having methyl groups containing ^3H attached (#71) in folate-free media in FR+ (KB) cells as a function of time (Left axis = 10^5 , Right axis = 10^4) ($n=3$).

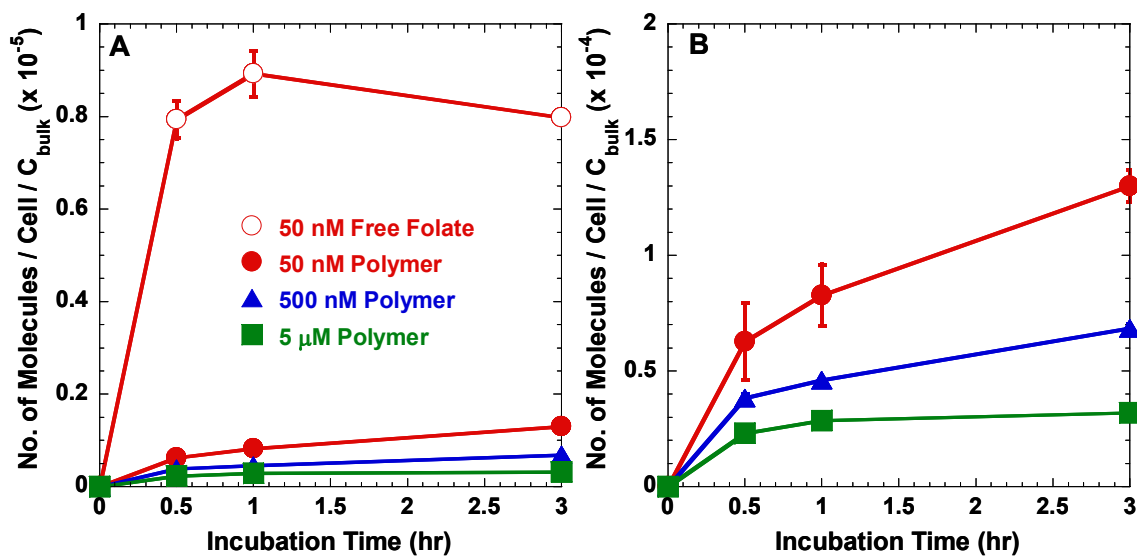


Figure 4.33. Comparison of normalized surface bound ^3H -folate or polymer with 98% of the linkers having PEG-3400-folate attached and the remaining 2% of the linkers having methyl groups containing ^3H attached (#71) in FR+ (KB) cells as a function of time (Left axis = 10^5 , Right axis = 10^4) ($n=3$).

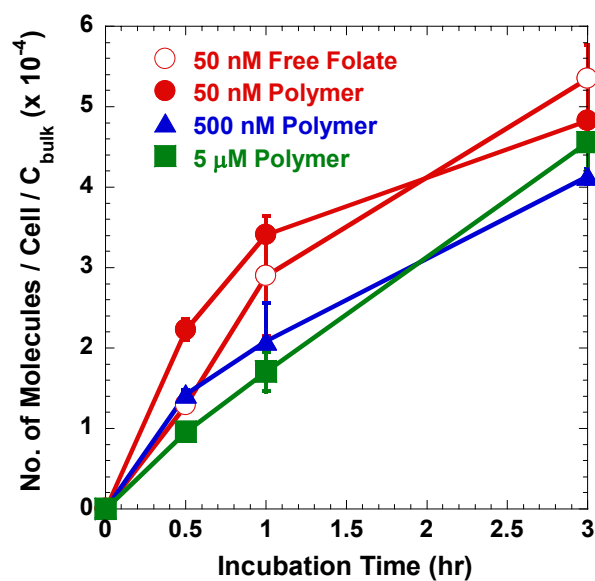


Figure 4.34. Comparison of normalized non-specific cellular uptake of ^3H -folate or polymer with 98% of the linkers having PEG-3400-folate attached and the remaining 2% of the linkers having methyl groups containing ^3H attached (#71) in FR+ (KB) cells as a function of time ($n=3$).

Figure 4.35 shows the normalized cell-associated ^3H -folate and folate containing polymer as a function of concentration. The results for uptake in folate free media are shown in A and the results for surface bound polymer are shown in B. Again, it appears that the FR is saturated with ^3H -folate as the bulk solution concentration is increased, since the uptake in folate-free media drops sharply and then levels out when normalized. In contrast, the normalized uptake of folate-containing polymer in folate-free media is nearly independent of concentration at all three time points. However, the normalized surface bound polymer shows similar behavior to normalized folate uptake in folate-free media with apparent saturation of the FR with increased concentration. This alternative analysis of the cell-association data affirms the inference that the polymer does bind to the FR at levels much lower than the non-specific uptake.

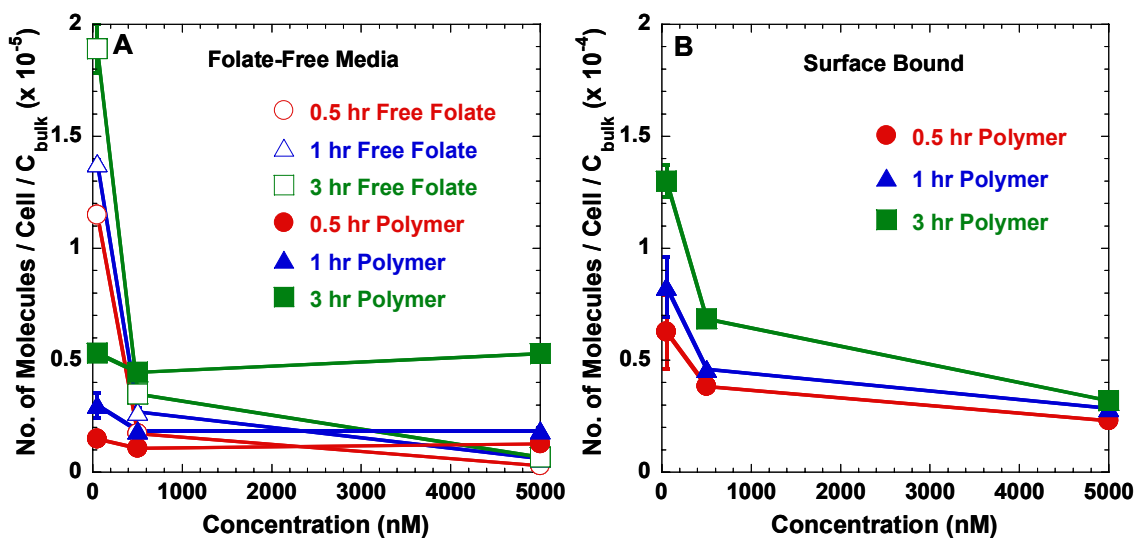


Figure 4.35. Comparison of normalized cellular uptake in folate-free media and surface bound ^3H -folate or polymer with 98% of the linkers having PEG-3400-folate attached and the remaining 2% of the linkers having methyl groups containing ^3H attached (#71) in FR+ (KB) cells as a function of concentration (n=3).

In summary, it is clear that polymer is taken up non-specifically in high amounts, as compared to specific uptake. An excess of unlabeled folate did not measurably decrease the uptake of polymer in folate-free media, even though it was able to decrease the uptake of labeled folate by competitive inhibition. Up- or down-regulation of the FR had no measurable effect on polymer uptake, but did affect folate uptake. Also, cleaving the FR with PI-PLC did not measurably affect polymer uptake, but did decrease folate uptake. When normalized, all non-specific uptake for folate and folate-containing polymer align, indicating the level of non-specific uptake for this cell line. It is also apparent that a low level of polymer does bind to the FR. For each polymer concentration, the amount of surface bound polymer is much lower than the total uptake of polymer in folate-free media. The curves for this surface bound polymer indicate saturation and binding to the FR. Finally, the amount of surface bound folate and polymer is decreased when treated with PI-PLC to remove FR, confirming the attachment to the FR.

4.3.6. Size measurement of polymer and free folate in folate-free media by DLS

A possible explanation for the inability to demonstrate selectivity with the folate targeted polymers could be that some of the attached folate molecules may not be available for binding, a phenomenon previously discussed in the literature [75]. Baker et al. used molecular dynamics simulations of folate-targeted dendrimers to show that local branch aggregation was observed, depending on capping of the surface amines, and folates were internalized, suggesting a decreased potential for receptor interaction. Since several of our polymers used in the uptake studies can not form micelles of the type envisioned in Figure 2.4 due to a lack of hydrophobic side chains, it may be likely that

the polymers are forming aggregates resulting from folate-folate and/or PEG-PEG interactions, possibly in the form of structured micelles, leaving most of the attached folate unavailable to bind to the FR. The self assembly of free folate in water has been investigated in the literature [76-79]. It was reported that folate forms tetrameric columns held together by hydrogen bonds in water. These results may be extended to the case of polymer bound folate.

To investigate the formation of polymer aggregates in solution, light scattering measurements were made to determine the size of particles in folate-free media for polymer with 100% of the linkers having PEG-3400-folate attached (#64), polymer with PEG-3400-COOH attached to the linkers (#67), polymer with 25% of the linkers having PEG-3400-folate attached and the remaining 75% of the linkers having ether-ester-linked hydrocarbon side chains (#61), and polymer with no folate and no side chains (#24). Polymer or free folate was dissolved in folate free media without serum. The results for the intensity averaged diameters are reported in Table 4.1. Included with the results are the date on which the solution was made and the date on which the measurement was made in order to assess any time-dependent behavior.

When measured the same day the 100 μM solution was made, polymer with 100% of the linkers having PEG-3400-folate attached (#64) formed aggregates that were 183 nm in size. However, 2 days after solution makeup the aggregates measured 69.5 nm and 14 days after solution makeup the aggregates measured 142 nm. Single polymer chains in solution would be on the order of 10 nm in diameter. Therefore it seems that aggregates of multiple polymers chains are forming and the formation of these aggregates is a dynamic process in which the aggregates increase and decrease over time. The 100 μM

solution of polymer with 100% of the linkers having PEG-3400-folate attached (#64) was diluted to 5 μ M, 500 nM, and 50 nM 2 days after the original solution was made up. These solutions were then measured by DLS the same day they were diluted in order to determine if aggregate size decreased with concentration. The 5 μ M solution measured aggregates of 73.4 nm, similar in size to the 69.5 nm aggregates in the 100 μ M solution. However, the 500 nM and 50 nM solutions did not scatter enough light to obtain a measurement. After 14 days in solution, the 5 μ M, 500 nM, and 50 nM solutions all did not scatter enough light to obtain a measurement. It is clear that when polymer with 100% of the linkers having PEG-3400-folate attached was at a high enough concentration to scatter light, aggregates were observed.

Polymer with PEG-3400-COOH attached to the linkers (#67) measured 57.2 nm in size after 2 days in solution, which was surprising since this polymer did not contain folate. Polymer with 25% of the linkers having PEG-3400-folate attached and the remaining 75% of the linkers having ether-ester-linked hydrocarbon side chains (#61) measured 120 nm the same day the solution was made. But neither scattered light after 2 weeks in solution. And polymer with no folate and no side chains (#24) did not scatter light in solution the day the solution was made or 2 weeks later.

It was thought that perhaps free folate in solution could also form aggregates and may influence the formation of aggregates of folate-containing polymer or increase the size of aggregates folate-containing polymer. Polymer with 100% of the linkers having PEG-3400-folate attached (#64) in solution at a concentration of 100 μ M with 50 nM free folate, representative of the concentrations in the competitive inhibition studies, formed aggregates 185 nm in size the same day the solution was made and 89.6 nm in size after 2

days in solution. These sizes are similar to those for polymer at the same concentration without free folate in solution, therefore it does not appear that the free folate greatly influences the formation or size of these aggregates. Finally, free folate in solution at 50 nM or 100 μ M did not scatter enough light to measure the size by DLS.

Table 4.1. Measurement of intensity averaged diameter of polymer with 100% of the linkers having PEG-3400-folate attached (#64), polymer with PEG-3400-COOH attached to the linkers (#67), polymer with 25% of the linkers having PEG-3400-folate attached and the remaining 75% of the linkers having ether-ester-linked hydrocarbon side chains (#61), polymer with no folate and no side chains (#24), and free folate in folate-free media with no serum by DLS (n=3).

Solution	Solution Makeup Date	Diameter (nm)		
		25-March-2009	27-March-2009	08-April-2009
100 μ M #64	25-March-2009	183 \pm 25	69.5 \pm 1.0	142 \pm 17
5 μ M #64	Diluted on 27-March-2009	-	73.4 \pm 23.0	Not Enough Scatter
500 nM #64	Diluted on 27-March-2009	-	Not Enough Scatter	Not Enough Scatter
50 nM #64	Diluted on 27-March-2009	-	Not Enough Scatter	Not Enough Scatter
100 μ M #67	25-March-2009	-	57.2 \pm 0.5	Not Enough Scatter
100 μ M #61	27-March-2009	-	120 \pm 2	Not Enough Scatter
100 μ M #24	27-March-2009	-	Not Enough Scatter	Not Enough Scatter
100 μ M #64 + 50 nM free folate	25-March-2009	185 \pm 11	89.6 \pm 10.3	-
50 nM free folate	25-March-2009	Not Enough Scatter	Not Enough Scatter	Not Enough Scatter
100 μ M free folate	25-March-2009	Not Enough Scatter	Not Enough Scatter	Not Enough Scatter

4.3.7. Comparison of theoretical calculations to experimental uptake results

It is clear from all of the experimental uptake data presented here, for polymer containing EPPT or folate, that we were not able to demonstrate the overwhelming selectivity that the polymers were designed to possess. As mentioned in Section 4.3.2 on the theoretical design of targeting polymers, certain assumptions were made when performing the design calculations. Likely these assumptions were not met; therefore the targeting was not demonstrated successfully. First, the assumption was made that neighboring ligands were not negatively cooperative, at least not to a large extent. However, it is possible that the ligands do negatively impact the binding of neighboring ligands, abrogating the polyvalent effect that we designed the polymers to contain. Second, it was assumed that all ligands were available for binding. This assumption likely fails, particularly for the folate system, given the DLS results showing aggregates in solution and the reports in the literature of aggregate formation of folate molecules. The failure of these assumptions likely resulted in the inability to demonstrate targeting.

4.3.8. Cellular uptake of free ^{125}I

As mentioned above, it was hypothesized that the iodination procedure was negatively impacting the ability of the targeting polymer to target the appropriate cells. One possibility was that free iodine remaining in the polymer solution, despite the separation procedure after the iodination reaction, was interfering with the uptake results. With the purpose of determining the impact of the free ^{125}I on the uptake experiments, *in vitro* experiments were performed to examine the cellular uptake of free ^{125}I . To simulate the separation process, a representative sample of free ^{125}I was passed through a

Sephadex column. The amount of free ^{125}I that passed through the column was measured by Kevin Brower. It was found that, in the worst separation case, there was $\sim 2,000,000$ CPM collected in the fractions in which polymer is typically collected. Therefore, uptake experiments were performed starting with solutions with activity levels in this range. The results of these experiments are shown in Figure 4.36. The uptake was observed to be 0.002-0.006 CPM per cell for all activities tested. In addition, in the presence of $100\ \mu\text{M}$ of backbone polymer with no ligand and no side chains (#24) the uptake of free iodine was equivalent to that in the absence of polymer, verifying that there is no carrier effect due to the polymer in solution. The results for the highest activity were also graphed as CPM per cell with the results for polymer with 100% of the linkers having ester-linked hydrocarbon side chains (#27) and polymer with 5% of the linkers having TEG-EPPT and the remaining 95% of the linkers having ester-linked hydrocarbon side chains (#37), shown in Figure 4.37. This comparison shows that the activity in each cellular sample due to any free iodine remaining the polymer solution is low, at most, 10% of the measured activity. Based on these results it is not likely that residual free iodine remaining in the polymer solution after the iodination and separation greatly impacts the results presented in this chapter.

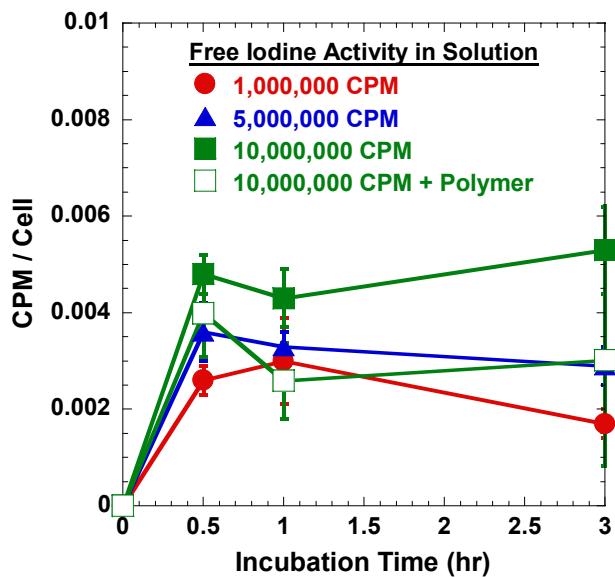


Figure 4.36. Cellular uptake of free iodine at levels mimicking residual free iodine remaining after polymer labeling in uMUC1+ (BT-20) cells (n=3).

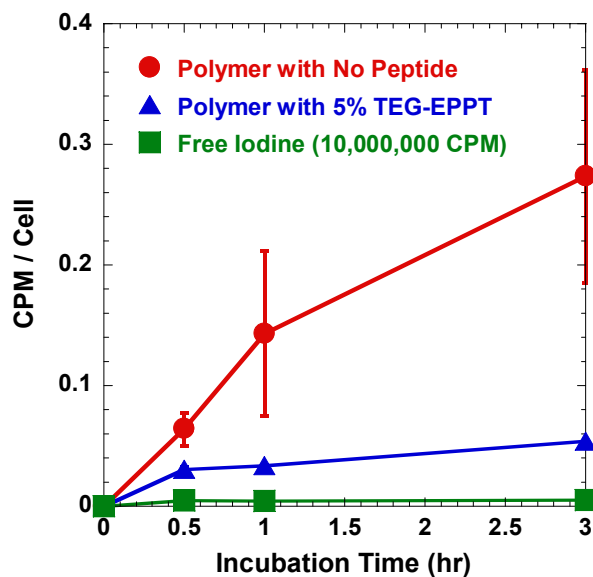


Figure 4.37. Cellular uptake of free iodine as compared to polymer with 100% of the linkers having ester-linked hydrocarbon side chains (#27) and polymer with 5% of the linkers having TEG-EPPT and the remaining 95% of the linkers having ester-linked hydrocarbon side chains (#37) in uMUC1+ (BT-20) cells (n=3).

4.4. Discussion

The alternating copolymers used in this study were taken up by cells *in vitro*. Microscopy images of the fluorescently labeled polymer alone demonstrated that the polymer was likely confined to vesicles within the cytoplasm and it was not found in the nucleus, but encapsulated doxorubicin was shown to be largely confined to the nucleus. These results verify the *in vitro* uptake of the polymers. However, the targeting abilities of these polymers were less clear.

Upon initial testing, the polymers used in this study appeared largely non-specific for the targeted cells when studied *in vitro*. The cellular uptake of polymer with 5% of the linkers having TEG-EPPT attached and the remaining 95% of the linkers having ester-linked hydrocarbon side chains was twice that of polymer with 100% of the linkers having ester-linked hydrocarbon side chains, although the difference was not statistically significant. In addition, increasing the percent of linkers containing the targeting ligand EPPT did not increase the uptake, especially without hydrocarbon side chains also on the polymer.

For polymers containing folate, regardless of the amount of folate attached, the length of the spacer used, or the type of radioactive label used, the uptake did not decrease in the presence of an excess of folate, indicating a high amount of non-specific uptake for all folate-containing polymers. However, when all of these folate-containing polymers were used to competitively inhibit ^3H -folate, the two polymers with PEG-3400-folate attached at the end of the polymer chain only inhibited the uptake of ^3H -folate slightly, but all other folate-containing polymers tested inhibited the uptake by 1 or 2 orders of magnitude, suggesting that the targeted polymers bind to the FR. Only one

polymer not containing folate was able to inhibit the uptake of ^3H -folate slightly, indicating that polymers with folate attached had an advantage to inhibiting free folate uptake.

The uptake results for polymer with 98% of the linkers having PEG-3400-folate attached and the remaining 2% of the linkers having methyl groups containing ^3H attached have shown that, at all three concentrations tested, the uptake was the same in the presence and absence of an excess of unlabeled folate. This agreed with the results for all other folate-containing polymers and indicated that either there was only non-specific uptake, since the uptake can not be decreased by competing with unlabeled folate, or the specific uptake was insignificant compared to the non-specific uptake.

Some papers in the literature state that coating particles in PEG can increase the cellular uptake of the particles without any targeting [80-82], however there are also several papers that say that attaching PEG inhibits cellular uptake [83-86]. Given the lack of agreement in the literature, it is unclear what effect PEG is having on the uptake of our polymer. The particles in the literature were all 40 nm to 700 nm in size. Additionally, there is an indication in the literature, in general, that non-specific uptake increases with decreased particle size for the range from 40-350 nm [87]. The largely non-specific uptake demonstrated with our polymers may be supported by the literature.

A more in-depth study of the cell-association of these polymers clarified that polymer was taken up non-specifically in high amounts. An excess of unlabeled folate, up- or down-regulation of the FR, and cleaving the FR did not measurably affect polymer uptake, but did alter folate uptake. All non-specific uptake for folate and folate-containing polymer align when normalized, indicating the level of non-specific uptake for

this cell line. Furthermore, it was also determined that a low level of polymer does bind to the FR. The amount of surface bound polymer was much lower than the total uptake of polymer in folate-free media for each polymer concentration investigated. In addition, the amount of surface bound folate and polymer decreased when the FR was cleaved, confirming the attachment of polymer to the FR.

Light scattering measurements showed that polymers that contain folate form aggregates of multiple polymers chains and the formation of these aggregates is a dynamic process in which the aggregates increase and decrease over time. Surprisingly, one polymer that did not contain folate did form aggregates. When polymer with folate attached was in solution with free folate, aggregates formed and were of similar size to polymer without free folate in solution, indicating that the free folate does not greatly influence the formation or size of these aggregates. Also, at concentrations representative of the uptake experiments, free folate in solution did not scatter enough light to measure the size by DLS. These results confirmed that polymer aggregation was occurring and this aggregation was likely causing at least a portion of the folate ligands to be hidden in the aggregate and unavailable for binding to the FR.

The aggregation of polymers is the most likely mechanistic cause of the failure of the folate-containing polymers to demonstrate targeting. Since many of the attached folate molecules were potentially inside of the aggregates, they were not available for binding thereby decreasing the effective concentration of folate. This would result in lower specific binding of polymer to the FR, as evidenced by the fact that the amount of surface bound polymer was lower than expected based on surface bound folate amounts. Future designs for targeting polymers should account for the lessons learned in the

studies discussed here. Namely, ligands should be chosen that have no likelihood of aggregating in solution such that all ligands are available for binding. In addition, aggregation concerns should be decreased by incorporating fewer ligands into the structure. In order to decrease the necessary number of ligands in the polymer, targeting ligands should be chosen that have extremely high affinity for their targets such that polyvalency is not required. The versatility of these polymer constructs allows for continued optimization of a targeting delivery system for drugs and imaging agents as lessons discovered from passed studies are incorporated into the design.

While these polymers did not have the selective advantage that was anticipated due to the high level of non-specific uptake and the low level of specific binding, it is clear that the polymers are taken up by cancerous cells *in vitro*. The alternating copolymers used in this study could be redesigned to contain an external charge in the corona to attempt to decrease the non-specific uptake such that the selective advantage could be discerned or new targeting ligands can be chosen to minimize the issues observed in this study. It was reported in Chapter 3 that the alternating copolymers studied here have had some success as drug delivery vehicles *in vitro*. Therefore, these polymers should be further tested as delivery platforms *in vitro* and in mouse models of human cancer to determine the *in vivo* delivery capabilities. The initial pharmacokinetic studies of these polymers *in vivo* are discussed in Chapter 5, although the work is ongoing by others (ie. Kevin Brower in the Colton group).

4.5. References

1. Langer, R., Drug delivery and targeting. *Nature*, 1998. 392(6679): p. 5-10.
2. Ferrari, M., Cancer nanotechnology: Opportunities and challenges. *Nature Reviews Cancer*, 2005. 5(3): p. 161-171.
3. Zhang, L., F.X. Gu, J.M. Chan, A.Z. Wang, R.S. Langer, and O.C. Farokhzad, Nanoparticles in medicine: Therapeutic applications and developments. *Clinical Pharmacology & Therapeutics*, 2008. 83(5): p. 761-769.
4. Torchilin, V.P., Recent advances with liposomes as pharmaceutical carriers. *Nature Reviews*, 2005. 4: p. 145-160.
5. Duncan, R., Polymer conjugates as anticancer nanomedicines. *Nature Reviews Cancer*, 2006. 6(9): p. 688-701.
6. Wagner, D., W.V. Kern, and P. Kern, Liposomal doxorubicin in aids-related kaposi-sarcoma - long-term experiences. *Clinical Investigator*, 1994. 72(6): p. 417-423.
7. Lee, K.S., H.C. Chung, S.A. Im, Y.H. Park, C.S. Kim, S.B. Kim, S.Y. Rha, M.Y. Lee, and J. Ro, Multicenter phase ii trial of genexol-pm, a cremophor-free, polymeric micelle formulation of paclitaxel, in patients with metastatic breast cancer. *Breast Cancer Research and Treatment*, 2008. 108(2): p. 241-250.
8. Matsumura, Y., Polymeric micellar delivery systems in oncology. *Jpn J Clin Oncol*, 2008. 38(12): p. 793-802.
9. Torchilin, V.P., Structure and design of polymeric surfactant-based drug delivery systems. *J Controlled Release*, 2001. 73: p. 137-172.
10. Allen, C., D. Maysinger, and A. Eisenberg, Nano-engineering block copolymer aggregates for drug delivery. *Colloids and Surfaces B: Biointerfaces*, 1999. 16: p. 3-27.
11. Kataoka, K., Harada, A., Nagasaki, Y., Block copolymer micelles for drug delivery: Design, characterization and biological significance. *Adv Drug Delivery Rev*, 2001. 47: p. 113-131.
12. Torchilin, V.P., Peg-based micelles as carriers of contrast agents for different imaging modalities. *Advanced Drug Delivery Reviews*, 2002. 54: p. 235-252.

13. Lavasanifar, A., J. Samuel, and G.S. Kwon, Poly(ethylene oxide)-*block*-poly(l-amino acid) micelles for drug delivery. *Advanced Drug Delivery Reviews*, 2002. 54: p. 169-190.
14. Savic, R., Luo, L., Eisenberg, A., Maysinger, D., Micellar nanocontainers distribute to defined cytoplasmic organelles. *Science*, 2003. 300: p. 615-618.
15. Mo, Y., Lim, L-Y., Paclitaxel-loaded plga nanoparticles: Potentiation of anticancer activity by surface conjugation with wheat germ agglutinin. *J Controlled Release*, 2005. 108: p. 244-262.
16. Bronich, T.K., Keifer, P. A., Shlyakhtenko, L. S., Kabanov, A. V., Polymer micelle with cross-linked ionic core. *JACS*, 2005. 127: p. 8236-8237.
17. Murthy, K.S., Ma, Q., Clark, Jr., C. G., Remsen, E. E., Wooley, K., L., Fundamental design aspects of amphiphilic shell-crosslinked nanoparticles for controlled release applications. *Chem Commun*, 2001: p. 773-774.
18. Kakizawa, Y., Harada, A., Kataoka, K., Glutathione-sensitive stabilization of block copolymer micelles composed of antisense DNA and thiolated poly(ethylene glycol)-*block*-poly(l-lysine): A potential carrier for systemic delivery of antisense DNA. *Biomacromolecules*, 2001. 2: p. 491-497.
19. Van Domeselaar, G.H., G.S. Kwon, L.C. Andrew, and D.S. Wishart, Application of solid phase peptide synthesis to engineering peo-peptide block copolymers for drug delivery. *Colloids and Surfaces B: Biointerfaces*, 2003. 30: p. 323-334.
20. Trubetskoy, V.S., Polymeric micelles as carriers of diagnostic agents. *Advanced Drug Delivery Reviews*, 1999. 37: p. 81-88.
21. Chan, J.M., L.F. Zhang, K.P. Yuet, G. Liao, J.W. Rhee, R. Langer, and O.C. Farokhzad, Plga-lecithin-peg core-shell nanoparticles for controlled drug delivery. *Biomaterials*, 2009. 30(8): p. 1627-1634.
22. Simone, E.A., T.D. Dziubla, and V.R. Muzykantov, Polymeric carriers: Role of geometry in drug delivery. *Expert Opinion on Drug Delivery*, 2008. 5(12): p. 1283-1300.
23. Xie, Z.G., T.C. Lu, X.S. Chen, Y.H. Zheng, and X.B. Jing, Synthesis, self-assembly in water, and cytotoxicity of mpeg-block-plla/dx conjugates. *Journal of Biomedical Materials Research Part A*, 2008. 88A(1): p. 238-245.
24. Hu, F.Q., P. Meng, Y.Q. Dai, Y.Z. Du, J. You, X.H. Wei, and H. Yuan, Pegylated chitosan-based polymer micelle as an intracellular delivery carrier for anti-tumor targeting therapy. *European Journal of Pharmaceutics and Biopharmaceutics*, 2008. 70(3): p. 749-757.

25. Moon, J.R., Y.H. Park, and J.H. Kim, Synthesis and characterization of novel thermo- and ph-responsive copolymers based on amphiphilic polyaspartamides. *Journal of Applied Polymer Science*, 2009. 111(2): p. 998-1004.
26. Cheng, J., J.X. Ding, Y.C. Wang, and J. Wang, Synthesis and characterization of star-shaped block copolymer of poly(epsilon-caprolactone) and poly(ethyl ethylene phosphate) as drug carrier. *Polymer*, 2008. 49(22): p. 4784-4790.
27. Sun, T.M., J.Z. Du, L.F. Yan, H.Q. Mao, and J. Wang, Self-assembled biodegradable micellar nanoparticles of amphiphilic and cationic block copolymer for sirna delivery. *Biomaterials*, 2008. 29(32): p. 4348-4355.
28. Thompson, C.J., C.X. Ding, X.Z. Qu, Z.Z. Yang, I.F. Uchegbu, L. Tetley, and W.P. Cheng, The effect of polymer architecture on the nano self-assemblies based on novel comb-shaped amphiphilic poly(allylamine). *Colloid and Polymer Science*, 2008. 286(13): p. 1511-1526.
29. Chen, W.Q., H. Wei, S.L. Li, J. Feng, J. Nie, X.Z. Zhang, and R.X. Zhuo, Fabrication of star-shaped, thermo-sensitive poly(n-isopropylacrylamide)-cholic acid-poly(epsilon-caprolactone) copolymers and their self-assembled micelles as drug carriers. *Polymer*, 2008. 49(18): p. 3965-3972.
30. Mahmud, A., X.B. Xiong, and A. Lavasanifar, Development of novel polymeric micellar drug conjugates and nano-containers with hydrolyzable core structure for doxorubicin delivery. *European Journal of Pharmaceutics and Biopharmaceutics*, 2008. 69(3): p. 923-934.
31. Wang, Y.C., L.Y. Tang, T.M. Sun, C.H. Li, M.H. Xiong, and J. Wang, Self-assembled micelles of biodegradable triblock copolymers based on poly(ethyl ethylene phosphate) and poly(epsilon-caprolactone) as drug carriers. *Biomacromolecules*, 2008. 9(1): p. 388-395.
32. Kim, B.S., S.W. Park, and P.T. Hammond, Hydrogen-bonding layer-by-layer assembled biodegradable polymeric micelles as drug delivery vehicles from surfaces. *Acs Nano*, 2008. 2(2): p. 386-392.
33. Matsumura, Y.a.M., H., A new concept for macromolecular therapeutics in cancer therapy: Mechanism of tumoritropic accumulation of proteins and the antitumor agents smancs. *Cancer Res.*, 1986. 46: p. 6387-6392.
34. Maeda, H.a.M., Y., Tumoritropic and lymphotropic principles of macromolecular drugs. *Crit. Rev. Ther. Drug Carrier Syst.*, 1989. 6: p. 193-210.
35. Maeda, H., Smancs and polymer-conjugated macromolecular drugs: Advantages in cancer chemotherapy. *Adv. Drug Delivery Rev.*, 1991. 6: p. 181-202.
36. Konno, T., Maeda, H., Iwai, K., Tashiro, S., Maki, S., Morinaga, T., Mochinaga, M., Hiraoka, T. and Yokoyama, I., Effect of arterial administration of high

- molecular weight anticancer agent smancs with lipid lymphographic agent on hepatoma: A preliminary report. *Eur. J. Cancer Clin. Oncol.*, 1983. 19: p. 1053–1065.
37. Iwai, K., Maeda, H. and Konno, T., Use of oily contrast medium for selective drug targeting to tumor: Enhanced therapeutic effect and x-ray image. *Cancer Research*, 1984. 44: p. 2115–2121.
 38. Konno, T., Maeda, H., Iwai, K., Maki, S., Tashiro, S., Uchida, M. and Miyauchi, Y., Selective targeting of anticancer drug and simultaneous image enhancement in solid tumors by arterially administered lipid contrast medium. *Cancer*, 1983. 54: p. 2367–2374.
 39. Iwai, K., Maeda, H., Konno, T., Matsumura, Y., Yamashita, R., Yamasaki, K., Hirayama, S. and Miyauchi, Y., Tumor targeting by arterial administration of lipids: Rabbit model with vx2 carcinoma in the liver. *Anticancer Res*, 1987. 7: p. 321–328.
 40. Seymour, L.W., Ulbrich, K., Steyger, P. S., Brereton, M., Subr, V., Strohaln, J. and Duncan, R., Tumour tropism and anticancer efficacy of polymer-based doxorubicin prodrugs in the treatment of subcutaneous murine b16 f10 melanoma. *Br. J. Cancer*, 1994. 70: p. 636–641.
 41. Sinn, H., Shrenk, H. H., Fredrich, E. A., Schilling, U. and Maier-Borst, W. A. A., Design of compounds having an increased tumour uptake: Using serum albumin as carrier. Part 1. *Nucl. Med. Biol.*, 1990. 17: p. 819–827.
 42. Wu, N.Z., Da, D., Rudoll, T. L., Needham, D., Whorton, A. R. and Dewhirst, M. W., Increased microvascular permeability contributes to preferential accumulation of stealth liposomes in tumor tissue. *Cancer Res.*, 1993. 53: p. 3765–3770.
 43. Yuan, F., Dellian, M., Fukumura, D., Leunig, M., Berk, D. A., Torchilin, V. P. and Jain, R. K., Vascular permeability in a human tumour xenograft: Molecular size dependence and cutoff size. *Cancer Res.*, 1995. 55: p. 3752–3756.
 44. Noguchi, Y., Wu, J., Duncan, R., Strohaln, J., Ulbrich, K., Akaike, T., Maeda, H., Early phase tumor accumulation of macromolecules: A great difference in clearance rate between tumor and normal tissues. *Jpn J Cancer Res*, 1998. 89: p. 307-314.
 45. Maeda, H., Wu, J., Sawa, T., Matsumura, Y., Hori, K., Tumor vascular permeability and the epr effect in macromolecular therapeutics: A review. *J Controlled Release*, 2000. 65: p. 271-284.
 46. Maeda, H., The enhanced permeability and retention (epr) effect in tumor vasculature: The key role of tumor-selective macromolecular drug targeting. *Adv Enzyme Regul*, 2001. 41: p. 189-207.

47. Hobbs, S.K., Monsky, W. L., Yuan, F., Roberts, W. G., Griffith, L., Torchilin, V. P., Jain, R. K., Regulation of transport pathways in tumor vessels: Role of tumor type and microenvironment. *PNAS*, 1998. 95: p. 4607-4612.
48. Dawson, J.Z., Physicochemical characterization of peg-based comb-like amphiphilic copolymer structures for possible imaging and therapeutic applications, in Department of Chemical Engineering. 2008, Massachusetts Institute of Technology: Cambridge, MA. p. 1-267.
49. Liang, H.-F., C.-T. Chen, S.-C. Chen, A.R. Kulkarni, Y.-L. Chiu, M.-C. Chen, and H.-W. Sung, Paclitaxel-loaded poly(g-glutamic acid)-poly(lactide) nanoparticles as a targeted drug delivery system for the treatment of liver cancer. *Biomaterials*, 2006. 27: p. 2051-2059.
50. You, J., X. Li, F. de Cui, Y.Z. Du, H. Yuan, and F.Q. Hu, Folate-conjugated polymer micelles for active targeting to cancer cells: Preparation, in vitro evaluation of targeting ability and cytotoxicity. *Nanotechnology*, 2008. 19(4).
51. Farokhzad, O.C., Cheng, J., Teply, B. A., Sherifi, I., Jon, S., Kantoff, P. W., Richie, J. P., Langer, R., Targeted nanoparticle-aptamer bioconjugates for cancer chemotherapy in vivo. *PNAS*, 2006. 103(16): p. 6315-6320.
52. Sivolapenko, G.B., V. Douli, D. Pectasides, D. Skarlos, G. Sirmalis, R. Hussain, J. Cook, N.S. Courtenay-Luck, E. Merkouri, K. Konstantinides, and A.A. Epenetos, . Breast cancer imaging with radiolabelled peptide from complementarity-determining region of antitumour antibody. *Lancet*, 1995. 346: p. 1662-1666.
53. Moore, A., Z. Medarova, A. Potthast, and G. Dai, In vivo targeting of underglycosylated muc-1 tumor antigen using a multimodal imaging probe. *Cancer Research*, 2004. 64: p. 1821-1827.
54. Leamon, C.P., Reddy, J. A., Folate-targeted chemotherapy. *Adv Drug Delivery Rev*, 2004. 56: p. 1127-1141.
55. Ke, C., Mathias, CJ, Green, MA, Folate-receptor-targeted radionuclide imaging agents. *Adv Drug Deliv Rev*, 2004. 56(8): p. 1143-60.
56. Hong, S., Leroueil, PR, Majoros, IJ, Orr, BG, Baker, JR Jr, Banaszak Holl, MM, The binding avidity of a nanoparticle-based multivalent targeted drug delivery platform. *Chem Biol*, 2007. 14(1): p. 107-15.
57. Saul, J., Annapragada, A, Natarajan, JV, Bellamkonda, RV, Controlled targeting of liposomal doxorubicin via the folate receptor in vitro. *J Control Release*, 2003. 92(1-2): p. 49-67.
58. Gabizon, A., Horowitz, AT, Goren, D, Tzemach, D, Mandelbaum-Shavit, F, Qazen, MM, Zalipsky, S, Targeting folate receptor with folate linked to

- extremities of poly(ethylene glycol)-grafted liposomes: In vitro studies. *Bioconjug Chem*, 1999. 10(2): p. 289-98.
59. Lee, E., Na, K, Bae, YH, Polymeric micelle for tumor ph and folate-mediated targeting. *J Control Release*, 2003. 91(1-2): p. 103-13.
60. Bae, Y., Jang, WD, Nishiyama, N, Fukushima, S, Kataoka, K, Multifunctional polymeric micelles with folate-mediated cancer cell targeting and ph-triggered drug releasing properties for active intracellular drug delivery. *Mol Biosyst*, 2005. 1(3): p. 242-50.
61. Yoo, H., Park, TG, Folate receptor targeted biodegradable polymeric doxorubicin micelles. *J Control Release*, 2004. 96(2): p. 273-83.
62. Yoo, H., Park, TG, Folate-receptor-targeted delivery of doxorubicin nano-aggregates stabilized by doxorubicin-peg-folate conjugate. *J Control Release*, 2004. 100(2): p. 247-56.
63. Paulos, C., Reddy, JA, Leamon, CP, Turk, MJ, Low, PS, Ligand binding and kinetics of folate receptor recycling in vivo: Impact on receptor-mediated drug delivery. *Mol Pharmacol*, 2004. 66(6): p. 1406-14.
64. Gargano, J.M., T. Ngo, J.Y. Kim, D.W.K. Acheson, and W.J. Lees, Multivalent inhibition of ab5 toxins. *J. Am. Chem. Soc.*, 2001. 123: p. 12909-12910.
65. Kamen, B.A., Capdevila, A., Receptor-mediated folate accumulation is regulated by the cellular folate content. *PNAS*, 1986. 83: p. 5983-5987.
66. Leamon, C., Low, PS, Folate-mediated targeting: From diagnostics to drug and gene delivery. *Drug Discov Today*, 2001. 6(1): p. 44-51.
67. Low, P., Henne, WA, Doorneweerd, DD, Discovery and development of folic-acid-based receptor targeting for imaging and therapy of cancer and inflammatory diseases. *Acc Chem Res*, 2007. 41(1): p. 120-9.
68. Varma, R. and S. Mayor, Gpi-anchored proteins are organized in submicron domains at the cell surface. *Nature*, 1998. 394: p. 798–801.
69. Lee, R.a.L., PS, Delivery of liposomes into cultured kb cells via folate receptor-mediated endocytosis. *J. Biol. Chem*, 1994. 269: p. 3198-3204.
70. Ghaghada, K., Saul, J, Natarajan, JV, Bellamkonda, RV, Annapragada, AV, Folate targeting of drug carriers: A mathematical model. *J Control Release*, 2005. 104(1): p. 113-28.
71. Jeppesen, C., J.Y. Wong, T.L. Kuhl, J.N. Israelachvili, N. Mullah, S. Zalipsky, and C.M. Marques, Impact of polymer tether length on multiple ligand–receptor bond formation. *Science*, 2001. 293: p. 465– 468.

72. Moon, W., Lin, Y, O'Loughlin, T, Tang, Y, Kim, DE, Weissleder, R, Tung, CH, Enhanced tumor detection using a folate receptor-targeted near-infrared fluorochrome conjugate. *Bioconjug Chem*, 2003. 14(3): p. 539-45.
73. Lauffenburger, D.A. and J.J. Linderman, *Receptors: Models for binding, trafficking, and signaling*. 1993, New York: Oxford University Press. 365.
74. Sudimack, J., Lee, RJ, Targeted drug delivery via the folate receptor. *Adv Drug Deliv Rev*, 2000. 41(2): p. 147-62.
75. Quintana, A., E. Raczka, L. Piehler, I. Lee, A. Myc, I. Majoros, A.K. Patri, T. Thomas, J. Mule', and J. James R. Baker, Design and function of a dendrimer-based therapeutic nanodevice targeted to tumor cells through the folate receptor. *Pharmaceutical Research*, 2002. 19(9): p. 1310-1316.
76. Bonazzi, S., M. Capobianco, M.M. Demorais, A. Garbesi, G. Gottarelli, P. Mariani, M.G.P. Bossi, G.P. Spada, and L. Tondelli, 4-stranded aggregates of oligodeoxyguanylates forming lyotropic liquid-crystals - a study by circular-dichroism, optical microscopy, and x-ray-diffraction. *Journal of the American Chemical Society*, 1991. 113(15): p. 5809-5816.
77. Bonazzi, S., M.M. Demorais, G. Gottarelli, P. Mariani, and G.P. Spada, Self-assembly and liquid-crystal formation of folic-acid salts. *Angewandte Chemie-International Edition in English*, 1993. 32(2): p. 248-250.
78. Ciuchi, F., G. Dinicola, H. Franz, G. Gottarelli, P. Mariani, M.G.P. Bossi, and G.P. Spada, Self-recognition and self-assembly of folic-acid salts - columnar liquid-crystalline polymorphism and the column growth-process. *Journal of the American Chemical Society*, 1994. 116(16): p. 7064-7071.
79. Kanie, K., T. Yasuda, S. Ujiie, and T. Kato, Thermotropic liquid-crystalline folic acid derivatives: Supramolecular discotic and smectic aggregation. *Chemical Communications*, 2000(19): p. 1899-1900.
80. Sun, C., Sze, R, Zhang, M, Folic acid-peg conjugated superparamagnetic nanoparticles for targeted cellular uptake and detection by mri. *J Biomed Mater Res A*, 2006. 78(3): p. 550-7.
81. Zhang, Y., N. Kohler, and M. Zhang, Surface modification of superparamagnetic magnetite nanoparticles and their intracellular uptake. *Biomaterials*, 2002. 23: p. 1553-1561.
82. Zhang, Y., C. Sun, N. Kohler, and M. Zhang, Self-assembled coatings on individual monodisperse magnetite nanoparticles for efficient intracellular uptake. *Biomedical Microdevices*, 2004. 6(1): p. 33-40.

83. Chang, E., N. Thekkek, W.W. Yu, V.L. Colvin, and R. Drezek, Evaluation of quantum dot cytotoxicity based on intracellular uptake. *Small*, 2006. 2(12): p. 1412-1417.
84. Guo, W. and R.J. Lee, Receptor-targeted gene delivery via folate-conjugated polyethylenimine. *AAPS Pharmsci*, 1999. 1(4).
85. Mok, H., K.H. Bae, C.-H. Ahn, and T.G. Park, Pegylated and mmp-2 specifically depegylated quantum dots: Comparative evaluation of cellular uptake. *Langmuir*, 2009. 25(3): p. 1645-1650.
86. van Steenis, J.H., E.M.v. Maarseveen, F.J. Verbaan, R. Verrijck, D.J.A. Crommelin, G. Storm, and W.E. Hennink, Preparation and characterization of folate-targeted peg-coated pdmaema-based polyplexes. *Journal of Controlled Release*, 2003. 87: p. 167-176.
87. Ma, L.L., P. Jie, and S.S. Venkatraman, Block copolymer 'stealth' nanoparticles for chemotherapy: Interactions with blood cells in vitro. *Advanced Functional Materials*, 2008. 18: p. 716-725.
88. Lorenz, M.R., V. Holzapfel, A. Musyanovych, K. Nothelfer, P. Walther, H. Frank, K. Landfester, H. Schrezenmeier, and V. Mailander, Uptake of functionalized, fluorescent-labeled polymeric particles in different cell lines and stem cells. *Biomaterials*, 2006. 27(14): p. 2820-2828.
89. Patil, S., A. Sandberg, E. Heckert, W. Self, and S. Seal, Protein adsorption and cellular uptake of cerium oxide nanoparticles as a function of zeta potential. *Biomaterials*, 2007. 28(31): p. 4600-4607.
90. Wilhelm, C., C. Billotey, J. Roger, J.N. Pons, J.C. Bacri, and F. Gazeau, Intracellular uptake of anionic superparamagnetic nanoparticles as a function of their surface coating. *Biomaterials*, 2003. 24(6): p. 1001-1011.
91. Yokoyama, M., Fukushima, S., Uehara, R., Okamoto, K., Kataoka, K., Sakurai, Y., Okano, T., Characterization of physical entrapment and chemical conjugation of adriamycin in polymeric micelles and their design for in vivo delivery to a solid tumor. *J Controlled Release*, 1998. 50: p. 79-92.
92. Sparano, J.A., U. Malik, L. Rajdev, C. Sarta, U. Hopkins, and A.C. Wolff, Phase I trial of pegylated liposomal doxorubicin and docetaxel in advanced breast cancer. *Journal of Clinical Oncology*, 2001. 19(12): p. 3117-3125.
93. Tardi, P.G., N.L. Boman, and P.R. Cullis, Liposomal doxorubicin. *Journal of Drug Targeting*, 1996. 4(3): p. 129-140.

Chapter 5. Initial Biodistribution Studies of Alternating Copolymers *In Vivo*

5.1. Introduction

Nanoparticles may be preferentially concentrated *in vivo* at tumor sites through strategic passive or active targeting. The phenomenon described as the “enhanced permeability and retention (EPR) effect” [1-10], in which nanoparticles accumulate in solid tumors in increased amounts as compared to normal tissue has been well documented [11-18] and is attributed to pathophysiological characteristics of solid tumors that are not observed in normal tissue. These characteristics include defective tumor blood vessel architecture (often termed “leaky vasculature”), defective lymphatic drainage system, and increased production of permeability mediators [5, 7]. It has been reported that particles >5 nm in diameter get trapped in the tumor tissue [8, 19], but tumors also exhibit a characteristic pore cutoff size of 200 nm or greater [4]. Therefore drug delivery particles in the 5-200 nm size range should passively target tumors due to the EPR effect. It was determined that micelles formed from our alternating copolymers are 8-22 nm in diameter [20], therefore these particles are optimal for passive targeting *in vivo*.

In addition to passive targeting, nanoparticles can be actively targeted to a tumor cell in order to kill the cancerous cells without damaging normal cells. There are many technologies which are being used to specifically target molecules or particles to tumor cells [21-34]. Often, a monoclonal antibody, a peptide fragment, or a small molecule is

used as the targeting agent. Typically these targeting agents form a binding pair with the target found on the tumor cell surface. Selectivity of the nanoparticles for specific cancer cells by targeting allows for reduced incidence of the adverse side effects of the chemotherapeutic drugs, however this comes at the expense of adding complexity to the nanoparticle preparation, potentially increasing particle size, and the risk of adverse biological reactions with the targeting agent.

Many studies in the literature have targeted tumors *in vivo* by passive targeting using the EPR effect [11-18]. Others have additionally used active targeting to tumor cells to increase accumulation of nanoparticles in the tumor [35-38]. The alternating copolymers used in this study, described in detail in Chapter 2, were designed to passively and actively target tumors. It was reported in Chapter 3 that these alternating copolymers are largely non-toxic and have had some success as drug delivery vehicles *in vitro*. The cellular uptake of these polymers was investigated in Chapter 4. While these polymers did not have the overwhelming selectivity that was anticipated and the specific uptake of these polymers through the targeted receptor-mediated endocytosis pathway can not be substantiated, it is clear that they are taken up by cancerous cells *in vitro*. These *in vitro* studies warranted initial investigation of these polymers in mouse models of human cancer to determine the *in vivo* delivery capabilities.

This chapter describes the *in vivo* experimental work that was done in collaboration with Kevin Brower from the Colton Lab in the Department of Chemical Engineering at the Massachusetts Institute of Technology. Preliminary pharmacokinetic studies were performed to examine the biodistribution and blood circulation of the alternating copolymers in xenograft models of human tumors in nude (*nu/nu*) mice using

radioactively labeled polymers. Results were obtained by collecting blood samples and harvesting organs at specified time points and measuring the radioactivity of these samples. A detailed description of the synthesis protocol for each polymer can be found in Appendix I. A list of all polymer structures used in this study is given in Appendix II. The numbers referred to throughout the remainder of this text correspond to the polymer structures as identified in the table presented in Appendix II.

5.2. Methods

5.2.1. Materials and reagents

All polymers were provided by our collaborators in the Arthur Watterson lab at the University of Massachusetts, Lowell. All reagents were obtained from commercial sources. Phosphate buffered saline (PBS), trypsin EDTA (1X, 0.25% trypsin/0.53 mM EDTA in HBSS), penicillin-streptomycin solution, and fetal bovine serum (FBS) were purchased from Mediatech, Inc. Minimum essential media, Eagle, with 2 mM L-glutamine and Earle's BSS adjusted to contain 1.5 g/L sodium bicarbonate, 0.1 mM non-essential amino acids, and 1.0 mM sodium pyruvate (EMEM) was purchased from ATCC. Hank's buffered salt solution (HBSS) was purchased from Lonza. Guava Viacount assay kit was purchased from Guava Technologies/Millipore.

5.2.2. Cell lines and culture

BT-20 cells (human breast carcinoma; underglycosylated mucin-1 positive (uMUC1+)) and KB cells (human epidermoid carcinoma; folate receptor positive (FR+)) were purchased from the American Type Culture Collection. BT-20 and KB cells were

cultured in EMEM supplemented with 10% FBS and 1% penicillin–streptomycin solution. All cells were grown at 37°C in a humidified atmosphere containing 5% CO₂ in preparation for tumor induction in mice.

5.2.3. Cell counting

After cells were detached from the flask with trypsin, cell number was evaluated by staining cells using a Guava Viacount assay solution and acquiring data with a Guava Personal Cell Analysis (PCA) flow cytometer using the Guava Viacount software. Dilution factors and original sample volumes were entered as appropriate for each sample. Each sample was run in triplicate and 1000 events were acquired per sample.

5.2.4. Tumor induction by subcutaneous injection in *nu/nu* mice

Once cells were counted, cells were centrifuged at 300 RCF for 5 minutes, washed with one volume of HBSS, centrifuged again, and finally suspended in the appropriate volume of HBSS to result in $2\text{-}5 \times 10^6$ cells per 50 uL. Each *nu/nu* mouse was injected with 50 uL of HBSS containing $2\text{-}5 \times 10^6$ cells subcutaneously in the flank. Mice that were injected with FR+ (KB) cells were fed a low-folate diet purchased from Research Diets to ensure up-regulation of the FR in the FR+ cells. Mice were cared for under compliance with the guidelines of the Committee on Animal Care in the Division of Comparative Medicine at the Massachusetts Institute of Technology.

5.2.5. Biodistribution

After tumors reached ~0.5 cm in diameter, as measured by micrometer (typically ~3 weeks), mice were injected intravenously with the ¹²⁵I-labeled polymer (0.86 mg).

Five or twenty-four hours later, animals were sacrificed. Tumors, fluids, and organs were removed and weighed. The collected tissue or fluid was analyzed in a gamma counter (Packard COBRA II Auto-Gamma). The activity of each sample was compared to the activity measurements of polymer solutions of known concentrations to calculate the amount of polymer taken up. Biodistribution results were expressed as the percentage of the injected dose per gram of tissue (% ID/g tissue) or percentage of injected dose (% ID). Experiments were performed using a protocol approved by the Committee on Animal Care in the Division of Comparative Medicine at the Massachusetts Institute of Technology.

5.2.6. Statistical analysis

All data were represented as mean \pm standard deviation. Statistical significance ($p < 0.05$) was determined, where appropriate, by a two-tailed Student t-test.

5.3. Results

5.3.1. Biodistribution of non-targeted polymers in mice with no tumors

In the first *in vivo* biodistribution study, twelve *nu/nu* mice were injected subcutaneously with uMUC1+ (BT-20) cells. After 2 months, no tumors had developed. With the help of Professor Anna Moore at the Martinos Center for Biomedical Imaging at Massachusetts General Hospital, it was determined that these cells were no longer tumorigenic. The cells were reordered twice from ATCC and none of the lots induced tumors in *nu/nu* mice. We proceeded with the study to investigate the biodistribution of the non-targeted polymer *in vivo* in the absence of a tumor.

Each mouse was injected retro-orbitally with 300 μL PBS containing 0.86 mg (10 μCi) of non-targeted polymer with 100% of the linkers having ester-linked hydrocarbon side chains (#27) labeled with ^{125}I . One hour after injection, each mouse was bled via the tail vein to collect a blood sample. After 24 hours, each mouse was euthanized and the blood, tumor, liver, spleen, kidney, heart, and lung were collected. The results of the biodistribution and blood circulation are shown in Figure 5.1. The biodistribution data (left) are shown as percent of injected dose per gram of tissue (% ID/g tissue). For all harvested organs, the % ID/g tissue was less than 0.5%. The blood circulation data (right) are presented as percent of injected dose (% ID). One hour after injection, the % ID in the blood was approximately 5% and 24 hours after injection, the % ID was less than 1%. These low values imply that a majority of the injected polymer is excreted within 24 hours. Approximately 10 μCi per mouse was crudely measured, using a sodium iodide detector, in the urine and the excretions in the cage, which was consistent with the low levels in the organs.

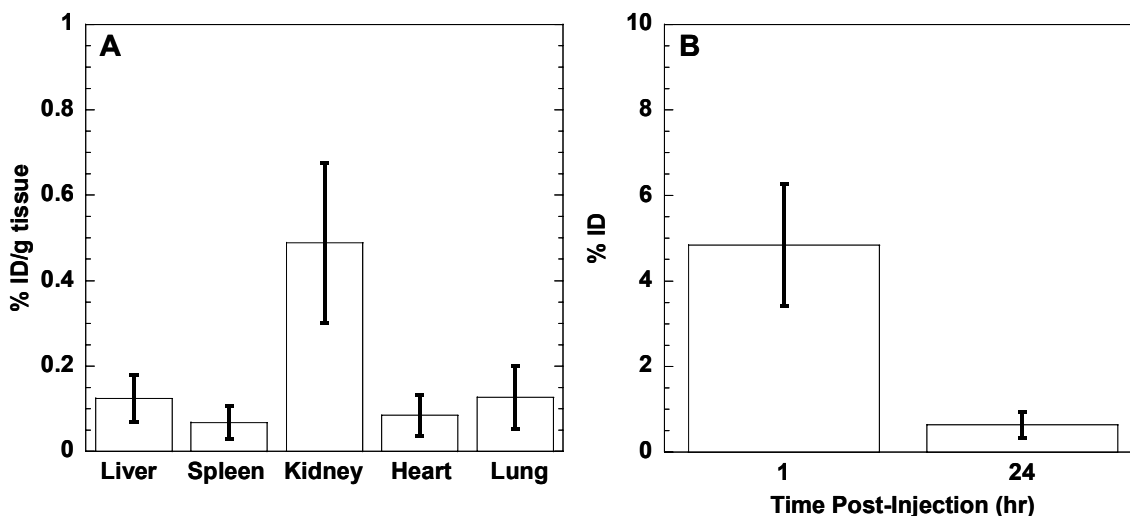


Figure 5.1. Biodistribution and blood circulation of non-targeted polymer with 100% of the linkers having ester-linked hydrocarbon side chains (#27) labeled with ^{125}I injected retro-orbitally in *nu/nu* mice.

5.3.2. Biodistribution of targeted polymers in mice with tumors

In the second biodistribution study, twelve *nu/nu* mice were injected subcutaneously with FR+ (KB) cells and six control mice received subcutaneous injections of HBSS. The tumor take rate was at 100% within three weeks in the mice injected with cells. Mice were divided into two groups. One group was injected retro-orbitally with 200 μL PBS containing 0.86 mg (10 μCi) of targeted polymer with 100% of the linkers having PEG-3400-folate attached (#64) labeled with ^{125}I . The second group was injected via the tail vein with 250 μL PBS containing 0.86 mg (10 μCi) of targeted polymer with 100% of the linkers having PEG-3400-folate attached (#64) labeled with ^{125}I . Mice were bled via the tail vein to collect blood at 1, 2, 5, and 24 hours. Mice were sacrificed at either 5 or 24 hours and samples were taken of tail, tumor, liver, spleen, kidney, heart, lung, and brain. The results of the biodistribution (left) and blood

circulation (right) for the mice injected retro-orbitally are shown in Figure 5.2. At the 5 hour and 24 hour time points, the highest % ID/g tissue was in the kidneys. It appears that the polymer did not cross the blood-brain barrier, due to the low levels in the brain. In addition, there was accumulation in the tumor, as desired, likely due to the passive targeting mentioned earlier. The values for each organ were lower at the 24 hour time point than the 5 hour time point. The % ID in the blood decreased over time and the blood half-life was calculated to be ~30 minutes.

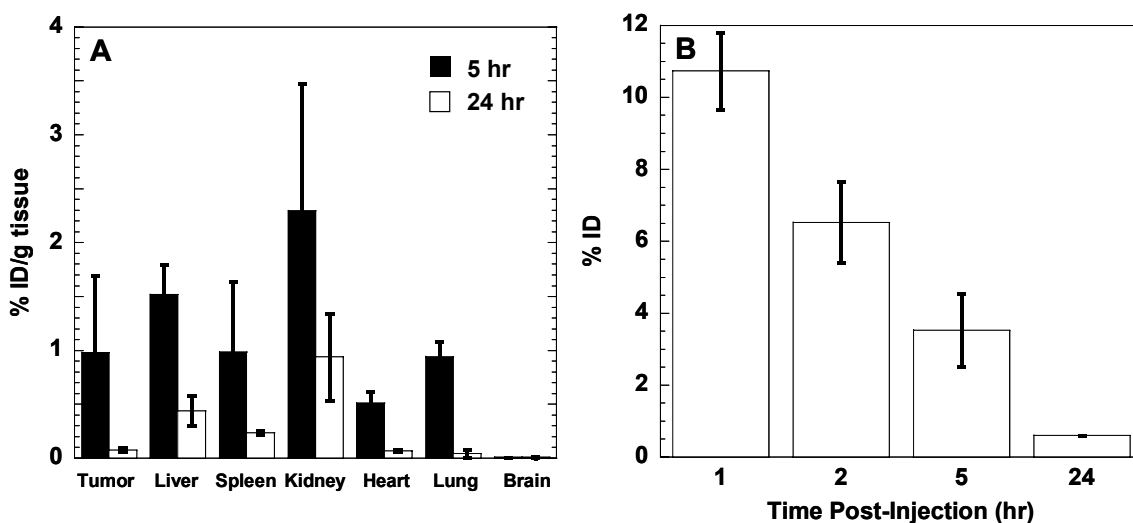


Figure 5.2. Biodistribution and blood circulation of targeted polymer with 100% of the linkers having PEG-3400-folate attached (#64) labeled with ^{125}I injected retro-orbitally in *nu/nu* mice.

The results of the biodistribution (left) and blood circulation (right) for the mice injected via the tail vein are shown in Figure 5.3. In the case of the tail vein injection, the tail was collected and the activity was measured. The activity in the tail was subtracted from the injected dose as it is assumed that this material was injected into the tail tissue rather than into the bloodstream. At the 5 hour and 24 hour time points, the highest %

ID/g tissue was in the kidneys, as with the retro-orbital injection. It appears the polymer did cross the blood-brain barrier in very low amounts, although it was not statistically different from the retro-orbital injection and these low amounts may have been due to cross-contamination during organ harvesting. Again, there was significant accumulation in the tumor, as desired. The values for each organ were lower at the 24 hour time point than the 5 hour time point, as expected. The % ID in the blood decreased over time and the blood half-life was again calculated to be ~35 minutes. There was no statistical difference in biodistribution between the two injection types. However, at 1 hour after injection, there were statistically higher levels of polymer in the blood of mice receiving the injection by the tail vein than by retro-orbital injection, although at all other time points there was no statistical difference in % ID in the blood. As with the first study with non-targeted polymer, nearly all the dose was excreted by 24 hours.

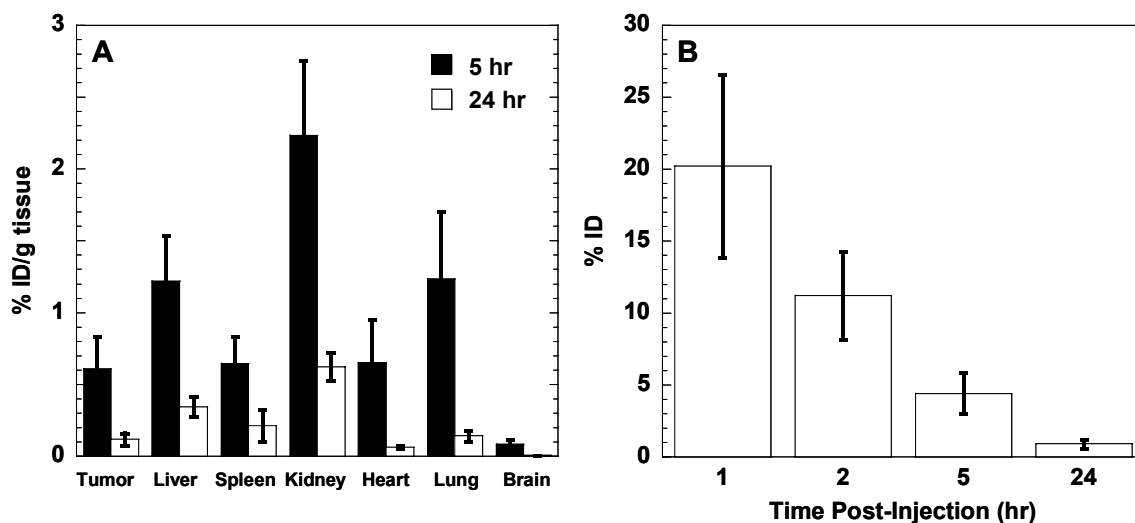


Figure 5.3. Biodistribution and blood circulation of targeted polymer with 100% of the linkers having PEG-3400-folate attached (#64) labeled with ^{125}I injected via the tail vein in *nu/nu* mice.

5.4. Discussion

The alternating copolymers used in this study do accumulate in tumors *in vivo*. Similar studies in the literature report levels of 0.04-2.7 % ID/g tissue [35-38], comparable to the levels of accumulation (0.08-1.0 % ID/g tissue) observed in these studies. These same studies from the literature report levels of 20-60 % ID/g tissue in the liver, while our polymers only accumulate 0.3-1.5 % ID/g tissue in the liver. It is desirable to minimize the accumulation in other organs, while maximizing the accumulation in the tumor tissue. Therefore, this preliminary study warrants continued investigation of our polymer platform as a delivery vehicle *in vivo*.

During the analysis of the results of these studies, it was determined that the most appropriate injection method is via the tail vein rather than by retro-orbital injection in order to more precisely ascertain the total injected dose. It was recommended that the tail and the injection syringe be measured for activity and that activity be subtracted from the theoretical injected dose in order to give the actual injected dose to be used in the calculations. Future experiments investigating the behavior of these alternating copolymers *in vivo* will be performed using the tail vein injection method by Kevin Brower from the Colton Lab in the Department of Chemical Engineering at the Massachusetts Institute of Technology.

5.5. References

1. Matsumura, Y.a.M., H., A new concept for macromolecular therapeutics in cancer therapy: Mechanism of tumoritropic accumulation of proteins and the antitumor agents smancs. *Cancer Res.*, 1986. 46: p. 6387–6392.
2. Maeda, H.a.M., Y., Tumoritropic and lymphotropic principles of macromolecular drugs. *Crit. Rev. Ther. Drug Carrier Syst.*, 1989. 6: p. 193–210.
3. Maeda, H., Smancs and polymer-conjugated macromolecular drugs: Advantages in cancer chemotherapy. *Adv. Drug Delivery Rev.*, 1991. 6: p. 181–202.
4. Hobbs, S.K., Monsky, W. L., Yuan, F., Roberts, W. G., Griffith, L., Torchilin, V. P., Jain, R. K., Regulation of transport pathways in tumor vessels: Role of tumor type and microenvironment. *PNAS*, 1998. 95: p. 4607-4612.
5. Noguchi, Y., Wu, J., Duncan, R., Strohmalm, J., Ulbrich, K., Akaike, T., Maeda, H., Early phase tumor accumulation of macromolecules: A great difference in clearance rate between tumor and normal tissues. *Jpn J Cancer Res*, 1998. 89: p. 307-314.
6. Kong, G., R.D. Braun, and M.W. Dewhirst, Hyperthermia enables tumor-specific nanoparticle delivery: Effect of particle size. *Cancer Research*, 2000. 60(16): p. 4440-4445.
7. Maeda, H., Wu, J., Sawa, T., Matsumura, Y., Hori, K., Tumor vascular permeability and the epr effect in macromolecular therapeutics: A review. *J Controlled Release*, 2000. 65: p. 271-284.
8. Maeda, H., The enhanced permeability and retention (epr) effect in tumor vasculature: The key role of tumor-selective macromolecular drug targeting. *Adv Enzyme Regul*, 2001. 41: p. 189-207.
9. Maeda, H., T. Sawa, and T. Konno, Mechanism of tumor-targeted delivery of macromolecular drugs, including the epr effect in solid tumor and clinical overview of the prototype polymeric drug smancs. *Journal of Controlled Release*, 2001. 74(1-3): p. 47-61.

10. Whitesides, G.M., The 'right' size in nanobiotechnology. *Nature Biotechnology*, 2003. 21(10): p. 1161-1165.
11. Konno, T., Maeda, H., Iwai, K., Tashiro, S., Maki, S., Morinaga, T., Mochinaga, M., Hiraoka, T. and Yokoyama, I., Effect of arterial administration of high molecular weight anticancer agent smancs with lipid lymphographic agent on hepatoma: A preliminary report. *Eur. J. Cancer Clin. Oncol.*, 1983. 19: p. 1053–1065.
12. Iwai, K., Maeda, H. and Konno, T., Use of oily contrast medium for selective drug targeting to tumor: Enhanced therapeutic effect and x-ray image. *Cancer Research*, 1984. 44: p. 2115–2121.
13. Konno, T., Maeda, H., Iwai, K., Maki, S., Tashiro, S., Uchida, M. and Miyauchi, Y., Selective targeting of anticancer drug and simultaneous image enhancement in solid tumors by arterially administered lipid contrast medium. *Cancer*, 1984. 54: p. 2367–2374.
14. Iwai, K., Maeda, H., Konno, T., Matsumura, Y., Yamashita, R., Yamasaki, K., Hirayama, S. and Miyauchi, Y., Tumor targeting by arterial administration of lipids: Rabbit model with vx2 carcinoma in the liver. *Anticancer Res*, 1987. 7: p. 321–328.
15. Seymour, L.W., Ulbrich, K., Steyger, P. S., Brereton, M., Subr, V., Strohalm, J. and Duncan, R., Tumour tropism and anticancer efficacy of polymer-based doxorubicin prodrugs in the treatment of subcutaneous murine b16 f10 melanoma. *Br. J. Cancer*, 1994. 70: p. 636–641.
16. Sinn, H., Shrenk, H. H., Fredrich, E. A., Schilling, U. and Maier-Borst, W. A. A., Design of compounds having an increased tumour uptake: Using serum albumin as carrier. Part 1. *Nucl. Med. Biol.*, 1990. 17: p. 819–827.
17. Wu, N.Z., Da, D., Rudoll, T. L., Needham, D., Whorton, A. R. and Dewhirst, M. W., Increased microvascular permeability contributes to preferential accumulation of stealth liposomes in tumor tissue. *Cancer Res.*, 1993. 53: p. 3765–3770.
18. Yuan, F., Dellian, M., Fukumura, D., Leunig, M., Berk, D. A., Torchilin, V. P. and Jain, R. K., Vascular permeability in a human tumour xenograft: Molecular size dependence and cutoff size. *Cancer Res.*, 1995. 55: p. 3752–3756.
19. Torchilin, V.P., Structure and design of polymeric surfactant-based drug delivery systems. *J Controlled Release*, 2001. 73: p. 137-172.
20. Dawson, J.Z., Physicochemical characterization of peg-based comb-like amphiphilic copolymer structures for possible imaging and therapeutic applications, in Department of Chemical Engineering. 2008, Massachusetts Institute of Technology: Cambridge, MA. p. 1-267.

21. Liang, H.-F., C.-T. Chen, S.-C. Chen, A.R. Kulkarni, Y.-L. Chiu, M.-C. Chen, and H.-W. Sung, Paclitaxel-loaded poly(g-glutamic acid)-poly(lactide) nanoparticles as a targeted drug delivery system for the treatment of liver cancer. *Biomaterials*, 2006. 27: p. 2051-2059.
22. You, J., X. Li, F. de Cui, Y.Z. Du, H. Yuan, and F.Q. Hu, Folate-conjugated polymer micelles for active targeting to cancer cells: Preparation, in vitro evaluation of targeting ability and cytotoxicity. *Nanotechnology*, 2008. 19(4).
23. Farokhzad, O.C., Cheng, J., Teply, B. A., Sherifi, I., Jon, S., Kantoff, P. W., Richie, J. P., Langer, R., Targeted nanoparticle-aptamer bioconjugates for cancer chemotherapy in vivo. *PNAS*, 2006. 103(16): p. 6315-6320.
24. Sivolapenko, G.B., V. Douli, D. Pectasides, D. Skarlos, G. Sirmalis, R. Hussain, J. Cook, N.S. Courtenay-Luck, E. Merkouri, K. Konstantinides, and A.A. Epenetos, . Breast cancer imaging with radiolabelled peptide from complementarity-determining region of antitumour antibody. *Lancet*, 1995. 346: p. 1662-1666.
25. Moore, A., Z. Medarova, A. Potthast, and G. Dai, In vivo targeting of underglycosylated muc-1 tumor antigen using a multimodal imaging probe. *Cancer Research*, 2004. 64: p. 1821-1827.
26. Leamon, C.P., Reddy, J. A., Folate-targeted chemotherapy. *Adv Drug Delivery Rev*, 2004. 56: p. 1127-1141.
27. Ke, C., Mathias, CJ, Green, MA, Folate-receptor-targeted radionuclide imaging agents. *Adv Drug Deliv Rev*, 2004. 56(8): p. 1143-60.
28. Hong, S., Leroueil, PR, Majoros, IJ, Orr, BG, Baker, JR Jr, Banaszak Holl, MM, The binding avidity of a nanoparticle-based multivalent targeted drug delivery platform. *Chem Biol*, 2007. 14(1): p. 107-15.
29. Saul, J., Annapragada, A, Natarajan, JV, Bellamkonda, RV, Controlled targeting of liposomal doxorubicin via the folate receptor in vitro. *J Control Release*, 2003. 92(1-2): p. 49-67.
30. Gabizon, A., Horowitz, AT, Goren, D, Tzemach, D, Mandelbaum-Shavit, F, Qazen, MM, Zalipsky, S, Targeting folate receptor with folate linked to extremities of poly(ethylene glycol)-grafted liposomes: In vitro studies. *Bioconjug Chem*, 1999. 10(2): p. 289-98.
31. Lee, E., Na, K, Bae, YH, Polymeric micelle for tumor ph and folate-mediated targeting. *J Control Release*, 2003. 91(1-2): p. 103-13.
32. Bae, Y., Jang, WD, Nishiyama, N, Fukushima, S, Kataoka, K, Multifunctional polymeric micelles with folate-mediated cancer cell targeting and ph-triggered

- drug releasing properties for active intracellular drug delivery. *Mol Biosyst*, 2005. 1(3): p. 242-50.
33. Yoo, H., Park, TG, Folate receptor targeted biodegradable polymeric doxorubicin micelles. *J Control Release*, 2004. 96(2): p. 273-83.
 34. Yoo, H., Park, TG, Folate-receptor-targeted delivery of doxorubicin nano-aggregates stabilized by doxorubicin-peg-folate conjugate. *J Control Release*, 2004. 100(2): p. 247-56.
 35. Kukowska-Latallo, J., Candido, KA, Cao, Z, Nigavekar, SS, Majoros, IJ, Thomas, TP, Balogh, LP, Khan, MK, Baker, JR Jr, Nanoparticle targeting of anticancer drug improves therapeutic response in animal model of human epithelial cancer. *Cancer Res.*, 2005. 65(12): p. 5317-24.
 36. Gu, F., L. Zhang, B.A. Teply, N. Mann, A. Wang, A.F. Radovic-Moreno, R. Langer, and O.C. Farokhzad, Precise engineering of targeted nanoparticles by using self-assembled biointegrated block copolymers. *Proceedings of the National Academy of Sciences of the United States of America*, 2008. 105(7): p. 2586-2591.
 37. Cheng, J., B.A. Teply, I. Sherifi, J. Sung, G. Luther, F.X. Gu, E. Levy-Nissenbaum, A.F. Radovic-Moreno, R. Langer, and O.C. Farokhzad, Formulation of functionalized plga-peg nanoparticles for in vivo targeted drug delivery. *Biomaterials*, 2007. 28(5): p. 869-876.
 38. Lee, E., Na, K, Bae, YH, Doxorubicin loaded ph-sensitive polymeric micelles for reversal of resistant mcf-7 tumor. *J Control Release*, 2005. 103(2): p. 405-18.

Appendix I. Description of Methods for Polymer Synthesis

I.i. Synthesis of backbone polymer

Backbone polymer was synthesized by the enzymatic reaction of dimethyl 5-amino-isophthalate (0.05mmol), dimethyl 5-hydroxy-isophthalate (0.95 mmol) and PEG-900 (1.0 mmol). This mixture was placed in a round-bottom flask, enzyme (10 wt % wrt monomers) was added, and the reaction vial was then placed in a constant temperature oil bath maintained at 90°C under vacuum. The reaction was allowed to proceed for 48 h, after which it was quenched by adding water and filtering off the enzyme and any unreacted monomer under vacuum. The filtrate was dialyzed using a membrane (MWCO 6000). After the completion of dialysis, the product was obtained as a semisolid by freeze-drying. Obtained product was fully characterized on the basis of its detailed spectral studies including ¹H-NMR, ¹³C-NMR, IR and GPC [1-3]. Alternatively, the procedure was performed without dimethyl 5-hydroxy-isophthalate but with 1.0 mmol dimethyl 5-amino-isophthalate to produce backbone polymer with 100% amino linkers or without dimethyl 5-amino-isophthalate but with 1.0 mmol dimethyl 5-hydroxy-isophthalate to produce backbone polymer with 100% hydroxy linkers. The synthesis was also carried out with PEG-600, PEG-1500, and PEG-10000 to produce backbone polymer with higher PEG ratios. The procedure was also performed with 4Å molecular sieves (20 wt% wrt monomers) to decrease the water content in the reaction mixture [4].

I.ii. Attachment of hydrocarbon side chains**I.ii.a. Ether bond**

Equimolar quantities of polymer with free hydroxyl groups on 100% of the linkers and bromodecane were dissolved in dry acetone, and to the resultant solution was added an equimolar amount of anhydrous potassium carbonate. The reaction mixture was refluxed, and progress of the reaction was monitored by TLC using ethyl acetate in petroleum ether (30%). After completion, the potassium carbonate was removed by filtration, and the solvent was removed under vacuum to give the product [1]. This procedure was also performed with bromononane or 11-bromoundecanoic acid in place of bromodecane. Other alternatives that were synthesized used polymers with free hydroxyl groups on 90% of the linkers or 95% of the linkers.

I.ii.b. Ester bond

Polymer with free hydroxyl groups on the linkers (1.0 mmol) was dissolved in anhydrous acetonitrile followed by the addition of anhydrous potassium carbonate (3.0 mmol) and nonanoyl chloride (1.2 mmol) under nitrogen. The reaction mixture was stirred at room temperature for 6 h under reflux and progress of the reaction was monitored by TLC using ethyl acetate in petroleum ether (30%). After completion of the reaction, salt was removed by filtration and the solvent removed under vacuum to give the product [4]. This procedure was also performed with decanoyl chloride or tetradecanoyl chloride in place of nonanoyl chloride. Other alternatives that were synthesized used polymers with free hydroxyl groups on 90% of the linkers or 95% of the linkers.

I.ii.c. Ether ester bond

To a solution of polymer with free hydroxyl groups on 90% of the linkers (1.0 mmol) in 25 ml of dry acetonitrile, anhydrous potassium carbonate (0.85 mmol) was added followed by decyl bromo acetate (0.81 mmol) and the resulting solution was refluxed in an oil bath maintained at 60°C. Progress of the reaction was monitored by TLC. After completion of the reaction, salts were filtered off and acetonitrile was removed to give the amphiphilic polymer as solid [3-5].

I.ii.d. Amide bond

Polymer with free amino groups on the linkers (1.0 mmol) was dissolved in anhydrous dichloromethane followed by the addition of anhydrous potassium carbonate (3.0 mmol) and nonanoyl chloride (1.2 mmol) under nitrogen. The reaction mixture was stirred at room temperature for 6 h under reflux and progress of the reaction was monitored by TLC using ethyl acetate in petroleum ether (30%). After completion of the reaction, salt was removed by filtration and the solvent removed under vacuum to give the product [4]. Other alternatives that were synthesized used polymers with free amino groups on 5% of the linkers.

I.iii. Attachment of perfluorocarbon side chains**I.iii.a. Ether ester bond**

To a solution of polymer with free hydroxyl groups on 90% of the linkers (1.0 mmol) in 25 ml of dry acetonitrile, anhydrous potassium carbonate (0.85 mmol) was added followed by 1H,1H,2H,2H-perfluorodecyl bromo acetate (0.81 mmol) and the

resulting solution was refluxed in an oil bath maintained at 60°C. Progress of the reaction was monitored by TLC. After completion of the reaction, salts were filtered off and acetonitrile was removed to give the amphiphilic polymer as solid [3-5]. This procedure was also performed with 1H,1H,2H,2H-perfluorododecyl bromo acetate in place of 1H,1H,2H,2H-perfluorodecyl bromo acetate. Other alternatives that were synthesized used polymers with free hydroxyl groups on 95% of the linkers or 100% of the linkers.

I.iii.b. Amide bond

To a solution of polymer with free amino groups on the linkers (1.0 mmol) in 25 ml of dry acetonitrile, anhydrous potassium carbonate (0.85 mmol) was added followed by perfluorooctanoyl chloride (0.81 mmol) and the resulting solution was stirred at room temperature. Progress of the reaction was monitored by TLC. After completion of the reaction, salts were filtered off and acetonitrile was removed to give the amphiphilic polymer as solid [4]. This procedure was also performed with perfluorononanoyl chloride in place of perfluorooctanoyl chloride.

I.iv. Attachment of fluorescent labels

I.iv.a. Rhodamine B

Rhodamine B was converted to its acid chloride using oxalyl chloride. Treatment of the polymer (substituted with a decane chain as the hydrophobic group on the linkers) with the Rhodamine B acid chloride and base gave a reaction to form an ester linkage with the CH₂OH groups at the ends of the polymer chains, binding it covalently to the polymer.

I.iv.b. FITC

FITC (fluorescein-5-isothiocyanate) dye (0.067 mmol) was added to a three-neck round bottom flask containing backbone polymer with free amino groups on 5% of the linkers (1.0 mmol) dissolved in anhydrous DMF (10 ml) under a nitrogen environment. The resulting mixture was stirred at room temperature for four hours. Upon completion of the reaction, DMF was removed by washing several times with excess hexane. Obtained residue was further dried under vacuum and then subjected to dialysis using a membrane (MWCO 6000-8000) to get rid of unreacted FITC in the obtained product [3, 4].

I.iv.c. Cy 5.5

Backbone polymer with free amino groups on 5% of the linkers (100 mg) in 0.5 M sodium bicarbonate with the pH adjusted to 9.6 was added to 1 mg of Cy5.5 dye (Amersham-Pharmacia, Cat.#Q15408). The mixture was incubated on a rotator overnight at room temperature. After incubation, the mixture was purified from non-reacted dye on G-25 Sephadex column equilibrated with 20 mM sodium citrate buffer with 0.15 M NaCl, pH 8.0 [6].

I.v. Attachment of targeting ligands**I.v.a. EPPT with triethylene glycol spacer***Attachment of triethylene glycol as spacer*

Polymer containing free hydroxyl groups on 5% of the linkers (1.0 mmol) was dissolved in anhydrous acetonitrile and added to a three-neck round bottom flask containing freshly fused K_2CO_3 (0.044mmol) under a nitrogen environment with constant

stirring. In a drop-wise manner, triethylene glycol bromo acetate (0.043mmol), dissolved in anhydrous acetonitrile, was added. The resulting reaction mixture was refluxed for 6-8 hours and the progress of the reaction was monitored by TLC. After completion of the reaction, salts were filtered off and the filtrate was concentrated at reduced pressure to get the desired product. Obtained product was characterized by its $^1\text{H-NMR}$ and $^{13}\text{C-NMR}$ spectrum [3, 4].

Activation of hydroxyl group on spacer

The activation was carried out under nitrogen by stirring disuccinimidyl carbonate (0.13 mmol) and polymer from the previous step (1.0 mmol) dissolved in anhydrous acetonitrile (20 ml) in a three-neck round bottom flask in the presence of a catalytic amount of DMAP (3 mg). The resulting mixture was stirred for 12 hours. After completion of the reaction, solvent was removed under vacuum at room temperature. Salts were removed by repeated precipitation with diethyl ether in acetonitrile. The obtained pure compound was dried, characterized, and used in the next step [3, 4].

Attachment of peptide (EPPT)

Activated polymer (1.0 mmol) was stirred with peptide (EPPT, 0.045 mmol) in phosphate buffer (pH 7.2) for 12 hours. Obtained product was dialyzed using a membrane (MWCO 6000). After the completion of dialysis, peptide attached polymer was obtained as a semisolid by freeze-drying [3, 4]. This entire scheme for attachment of the EPPT peptide with the triethylene glycol linker was also performed with polymer containing free hydroxyl groups on 7% of the linkers and 34% of the linkers.

I.vi. Radiolabeling of polymers**I.vi.a. Iodination with ^{125}I**

Immediately before use, wash Pierce iodination beads with 500 μl of phosphate buffered saline (PBS) per bead. Dry the beads on filter paper. Add beads to a solution of carrier-free Na^{125}I (approximately 1 mCi per 100 μg of protein) diluted with PBS and incubate for 5 minutes. A small reaction vial is optimal for this step. Dissolve or dilute protein in PBS and add to the reaction vessel. Incubate reaction mixture for 15 minutes. Stop the reaction by removing the solution from the reaction vessel. Once beads are separated from the solution, the reaction will stop [7]. Wash with sodium metabisulfite (12 mg/mL in PBS) and BSA solution (2 mg/mL in PBS). Separate the product by size-exclusion chromatography using Sephadex G-15. Weigh out the appropriate amount of dry Sephadex for the required bed volume of your column. To prepare the column, add enough buffer to the Sephadex to equal the total volume of the column plus 30%. Swell for 3 hours. After swelling is complete, decant the supernatant. Add buffer to make a 75% suspension. Degas the suspension before packing. Pour the entire slurry into the column in one portion, taking care not to trap air bubbles. Start the gravity flow to initiate packing [7]. Once the column is prepared, pour reaction solution into column and collect samples at bottom of column.

I.vi.b. Methylation with ^3H

Polymer is treated with anhydrous potassium in acetonitrile, followed by addition of radioactive methyl iodide ($\text{C}^3\text{H}_3\text{I}$). Stir for 6 hours. After completion of the reaction, K_2CO_3 is filtered and filtrate is concentrated to get the desired product.

I.vii. Encapsulation of chemotherapeutic drugs in polymer micelles**I.vii.a. Doxorubicin**

Make separate solutions of 200 mg polymer (any polymer containing hydrophobic side chains which can form a micelle) in 5 mL water and 5 mg doxorubicin in 5 mL water. Mix the two solutions together and further dilute it to make a resultant solution of 20 mL. Dialyze against water (100 mL) using a membrane (MWCO 1000). Frequently change the water (approximately every 6 hours), continuing the dialysis until the water in the flask is colorless (~1 week). Freeze-dry the sample to remove water and obtain the encapsulated product. Estimate the percent of encapsulated material by UV spectrum [8].

I.vii.b. Paclitaxel

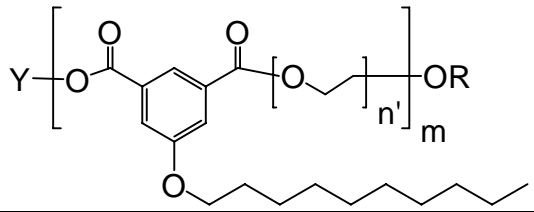
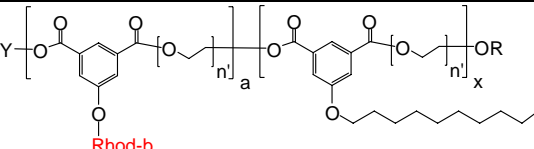
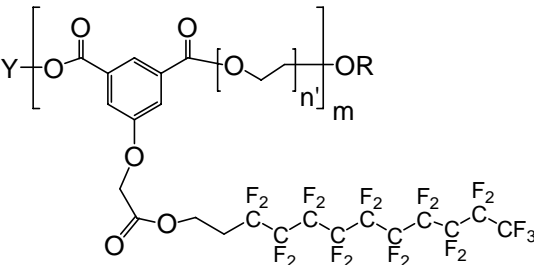
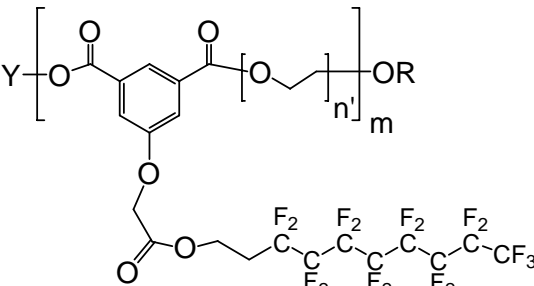
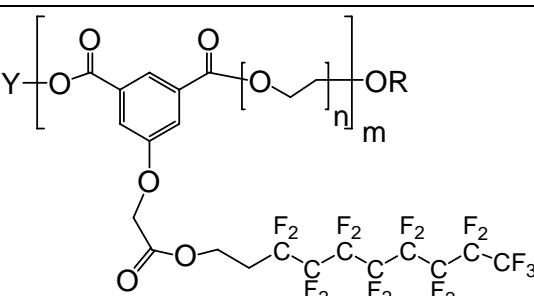
The amphiphilic polymer and the hydrophobic drug paclitaxel were dissolved in methanol to obtain 1:5 drug/polymer w/w ratios, and they were mixed for 15 min. Organic solvent was removed under vacuum, and the highly viscous mixture of drug and polymer obtained was dissolved with an extensive vortexing in water to form nanomicelles. The mixture was dialyzed using a membrane (MWCO 1000). The product was freeze-dried to obtain the paclitaxel-loaded nanoparticles [1, 4, 9].

I.viii. References

1. Kumar, R., M.H. Chen, V.S. Parmar, L.A. Samuelson, J. Kumar, R.A. Nicolosi, S. Yoganathan, and A.C. Watterson, Supramolecular assemblies based on copolymers of peg600 and functionalized aromatic diesters for drug delivery applications. *Journal of the American Chemical Society*, 2004. 126(34): p. 10640-10644.
2. Kumar, R., N.A. Shakil, M.-H. Chen, V.S. Parmar, L.A. Samuelson, J. Kumar, and A.C. Watterson, Chemo-enzymatic synthesis and characterization of novel functionalized amphiphilic polymers. *Journal of Macromolecular Science*, 2002. A39(10): p. 1137-1149.
3. Pandey, M.K., Tyagi, Rahul, Kumar, Rajesh, Parmar, Virinder S., Watterson, Arthur C., Kumar, Jayant, Hardiman, Michelle T. Zhou, Jin, Brower, Kevin P., Fisher, Robert J., Colton, Clark K., Design and synthesis of novel amphiphilic polymers for mri and selective targeting in cancer diagnosis / therapy. *Polymeric Materials: Science and Engineering*, 2007. 96: p. 855-6.
4. Tyagi, R., Unknown title, in Department of Chemistry. 2008, University of Massachusetts, Lowell: Lowell, MA. p. 1-163.
5. Kumar, R., Tyagi, R., Parmar, V. S., Watterson, A. C., Kumar, J., Zhou, J., Hardiman, M., Fisher, R., Colton, C. K., Perfluorinated amphiphilic polymers as nano probes for imaging and delivery of therapeutics for cancer. *Polymer Preprints*, 2005.
6. Josephson, L., C.H. Tung, A. Moore, and R. Weissleder, High-efficiency intracellular magnetic labeling with novel superparamagnetic-tat peptide conjugates. *Bioconjugate Chemistry*, 1999. 10(2): p. 186-91.
7. Dawson, J.Z., Physicochemical characterization of peg-based comb-like amphiphilic copolymer structures for possible imaging and therapeutic applications, in Department of Chemical Engineering. 2008, Massachusetts Institute of Technology: Cambridge, MA. p. 1-267.
8. Tyagi, R., Personal communication: Doxorubicin encapsulation method. 2008.
9. Sharma, S.K., R. Kumar, S. Kumar, R. Mosurkal, V.S. Parmar, L.A. Samuelson, A.C. Watterson, and J. Kumar, Influence of eda-pi interactions in drug encapsulation using nanospheres. *Chemical Communication*, 2004. 23: p. 2689-2691.

-Intentionally Left Blank-

Appendix II. Table of Polymers

#	Structure	PEG MW	Polymer MW	Side Chains and Encapsulant
1		600	-	100% O(CH ₂) ₉ CH ₃
4		600	-	10% Rhodamine B, 90% O(CH ₂) ₉ CH ₃
8		600	-	100% CH ₂ OCO(CH ₂) ₂ (CF ₂) ₉ CF ₃
9		600	-	100% OCH ₂ OCO(CH ₂) ₂ (CF ₂) ₇ CF ₃
10		900	7572	100% OCH ₂ OCO(CH ₂) ₂ (CF ₂) ₇ CF ₃

APPENDIX II. TABLE OF POLYMERS

#	Structure	PEG MW	Polymer MW	Side Chains and Encapsulant
12		600	-	100% NHCO(CF ₂) ₆ CF ₃
13		900	-	95% OCH ₂ OCO(CH ₂) ₂ (CF ₂) ₇ CF ₃ 5% FITC
14		900	-	100% O(CH ₂) ₉ CH ₃ Doxorubicin Encapsulated
15		900	-	100% OCH ₂ OCO(CH ₂) ₂ (CF ₂) ₉ CF ₃ Doxorubicin Encapsulated
16		900	-	95% OCO(CH ₂) ₇ CH ₃ 5% FITC
17		900	-	95% OCO(CH ₂) ₇ CH ₃ 5% Cy5.5

APPENDIX II. TABLE OF POLYMERS

#	Structure	PEG MW	Polymer MW	Side Chains and Encapsulant
18		900	-	90% OCO(CH ₂) ₇ CH ₃ 5% FITC 5% TEG-EPPT
19		900	-	95% OCO(CH ₂) ₇ CH ₃ 5% TEG-EPPT
20		900	-	90% OCH ₂ OCO(CH ₂) ₂ (CF ₂) ₇ CF ₃ 5% FITC 5% TEG-EPPT
21		900	-	95% O(CH ₂) ₉ CH ₃ 5% FITC
22		900	-	100% OCO(CH ₂) ₇ CH ₃
23		900	-	95% OH 5% NH ₂
24		900	-	100% OH
25		900	-	95% OCO(CH ₂) ₇ CH ₃ 5% NHCO(CH ₂) ₇ CH ₃

APPENDIX II. TABLE OF POLYMERS

#	Structure	PEG MW	Polymer MW	Side Chains and Encapsulant
26		900	5785	100% O(CH ₂) ₉ CH ₃
27		900	5785	100% OCO(CH ₂) ₇ CH ₃
28		900	-	95% O(CH ₂) ₉ CH ₃ 5% FITC
29		900	-	90% OCH ₂ OCO(CH ₂) ₂ (CF ₂) ₇ CF ₃ 5% FITC 5% TEG-EPPT
30		900	-	95% OCO(CH ₂) ₇ CH ₃ 5% TEG-EPPT Doxorubicin Encapsulated
31		900	-	100% OCO(CH ₂) ₈ CH ₃
32		900	-	100% NH ₂

APPENDIX II. TABLE OF POLYMERS

#	Structure	PEG MW	Polymer MW	Side Chains and Encapsulant
33		900	-	95% OH 5% TEG-EPPT
34		900	-	100% O(CH ₂) ₈ CH ₃
35		900	-	100% OCO(CH ₂) ₇ CH ₃ Doxorubicin Encapsulated
36		900	-	95% OCH ₂ OCO(CH ₂) ₂ (CF ₂) ₇ CF ₃ 5% TEG-EPPT
37		900	6200	95% OCO(CH ₂) ₇ CH ₃ 5% TEG-EPPT
38		900	-	95% OCO(CH ₂) ₇ CH ₃ 5% TEG-EPPT Doxorubicin Encapsulated
39		900	5552	90% OH 5% FITC 5% HEG-EPPT

APPENDIX II. TABLE OF POLYMERS

#	Structure	PEG MW	Polymer MW	Side Chains and Encapsulant
40	<p>The structure shows a copolymer chain with two repeating units. The first unit has a FITC group (HN) and a hydroxyl group (OH) on the benzene ring. The second unit has a hydroxyl group (OH) on the benzene ring. The side chains are labeled as FITC and OH.</p>	900	-	95% OH 5% FITC
41	<p>The structure shows a copolymer chain with a perfluorinated side chain. The side chain is labeled as OCH₂OCO(CH₂)₂(CF₂)₇CF₃.</p>	1500	-	100% OCH ₂ OCO(CH ₂) ₂ (CF ₂) ₇ CF ₃
42	<p>The structure shows a copolymer chain with two repeating units. The first unit has a TEG group and an EPPT group on the benzene ring. The second unit has a hydroxyl group (OH) on the benzene ring. The side chains are labeled as TEG and EPPT.</p>	900	5636	93% OH 7% TEG-EPPT
43	<p>The structure shows a copolymer chain with a perfluorinated side chain. The side chain is labeled as OCH₂OCO(CH₂)₂(CF₂)₇CF₃.</p>	600	-	100% OCH ₂ OCO(CH ₂) ₂ (CF ₂) ₇ CF ₃
44	<p>The structure shows a copolymer chain with two repeating units. The first unit has a TEG group and an EPPT group on the benzene ring. The second unit has a hydroxyl group (OH) on the benzene ring. The side chains are labeled as TEG and EPPT.</p>	900	8091	66% OH 34% TEG-EPPT
49	<p>The structure shows a copolymer chain with a long alkyl side chain. The side chain is labeled as OCO(CH₂)₇CH₃.</p>	900	-	100% OCO(CH ₂) ₇ CH ₃ Paclitaxel Encapsulated

APPENDIX II. TABLE OF POLYMERS

#	Structure	PEG MW	Polymer MW	Side Chains and Encapsulant
50	<p>Chemical structure of a copolymer consisting of two PEG blocks of lengths w and y. The first PEG block is attached to a benzene ring that also has a folate group and a hydroxyl group. The second PEG block is attached to another benzene ring that has a hydroxyl group. The polymer ends with an OR group.</p>	900	5221	90% OH 10% Folate
51	<p>Chemical structure of a copolymer consisting of two PEG blocks of lengths w and y. The first PEG block is attached to a benzene ring that also has a folate group. The second PEG block is attached to another benzene ring that has a decyl chain. The polymer ends with an OR group.</p>	900	6006	90% $O(CH_2)_9CH_3$ 10% Folate
52	<p>Chemical structure of a copolymer consisting of two PEG blocks of lengths n and m. The first PEG block is attached to a benzene ring that also has an amide group with a decyl chain. The second PEG block is attached to another benzene ring. The polymer ends with an OR group.</p>	600	-	100% $NHCO(CH_2)_7CH_3$
53	<p>Chemical structure of a copolymer consisting of two PEG blocks of lengths n and m. The first PEG block is attached to a benzene ring that also has an amide group with a decyl chain. The second PEG block is attached to another benzene ring. The polymer ends with an OR group.</p>	900	-	100% $NHCO(CH_2)_7CH_3$
54	<p>Chemical structure of a copolymer consisting of two PEG blocks of lengths n and m. The first PEG block is attached to a benzene ring that also has an amide group with a decyl chain. The second PEG block is attached to another benzene ring. The polymer ends with an OR group.</p>	1500	-	100% $NHCO(CH_2)_7CH_3$
56	<p>Chemical structure of a copolymer consisting of a PEG₃₄₀₀ block, a PEG block of length n', and a hydroxyl group. The PEG₃₄₀₀ block is attached to a benzene ring that also has a hydroxyl group. The PEG block of length n' is attached to another benzene ring. The polymer ends with an OR group.</p>	900	8841	100% OH PEG3400-Folate at end of chain

APPENDIX II. TABLE OF POLYMERS

#	Structure	PEG MW	Polymer MW	Side Chains and Encapsulant
57		900	-	100% OCH ₂ OCO(CH ₂) ₇ CH ₃
58		900	5795	100% OCH ₂ OCO(CH ₂) ₅ CH ₃
59		900	9636	100% OCH ₂ OCO(CH ₂) ₅ CH ₃ PEG3400-Folate at end of chain
60		900	11501	75% OH 25% PEG3400-Folate
61		900	12296	75% OCH ₂ OCO(CH ₂) ₅ CH ₃ 25% PEG3400-Folate
62		900	-	100% OCH ₂ OCO(CH ₂) ₁₁ CH ₃

APPENDIX II. TABLE OF POLYMERS

#	Structure	PEG MW	Polymer MW	Side Chains and Encapsulant
64	<p>PEG₃₄₀₀-Folate</p>	900	31005	100% PEG3400-Folate
65	<p>PEG₃₄₀₀-EPPT</p>	900	37890	100% PEG3400-EPPT
66	<p>CH₃</p>	900	5075	100% OCH ₃
67	<p>PEG₃₄₀₀-COOH</p>	900	28800	100% PEG3400-COOH
71	<p>PEG₃₄₀₀-Folate</p> <p>CH₃</p> <p>w=98%, y=2%</p>	900	30485	98% PEG3400-Folate 2% CH ₃

Note: Polymers numbered 23 and higher were synthesized in the absence of triethylamine (TEA).

Y=PEG, CH₃, or H

R=H, linker, or sidechain

z,w = 5%, v = 7% or 34%, u = 10%, x = 90%, y = 95%, except where noted

PEG = polyethylene glycol

TEG = triethylene glycol

Calculation of MW:

For each polymer, the backbone was assumed to have a MW of 5000 g/mol. Typical MW of backbone was typically in the range of 3000-7000 g/mol. It was also assumed that each polymer backbone has 5 linker molecules. The MW of one polymer chain was calculated based on the known MW of each side chain and the percent of substitution of the side chains.

Appendix III. Cell Counting by Flow Cytometry

III.i. Methods

III.i.a. Materials and reagents

All polymers were provided by our collaborators in the Arthur Watterson lab at the University of Massachusetts, Lowell. All reagents were obtained from commercial sources. Trypsin EDTA (1X, 0.25% trypsin/0.53 mM EDTA in HBSS), penicillin-streptomycin solution, and fetal bovine serum (FBS) were purchased from Mediatech, Inc. Minimum essential media, Eagle, with 2 mM L-glutamine and Earle's BSS adjusted to contain 1.5 g/L sodium bicarbonate, 0.1 mM non-essential amino acids, and 1.0 mM sodium pyruvate (EMEM) was purchased from ATCC. Guava Viacount assay kit was purchased from Guava Technologies/Millipore.

III.i.b. Cell lines and culture

KB cells (human epidermoid carcinoma; FR+) and HT-1080 cells (human fibrosarcoma; FR-) were purchased from the American Type Culture Collection. KB and HT-1080 cells were cultured in EMEM supplemented with 10% FBS and 1% penicillin-streptomycin solution. All cells were grown at 37°C in a humidified atmosphere containing 5% CO₂.

III.i.c. Seeding of cells and solution make up

The cells growing as a mono-layer were harvested with trypsin EDTA (1X, 0.25% trypsin/0.53 mM EDTA in HBSS). Each cell line was seeded on a 96-well plate at a cell density of 2×10^5 cells/mL 1 day before the start of the experiment. Cells were incubated under sterile conditions at 37°C in a humidified atmosphere containing 5% CO₂. The polymer solution was made by dissolving polymer (1 g/L) in cell media and sterile filtered through a 0.2 µm filter.

III.i.d. Cell counting

At each time point (0, 2, 6, 24, and 48 hours), cells were detached from the well with trypsin and cell number was evaluated by staining cells using a Guava Viacount assay solution and acquiring data with a Guava Personal Cell Analysis (PCA) flow cytometer using the Guava Viacount software. Dilution factors and original sample volumes were entered as appropriate for each sample. Typically, 360 µL of Guava Viacount assay solution were added to 40 µL of cell suspension. Each sample was run in triplicate and 1000 events were acquired per sample.

III.ii. Results and Discussion

Cells were counted during incubation in cell media (control) or a 1 g/L solution of polymer with 100% of the linkers having ether-ester linked hydrocarbon side chains (#57). As mentioned, cells were plated at a cell density of 2×10^5 cells/mL 1 day before the start of the experiment. Cells were counted at time points corresponding to those in the cytotoxicity assay described in Chapter 3. The results are shown in Figure III.1. In the

FR- (HT-1080) cells, the cells grew at the same rate, ~ 3000 cells/mL/hr, when incubated in cell media or polymer solution. The cell growth in FR+ (KB) cells is less clear. It appears that the cells began the experiment in a lag phase of growth, however, the cells seem to have replicated between seeding the previous day and the start of the experiment, since at $t=0$ cells were at a density of $\sim 3.5 \times 10^5$ cells/mL. After the 24 hour time point, the cells proliferate, however the growth rates are different in cell media and polymer solution. Cells incubated in cell media grew at a rate of $\sim 20,000$ cells/mL/hr and cells incubated in polymer solution grew at a rate of $\sim 8,000$ cells/mL/hr. Overall, the cell density was not affected by incubation in polymer solution in either cell line, with the exception of the 48 hour time point in FR+ (KB) cells.

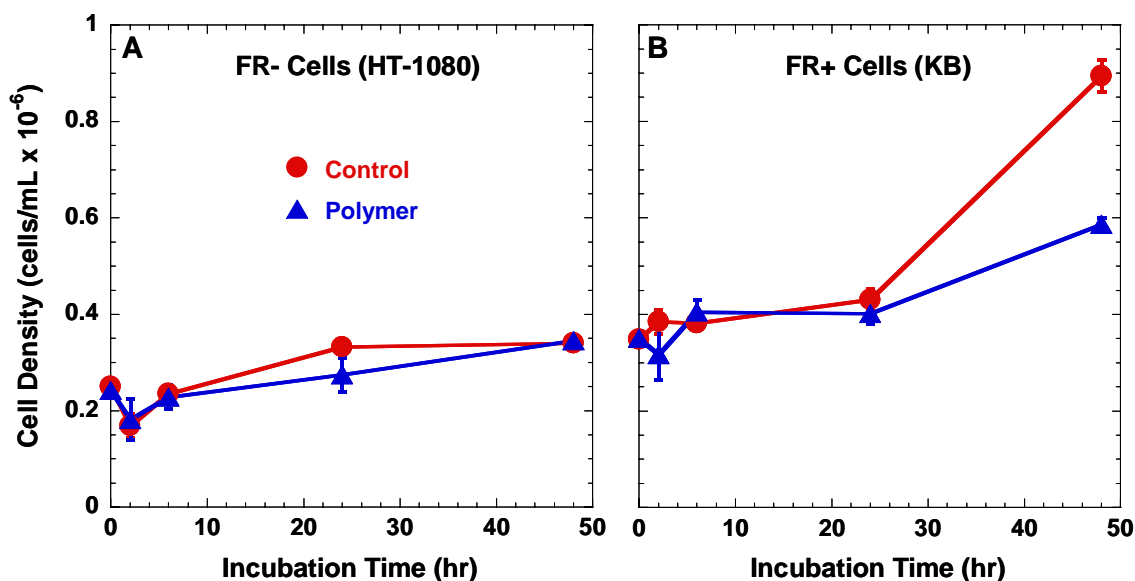


Figure III.1. Cell counting during incubation with cell media (control) or a 1 g/L solution of polymer with 100% of the linkers having ether-ester linked hydrocarbon side chains (#57) in FR- (HT-1080) and FR+ (KB) cells (n=3).

-Intentionally Left Blank-

Appendix IV. Validation of Scintillation Counting Sample Preparation

IV.i. Methods

IV.i.a. Materials and reagents

All polymers were provided by our collaborators in the Arthur Watterson lab at the University of Massachusetts, Lowell. All reagents were obtained from commercial sources. Phosphate buffered saline (PBS), distilled deionized sterile water, trypsin EDTA (1X, 0.25% trypsin/0.53 mM EDTA in HBSS), penicillin-streptomycin solution, and fetal bovine serum (FBS) were purchased from Mediatech, Inc. Minimum essential media, Eagle, with 2 mM L-glutamine and Earle's BSS adjusted to contain 1.5 g/L sodium bicarbonate, 0.1 mM non-essential amino acids, and 1.0 mM sodium pyruvate (EMEM) was purchased from ATCC. RPMI Medium 1640 (without folic acid) was purchased from GIBCO. ³H-folate was purchased from American Radiolabeled Chemicals, Inc. Guava Viacount assay kit was purchased from Guava Technologies/Millipore. Triton X-100 lysis buffer were purchased from EMD Chemicals. SOLVABLE™ was purchased from Perkin Elmer.

IV.i.b. Cell lines and culture

KB cells (human epidermoid carcinoma; FR+) were purchased from the American Type Culture Collection. KB cells were cultured in EMEM supplemented with 10% FBS

and 1% penicillin–streptomycin solution. All cells were grown at 37°C in a humidified atmosphere containing 5% CO₂.

IV.i.c. Validation of scintillation counting sample preparation

Cells were grown in RPMI Medium 1640 (without folic acid) supplemented with 10% FBS and 1% penicillin–streptomycin solution for 2 days before the experiment. Cells growing as a mono-layer were harvested with trypsin and seeded at a concentration of 1×10^6 cells/mL 1 day before the start of the experiment. Cells were incubated with ³H-folate (50 nM) or polymer with 98% of the linkers having PEG-3400-folate attached and the remaining 2% of the linkers having methyl groups containing ³H attached (#71) (50 nM, 500 nM, or 5 μM) at 37°C in a humidified 5% CO₂ atmosphere for 3 hours. At each time point, the cells were washed three times with 100 μL PBS. Cells were lysed by adding 100 μL lysis buffer. To half of the samples, 400 μL of deionized water and 3.5 mL of scintillation cocktail (Ultima Gold XR) were added. To the other half of the samples, 100 μL of SOLVABLE™, 300 μL of deionized water, and 3.5 mL of scintillation cocktail (Ultima Gold XR) were added. The samples were vortexed and then analyzed in a scintillation counter (Beckman Coulter LS6500 Multipurpose Scintillation Counter). All experiments were performed in triplicate. The activity of each sample was reported as counts per minute (CPM).

IV.i.d. Statistical analysis

All data are represented as mean ± standard deviation. Statistical insignificance ($p > 0.05$) was determined, where appropriate, by an unpaired, two-tailed Student t-test.

IV.ii. Results and Discussion

The purpose of this validation was to show that it was not necessary to use SOLVABLE to solubilize all of the cellular debris and that the scintillation counter results were the same in the presence or absence of SOLVABLE. The results for the case of the uptake of ^3H -folate in FR+ cells are shown in Figure IV.i. No statistically significant difference in activity was observed between cells treated with lysis buffer and cells treated with lysis buffer and SOLVABLE. The p-value calculated by the Student's t test was greater than 0.6, verifying that there was no statistical difference between the two sample preparation methods. The results for the case of the uptake of ^3H -polymer in FR+ cells are shown in Figure IV.ii. Notably, no statistically significant difference in activity between cells treated with lysis buffer and cells treated with lysis buffer and SOLVABLE was observed at any of the three concentrations. The p-value calculated by the Student's t test was greater than 0.3, additionally verifying that there was no statistical difference between the two sample preparation methods.

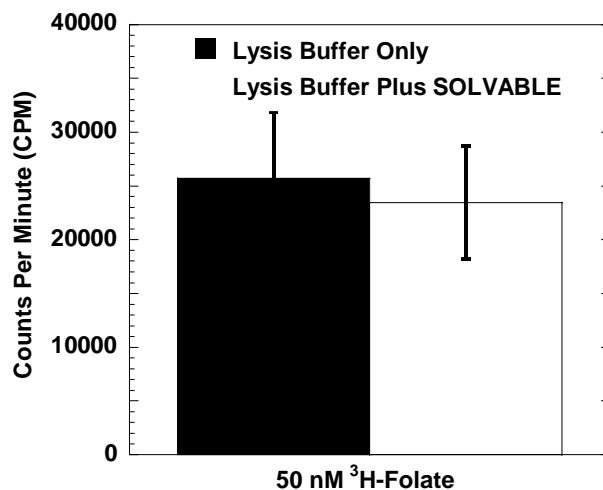


Figure IV.i. Validation of scintillation counting preparation method using 50 nM ³H-folate.

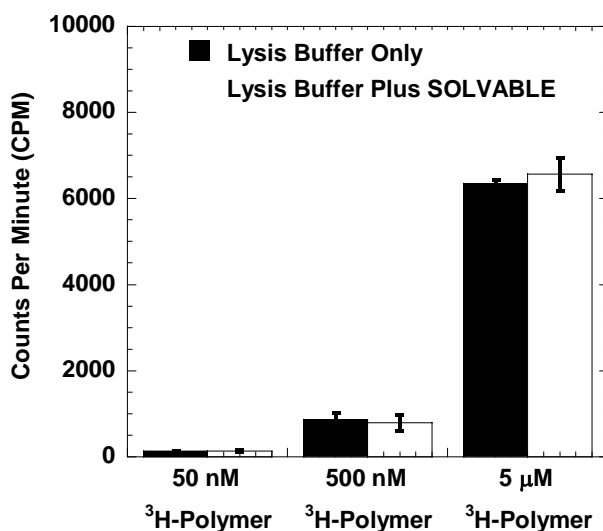


Figure IV.ii. Validation of scintillation counting preparation method using 50 nM, 500 nM, and 5 μM ³H-polymer.

Appendix V. Detailed Calculations for Theoretical Design of Targeting Polymers

V.i. Calculations for EPPT

V.i.a. Cooperativity polyvalency calculations

A cooperativity model from the literature [1], the derivation of which is shown in Chapter 4, can be used to calculate the apparent dissociation constant of a polyvalent particle containing EPPT from the equation

$$K_{D,Apparent} = (K_D)^{\alpha N} \quad (1)$$

where $K_{D,Apparent}$ is the apparent dissociation constant of a polyvalent particle, K_D is the dissociation constant for one ligand, α is the degree of cooperativity between ligands, and N is the number of ligands per particle. The binding of EPPT with the underglycosylated mucin-1 (uMUC1)-derived PDTRP epitope has a dissociation constant of 2.5×10^{-5} M [2]. For positive cooperativity, noncooperativity, and negative cooperativity, α is greater than 1, equals 1, and is less than 1, respectively, therefore for these calculations we chose values of 2, 1, and 0.5 for α . The results of these calculations are shown in Table V.i.

Table V.i. Calculated apparent dissociation constant, $K_{D,Apparent}$, for EPPT-containing particles from the cooperativity model.

N	$\alpha=2$	$\alpha=1$	$\alpha=0.5$
1	6.25×10^{-10}	2.50×10^{-5}	5.00×10^{-3}
2	3.91×10^{-19}	6.25×10^{-10}	2.50×10^{-5}
3	2.44×10^{-28}	1.56×10^{-14}	1.25×10^{-7}
4	1.53×10^{-37}	3.91×10^{-19}	6.25×10^{-10}
5	9.54×10^{-47}	9.77×10^{-24}	3.13×10^{-12}

V.i.b. Structural polyvalency calculations

A structural model from the literature [3], the description of which is given in Chapter 4, can be used to calculate the apparent dissociation constant of a polyvalent particle containing EPPT from the equations

$$K_{D,Apparent} = K_D (nBE)^{-1} \quad (2)$$

$$BE = F \left[sK_D^{-1} (10^{-2}) \right]^{n-1} \quad (3)$$

where $K_{D,Apparent}$ is the apparent dissociation constant of a polyvalent particle, K_D is the dissociation constant for the ligand, BE is the binding enhancement per ligand, F is a system-specific statistical factor, s is 30 divided by the distance between binding sites on the receptor, in Å, and n is the lesser of the number of binding sites on the receptor or the number of ligands or binding sites on the particle. Again, the binding of EPPT with the uMUC1-derived PDTRP epitope has a dissociation constant of 2.5×10^{-5} M [2]. The statistical factor, F, was assumed to be 1 based on the literature [3]. There are 60 carbon-carbon and carbon-nitrogen bonds in one 20 amino acid PDTRP repeat unit and the bond length of a carbon-carbon or carbon-nitrogen bond is ~150 pm. Therefore, the distance

between PDTRP sequences on uMUC1, assuming 100% underglycosylation, was calculated to be 90 Å. Therefore, s is equal to 0.33. The results of the calculations of apparent dissociation constants are shown in Table V.ii.

Table V.ii. Calculated apparent dissociation constant, $K_{D,Apparent}$, for EPPT-containing particles from the structural model.

n	BE	$K_{D,Apparent}$
1	1.0×10^0	2.5×10^{-5}
2	1.3×10^2	9.4×10^{-8}
3	1.8×10^4	4.7×10^{-10}
4	2.4×10^6	2.6×10^{-12}
5	3.2×10^8	1.6×10^{-14}

V.ii. Calculations for Folate

V.ii.a. Cooperativity polyvalency estimates

As with EPPT, the cooperativity model from the literature [1] can be used to calculate the apparent dissociation constant of a polyvalent particle containing folate from the equation

$$K_{D,Apparent} = (K_D)^{\alpha N} \quad (4)$$

where $K_{D,Apparent}$ is the apparent dissociation constant of a polyvalent particle, K_D is the dissociation constant for one ligand, α is the degree of cooperativity between ligands, and N is the number of ligands per particle. The folate receptor (FR) is a high affinity receptor for the small molecule folate, or folic acid, with a dissociation constant, K_D , for this binding event of 1×10^{-10} M [4-6]. For positive cooperativity, noncooperativity, and

negative cooperativity, α is greater than 1, equals 1, and is less than 1, respectively, therefore for these calculations we chose values of 2, 1, and 0.5 for α . The results of these calculations are shown in Table V.iii.

Table V.iii. Calculated apparent dissociation constant, $K_{D,Apparent}$, for folate-containing particles from the cooperativity model.

N	$\alpha=2$	$\alpha=1$	$\alpha=0.5$
1	1.00×10^{-20}	1.00×10^{-10}	1.00×10^{-5}
2	1.00×10^{-40}	1.00×10^{-20}	1.00×10^{-10}
3	1.00×10^{-60}	1.00×10^{-30}	1.00×10^{-15}
4	1.00×10^{-80}	1.00×10^{-40}	1.00×10^{-20}
5	1.00×10^{-100}	1.00×10^{-50}	1.00×10^{-25}

V.ii.b. Structural polyvalency estimates

Also as with EPPT, the structural model from the literature [3] can be used to calculate the apparent dissociation constant of a polyvalent particle containing folate from the equations

$$K_{D,Apparent} = K_D (nBE)^{-1} \quad (5)$$

$$BE = F \left[sK_D^{-1} (10^{-2}) \right]^{n-1} \quad (6)$$

where $K_{D,Apparent}$ is the apparent dissociation constant of a polyvalent particle, K_D is the dissociation constant for the ligand, BE is the binding enhancement per ligand, F is a system-specific statistical factor, s is 30 divided by the distance between binding sites on the receptor, in Å, and n is the lesser of the number of binding sites on the receptor or the number of ligands or binding sites on the particle. Again, the FR is a high affinity

receptor for folate with a dissociation constant, K_D , for this binding event of 1×10^{-10} M [4-6]. The statistical factor, F , was assumed to be 1 based on the literature [3]. GPI-anchored FRs are clustered in microdomains of around 70 nm in size containing approximately 50 FRs, therefore they are an average of 100 Å apart [7]. Therefore, s is equal to 0.30. The results of the calculations of apparent dissociation constants are shown in Table V.iv.

Table V.iv. Calculated apparent dissociation constant, $K_{D,Apparent}$, for folate-containing particles from the structural model.

n	BE	$K_{D,Apparent}$
1	1.0×10^0	1.0×10^{-10}
2	3.0×10^7	1.7×10^{-18}
3	9.2×10^{14}	3.6×10^{-26}
4	2.8×10^{22}	9.0×10^{-34}
5	8.4×10^{29}	2.4×10^{-41}

V.ii.c. Ligand tether length calculations

A geometric model was used, assuming spherical particles, to calculate the fraction of the surface area of the particle able to bind to the surface of the cell for a given tether length [8] in order to determine the length of the tether attaching the ligand to the polymer particles that is necessary to allow for polyvalency. This model was described in Chapter 4. Assuming that the tether is in a fully extended conformation and using simple geometry, the active fractional area of the carrier is given by

$$A = \frac{2\pi RH}{4\pi R^2} = \frac{H}{2R} \quad (7)$$

where R is the radius of the carrier and H is given by $L - d_B$ when $L \leq R + d_B$. Here, L is the sum of ligand length and the maximum extended length of the tether and d_B is the binding distance of the ligand and the receptor. The effect of tether length on binding distance was determined, as reported in the literature, by using a combination of Monte Carlo simulations, diffusion reaction theory, and surface force measurements [9]. When $L > R + d_B$, H becomes $R + x$, where x is the vertical distance above the horizontal line passing through the center of the carrier, indicating the position of the fully extended tether on the carrier surface that is tangent to the surface of the carrier and reaching the cell surface. These parameters are more clearly depicted in the schematic in Figure V.i. The MATLAB code used to calculate the active fractional area of the carrier as a function of tether length is shown. This analysis was performed at particle diameters of 10, 25, 50, 100, and 150 nm and for tethers from PEG 900 to PEG 10,000.

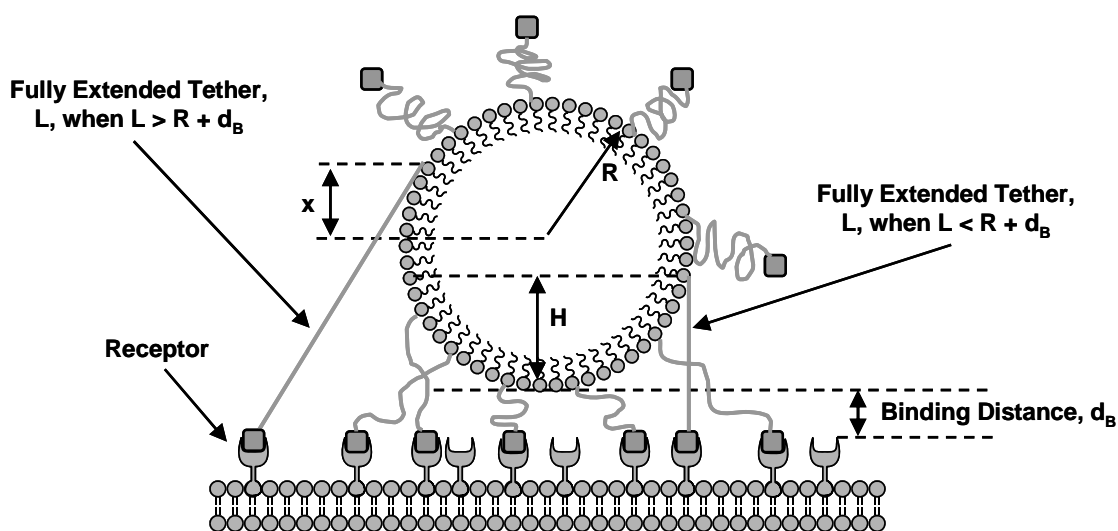


Figure V.i. Schematic of parameters used for ligand tether length calculations adapted from [8].

V.ii.c.1. MATLAB code for ligand tether length calculations

```

%Calculating Active Fractional Area of Carrier (AFAC)
%Reference: Ghaghada, Journal of Controlled Release, 104 (2005) 113-128

function AFAC = calc_AFAC_for_graph()

%Make a vector of carrier diameters and calculate the radius, R, in nm.
Carrier_diameter=[10, 25, 50, 100, 150];
R=Carrier_diameter/2;

%Make a vector of PEG molecular weights to base the calculation on and
calculate the tether length, L, in nm.
%Length of one PEG repeat is 350 pm.
%Length of folate calculated from Ghaghada (2005) to be 2.107 nm.
%Molecular weight of one PEG repeat is 44.
PEG_MW=900:100:10000;
L=(PEG_MW/44*350)/1000+2.107;

%Calculate binding distance, db, in nm.
%Reference: Jeppeson, Science, 293 (2001) 465-468
db=0.0036*PEG_MW+5.9968;

%Iterate through each carrier diameter and each PEG molecular weight.
for i=1:length(R);
    for j=1:length(L);
        if L(j) <= R(i) + db(j);
            H=L(j)-db(j);
        else L(j) > R(i) + db(j);
            x=calc_x(R(i),db(j),L(j));
            H=R(i)+x;
        end;
        AFAC(i,j)=H/(2*R(i));
    end;
end;

%Make a figure of the results.
figure;
plot(PEG_MW, AFAC);
axis square;
legend('10 nm', '15 nm', '20 nm', '25 nm', '50 nm', '75 nm', '100 nm',
'120 nm', '150 nm');
xlabel('PEG Molecular Weight');
ylabel('AFAC');

%Save the results in a text file.
save AFAC.txt AFAC -ASCII;

end

```

V.iii. Comparison to experimental data in literature

As mentioned in Chapter 4, the validity of the theoretical calculations, both polyvalency estimates and ligand tether length calculations, was tested by using experimental data from the literature. Moore et al. investigated the *in vitro* uptake of cross-linked iron oxide nanoparticles modified with Cy5.5 dye and carrying EPPT peptides attached to the dextran coat of the nanoparticles [10]. The structural properties of these nanoparticles reported in the literature (ie. 35.8 nm in size, 14 EPPT per particle) were used to calculate the active fractional area of the particle. Assuming the bond length of a carbon-carbon or carbon-nitrogen bond is ~ 150 pm, the length of a fully extended EPPT-FITC was calculated to be 9.6 nm. Since there was no tether used in these iron oxide particles, L , the sum of ligand length and the maximum extended length of the tether, used in the calculation of the active fractional area of the particle was 9.6 nm and d_B , the binding distance, was 6 nm. Since the diameter of the particle was 35.8 nm, the radius, R , was 17.9 nm, therefore H , given by $L - d_B$ since $L \leq R + d_B$, is 3.6 nm. The active fractional area of the particles was calculated to be $\sim 10\%$ of the surface, therefore ~ 1.4 EPPT were accessible per particle since there were 14 EPPT per particle. For the calculation of the apparent dissociation constant, $K_{D, \text{Apparent}}$, from the experimental data in Moore et al., see Appendix V.

V.iv. References

1. Hong, S., Leroueil, PR, Majoros, IJ, Orr, BG, Baker, JR Jr, Banaszak Holl, MM, The binding avidity of a nanoparticle-based multivalent targeted drug delivery platform. *Chem Biol*, 2007. 14(1): p. 107-15.
2. Sivolapenko, G.B., V. Douli, D. Pectasides, D. Skarlos, G. Sirmalis, R. Hussain, J. Cook, N.S. Courtenay-Luck, E. Merkouri, K. Konstantinides, and A.A. Epenetos, . Breast cancer imaging with radiolabelled peptide from complementarity-determining region of antitumour antibody. *Lancet*, 1995. 346: p. 1662-1666.
3. Gargano, J.M., T. Ngo, J.Y. Kim, D.W.K. Acheson, and W.J. Lees, Multivalent inhibition of ab5 toxins. *J. Am. Chem. Soc.*, 2001. 123: p. 12909-12910.
4. Kamen, B.A., Capdevila, A., Receptor-mediated folate accumulation is regulated by the cellular folate content. *PNAS*, 1986. 83: p. 5983-5987.
5. Leamon, C., Low, PS, Folate-mediated targeting: From diagnostics to drug and gene delivery. *Drug Discov Today*, 2001. 6(1): p. 44-51.
6. Low, P., Henne, WA, Doorneweerd, DD, Discovery and development of folic-acid-based receptor targeting for imaging and therapy of cancer and inflammatory diseases. *Acc Chem Res*, 2007. 41(1): p. 120-9.
7. Varma, R. and S. Mayor, Gpi-anchored proteins are organized in submicron domains at the cell surface. *Nature*, 1998. 394: p. 798–801.
8. Ghaghada, K., Saul, J, Natarajan, JV, Bellamkonda, RV, Annapragada, AV, Folate targeting of drug carriers: A mathematical model. *J Control Release*, 2005. 104(1): p. 113-28.
9. Jeppesen, C., J.Y. Wong, T.L. Kuhl, J.N. Israelachvili, N. Mullah, S. Zalipsky, and C.M. Marques, Impact of polymer tether length on multiple ligand–receptor bond formation. *Science*, 2001. 293: p. 465– 468.
10. Moore, A., Z. Medarova, A. Potthast, and G. Dai, In vivo targeting of underglycosylated muc-1 tumor antigen using a multimodal imaging probe. *Cancer Research*, 2004. 64: p. 1821-1827.

-Intentionally Left Blank-

Appendix VI. Theoretical Modeling of Cellular Uptake

VI.i. Analysis of EPPT cellular uptake

VI.i.a. Calculation of experimental specific uptake

Experimental specific uptake was calculated by subtracting non-specific uptake in the uMUC1- cell line from total uptake in uMUC1+ cell line. Figure VI.i shows the results of this calculation. The graph of the specific uptake can be used to estimate the kinetic parameters, such as the forward rate constant, k_f , and the reverse rate constant, k_r . The theoretical model discussed later is compared to this specific uptake data. Note that this calculation assumes that the non-specific uptake is equivalent in both cell lines.

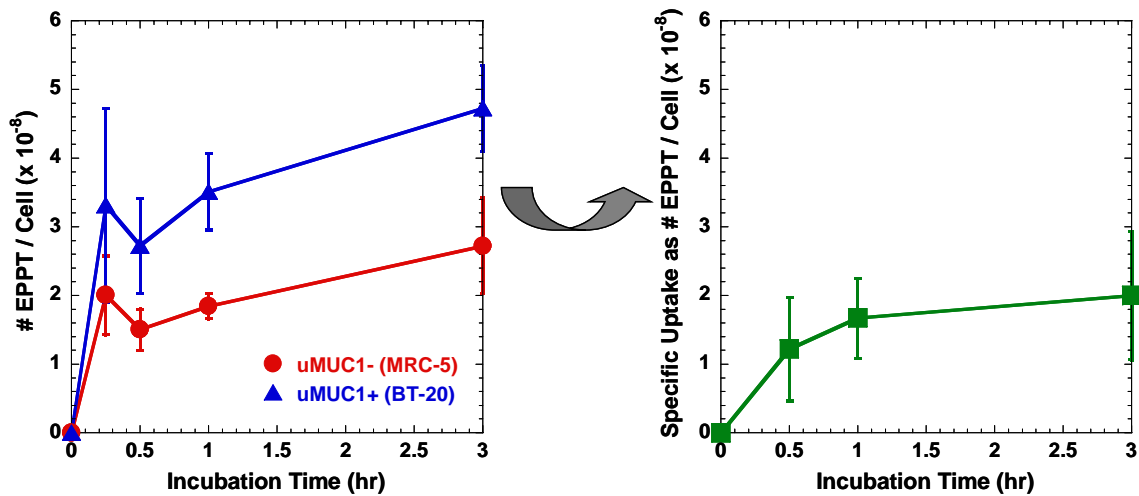


Figure VI.i. Calculation of specific uptake from total uptake in uMUC1+ cells and non-specific uptake in uMUC1- cells.

VI.i.b. Kinetic parameters for uptake model

VI.i.b.1. Scatchard analysis from literature

The number of underglycosylated mucin-1 (uMUC1) proteins per cell was not found in the literature. In order to estimate this value, a Scatchard plot analysis was performed on data of uptake of polyvalent particles containing EPPT from Moore et al. [1] to determine the number of uMUC1 proteins per cell for uMUC1+ (BT-20) cells. In the simplest case of binding



where P is the surface protein, here the uMUC1 protein, L is the ligand, here EPPT, and C is the complex of EPPT with the PDTRP sequence. It is assumed here that only one polyvalent nanoparticle can bind per uMUC1. At equilibrium,

$$K_D = \frac{k_r}{k_f} = \frac{[P][L]}{[C]} \quad (9)$$

where K_D is the dissociation constant for the binding interaction, k_f is the forward reaction rate, k_r is the reverse reaction rate, $[P]$ is the concentration of protein, $[L]$ is the concentration of ligand, and $[C]$ is the concentration of complex. By material balance,

$$[P] = [P]_o - [C] \quad (10)$$

where $[P]_o$ is the initial concentration of protein. This value represents the number of uMUC1 per cell. Inserting equation (3) into equation (2) gives

$$K_D = \frac{([P]_o - [C])[L]}{[C]} \quad (11)$$

which leads to

$$[C] = \frac{[P]_o [L]}{K_D + [L]} \quad (12)$$

Rearranging equation (5) gives

$$\frac{[C]}{[L]} = -\frac{1}{K_D} [C] + \frac{[P]_o}{K_D} \quad (13)$$

From this equation it is clear that plotting $[C]$ versus $[C]/[L]$ leads to a straight line with a slope of $-1/K_D$ and a y-intercept of $[P]_o/K_D$. Data was estimated for BT-20 cells from Figure 2 in Moore et al. [1] and plotted as $[C]$ versus $[C]/[L]$, as shown in Figure VI.ii. The slope of a linear fit to this line was -2×10^{-7} and the y-intercept was 9, therefore K_D was calculated to be 8×10^{-9} M and $[P]_o$, the number of uMUC1 per cell, was found to be 3×10^7 .

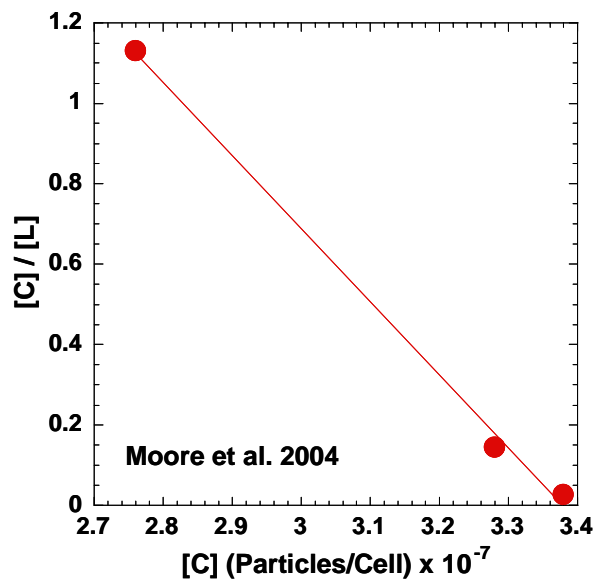


Figure VI.ii. Scatchard plot analysis using data from Moore et al. [1].

VI.i.b.2. Graphic analysis from experimental specific uptake

In order to pursue a theoretical model to describe the uptake of EPPT, kinetic parameters for the binding interaction were needed. The dissociation constant, K_D , for the interaction of EPPT with the PDTRP sequence has been reported in the literature as 2.5×10^{-5} M [2], however the forward and reverse reaction rates, k_f and k_r respectively, were not reported. The rate law describing the interaction of EPPT with PDTRP is given by

$$\frac{d[C]}{dt} = k_f [P][L] - k_r [C] \quad (14)$$

The experimental specific uptake calculated earlier can be used to estimate k_f and k_r using this equation. The specific uptake data is shown again in Figure VI.iii divided into two regions, I and II. During region I, the initial uptake period, the reverse reaction can be assumed to be zero, therefore the slope, $d[C]/dt$, can be used to calculate k_f given $[P]$ and $[L]$. From the slope of the dashed line for region I in Figure VI.iii, k_f was calculated to be $1.4 \times 10^{-4} \text{ M}^{-1} \text{ hr}^{-1}$. Given the calculated k_f , the full form of equation (7) was applied, using the slope of region II for $d[C]/dt$, to calculate k_r as $3.4 \times 10^{-9} \text{ hr}^{-1}$.

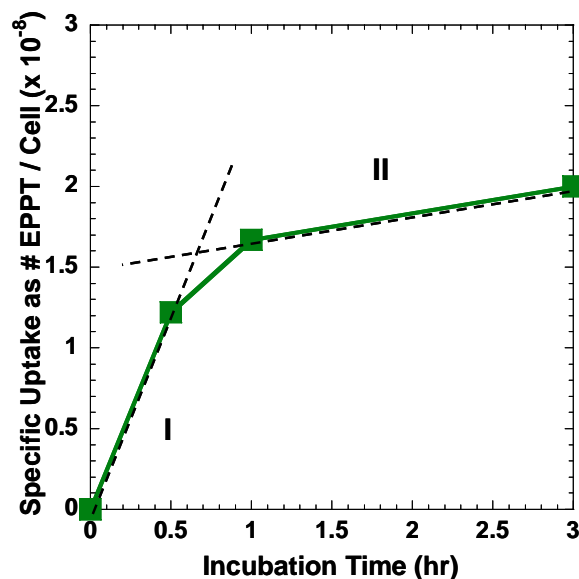


Figure VI.iii. Estimation of kinetic parameters from experimental uptake data.

VI.i.c. Theoretical model of EPPT cellular uptake

The parameters which have been described here, namely number of uMUC1 per cell, k_f , k_r , and K_D , can be used in a simple theoretical model of cellular uptake for the purpose of comparing to experimental data. The simplest model considers one EPPT binding per PDTRP sequence and no internalization into the cell. Attempts were made to include internalization in the model, but convergence of the ODE solver was never achieved. Since each uMUC1 protein contains 30-90 repeat units of the PDTRP sequence [3], the concentration of binding sites is p times $[P]$, where p , the number of PDTRP sequences per uMUC1, is conservatively assumed to be 30 for the following calculations. Including this in the rate law governing the interaction of EPPT and uMUC1 gives

$$\frac{d[C]}{dt} = k_f p [P][L] - k_r [C] \quad (15)$$

where k_f is the forward reaction rate, k_r is the reverse reaction rate, p is the number of PDTRP sequences per uMUC1, $[P]$ is the concentration of uMUC1, $[L]$ is the concentration of EPPT, and $[C]$ is the concentration of complexes of EPPT with PDTRP.

The material balances are

$$p[P] = p[P]_0 - [C] \quad (16)$$

$$[L] = [L]_0 - [C] \quad (17)$$

where $[P]_0$ is the initial concentration of uMUC1 and $[L]_0$ is the initial concentration of EPPT. The ordinary differential equation in (8) was solved using an ODE solver in MATLAB. The MATLAB code is shown below. The results of this calculation are shown in Figure VI.iv as compared to the experimental data. The theoretical model agrees well with the experimental data when 7-10 EPPT are bound per uMUC1.

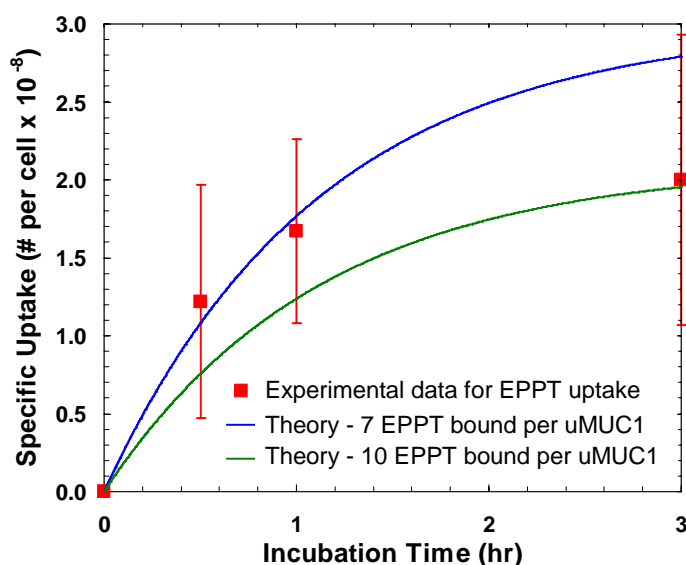


Figure VI.iv. Theoretical model of EPPT uptake compared to experimental data.

```
%EPPT Uptake Kinetic Model with Material Balance in BT20 cells.
%Notes: ONE Bond, no internalization, no clusters.
```

```

function uptake = EPPT_uptake_BT20_Cells()

clear;

%Definitions:
%N_T = Total number of surface receptors per cell for BT20 cells.
%kf = 2-D binding rate constant, nm^2/mol/hr.
%kr = 2-D dissociation rate constant, 1/hr.
%Kd = 2-D equilibrium constant, mol/nm^2.
%C_carrier_initial = Initial concentration of free carrier in solution,
mol/nm^3.
%C_carrier_total = Total concentration of free carrier per area,
mol/nm^2.
%C_carriers_free = Concentration of free receptors, mol/nm^2.
%C_receptors_free = Concentration of free receptors, mol/nm^2.
%C_bound = Concentration of bound carriers, mol/nm^2.
%N = number of cells per well.
%a = total number of ligands per carrier available for binding.
%b = total number of binding sites per receptor available for binding.

%Parameters:
C_carrier_initial=5.5e-5; %M
N_T=3e7; %Receptors/cell
Cells_per_well=50000; %Cells per well
Volume_per_well=100e-6; %Volume of solution in L
Volume_per_well=Volume_per_well*1e24; %Volume of solution in nm^3
Cells_per_volume=Cells_per_well/Volume_per_well; %Cells/nm^3
Cell_surface_area=5e8; %nm^2
Z=Cells_per_volume*Cell_surface_area; %nm^2/nm^3
C_carrier_total=C_carrier_initial/1e24/Z; %mol/nm^2
max_binding_per_receptor=10; %Assumed 10 carrier max bind per receptor.
C_receptors_initial=N_T*max_binding_per_receptor/Cell_surface_area/6e23
; %mol/nm^2
C_receptors_total=C_receptors_initial; %mol/nm^2
p=30;

%Rate Constants:
Kd=2e-5; %M (Moore, 2004. Sivolapenko, 1995 gives 2.5e-5 M.)
Kd=Kd/1e24; %mol/nm^3
Kd=Kd/Z; %mol/nm^2
kf=1.35e4; %1/M/hr
kf=kf*1e24; %nm^3/mol/hr
kf=kf*Z; %nm^2/mol/hr
kr=kf*Kd; %1/hr

a=1;
b=p;
Inputs = [kf, kr, C_carrier_total, C_receptors_total, a, b];
tspan=[0 3];
[T,uptake]=ode15s(@EPPT_uptake_ODEs,tspan,0,[],Inputs);

%Make figures of the results.
uptake=uptake*Cell_surface_area*6e23;
uptake(:,2)=C_carrier_total*Cell_surface_area*6e23-uptake(:,1);
uptake(:,3)=C_receptors_total*Cell_surface_area*6e23-uptake(:,1);
t_expt=[0 0.5 1 3];

```

```

uptake_expt=[0 1.22e8 1.67e8 2e8];
std_dev=[0 0.751000477e8 0.588744352e8 0.931897145e8];
figure;
subplot(4,1,1);
errorbar(t_expt, uptake_expt,std_dev,'ro');
axis([0 3 0 3e8]);
xlabel('Time (hr)');
ylabel('Number per cell');
legend('Bound Ligand - Experiment');
subplot(4,1,2);
plot(T, uptake(:,1));
xlabel('Time (hr)');
ylabel('Number per cell');
legend('Bound Ligand - Theory');
subplot(4,1,3);
plot(T, uptake(:,2));
xlabel('Time (hr)');
ylabel('Number per cell');
legend('Free Ligand');
subplot(4,1,4);
plot(T, uptake(:,3));
xlabel('Time (hr)');
ylabel('Number per cell');
legend('Free Receptors');

%Save the results in a text file.
save('EPPT_Uptake_BT20_Cells.txt','uptake','-ASCII');
save('EPPT_Uptake_BT20_Cells_Time.txt','T','-ASCII');
save
('EPPT_Uptake_BT20_Cells_Variables.txt','a','b','max_binding_per_receptor',
'N_T','-ASCII');

end

%EPPT Uptake Kinetic Model with Material Balance - Differential
Equations

function dC_dt = EPPT_uptake_ODEs(t,C,Inputs)

%C = [C_bound]
%Inputs = [kf, kr, C_carrier_total, C_receptors_total, a, b]
kf=Inputs(1);
kr=Inputs(2);
C_carrier_total=Inputs(3);
C_receptors_total=Inputs(4);
a=Inputs(5);
b=Inputs(6);

dC_dt(1)=kf*a*(C_carrier_total-C(1))*b*(C_receptors_total-C(1))-
kr*C(1);

return;

```

VI.ii. Analysis of folate cellular uptake

VI.ii.a. Scatchard analysis from experimental data

The number of folate receptors (FRs) per cell was calculated from experimental data as described in section VI.i.b.1. Again using the equation,

$$\frac{[C]}{[L]} = -\frac{1}{K_D}[C] + \frac{[P]_o}{K_D} \quad (18)$$

experimental data of folate uptake, from Figure 4.19 in Chapter 4, was plotted as $[C]$ versus $[C]/[L]$. The plotted data is shown in Figure VI.v and the resulting $[P]_o$, the number of FRs per cell, was found to be 3×10^7 . This value was used in the theoretical model of folate uptake discussed in the next section.

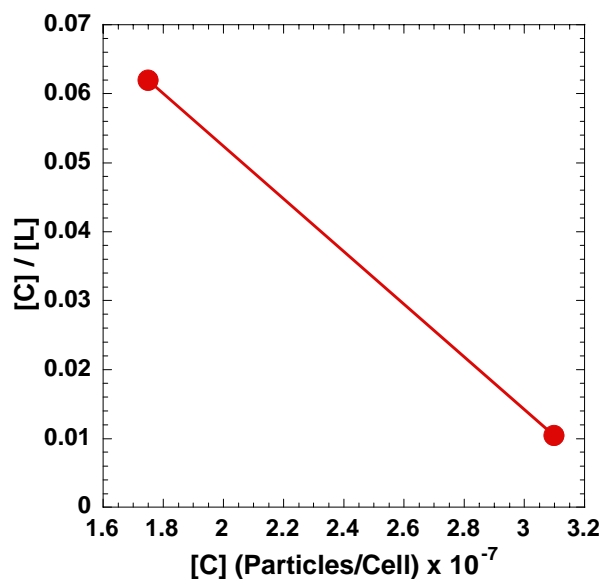


Figure VI.v. Scatchard plot analysis using experimental data of folate uptake.

VI.ii.b. Theoretical model of folate cellular uptake

The same simple theoretical model of cellular uptake that was used for EPPT was used to predict the uptake of folate. The number of FRs per cell was as calculated earlier and K_D , k_f , and k_r were from the literature [4, 5]. In the case of folate, only one folate could bind per FR, therefore the parameter p used for EPPT is not necessary here. Again the model considers one binding event and no internalization into the cell. Once more, attempts were made to include internalization in the model, but convergence of the ODE solver was never achieved. The rate law governing the interaction is

$$\frac{d[C]}{dt} = k_f [P][L] - k_r [C] \quad (19)$$

where k_f is the forward reaction rate, k_r is the reverse reaction rate, $[P]$ is the concentration of FRs, $[L]$ is the concentration of folate, and $[C]$ is the concentration of complexes of folate with FR. The material balances are

$$[P] = [P]_o - [C] \quad (20)$$

$$[L] = [L]_o - [C] \quad (21)$$

where $[P]_o$ is the initial concentration of FR and $[L]_o$ is the initial concentration of folate. The ordinary differential equation in (12) was solved using an ODE solver in MATLAB. The MATLAB code is shown below. The results of this calculation are shown in Figure VI.vi as compared to the experimental data from Figure 4.19 in Chapter 4. The theoretical model agrees well with the experimental data at long times, although at early times there is some disagreement.

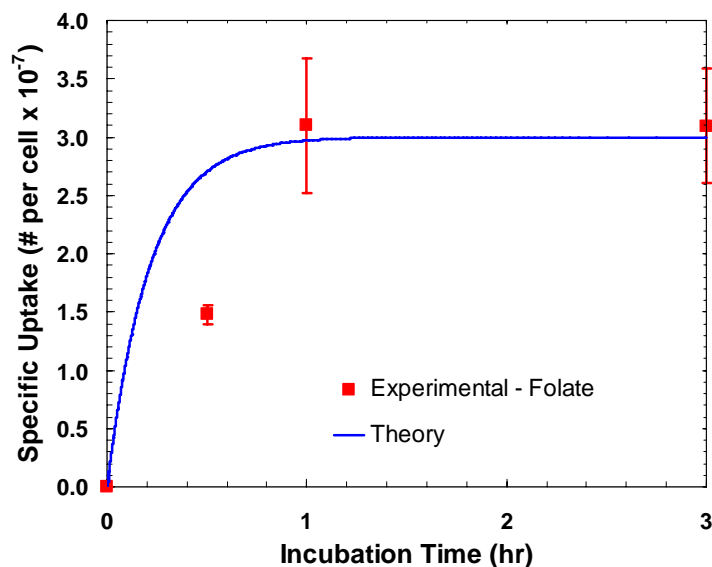


Figure VI.vi. Theoretical model of folate uptake compared to experimental data.

```
%Folate Uptake Kinetic Model with Material Balance in KB cells.
%Reference: Ghaghada, Journal of Controlled Release, 104 (2005) 113-128
%Note: This analysis does NOT include downregulation of the folate
receptor
%when the threshold concentration is reached.
%Note: ONE Bond, no internalization, no clusters.
```

```
function uptake = folate_uptake_KB_Cells()

clear;

%Definitions:
%N_T = Total number of surface receptors per cell for KB cells.
%kf = 2-D binding rate constant, nm^2/mol/hr.
%kr = 2-D dissociation rate constant, 1/hr.
%Kd = 2-D equilibrium constant, mol/nm^2.
%C_carrier_initial = Initial concentration of free carrier in solution,
mol/nm^3.
%C_carrier_total = Total concentration of free carrier per area,
mol/nm^2.
%C_carriers_free = Concentration of free receptors, mol/nm^2.
%C_receptors_free = Concentration of free receptors, mol/nm^2.
%C_bound = Concentration of bound carriers, mol/nm^2.
%N = number of cells per well.
%a = total number of ligands per carrier available for binding.
%b = total number of binding sites per receptor available for binding.

%Parameters:
C_carrier_initial=5e-6; %M
N_T=3e7; %From Scatchard plot analysis of experimental data.
Cells_per_well=100000; %Cells per well
```

```

Volume_per_well=100e-6; %Volume of solution in L
Volume_per_well=Volume_per_well*1e24; %Volume of solution in nm^3
Cells_per_volume=Cells_per_well/Volume_per_well; %Cells/nm^3
Cell_surface_area=5e8; %nm^2
Z=Cells_per_volume*Cell_surface_area; %nm^2/nm^3
C_carrier_total=C_carrier_initial/1e24/Z; %mol/nm^2
max_binding_per_receptor=1; %Assumed 10 carrier max bind per receptor.
C_receptors_initial=N_T*max_binding_per_receptor/Cell_surface_area/6e23
; %mol/nm^2
C_receptors_total=C_receptors_initial; %mol/nm^2
a=1;
b=1;

%Rate Constants:
Kd=1e-10; %M (Low, P., et al., Acc Chem Res, 2007. 41(1): p. 120-9.)
Kd=Kd/1e24; %mol/nm^3
Kd=Kd/Z; %mol/nm^2
kf=1.5524e4; %1/M/min %Reference: Ghaghada, Journal of Controlled
Release, 104 (2005) 113-128
kf=kf*60; %1/M/hr
kf=kf*1e24; %nm^3/mol/hr
kf=kf*Z; %nm^2/mol/hr
kr=kf*Kd; %1/hr

Inputs = [kf, kr, C_carrier_total, C_receptors_total, a, b];
tspan=[0 3];
[T,uptake]=ode15s(@folate_uptake_ODEs,tspan,0,[],Inputs);

%Make figures of the results.
uptake=uptake*Cell_surface_area*6e23;
uptake(:,2)=C_carrier_total*Cell_surface_area*6e23-uptake(:,1);
uptake(:,3)=C_receptors_total*Cell_surface_area*6e23-uptake(:,1);
t_expt=[0 0.5 1 3];
uptake_expt=[0 8.71e6 1.06e7 1.27e7];
std_dev=[0 4.66e5 4.83e5 5.20e5];
figure;
subplot(4,1,1);
errorbar(t_expt, uptake_expt,std_dev,'ro');
axis([0 3 0 2e7]);
xlabel('Time (hr)');
ylabel('Number per cell');
legend ('Bound Ligand - Experiment');
subplot(4,1,2);
plot(T, uptake(:,1));
xlabel('Time (hr)');
ylabel('Number per cell');
legend ('Bound Ligand - Theory');
subplot(4,1,3);
plot(T, uptake(:,2));
xlabel('Time (hr)');
ylabel('Number per cell');
legend ('Free Ligand');
subplot(4,1,4);
plot(T, uptake(:,3));
xlabel('Time (hr)');
ylabel('Number per cell');

```

```
legend ('Free Receptors');

%Save the results in a text file.
save ('Folate_Uptake_KB_Cells.txt', 'uptake', '-ASCII');
save ('Folate_Uptake_KB_Cells_Time.txt', 'T', '-ASCII');
save
('Folate_Uptake_KB_Cells_Variables.txt', 'a', 'b', 'max_binding_per_recept
or', 'N_T', '-ASCII');

end

%Folate Uptake Kinetic Model with Material Balance - Differential
Equations

function dC_dt = folate_uptake_ODEs(t,C,Inputs)

%C = [C_bound]
%Inputs = [kf, kr, C_carrier_total, C_receptors_total, a, b]
kf=Inputs(1);
kr=Inputs(2);
C_carrier_total=Inputs(3);
C_receptors_total=Inputs(4);
a=Inputs(5);
b=Inputs(6);

dC_dt(1)=kf*a*(C_carrier_total-C(1))*b*(C_receptors_total-C(1))-
kr*C(1);

return;
```

VI.iii. References

1. Moore, A., Z. Medarova, A. Potthast, and G. Dai, In vivo targeting of underglycosylated muc-1 tumor antigen using a multimodal imaging probe. *Cancer Research*, 2004. 64: p. 1821-1827.
2. Sivolapenko, G.B., V. Douli, D. Pectasides, D. Skarlos, G. Sirmalis, R. Hussain, J. Cook, N.S. Courtenay-Luck, E. Merkouri, K. Konstantinides, and A.A. Epenetos, . Breast cancer imaging with radiolabelled peptide from complementarity-determining region of antitumour antibody. *Lancet*, 1995. 346: p. 1662-1666.
3. Barratt-Boyes, S.M., Making the most of mucin: A novel target for tumor immunotherapy. *Cancer Immunology, Immunotherapy*, 1996. 43: p. 142-151.
4. Ghaghada, K., Saul, J, Natarajan, JV, Bellamkonda, RV, Annapragada, AV, Folate targeting of drug carriers: A mathematical model. *J Control Release*, 2005. 104(1): p. 113-28.
5. Low, P., Henne, WA, Doorneweerd, DD, Discovery and development of folic-acid-based receptor targeting for imaging and therapy of cancer and inflammatory diseases. *Acc Chem Res*, 2007. 41(1): p. 120-9.

Appendix VII. Kinetic Analysis of Experimental Uptake of EPPT and EPPT-Containing Polymer

VII.i. Analysis of kinetics of cellular uptake

VII.i.a. Separation of internalized and surface bound material

An analysis of the kinetics of the binding and internalization of EPPT and EPPT-containing polymer can be performed from the experimental uptake data. It was assumed that a line can be fit to the data for the long times and extrapolated back to the y-axis. A horizontal line from this point on the y-axis, parallel to the x-axis, indicates the level of surface bound peptide or polymer. The value between this horizontal line and the linear fit to the long time data points gives the internalized peptide or polymer. These analyses are shown in Figure VII.i for EPPT peptide, Figure VII.ii for polymer with 5% EPPT and 95% hydrocarbon side chains (#37), and Figure VII.iii for polymer with 5% EPPT and 5% FITC with no other side chains (#39).

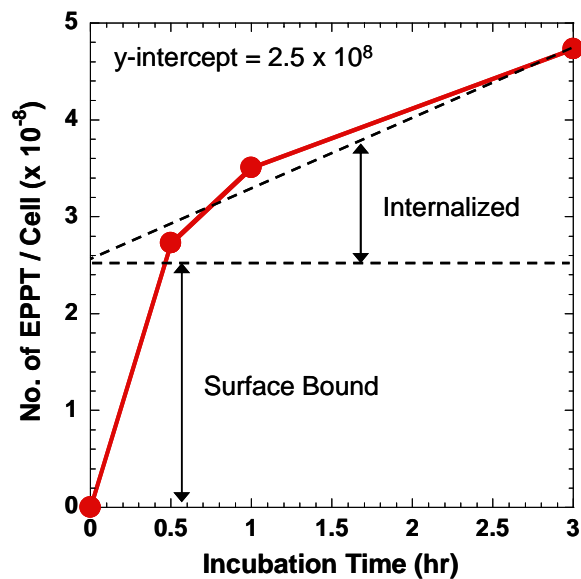


Figure VII.i. Separation of surface bound and internalized EPPT peptide.

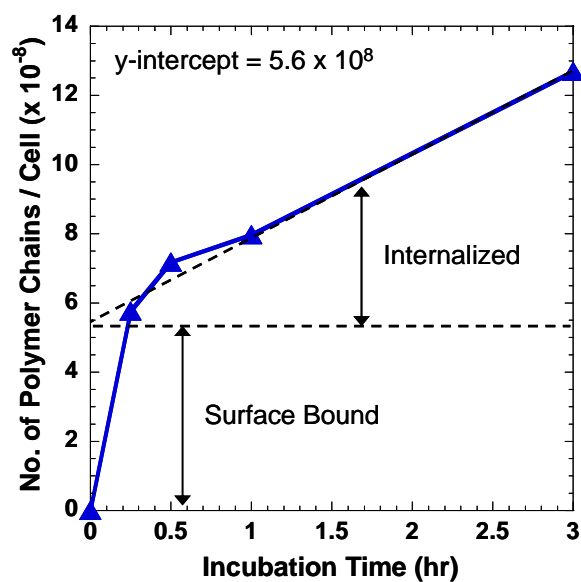


Figure VII.ii. Separation of surface bound and internalized polymer with 5% EPPT (#37).

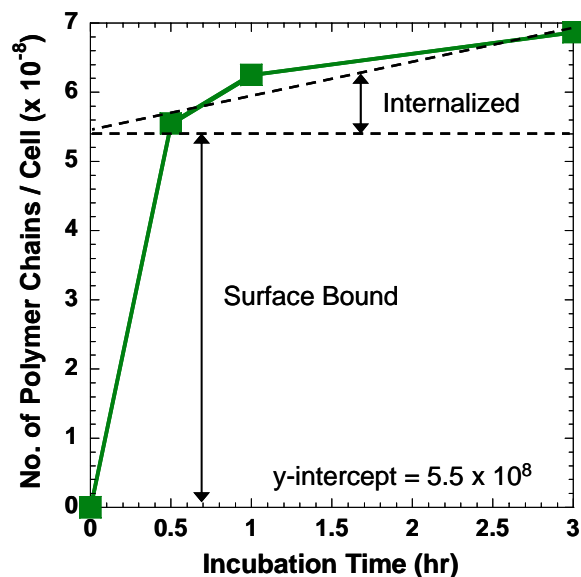


Figure VII.iii. Separation of surface bound and internalized polymer with 5% EPPT and 5% FITC (#39).

VII.i.b. Comparison of internalized and surface bound material for EPPT peptide and EPPT-containing polymer

The surface bound and internalized amounts can be compared between EPPT peptide, polymer with 5% EPPT (#37) and polymer with 5% EPPT and 5% FITC (#39), as shown in Figure VII.iv. The amount of surface bound polymer is ~2X that of EPPT. This is likely due to the formation of polymer micelles such that several polymer chains were bound for each EPPT bound on the micelle. In addition, the rate of internalization of polymer with 5% EPPT is ~3X that of EPPT and polymer with 5% EPPT and 5% FITC. Again this can be explained by several polymer chains being internalized per EPPT due to the formation of micelles.

APPENDIX VII. KINETIC ANALYSIS OF EXPERIMENTAL UPTAKE OF EPPT AND EPPT-CONTAINING POLYMER

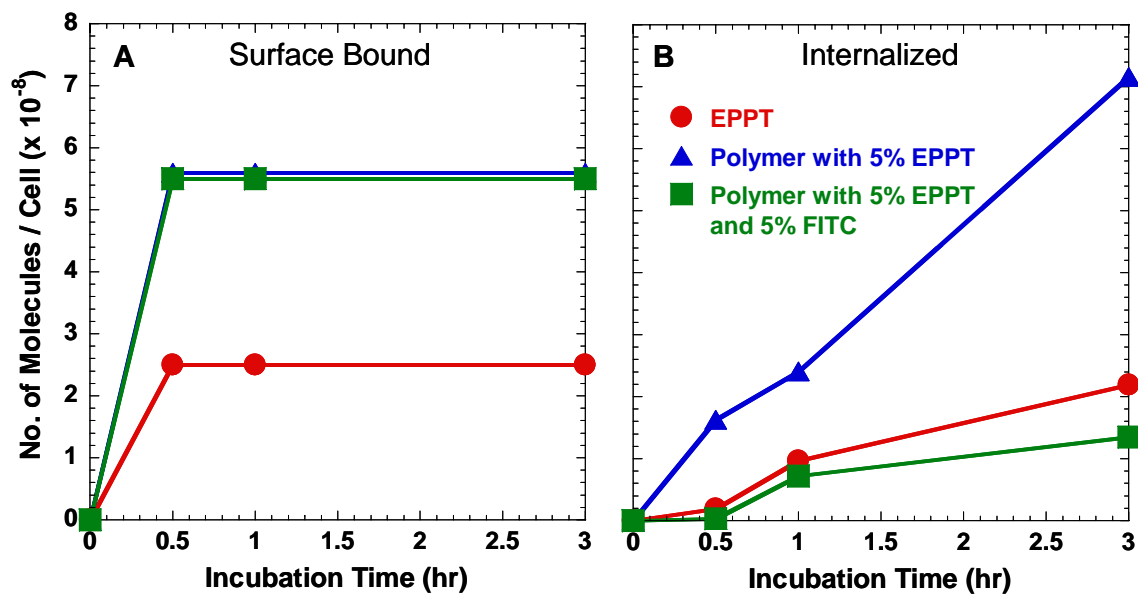


Figure VII.iv. Comparison of surface bound and internalized EPPT peptide, polymer with 5% EPPT (#37), and polymer with 5% EPPT and 5% FITC (#39).